Reactive Inkjet Printing of Novel Silk Dental Barrier Membranes

By:

Patrick Michael Rider

A thesis submitted in partial fulfilment of the requirements for the degree of

Doctor of Philosophy

The University of Sheffield

Faculty of Medicine, Dentistry and Health

School of Clinical Dentistry

March 2017

Acknowledgements

I would firstly like to thank Nobel Biocare for the research grant that made this research a possibility. I would like to convey my gratitude to my supervisors, Professor Ian Brook for organising the funding that made this research a reality, Dr Cheryl Miller for her support and believing in me, and Dr Patrick Smith for always having an open door to give me advice and provide me with inspiration. I would also like to sincerely thank Dr Robert Moorhead, who acted as maternity cover whilst I was writing up, and was very helpful in putting this thesis together. I would like to give my sincerest thanks to all of my supervisors, who supported me in my decision to move to Germany whilst I was writing up.

I am thankful to Dr Aileen Crawford who provided advice on my tissue culture studies. I would also like to thank my fellow researchers whom have provided their expertise; Dr Caroline Wilcock and Dr Yulia Ryabenkova for showing me how to synthesise and analyse nano-hydroxyapatite, Dr Jill Callaghan for teaching me the basics of tissue culture, and Dr Jonathan Stringer who was always there to provide support in the inkjet lab.

I would also like to express my deepest gratitude to my family for their constant support and encouragement. They have always let me know that I can achieve anything I put my mind to. Finally, I would like to thank Anuschka, for her infinite patience, her calming influence, and her never-ending support, for which I am eternally grateful.

Abstract

Periodontitis is a dental disease which can result in a loss of integrity of the periodontal tissues and lead to eventual tooth loss. Barrier membranes can be used in conjunction with guided bone regeneration (GBR) to help repair the damage caused by periodontitis. GBR promotes and directs the growth of new bone, whilst the barrier membrane secludes the defect site from infiltration by fast growing connective and epithelial tissues which would otherwise fill the defect space. The ideal properties for a barrier membrane are: to have a controllable degradation rate, be biocompatible, prevent surrounding tissues from collapsing into the defect space, and provide cell occlusivity.

Current commercial barrier membranes are produced out of materials which are either non-resorbable, requiring a secondary surgery for their extraction, or made from resorbable materials which can have poor structural integrity or degrade into acidic by-products. Silk has had a long history of use as a biomaterial. It degrades into non-toxic components and has adaptable mechanical properties. When used in its regenerated silk fibroin form (RFS), it has recently been used for tissue engineering scaffolds.

RSF has several polymorphs of which silk I and silk II are of interest. Silk I is non-crystalline and water soluble while silk II has a crystalline β-sheet structure that is non-water soluble. Silk I converts to silk II upon exposure to methanol, heat treatments and stretching. The ability to transform RSF from a water soluble structure into a non-water soluble structure makes it ideal for a variety of processing techniques.

In this thesis, reactive inkjet printing has been investigated as a possible processing method of RSF for the manufacture of barrier membranes. Reactive inkjet printing has been used to control the structural conversion of silk I to silk II by printing different volumes of methanol during film fabrication.

It was established that RSF crystallinity (and silk II content) was dependant on the volume of methanol printed. RSF film degradation rate was shown to be related to RSF crystallinity, and hence the volume of printed methanol. Cell studies performed on the RSF films showed that MG-63 osteosarcoma cells remained metabolically active and continued to proliferate during the duration of the study, as well as showing signs of osteogenic activity.

RSF films were investigated with the inclusion of nano-hydroxyapatite (nHA) to promote osteogenic activity. nHA/RSF films were produced from a composite ink containing both nHA and RSF. It was found that the inclusion of nHA within the ink impeded the transition of silk I to silk II, and instead increased β-turn structural content, which is an intermediate structure in the transition of silk I to silk II. The inclusion of nHA within the RSF films was shown to improve the osteogenic response of the MG-63 cells.

Overall, the work presented in this thesis has demonstrated for the first time that reactive inkjet printing can produce biocompatible RSF films with controllable crystallinity and degradation rate. As a result, a controllable degradation rate, the possibility of including bioactive components such as nHA, in addition to the other promising properties of RSF, make reactively inkjet printed RSF as a viable alternative for use as a barrier membrane.

Table of Contents

Abbreviations

Ala	Alanine
ALP	Alkaline Phosphatase
ATR	Attenuated Total Reflection
BCP	Biphasic Tricalcium Phosphate
BMP	Bone Morphogenetic Protein
dH_2O	Distilled Water
DoD	Drop on Demand
dPTFE	Dense Polytetrefluoroethylene
dsDNA	Double Stranded DNA
ECM	Extra Cellular Matrix
ePTFE	Expanded Polytetrafluoroethylene
FSD	Fourier Self Deconvolution
FTIR	Fourier Transform Infrared Spectroscopy
FWHM	Full Width at Half Maximum
GBR	Guided Bone Regeneration
Gly	Glycine
HA	Hydroxyapatite
hMSC	Human Mesenchymal Stem Cells
LiBr	Lithium Bromide
nAP	Nano-Apatite
nHA	Nano-Hydroxyapatite
$nTiO_2$	Titanium Dioxide Nanoparticles
Oh	Ohnesorge Number
p-NPP	Para-Nitrophenyl Phosphate
PBS	Phosphate Buffered Saline
PCL	Polycaprolactone
PEG	Poly(ethylene glycol)
PGA	Polyglycolic Acid
PLA	Polylactic Acid
PLGA	Poly(lactic-co-glycolic acid)
RIJ	Reactive Inkjet Printing
RSF	Regenerated Silk Fibroin
SEM	Scanning Electron Microscopy
Ser	Serine
TCP	Tricalcium Phosphate
TEM	Transmission Electron Microscopy
Tyr	Tyrosine
XRD	X-Ray Diffraction
β-TCP	Beta Tricalcium Phosphate

Table of Figures

Table of Tables

Table of Equations

Chapter 1: Literature Review

1.1   Introduction

This chapter will explain the periodontal region and what can go wrong, current methods to repair damage caused by periodontitis focusing on barrier membranes used for guided bone regeneration (GBR). It will then explore the commercially available membranes, current research for producing the ideal membrane and the materials being used. It will then discuss regenerated silk fibroin (RSF) as an alternative material to the current commercially used materials with the possibility of using reactive inkjet printing as a way of processing the RSF to produce a barrier membrane.

1.2   Periodontal Region

1.2.1   Tooth Structure

The periodontium consists of tissues which surround and support teeth. Teeth perform many important functions on a day to day basis. They are mainly used as tools for eating by mechanically breaking down food, but also play a role in vocal, social communication and social interaction. Teeth along with the lips, tongue and palette are used in the formation of different sounds.

Figure 1.1 outlines the main structures of the tooth and surrounding periodontal tissues. Each tooth is coated with a layer of enamel where the tooth protrudes out of the gums. Enamel is the hardest and most mineralised tissue of the body. The hardness of enamel enables the teeth to slice and grind food without wearing down. Underneath the enamel is dentin which helps to support the enamel by dissipating the forces applied during mastication. Enamel is quite brittle and could shatter without proper support. The tooth root begins under the gum line where the layer of enamel ends, and is coated in cementum. Pulp, situated in the central region of the tooth, is a soft connective tissue containing blood vessels and nerves. The nerves and blood vessels enter and exit the teeth via the apex of the tooth root which is anchored to the periodontium via the maxilla and mandible bones.

The periodontium consists of multiple tissues which provide support for the teeth, anchor the teeth to either the maxilla or mandible bones and supplies nourishment. During mastication the periodontium dissipates forces applied to the teeth, thereby avoiding injury to the teeth and surrounding bone. Cementum is a calcified connective tissue which covers the root surface. It is avascular, receiving nutrition from periodontal ligament fibres which are anchored to its surface. Periodontal ligament fibres are attached between cementum and alveolar bone and act as shock absorbance and to dissipate forces. The alveolar bone provides support for the teeth and the gingival tissues.
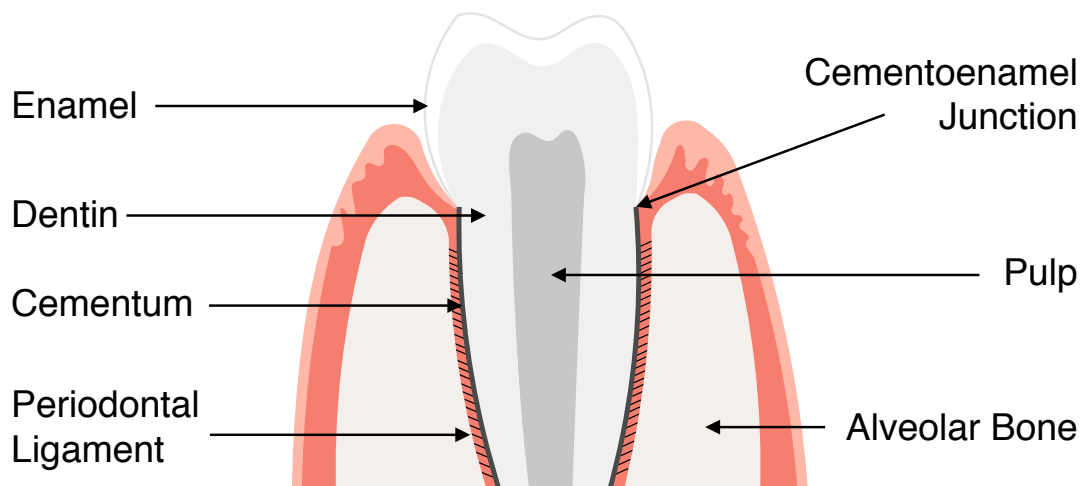
Figure 1.1: Illustration of the tooth structure and surrounding periodontal tissues

1.2.2 Dental Health

Problems can occur with teeth which impede their function and cause pain. Common oral health issues include the development of caries (cavities), which occur when there is a build-up of plaque and tartar over the teeth. Plaque is a film of bacteria and their secretions which develops after eating and drinking, especially after the consumption of sugary foods. Plaque is easily removed by brushing, however when left for long periods of time the thin film begins to mineralise and harden forming tartar. The removal of tartar requires a dentist to scrape it from the tooth. When plaque and tartar remain on the tooth the bacteria begin to erode the enamel.

Another way in which the enamel can be removed is through acid erosion. This occurs when lots of acidic food and drink is consumed. When something acidic is consumed a little bit of mineral is lost from the enamel surface causing it to soften. Over time

the acidity is neutralised by saliva and the tooth is restored to its hardened state, however regularly eating or drinking acidic products prevents the neutralisation process from occurring enabling the enamel to be more easily removed. Once a hole in the enamel occurs the bacteria are able to damage in inner structure of the tooth.

Other problems which can develop are gingivitis and periodontitis. Gingivitis and periodontitis are caused by poor dental hygiene. Gingivitis is the inflammation of the surface of the gums around the teeth caused by bacteria adhered to the tooth surface. Periodontitis is the inflammation of the supporting structures of the tooth. Unlike gingivitis, periodontitis is destructive causing a loss of alveolar bone around the base of the tooth. This report will concentrate on the damage caused by periodontitis and solutions for restoring the periodontium.

1.2.3   Periodontitis

Periodontitis is a disease caused by bacterial stimulation which begins with a chronic inflammation reaction and an immune response. A prolonged exposure to the bacteria results in a loss of integrity of the periodontal tissues. Soft tissues detach from the tooth as the gingival margin separates from the tooth surface leading to root exposure, known as gingival recession. As the alveolar bone around the root of the tooth disintegrates a gap known as a periodontal pocket is formed around the tooth. This secluded environment provides a breeding ground for anaerobic bacteria to colonize [1]. If untreated, periodontitis can eventually result in tooth loss.

Due to medical advancements and improved standards of living, first world countries have an increasing elderly population. Eke *et al.* studied the prevalence of periodontitis along with its severity among the data of 3,742 adults aged 30 years and over, collected by the National Health and Nutrition Examination Survey (NHANES) cycle between 2009 and 2010. Their data showed that periodontitis of a mild to severe form was present in 24.4 % of adults aged between 30 and 34 years. This increased to 70.1 % of adults aged 65 years and over [2].

1.2.4 Periodontitis Treatments

1.2.4.1 Non-Surgical Treatment

Once a periodontal disease has been established within a patient, further damage to the periodontium can be prevented through clinical and surgical intervention. Non-surgical approaches are aimed at reducing infective components and the reattachment of the gingival epithelium to a cleaned root surface [3]. Plaque control is a crucial part in treating periodontitis, and patients are given an oral hygiene education which includes instructions on tooth brushing and interdental cleaning. Plaque and tartar can be scraped from the surface of the enamel by the dentist, however remnants of tartar can remain attached to the cementum which could promote mineralisation of new plaque [3].

To clean the cementum and the periodontal pocket, root surface debridement is performed on patients with a periodontal pocket depth of 4 mm or larger [4]. Root surface debridement removes the bacterial plaque biofilm and tartar on the root surface and within the periodontal pocket. Antibiotics can be used in combination with root surface debridement to eliminate remaining pathogenic microbes. However, due to a mixed success rate of antibiotics such as metronidazole, tetracyclines and amoxicillin, as well as the development of bacterial resistance, antibiotics are not used in every case [3].

1.2.4.2 Surgical Treatment

If periodontitis is not treated early enough, or the periodontal condition continues to decline, it may be necessary for surgical intervention. Surgical intervention requires oral rehabilitation which is provided by either dental implants or periodontal regeneration. To aid with the fixation of dental implants, dental barrier membranes are used in over 40% of implantations to improve bone augmentation [5].

Different methods have been employed to try and restore function to the periodontium after periodontitis. All strategies aim to reduce and eliminate inflamed tissue around the defect site, correct the damage of the defects and anatomical

problems created by the disease, and if possible, regenerate all periodontal tissues [1]. In order for a patient to receive a dental implant they are required to have sufficient quantity and quality of bone to anchor and support the implant. Guided bone regeneration (GBR) is a surgical method of inducing and directing new bone and gingival tissue growth.

The formation of new bone is called Osteogenesis and occurs at the bony defect site once the unhealthy tissue has been removed. The new bone formation is similar to healing by scar tissue, whereby the newly formed bone is subsequently remodelled into a lamellar or mature bone structure. GBR can be used to improve the quantity and quality of the regenerated bone. Scaffolds are used which have osteoconductive factors, whereby progenitor cells and bone cells are recruited from host tissues onto the scaffold surface. Scaffolds can be obtained from biological sources such as allografts (demineralised human bone grafts from tissue banks) and xenografts (grafts from other species), or be synthetically made, such as with porous hydroxyapatite.

Growth factors, and/or stem/osteoprogenitor cells can be used to facilitate healing and for augmentation of defect sites [6], [7]. The growth factors and cells can be obtained from autologous bone (an autograft from another part of the patient's body) or more rarely from an allograft. However, modern treatments to reduce cross infection from an allograft tend to destroy the proteins in such grafts and thus also the factors that stimulate bone growth.

Barrier membrane are often used in conjunction with GBR to seclude the defect site and thereby prevent the infiltration of connective and epithelial tissues from filling the defect space. The barrier membrane is positioned above the defect site and below the gingiva (Figure 1.2). By separating the faster growing connective and epithelial tissues out of the defect, space is provided for progenitor cells positioned within surrounding tissues such as the periodontal ligaments, alveolar bone and in the blood, to repopulate the area [1], [7]. GBR performed with a barrier membrane provides improved results.
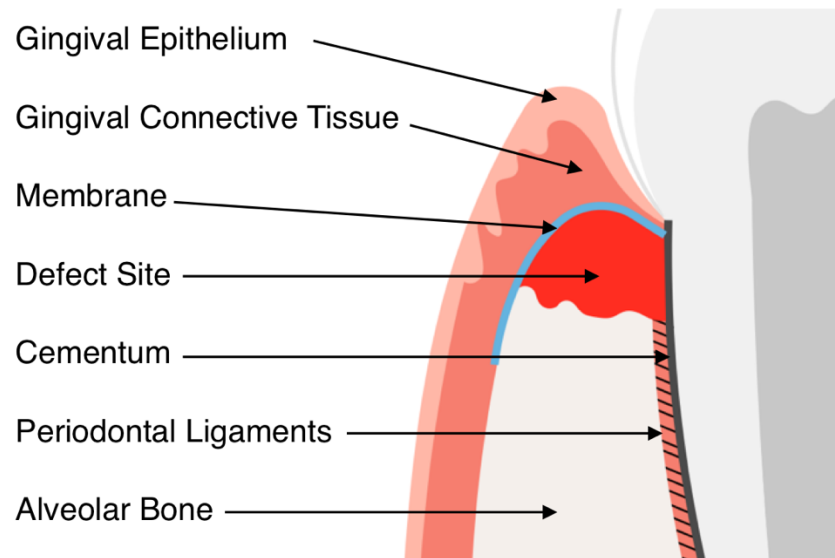
Figure 1.2: Illustration of a damaged periodontium with a barrier membrane positioned between the defect and the gingiva

1.3   GBR Barrier Membranes

1.3.1   Barrier Membrane Requirements

Barrier membranes used in GBR aim to provide a predictable method to restore and develop periodontal tissues. The membranes act as an interface for repairing periodontal ligaments, cementum and alveolar bone to restore full function to the affected area [1], [8]. The different objectives for GBR barrier membranes are as follows [9];

- The membrane should aid with the augmentation of alveolar ridge defects
- Induce bone healing around dental implants
- Produce complete regeneration of defective bone
- Improve bone grafting results and to help treat failing implants.

Research into GBR membranes began in the early 1980's and since then many different designs have been tested with varying successes. Due to improved techniques and greater control over material properties such as biodegradation, a criterion was produced during the 1992 University of Pennsylvania Symposium which are now used for evaluating all new barrier membranes [5]. The criterion listed are; 1) the membrane must allow for proper tissue integration; 2) have cell-occlusivity,

preventing cells from penetrating the membrane; 3) be clinically manageable; 4) provide space provision; and 5) be biocompatible.

Tissue integration is important as it secures the membrane in position and replaces degrading structures. Surface topography of a scaffold offering different degrees of porosity have been shown to integrate with soft and hard tissues [10]. Soft tissue showed better integration for a highly porous structure with pores sizes ranging between 6-20 μm, whilst bone responded best when presented with a minimally porous structure with significant nodes and a pore size between 18-60 μm.

Surface hydrophilicity is also an important factor for tissue integration. A scaffold with surface hydrophilicity will promote early cell adhesion [10], [11]. Polyesters are commonly used to produce degradable membranes yet possess hydrophobic characteristics. In order to prevent this a polyester scaffold treated with a polyethylene oxide dip coating has a considerably improved wettability with no significant difference to mechanical properties [11].

Occlusivity in a dental membrane is a subject of much debate, however most research indicates the requirement for an occlusive barrier. An occlusive membrane prevents epithelial and connective tissues from overpopulating the defect site and producing fibrous tissue, allowing the slower growing bone cells to proliferate and populate the area [6]. Bone augmentation has been successfully achieved with the use of an occlusive barrier [10], [12]-[18]. Polimeni *et al.*, investigated occlusive and non-occlusive membranes and came to the conclusion that regeneration was greatly improved for defects receiving an occlusive membrane [12]. Conversely Wikesj *et al.*, reported no significant difference in regeneration between macroporous expanded polytetrafluoroethylene (ePTFE) membranes and occlusive ePTFE membranes, but stated that an occlusive membrane might be required to give more optimal results [18].

A clinically manageable membrane is more appealing for surgeons. A design which is easy for the surgeon to handle reduces surgery times and therefore morbidity rates.

Membranes are required to fit defect spaces and shapes in order to function properly. This can be achieved by using a malleable material, however if the material is too malleable then the procedure will be non-reproducible leading to varied results. If the material is too stiff then the edges of the membrane could pierce through the gingival tissue creating a gateway for bacterial infections. One solution is to have a material which hardens after implantation. This idea has been investigated by Owen *et al.*, who used plasticizers in a poly(lactic-co-glycolic acid) (PLGA) matrix to increase flexibility and elasticity in dry conditions. After placement the plasticizers would leach out of the membrane to give a more rigid structure. Samples seeded with porcine periodontal ligament cells were shown to have reached confluent layers after 7 days in culture [19].

Provision of space under the membrane enables the ingrowth of bone tissue into the defect site [12], [20]-[22]. The membrane needs to withstand forces produced during mastication to maintain space whilst having enough elasticity to prevent mucosal compression [6]. Polimeni *et al.*, suggested that it was more important that the membrane offered space provision than osteoconductivity [20].

Membranes are designed to promote early clot formation. Coagulation around the membrane protects damaged tissue and begins the formation of a provisional matrix to which cells can adhere. It has since been proven that the use of a membrane can secure a fibrin clot and help to prevent the wound from rupturing [23]. Clot formation also provides anchorage of the membrane and the proliferation of new tissue [5]. As tissue integrates with the membrane, a barrier is formed between the bone and the barrier membrane material, thus acting to prevent the migration of fibrous tissues around the membrane. As the tissues populate the membrane its structural integrity is increased, reducing the risk of it collapsing.

Successful procedures are reliant upon many contributing factors, not just successful GBR design. Suitable surgical techniques are required to deal with aspects such as gingival flap management and proper site preparation to remove debris. The gingival flap should provide full coverage and maintain its position over the membrane with

the wound margin positioned away from the healing defect [7]. Failure of the membrane can be caused by exposure through poor gingival flap management, which can lead to bacterial infiltration and infection [5], [7]. An adequate blood supply available at the defect site is required to help supply nutrients to the healing cells and remove waste products. Furthermore, a blood supply provides progenitor cells, which are also found in the surrounding tissues such as the periodontal ligament, to help with the rejuvenation of the wound [6].

1.3.2 Current Barrier Membranes

Since research began on GBR membranes in 1982 there have been many variations in designs. Each model offers different successes, however there is yet to be established an idealized model which can offer full restoration of a defect with minimal complications. Current designs can be split into two categories; resorbable and non-resorbable membranes. A summary table of different commercial membranes can be found in the appendix.

1.3.2.1 Non-Resorbable Membranes

Between the 1990's and 2000's one of the most widely used scaffolds was the Gore-Tex® Regenerative Membrane [1], [6], [24]. Originally, Gore-Tex® scaffolds were used for tissue repair in other areas of the human body including parts of the cardiovascular system before being used for bone repair. The structure is formed out of expanded polytetrafluoroethylene (ePTFE). Investigations for its use as a dental material initially began to determine its ability to prevent the migration of epithelium around dental implants, and due its success a new term 'contact inhibition' was produced to explain the occurrence [25]. Through its long use as a medical material, inertness and tissue compatibility, ePTFE built up a reputation as the gold standard for barrier membranes [9], [24]. However, in cases where inflammation had been reported, the ePTFE membranes had to be extracted immediately [6]. Due to the possibility of eliciting a severe immune reaction, ePTFE has ceased being used as a material for dental restorative work and hence the

discontinuation of Gore-Tex® Regenerative membranes for dental use. Nevertheless, through its past successes it is still used as a comparative for future designs.

The Gore-Tex® dental membrane consisted of two sections; a coronal border and an occlusive middle portion. The coronal border had an open microstructure with an internodal distance of 25 μm. The open structure enabled early blood clot formation with eventual collagen fibre penetration. The occlusive portion had an internodal distance of less than 8 μm. The size of the occlusive pores inhibited the penetration of epithelial tissues through the barrier whilst enabling the diffusion of nutrients [6], [9]. Gore-Tex® also offered a titanium design incorporated into the ePTFE structure. The titanium reinforced the ePTFE to maintain its shape and structure *in-situ*, resisting compressive forces of surrounding soft tissue.

The company Cytoplast™ offer clinically available dense Polytetrafluoroethylene (dPTFE) dental barrier membranes. Their products Cytoplast™ Regentex GBR-200 and TXT-200 membranes claim to be impervious to food and bacteria without affecting function should the membrane become exposed [6], [26]. Each membrane has a structure with a submicron pore size less than 0.3 μm, preventing the infiltration of bacteria. dPTFE has a poor adhesion to tissue which aids easier extraction of the membrane.

Titanium mesh membranes offer high structural strength with minimal weight. Cytoplast™ also offer a dPTFE membrane with titanium reinforcement. Cytoplast™ Ti-250 was the first of its kind offering titanium reinforcement [27]. The incorporation of titanium within the structure provides resistance against compressive forces and also enables the membrane to be positioned without the necessity for a full encapsulation by soft tissue. Titanium exhibits elasticity and plasticity enabling it to be moulded to a defect shape. Previous tests performed using titanium have reported problems regarding its stiffness and sharp edges resulting in scaffolds protruding through the soft tissues. However, where this has occurred some studies have reported that infections were not caused due to exposure [6].

Using a non-resorbable membrane for the regeneration of a defect has many advantages, primarily that the length of time that the membrane is *in-situ* can be adapted. Mechanical properties of the membrane remain constant throughout the healing process. However, by using a non-resorbable membrane there is a requirement for a second surgery which increases costs and trauma for patients.

1.3.2.2 *Resorbable Membranes*

Resorbable membranes can be produced from synthetic polymers such as polyesters or natural polymers such as collagen. Polyester based membranes have better manageability than non-resorbable membranes, however they have shown a lower biocompatibility. Collagen based membranes have excellent biocompatibility but have poor degradation qualities. Most designs available clinically are made from polyesters; PGA, PLA, PCL and their copolymers [1], [27].

As resorbable regenerative membranes began to be developed, the previously mentioned design criteria for dental barrier membranes was adapted to include new criteria not considered for a non-resorbable design, these included membrane immunogenicity, biocompatibility and degradation/resorption timings [5], [25].

The most notable advantage with using a resorbable material over a non-resorbable material is that there is no requirement for a second surgery to remove the implant. This decreases the overall cost of the procedure and also reduces site morbidity. Another advantage by using a resorbable membrane is that should the membrane become exposed, the open areas of the scaffold will degrade limiting the area for bacterial contamination [24].

Guidor Membrane® produced by Sunstar Americas, Inc. was the first resorbable membrane which was designed as an alternative to the Gore-Tex® ePTFE model in periodontal tissues [5], [27]. It was formed from polylactic acid (PLA) with a citric acid plasticiser which is hydrolysable and added flexibility for a better fit [27]. Formed from two layers the membrane promoted gingival connective tissue integration but prevent penetration through its structure.

Commercially available resorbable polyester membranes include; Resolut® LT, Epi-Guide® Bioresorbable Barrier Matrix and Vicryl® Periodontal Mesh. Each membrane has its own degradation timings ranging from weeks with Vicryl® to months with Resolut® [27]. Epi-Guide®, Kensey Nash Corp, has a three-layered structure to promote fibroblast and epithelial cell migration and to maintain space around the defect. It is hydrophilic to absorb blood and cause early clot formation [28].

Atrisorb®, Tolmar, Inc. is a resorbable gel formed from Poly-DL-lactide dispersed in a solvent N-methyl-2-pyrrolidone [1]. It is designed to be applied *in-situ* as a viscous gel which isolates the periodontium. The gel aims to shorten surgical times through reduced handling of the membrane as the gel is applied directly to the defect site.

Commercially available collagen membranes are sourced from different animals. Cytoplast® RTM, Osteogenics and BioMend Extend® Collagen, Zimmer Dental, use collagen from the bovine Achilles tendon [29], [30], Bio-Gide®, Geistlich Pharma, uses collagen derived from porcine skin [31], Parasorb Resedont® and Sombrero®, Resorba, use equine collagen [32] and Alloderm®, BioHorizons uses allografts as a source of collagen [33]. The advantages of using a collagen membrane is that it is the extracted extra cellular matrix rather than a recreation. In this way a scaffold is produced replicating the exact structure suitable for the cells, giving excellent biocompatibility and cell-cell affinity [1].

Bio-Gide® has had over a decade of use within the medical field and is one of the more popular choices of membrane with surgeons. It has reliably demonstrated good biocompatibility and vascularization of membrane sites. It has a bi-layered structure with a dense layer used for granulation tissue and blood vessel growth that provides cell occlusion and a porous section positioned for bony ingrowth.

Degradation rate can be affected by different material properties of the membrane such as the molecular weight of the polymer material, crystallinity, blending and porosity. External factors can also affect the degradation process such as the pH environment and temperature. Catalytic molecules and ions will only react on the

surface of the polymer and will not diffuse into the polymer structure [13]. Therefore, membranes broken down through biodegradation have a degradation rate directly linked to their surface area. Rate of biodegradation is affected by the thickness of the membrane. Polymer membranes will degrade via bulk degradation mechanisms up to a certain thickness, beyond which the polymer will degrade by surface erosion [13].

Comparison studies between resorbable and non-resorbable membranes have been performed to determine which offer the best characteristics for GBR. Structural integrity of membranes were investigated to determine if soft and hard tissue responses to changing mechanical support influences regeneration. It was concluded that resorbable membranes which offer a high level of stiffness are able to offer similar levels of bone formation as a non-resorbable membrane [6], [24]. Soft tissue responses were improved when using a resorbable membrane with better tissue integration when compared to non-resorbable membranes [24] [34], [35].

A period of 4-6 weeks before a loss in structural integrity of the membrane is sufficient for successful regeneration to occur [1], [7], [36]. Some of the available polyester based membranes; Resolut®LT and Biofix®, when tested under laboratory conditions lost most of their structural strength by 4 weeks. The membranes began with a tensile strength between 12-14 MPa, however by 4 weeks this had dropped to around 1 MPa [1]. If the resorption time exceeds a 6-12 month period then the benefits offered by a resorbable material are lost [24].

To determine if there was a difference between commercially available resorbable and non-resorbable membranes, Resolut® Regenerative Material resorbable membrane was clinically compared to Gore-Tex®'s non-resorbable membrane. The study concluded that there was no significant difference between either membrane when used for Class II furcations (a horizontal bone loss of 3mm) and intrabony defects [37]. The same result was observed when Resolut® Regenerative Material membranes where compared to Teflon membranes for degree III furcations (3 x 4 mm) [38]. Early studies (in 1998) comparing the effectiveness of a resorbable

material to that of ePTFE showed ePTFE to give the better results [39]. The better results could be related to a greater experience working with the ePTFE barrier membranes. Since this study was carried out surgical techniques for resorbable membranes will have improved.

1.4 Current Research

1.4.1 Materials

For this study biodegradable materials will be used. Non resorbable membrane can offer long term stability and support to a defect site, however the requirement for a second surgery for membrane removal increases costs and trauma for patients. This can be avoided with a biodegradable design. This section will explore different biodegradable materials and the benefits and issues related to each material.

The choice of materials selected for dental resorbable membranes are a combination of synthetic and natural polymers, ceramics and bioactive glasses. Biodegradable/ bioresorbable materials implanted into the human body must provide stability and structural integrity until their purpose is fulfilled, produce non-toxic by-products and not induce an illicit immune response.

Collagen has been used in many membrane designs [40]-[47] and is available in commercial products Bio-Gide® and BioMend® [27]. It is an ideal material to use for membranes as it has a proven history of wound healing abilities, is non-antigenic and bioresorbable. The extracted collagen is formed from extra cellular matrix and is commercially sourced from animals. Precautionary steps are performed to ensure all cellular material is removed which could invoke immune response reactions within the patient. The quality of each membrane is dependent on the source with irregularities occurring in its structure from improperly sourced material. Even with thorough screening techniques there is the possibility of disease transmission. Collagen exhibits poor structural performance with fast degradation times. This can be improved with the use of crosslinking [1], however this does not prevent rapid degradation when the membrane is exposed to the oral environment [46].

Most commonly commercially available resorbable membranes are produced from polyester. Polyesters can be biodegradable with adjustable degradation times, are easily processed and offer low rigidity. They have a naturally high contact angle which can be used to prevent cellular adhesion [42], [48]. When two degradable membranes, Geistlich's resorbable bilayer Bio-Gide® membrane made from porcine collagen, and a synthetic polymer Inion GTR™ Biodegradable Membrane System composed of L-lactic acid, D-lactic acid, glycolic acid and trimethylene carbonate [49] were compared, no significant difference was observed [50]. Both membranes showed similar amounts of bone regeneration and barrier properties.

Biodegradable polymers implanted into the body break up into naturally forming compounds removable by the body. Accumulation of by-products produced during degradation can have an effect on the local environment if tissues are unable to transport and remove the substances fast enough. Most commonly an acid is produced which can lower pH levels in the local environment to a cytotoxic level. To counteract this, ceramic and/or bioactive glass compounds can be included into polymer membrane structures. During degradation of the membrane the ceramic and bioactive glass compounds release charged molecules which help to combat the reduction in pH. Hydroxyapatite (HA) or beta-tricalcium phosphate (β-TCP) can be added to polymer blends to act as a buffer but also to improve bone cell adhesion [11], [43], [51]-[57]. During degradation, HA releases OH^- molecules which neutralise the acid formation [11], [54].

Hydroxyapatite (HA), tricalcium phosphate (TCP) and bioactive glass are osteoconductive, biologically stable and bioresorbable. These compounds have a brittle nature and require a polymer for a structural base to provide flexibility to dental membrane designs. Yang *et al*. compared the effect of different concentrations of nano apatite (nAp) on PCL electrospun membranes. Pure PCL and 33 wt% nAp film had the highest stiffness however the addition 20 wt% nAp produced the most ductile film. Bioactivity of the films measured by calcium phosphate precipitation increased with increasing nAp content. Osteoblast cell proliferation occurred fastest on the pure PCL film with cell numbers decreasing with

nAp content, however nAp was shown to cause early cell differentiation with increased ALP activity after 8 days [53]. Other studies have shown the increased osteogenic activity of polymer films with increasing hydroxyapatite content [58], [59].

BCP is a ceramic made as a balance between the properties of HA and TCP. TCP is more soluble than HA leading to faster degradation rates. By mixing a ratio of the two ceramics a material can be produced with tailored mechanical and biological performance [60], [61]. Previous studies indicate BCP's potential to stimulate bone growth and bridge developing bone to scaffold surfaces proving excellent osteointegration [47], [62], [63]. Not all studies have concluded on the positive use of BCP. When used in a clinical trial comparing its use to deproteinised bovine bone as a control, similar results were observed [47]. BCP also had no significant effect in patients when used in conjunction with enamel matrix derivative [64].

A material is yet to be found which offers all the qualities desired for a dental membrane. Collagen can offer excellent tissue integration, but at the expense of structural integrity. Polyesters can be tailored to a desired degradation rate, yet release by-products during degradation which can cause an immune response. Ceramics such as HA can offer excellent osteointegration, but are brittle and require a polymer matrix to provide support. So far the best results have been achieved through the use of composite membranes, where the properties of several materials combine to produce the desired effect.

1.4.2   Silk

Silk could be considered as a possible alternative material as it already has a long history of use as a medical material [65], [66]. Silk was originally used as a suture material and is still used in oral, skin, lip and eye surgeries [67]. More recently silk has been developed into regenerated silk fibroin (RSF) structures such as sponges, films, hydrogels and mats   [67], [68]. Many structural characteristics such as biodegradation rate and mechanical strength can be adapted by using regenerated silk fibroin [69]-[71]. These adaptable properties make it ideal for use as a tissue

engineering scaffold material where control over all aspects of the material are required. Other properties of silk which make it a desirable material include versatility of sterilisation techniques [68], [72], [73], solvent and water based processing and the ability to modify chemical groups along its structure [74].

Silk is produced by arthropods such as spiders and Bombyx Mori (B. Mori) larva, however the silk they produce differ in structural design and properties. Silk produced by spiders is hard to mass produce due to the cannibalistic nature of spiders [75], therefore, silk produced by B. Mori larva is most commonly used. Silk produced from the B. Mori larva, commonly referred to as a silkworm, is the most widely used in the textile industry which produces around 400 tons of dry silkworm silk a year [68]. Each cocoon produced by the B. Mori silkworm yields between 600-1500 meters of silk [67]. A photo of B. Mori silkworm cocoons with the worm removed is shown in Figure 1.3. Due to the well established processing methods as well as its use in current tissue engineering research [76]-[80], B. Mori silkworm silk will be used in this study and will now be discussed further. All future references to silk will be referring to B. Mori silkworm silk.

Figure 1.3: Bombyx Mori silkworm cocoons with worm removed

Silk is composed of a core made from fibroin proteins and an outer coating of sericin proteins. The core contains light (26 kDa) and heavy (390 kDa) protein chains which are connected by a singular disulphide bond [81], [75]. A small glycoprotein called P25 is covalently linked to the core structure. The ratio of light to heavy chains and

the quantity of P25 changes depending on the arthropod. In B. Mori silk the ratio between light and heavy chains as well as the P25 glycoprotien is 6:6:1 [82]. Sericin proteins (20-310 kDa) make up to 20-30% of the native silk mass and envelope the core [75]. Sericin is used by the silkworm during cocoon production to bind the structure together. The sericin component of silk is responsible for causing foreign body reactions with increased inflammation when native silk fibres have been implanted in the body (however there are some conflicting reports [83], [84]), and it is normally extracted before use as a biomaterial. The removal of sericin is also routinely performed in the textile industry which uses an enzyme or alkali degumming procedure [67]. These procedures are well established and easily performed to purify the silk fibroin. The method of purification produces a reduced risk of infection when compared to other protein based biomaterials with an allogeneic or xenogeneic origin.

B. Mori silk fibroin is composed of the following amino acids: 45.9 % glycine (Gly), 30.3 % alanine (Ala), 12.1 % serine (Ser), 5.3 % tyrosine (Tyr) and 1.8 % valine, with the remaining 4.7 % being composed of 15 other amino acid types [81]. The silk fibroin heavy chain is formed of a repetitive core of 12 crystalline regions and 11 amorphic regions [75], [85]. The crystalline domains have a low level of complexity and are formed primarily of Gly-x repeats [75], [81]. The 12 crystalline domains are what form the β-sheet crystals, and are mainly composed of the amino acid sequence (Gly-Ala-Gly-Ala-Gly-Ser) [86], [87], whilst the amorphic regions are mainly composed of (Gly-Ala-Gly-Ala-Gly-Tyr) [88].

The amorphic regions of the heavy chain are hydrophilic and allow the backbone of the molecule to change direction by 180°, enabling anti-parallel β-sheet stacking [87]. The glycine, alanine and serine residues contain short side chains which enable dense stacking of the β-sheets. Intra-sheet bonding is formed through hydrogen bonds between carbonyl oxygens and amide hydrogens of neighbouring polypeptide chains and Van der Waals inter-sheet interactions occur between the hydrophobic side chains [75], shown in Figure 1.4. Hydrogen bonds form between polar side groups, positioning the polar groups within the β-sheet blocks and therefore increase

hydrophobicity with increasing β-sheet content [86]. As the heavy chain is comprised of 12 crystalline and 11 amorphic domains, it is possible for each silk fibroin molecule to produce 12 intramolecular anti-parallel β-sheet strands with 11 turns [86], [89].
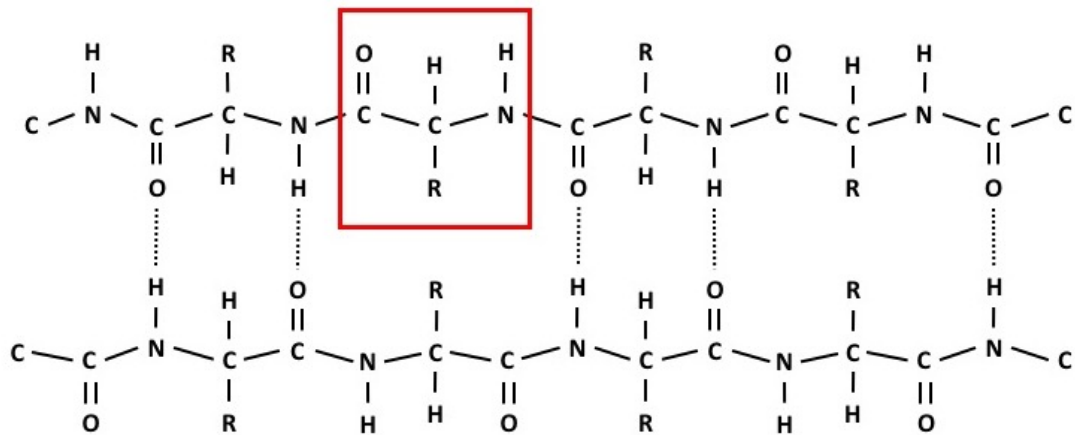
Figure 1.4: Anti-parallel β-sheet structure of fibroin. The red box represents an amino acid subunit. The 'R' represents the R-group of the amino acid, which consists of a specific side chain that defines the amino acid.

An α-helical structure is formed by hydrogen bonding between amino acids that are 4 amino acids apart along the same molecule, and a full helical rotation consists of an average of 3.6 amino acid subunits. Hydrogen bonding is formed between the hydrogen attached to the nitrogen of the polypeptide backbone, and the carboxyl oxygen atom four amino acid units along from the amino terminal side of the peptide bond [90], and is shown in Figure 1.5.
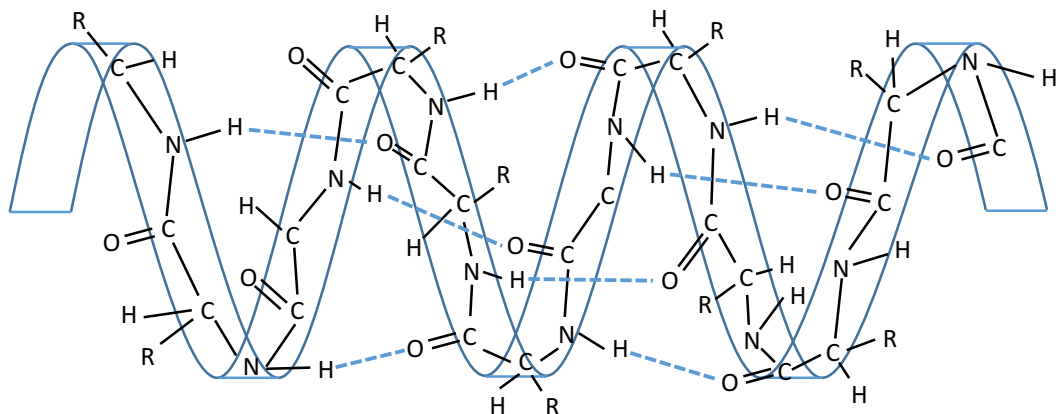
Figure 1.5: α-helix structure of fibroin. Blue dashed lines indicate hydrogen bonds

Silk fibroin has several polymorphs; silk I, silk II and silk III. Silk I has an unordered structure which is water soluble and present within the silkworm gland before spinning; silk II has a crystalline structure that is non-water soluble and produced during spinning from the silk worm spinneret; silk III is an unstable structure which forms at the water-air interface. As regards the current research silk I and silk II are of interest.

Silk I consists of an unordered fibroin structure, mostly composed of α-helix and random coils. Silk II is mostly composed of β-sheet structure. Silk I can be transformed into silk II by exposure to methanol or potassium chloride [90]-[92], stretching [93], as well as through heat treatments [94]. Methanol converts the unordered random coil structural component of silk I into anti-parallel β-sheets by dehydrating the α-helix, thereby creating a water insoluble silk II structure [90], [91]. The ability to change silk I to silk II make it ideal for processing and manufacture.

Chen *et al.* performed time resolved FTIR spectroscopy upon RSF membranes submerged in a 70 % ethanol solution [95]. The RSF films were 5 μm thick and therefore give an indication of how thicker membranes transform from a silk I to silk II structure, but over a shorter period of time. The RSF membranes began with a high random coil content without the presence of β-sheet, however upon exposure to ethanol, the amount of random coil content reduced and there was a large increase in β-sheet content. The time resolved FTIR demonstrated that there was an initial burst phase of around 6 seconds, in which 50 % of the RSF had converted into a β-sheet structure. The burst phase was followed by a much more gradual transition.

The work by Chen *et al.* theorises that the burst phase is caused by the large proportion of Gly-Ala-Gly-Ala-Gly-Ser repeats along the fibroin molecular chain. These segments could already by in a partially folded state. When the segments are exposed to ethanol, they quickly convert into a β-sheet structure. Once the burst phase has ended, the formation of β-sheet is slower as the fibroin molecular chains are rearranged for intermolecular β-sheet bonding [95].

Different regenerated silk fibroin (RSF) structures have previously been investigated such as films, electrospun fibres, hydrogels, 3D porous scaffolds and as particles [67], [68], [96]. Silk films, which are of interest in the current study, have been successfully applied to ocular [76], hepatic tissue [77], Urethra [78], skin [79] and eardrum [80] regenerations.

Previous methods for producing RSF films have involved the casting of an aqueous solution, casting acidic or ionic silk solution, spin drying and electrospinning [67]. Different treatments are used to improve mechanical properties by increasing β-sheet concentration. Controlled drying or water annealing are used during the setting of films. Stretching and alcohol immersion are used after the film has set. Different processes give variations in the overall mechanical properties and degradation rates [69], [71]. RSF Films which are water annealed have a greater flexibility and degrade faster than films which are methanol treated [69]. These variations are caused by different concentrations in amorphic and crystalline regions.

Silk will only degrade in the presence of enzymes and will degraded into non-harmful free amino acids and peptides [97], [98]. These products are easily recycled by the body. Other materials used in tissue engineering such as for guided tissue regeneration use biodegradable materials like polyesters. Polyesters degrade into acidic by-products which if left to accumulate in the vicinity of the implant can causes increased inflammation. Degradation of silk can be controlled by its crystallinity, porosity and molecular weight distribution [68] and degrades into non-toxic components. This could make it an ideal alternative to some of the current materials.

Sterilisation of a biomaterial is vital to prevent bacterial infections upon implantation. Certain materials such as collagens are difficult to sterilise. Silk's morphology and structure are unchanged when heated to around 250°C [73], autoclaved to 120°C [72] or treated with ethylene oxide or 70% ethanol [68]. This enables a choice of sterilisation techniques more suited to scaffold designs.

1.4.3 Use of Silk for GBR

Research in to the use of silk films for GBR has only recently started to build momentum, with much of the previous research concentrating on soft tissue regenerations [76]-[80]. Although several studies have already been conducted into the use of silk as a barrier membrane for bone regenerations [74], [99]-[106], there are currently none commercially available for use in GBR. Seri® Surgical Scaffold by Serica Technologies, Inc., is a commercially available silk scaffold available for soft tissue repair, and has been used successfully in hernia repair and breast reconstruction [107]. The scaffold is made from silk sourced from Bombyx Mori silkworm cocoons and formed into shape by twisting the degummed silk fibres into multifilament fibres which are then knitted together. FibroFix™ by Orthox Limited offer a Bombyx Mori silk scaffold formed using RSF. Their scaffold is aimed at the repair of meniscal cartilage. However, the FibroFix™ is not yet commercially available and has only recently completed its first clinical trial with results yet to be published [108].

Hayden *et* al. performed a long term cell culture study on cast RSF films. The study was performed over a 32-week period and used human mesenchymal stem cells (hMSC)-derived osteoblasts and THP-1 human acute monocyclic leukaemia cell line-derived osteoclasts, either in separate cultures, or, as a co-culture. Osteoblast cultures showed mineral deposits on the RSF films by week 8 which continued to grow in size, yet remained as discrete deposits. The co-culture also developed mineral deposits by week 8, however the mineral deposits were much larger than that of the osteoblast culture. The co-cultures mineralised the surface of the RSF films into large stretches of extra cellular matrix (ECM) which continued to grow up until week 24. The osteoclast culture caused pits to form on the surface of the films as they degraded the RSF, increasing surface roughness. It was hypothesised that the co-culture caused a higher deposition of mineral due to a combination of the interactions between the osteoblasts and osteoclasts, as well as the increased surface roughness caused by the osteoclast degradation of the RSF. Overall, RSF was shown to be a promising substrate for bone regeneration by maintaining bone cell

growth over a sustained period of time and developing a highly mineralised surface [104].

When RSF membranes have been implanted to treat calvarial detects in rabbits, they were reported to increase bone growth [99], [100]. 8 mm defects treated with an RSF membrane were seen to have formed bridged across the defect after 8 weeks, and completely healed with new bone by 12 weeks [99]. Although in both experiments the use of the RSF membranes were only compared to sham surgeries, they show the potential for RSF as a barrier membrane.

In comparison to other materials such as collagen and PLA, silk has been shown to induce lower levels of inflammation [74], [101]. When a silk cocoon separated into layers and used as a membrane was compared to commercially available collagen membrane (Rapi-Guide, Dalimtissen) and dPTFE membrane (TXT-200, Osteogenics), and used to treat critical-sized parietal bone defects in rats, the silk membrane was shown to induce greater bone formation. The silk membrane caused lower levels of inflammation compared to the collagen membrane as well as showed signs of a well organised vascular network. The dPTFE membrane, although having low levels of inflammation, became encapsulated in fibrous tissue [101].

A study comparing cast RSF membranes to that of a commercially available collagen membrane (Bio-Gide®, Gleistlich), found that the collagen membrane induced faster bone formation [106]. The study, performed on male Sprague Dawley rats with 5 mm circular calvarial bony defects, showed that a sham procedure (without a membrane) would allow the defect to fill with fibrous tissue over an 8-week period. The Bio-Gide membrane had the highest bone regeneration after 4 weeks, with the largest increase in bone formation occurring between weeks 2 and 4. The RSF membrane displayed a steady rate of bone formation over an 8-week period, finishing with a similar amount of regenerated bone as the Bio-Gide membrane. By week 8 neither the RSF membrane nor the collagen membrane were visible in a histological examination. During the regeneration of a bony defect, the defect site is initially capped with the formation of a thin layer of new bone which then thickens leading

to the eventual full closure of the defect site. The Bio-Gide membrane caused a rapid closure of the defect site, yet the bone took longer to thicken compared to the RSF membrane [106]. Therefore, it is possible that the bone being formed under the RSF membrane was of a higher quality than that of the collagen membrane.

Research is also being conducted into improving the osteoconduction and mechanical properties of the RSF films by creating RSF composite materials. Yang *et al.* used electrospinning to produce scaffolds which replicated extra cellular matrix. The electrospun scaffolds were soaked in a solution of RSF with HA particles which caused membranous formations between electrospun nano-fibres. The inclusion of HA up to a concentration of 5 % was seen to improve the mechanical properties of the RSF. Scaffolds of RSF with and without HA were compared to collagen sponges. When cultured with human osteoblasts (hFOB1.19) cells, after a 2-week period there was significantly higher cell proliferation on the RSF scaffolds (with and without HA) in comparison to the collagen sponge. SEM of the scaffolds showed that the cells on the collagen sponge had remained as a singular layer, whilst the cells on the RSF scaffolds had formed multiple layers. An animal study was performed using the RSF films with a 5 % concentration of HA with and without the inclusion of BMP-2. Rats with a critical calvarial defect of 5 mm were left without a scaffold (control) or had RSF/HA or RSF/HA/BMP-2 scaffolds. There was no difference in bone growth after a 4-week period, however, after 8 weeks there was significant bone formation with the RSF scaffolds. Micro-CT performed on the defects showed that there was an 83 % and 94 % regeneration of the defect site for the RSF/HA and RSF/HA/BMP-2 scaffolds respectively. Over the course of the study there was no inflammation for any of the samples [103].

Kim *et al.* produced a composite scaffold of RSF, titanium dioxide nanoparticles ($nTiO_2$) and nano-hydroxyapatite (nHA). The $nTiO_2$ were included to improve the mechanical properties of the RSF whilst the nHA was included to improve the osteogenic response. Using a casting and salt leaching technique they produced a porous scaffold. Scaffolds were compared consisting of pure RSF, RSF with $nTiO_2$, RSF with nHA, and RSF with $nTiO_2$ and nHA. The mechanical properties of the RSF was not

seen to improve with the inclusion of nHA at a 10 % concentration, however the nTiO$_2$ increased the compressive strength and compressive modulus by around 20 %. All of the scaffolds with inclusions were seen to have higher cell proliferation rates in comparison to the pure RSF scaffold. ALP activity was significantly increased with the addition of nHA. However, it was the combination of nHA with nTiO$_2$ which yielded the highest ALP activity, possibly by a combination of the osteoconductivity of the nHA and the hardness of the substrate induced by the nTiO$_2$ [105].

Yongzhong Wang *et al.* compared the *in vivo* degradation rates for RSF scaffolds that were either cast from an aqueous RSF solution, or formed via a freeze-drying method and dissolved in an organic solvent. [109]. The cylindrical shaped scaffolds with a diameter of 5 mm and a depth of 2.5 mm, were implanted subcutaneously into Lewis rats.

Their short term *in vivo* degradation study indicated that RSF scaffolds prepared from an aqueous solution degraded faster than those formed with an organic solvent. RSF concentration was shown to have a larger influence upon degradation rates. Both the aqueous and organic solvent derived scaffolds formed from a 6 % concentrated solution lost a greater structural integrity compared to those formed from a 10 % concentration.

They performed a long term study conducted over 1 year, which showed that the aqueously derived scaffolds lost all structural integrity after 6 months *in vivo*, whilst RSF scaffolds produced with an organic solvent had a much slower degradation rate, with pieces of the scaffold still remaining after 1 year in vivo. This study demonstrated how different RSF processing techniques can create vastly different degradation characteristics. However, for both processing methods, the RSF scaffolds gave comparable results to current barrier membranes, as commercial collagen membranes have a degradation rate between 16 – 34 weeks, and commercial polyesters membranes between 5 – 12 months [1].

1.4.4   RSF Film Manufacture

The solubility of RSF polymorphs, silk I and silk II, and the ability to easily transform silk I into silk II, make RSF ideal for a range of processing techniques. Current methods for producing an RSF film involve either casting, spin drying or electrospinning, however these methods have a limited control over the final structure. Cast films are reliant upon moulds to provide the final shape, sometimes using salt leaching to provide an internal porous structure. Spin drying produces flat films with no control over surface topography. Electrospinning produces a random assortment of fibres, which can be aligned if spun onto a rotating drum, however, reproducing exact replicas of scaffolds is difficult to achieve. These methods of production also require a secondary processing step in order to induce β-sheet formation and thereby improve mechanical and degradation properties.

The first instance of RSF processing with an inkjet printer was demonstrated by Suntvich *et al*. in 2014 who modified fibroin side chains with poly-(L-lysine) and poly-(L-glutamic acid) to produce oppositely charged polyelectrolytes. The modified fibroin was then printed and paired in bilayers which bound together to form a silk II structure. Silk nests were produced by building up layers of bilayers which they used for cell entrapment [110]. In 2015 Tao *et al*. demonstrated a range of different applications for inkjet printed RSF by printing different structures as well as printing RSF with different active components such as gold nanoparticles, enzymes, and antibiotics [111].

Tao *et al*. postulated that a composite RSF ink would need to be formulated in order to control mechanical properties, however they had not considered the use of reactive inkjet printing. Reactive inkjet printing was first recognised as a means of controlling reactions over twenty years ago. There are two types of reactive inkjet printing (RIJ); 'Single RIJ' and 'Full RIJ' [112]. Single RIJ requires the substrate to be coated in a reactant, usually through another processing technique other than inkjet printing. Small volumes of another reactant are then selectively printed onto the substrate to induce a reaction. This method of RIJ is usually limited to a two component reaction. Full RIJ uses the inkjet printer to print all components of the

reaction and requires multiple printheads. Full RIJ is able to produce reactions with several reactants, only limited by the number of printheads to print each reactant. Full RIJ can be used in the production of RSF scaffolds by printing RSF solution alongside methanol to induce β-sheet formation, thereby controlling the mechanical and degradation properties of the RSF within one processing step, as depicted in Figure 1.6.
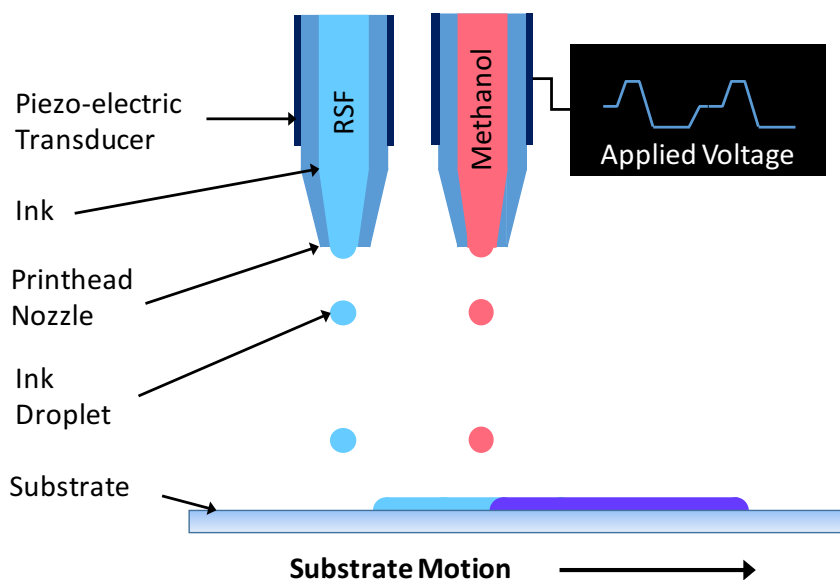
Figure 1.6: Reactive inkjet printing of RSF and methanol, combining film production with methanol treatment to induce β-sheet formation

By using reactive inkjet printing the proportions of reactants can be readily controlled due to the high degree of reproducibility in the size, number and placement of droplets on to a substrate. Inkjet printing builds structures layer by layer, which gives greater control over the finished product and, if required, allows a substrate to be selectively patterned. Therefore, inkjet printing may offer the ability to produce RSF barrier membranes with customisable mechanical and degradation characteristics and a high level of repeatability between samples.

1.5   Inkjet Printing

Inkjet printing is a well-known technology used to apply layers of ink to produce text and images onto porous surfaces such as paper. It is also commonly used to mark

dates onto cans and bottles. However, these processing methods do not usually demonstrate the versatility of inkjet printing. More recently, inkjet printing has been used for more complex tasks such as producing organic transistors, conducting polymers, biosensors and tissue engineering constructs [113].

Inkjet printing is ideally suited for these applications as it is a minimal to non-contact method of production. Droplets are ejected from a nozzle directly onto a substrate which reduces the risk of contaminating samples. It offers a high precision and accuracy, with an excellent repeatability between samples as designs are written in a computer program which is then fed to the printer. Minimal waste is produced as exact volumes of droplets are applied to the substrate which have nano and pico litre volumes.

Inkjet printing can be split into two main categories; Continuous or Drop on Demand (DoD). Continuous inkjet printing has a steady stream of charged droplets pumped through the nozzle. Through the use of electrically charged plates the droplets are directed to specific points on a substrate or towards a collection bucket where unused ink is recirculated. Continuous inkjet printing is used for high speed applications such as graphical designs and labelling [114]. DoD inkjet printing uses a pulse to produce smaller droplets with a higher precision over droplet placement, with position accuracies below 30 μm [115]. During printing the printhead is positioned directly over the area to be patterned. DoD printing is suited for research as there is a high control over droplet placements and ink is not recirculated which could otherwise contaminate samples.

DoD inkjet printing can be split further into two groups; thermal and piezoelectric inkjet printing. Thermal inkjet printing ejects ink through thermally induced expansion of air bubbles. The ink in the printhead is locally heated to nucleate an air bubble. Through further heating this bubble rapidly expands causing a droplet to be ejected. Thermal printing is usually restricted to water based inks limiting available polymers that can be printed, although some non-aqueous inks are available [114]. A piezoelectric inkjet printer uses a piezo material to apply acoustic waves to the

printhead to eject droplets. Piezoelectric inkjet printers have a greater selection of available solvents and therefore have a larger variety of inks that can be jetted. For the purposes of the research in this report, piezoelectric inkjet printing was selected as the method of application due to the versatility of inks and control over droplet placement.

1.5.1 Droplet Ejection

H. Yoo *et al.* broke down droplet generation into a 2 step process: liquid ejection followed by its detachment [116]. The ejection process is determined by the infinite shear viscosity which effects the flow of fluid through the nozzle, and hence, the volume of the droplet. Flow though the nozzle can also be influenced by the elasticity of the fluid, although only slightly. Detachment is controlled by the extensional viscosity and the inertia of the fluid as it is ejected from the nozzle. As the fluid elongates before detachment, the polymer molecules are stretched due to the large strain rates. This creates large extensional forces which slows down the inertia of the droplet [116]. Detachment of the droplet can be sped up when a pull-back is produced by the piezo.

Piezoelectric inkjet printers apply a changing voltage across a piezoelectric material positioned around a capillary tube to produce droplets (Figure 1.7A). The capillary tube is linked up to a reservoir at one end and a nozzle aperture at the other. The capillary tube is filled with ink prior to printing. With an applied voltage, the piezo begins to change shape which in turn induces acoustic waves within the capillary tube leading to the propagation and eventual ejection of a droplet. As depicted in Figure 1.7B, when the piezo moves outwards a negative pressure wave is produced within the capillary (B1). The negative pressure wave splits in two and travels in opposite directions along the capillary tube (B2). The negative pressure wave that reaches the nozzle is reflected back, whilst the wave reaching the ink supply draws in ink and is reflected back down the capillary tube as a positive pressure wave (B3). As the waves converge in the centre of the capillary tube a positive pressure wave is created by the piezo (B4). The newly created positive wave cancels out the negative wave and increases the size of the positive wave travelling towards the nozzle (B5).

As the positive pressure wave reaches the nozzle it causes the ejection of a droplet [117].
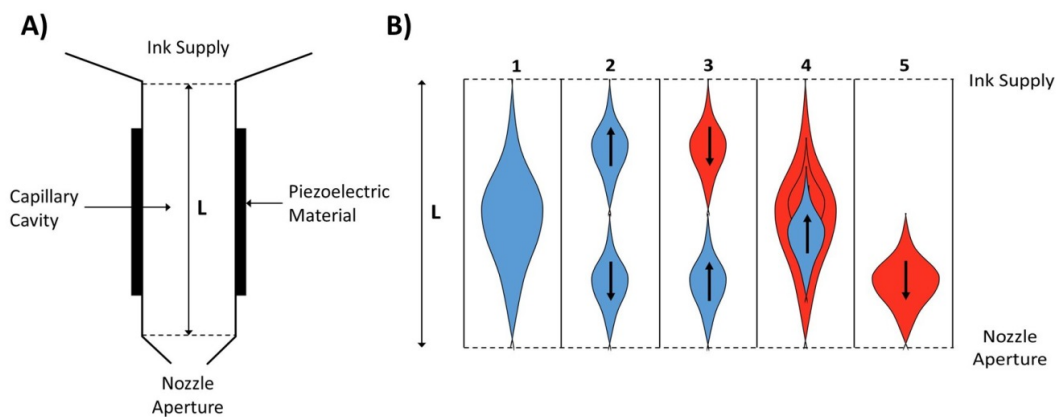
Figure 1.7: A) A common schematic for a piezoelectric printhead, B) depicts the propagation of a pressure wave during droplet formation (blue represents a negative pressure wave and red represents a positive pressure wave)

A droplet is ejected when the amount of kinetic energy transferred to the nozzle aperture is able to overcome the surface energy of the fluid meniscus. The amount of energy supplied to the system is directly related to the voltage applied across the piezo material. For Newtonian fluids, the voltage does not affect the volume of liquid ejected, therefore changes of voltage will not change droplet size [118]. However, H. Yoo *et al.* reported that for non-Newtonian fluids, the direct opposite was true and that in fact droplet volume was shown to be a function of the driving voltage [116].

Due to the necessity of acoustic wave propagation for droplet ejection, viscosity will have a direct influence on droplet formation. High viscosities will dampen out acoustic waves before a droplet is formed. Viscosities also need to enable refilling of the capillary tube in between droplet formation with an estimated refill time of around 100 µs [113]. Values suitable for jetting are reported to be between 0.4 mPa.s up to 160 mPa.s [113], [119], however to print with such a high viscosity requires a very high voltage to supply the system with enough energy to eject a droplet. To achieve more reliable printing, values below 20 mPa.s are more commonly used [114].

Viscosity has also been linked to the stability of droplets by preventing instabilities from forming before breakup [118], [120], [121]. D. Vadillo *et al.* noted that as the concentration of the ink increased, hence as the viscosity increased, fewer satellite droplets were produced during printing. As a droplet is ejected, the bulk of the droplet fluid remains attached to the nozzle via a filament or tail. As the bulk fluid of the droplet moves further away from the nozzle the filament continues to grow in length and shrink in diameter until it breaks. Depending upon the fluid properties and driving voltage waveform, bulbous formations, otherwise known as beading, can occur along the filament, which upon filament breakup can form satellite droplets. Higher ink concentrations caused viscoelastic properties to dominates over surface tension, which led to the dissipation of beading along the filament as the filament became more stable and lasted for a longer period of time [121].

Surface tensions are required to hold a meniscus at the nozzle and prevent flooding of the nozzle tip. Film formation over the nozzle or faceplate acts as another barrier through which the droplet must pass before ejection. The film can induce spraying of the droplet or prevent droplet ejection. Surface tensions between 28 mN.m^{-1} - 350 mN.m^{-1} have reportedly been printed [113], [114]. Surface tension is not significant in the early stages of drop development with little effect on ejection speeds. However, high surface tensions will cause faster necking and separation of the droplet from the nozzle, as well as larger droplets formation [118]. During ejection surface tension will cause the retraction of the tail toward the droplet head.

1.5.2   The Z Number

The Z number is a dimensionless number, originally discussed by J. E. Fromm, and is used to predict the suitability of an ink for printing [122]. The Z number is the inverse of the Ohnesorge number (Oh) which includes viscosity and surface tension values in its calculation (Equation 1 and 2). If an ink has a Z number between 1 and 10 it is thought to be suitable for reliable inkjet printing [115], [117], [123], [124]. Low Z numbers indicate viscous inks while high numbers have an increased likelihood of satellite droplet formation [124].

$$Oh = \frac{\eta}{\sqrt{(\rho \gamma a)}}$$

Equation 1

$$Z\ number = \frac{1}{Oh}$$

Equation 2

Where 'η' is the viscosity of the ink, 'ρ' is the density of the fluid, 'γ' is the surface tension and 'a' is the radius of the nozzle.

With Newtonian fluids the zero viscosity is used to calculate the Z number. However, for a non-Newtonian fluid the viscosity becomes a function of shear, meaning that the Z number is harder to predict. A non-Newtonian fluid can have a zero viscosity vastly different to that of the infinite viscosity, which as mentioned previously, is experienced by the droplet during ejection. Thus the infinite viscosity might be more appropriate to use in the calculation of the Z number of non-Newtonian fluids. H. Yoo *et al.* have shown that the exit velocity is also linked to the infinite shear viscosity and not the zero viscosity [116].

1.6   Summary

Periodontitis is a disease which can lead to the deterioration of periodontal tissues such as the alveolar bone and the gingiva. Periodontal tissues are important as they support the teeth and help dissipate forces induced during mastication. If periodontitis is left untreated it can lead to eventual tooth loss. Regeneration of the defect site caused by periodontitis can require guided bone regeneration (GBR). GBR uses a scaffold to fill the defect space and provide support for regenerating bone tissue. In order to seclude the defect site from faster growing epithelial and fibrous tissues, a barrier membrane is often used in conjunction with GBR.

Barrier membranes are required to be biocompatible, cell occlusive, clinically manageable and allow for tissue integration. Resorbable membranes must also not cause an immunogenic response upon degradation and degrade at a stable rate suitable for the regenerating defect site.

Current commercially available membranes are available in non-resorbable and resorbable forms. Previously Gore-Tex® Regenerative ePTFE membrane, a non-resorbable membrane, became a gold standard for use in dental restorations. However, in certain cases, inflammation around the membrane required for its extraction. Eventually this led to ban on the use of ePTFE in dental restorations.

Non-resorbable membranes have the benefit of providing mechanical support to the defect site for as long as required, with the length of time remaining *in-situ* being easily adapted. However, the requirement for a second surgery to remove the membrane causes increased trauma and cost. An idealised membrane would therefore provide mechanical support and remain *in situ* for as long as required but degrade once the site had regenerated.

Resorbable materials used for barrier membranes are synthetic polymers such as polyesters or natural polymers such as collagen. Each of these materials have their own advantages and disadvantages. Polyesters are easily processed as well as having adjustable mechanical and degradation characteristics. However, polyesters degrade into acidic by-products which can cause increased inflammation if left to accumulate. Collagen has shown excellent biocompatibility but suffers from poor mechanical properties and can pose a risk of infection from contaminated sources. The animal source for the collagen may also be a problem for certain religious groups.

A promising material which has had a long history as a medical material, but has only recently been investigated for bone regeneration, is silk. Silk has become more utilised in tissue engineering in its regenerated silk fibroin (RSF) form. RSF is able to be processed into different shapes with adaptable mechanical and degradation characteristics. When it degrades, it degrades into peptide chains and amino acids easily processed by the body. It also offers high levels of biocompatibility similar to collagen.

Current methods of producing RSF membranes are limited in film design and control over the structure of the films, requiring separate procedural processing steps to

control mechanical and degradation properties. Recent work has been performed using inkjet printing to produce RSF in different forms with bioactive inclusions and offers an alternative method for producing barrier membranes. Inkjet printing is highly precise and accurate with an excellent reproducibility between samples. The precision and accuracy of printing enables intricate topographies to be produced which could be used to stimulate tissue integration. As the printer is controlled by a computer program, changes in design can be easily implemented. However, current inkjet printed RSF designs have relied on either secondary procedural steps, or producing RSF composites, to improve mechanical properties.

Reactive inkjet printing is suggested as an alternative processing method of RSF. To reactively inkjet print RSF membranes, two inks would be used; one ink would be an aqueous silk I solution and the second methanol. By printing the two inks together enables control over silk polymorph concentrations *in situ,* thus controlling mechanical and degradation properties.

The current methods for producing RSF films require multiple procedural steps to increase RSF β-sheet content. Films are first manufactured after which the films are treated to induce β-sheet content. Inkjet printing however, can print multiple inks and therefore, combine film production and methanol treatment into a singular procedural step. As inkjet printing is a form of additive manufacture, structures are built from the bottom up. Building the membranes from the bottom up gives control over film structure, and even offers the possibility of producing a graduated structure which has different properties, such as in β-sheet concentration, on opposing side of the film. The flexibility of film design and accurate control over β-sheet content would make reactive inkjet printing a unique method of RSF film production compared to the current methods.

The production of a suitable ink for inkjet printing can be quite demanding. Inkjet printing requires an ink with a low viscosity and middle to low value ranged surface tensions in order to produce a stable droplet. To help predict the printability of an

ink, Z numbers can be calculated. Using the Z number as an indication of ink properties will be useful in the development of an RSF ink.

Chapter 2: Aims and Objectives

2.1   Introduction

This project is concerned with the development of a dental barrier membrane. Dental barrier membranes are used to seclude bony defect sites from fast growing epithelial and connective tissues as well as aid with the regeneration of the site. Although research into barrier membranes for use in guided bone regeneration has been conducted since the 1980's, there is yet to be established an idealised membrane.

After performing a literature review of dental barrier membranes, current research and its limitations, it has been determined that an ideal barrier membrane will be biocompatible, resorbable with a controllable degradation rate to match the defect site requirements, degrade into non-toxic by-products, be cell occlusive and promote tissue integration. The development of resorbable dental barrier membranes has, so far, focused on the use of synthetic polymers such as polyesters and a non-synthetic polymer collagen.

Polyesters are easily processed with controllable characteristics such as hardness and degradation rate, however, upon degradation they release acidic by-products which if left to accumulate can cause inflammation and an immune response in the surrounding tissues. Collagen has excellent biocompatible characteristics, however suffers from poor structural integrity and risks infection from contaminated sources. An alternative system is silk, which when used in its regenerated silk fibroin (RSF) form is easily processed, with controllable physical properties dependant upon its β-sheet content [125], degrades into peptide chains and amino acid subunits which are non-harmful to the body [97], [98], and has been shown to have a similar biocompatibility to collagen [101], [106].

It has also been shown that the inclusion of bioactive particles can promote better regeneration of a defect site [57], [126]. Hydroxyapatite has been shown to have excellent osteointegration properties [47], [62], [63] which could be useful for

inducing better interactions between the barrier membrane and the regenerating bony defect.

Usually the method to control the mechanical properties of RSF films is dependant upon post-production treatments such as stretching, methanol submersion, or heat treatments [90]-[94]. It is proposed that by reactively inkjet printing RSF solution with methanol, a film can be produced with a controllable β-sheet content *in-situ* during production. Reactive inkjet printing means one reactant is printed on top of a second. Using an inkjet printer offers high precision in structural design as well as the possibility of producing graduated structures. By producing a graduated structure, a membrane could be produced which changes in characteristics for interaction with the gingiva on one interface of the membrane, and with the bony defect site on the other.

2.2   The Aim

The aim of this research is to determine the suitability of reactive inkjet printing and the use of regenerated silk fibroin (RSF) for the development of dental barrier membranes.

2.3   The Objectives

1. To determine if RSF can be reactively inkjet printed, e.g. if RSF can be transformed from a silk I to silk II structure *in-situ* using an inkjet printer.
2. To determine if the transition of silk I to silk II can be controlled so that RSF films can be produced with different characteristics based upon their β-sheet content.
3. Assess the degradation properties of reactively inkjet printed RSF films and determine if the degradation rate can be controlled.
4. Evaluate the cellular interaction of RSF films with that of MG-63 osteosarcoma cells
5. To assess if the RSF inks can be printed with an nHA bioactive component and what influence this has on the transition of silk I to silk II *in-situ*.

6. To evaluate the effect of nHA inclusion and concentration within RSF films on MG-63 osteosarcoma cells.

Chapter 3: Materials and Methods

3.1 Introduction

This chapter explains the methods used to create the materials used in printing, the printing methodology, characterisation experiments of the materials and printed films, as well as assays performed to analyse their performance.

3.2 Material Synthesis

3.2.1 Regenerated Silk Fibroin Synthesis

Regenerated silk fibroin (RSF) was extracted from Bombyx Mori silkworm cocoons (Wild Fibres, Birmingham, UK), based on the protocol described by D. N. Rockwood *et al.*[127]. Cocoons were cut open to remove the silkworms (Figure 3.1A). The cocoons were boiled in an alkaline solution to remove the water soluble sericin protein coating. A 2 litre 0.02 molar alkaline solution was made by mixing 4.24 g sodium carbonate (Na_2CO_3) ($\geq$99.5 % purity, ACS reagent, Sigma Aldrich, UK), with distilled water (dH_2O). Using a hotplate, the solution was heated until boiling and 5 g of cocoons were added (Figure 3.1B). The boiling solution was stirred regularly with a plastic spatula. After 30 minutes the silk fibres had been released from their sericin coating and were removed from the solution. The fibres were rinsed by submerging in 1 litre of dH_2O and stirred with a magnetic stirrer for 20 minutes, after which, the dH_2O was replaced and the washing process repeated a further two times. The silk fibres were then spread out by hand on a sheet of aluminium foil and left in a fume hood for 24 hours to dry (Figure 3.1C).

To transform the silk fibroin into a water-soluble state, the silk fibres were heated in a chaotropic solvent. Chaotropic solvents break up the strong hydrogen bonds holding together the crystalline regions of the silk turning it into an amorphous, water soluble, silk I structure. A 9.3 M solution of lithium bromide (LiBr) ($\geq$99% purity, ReagentPlus®, Sigma Aldrich, UK) was the chaotropic solvent used in this study.

The silk fibres were placed in a 50 mL glass beaker and the 9.3 M LiBr solution poured on top. To ensure that the fibres were properly coated, the fibres and solution were mixed with a spatula. The top of the beaker was covered in aluminium foil and placed in an oven at 70 °C for 3 hours 30 minutes (Figure 3.1D), as recommended by M. K. Sah *et al.* [128]. Silk fibres were observed to have completely dissolved after 3 hours 30 minutes resulting in a regenerated silk fibroin (RSF) solution

To remove the LiBr from the RSF solution, the solution was dialysed against 1 litre of dH$_2$O. 12 mL of the RSF solution was transferred into a 3-12 mL dialysis cassette (Slide-A-Lyzer™ Dialysis Cassettes, 3.5K MWCO, 12 mL, ThermoFisher Scientific, UK) using a syringe and needle while the solution was still warm to decrease its viscosity and aid its transferal (Figure 3.1E). To reduce the likelihood of inducing β-sheet formation through shear, the RSF solution was first collected in the syringe without the needle attachment and transferred with a slow and steady rate into the dialysis cassette through the syringe with the needle attached. The cassette was attached to a buoyancy aid (Slide-A-Lyzer™ Cassette Float Buoys for 12 mL Cassettes, ThermoFisher Scientific, UK) and placed in 1 litre of dH$_2$O. The water was placed onto a magnetic stir plate and was stirred with a large magnetic stirring bar at the lowest speed setting. The dH$_2$O was replaced after: 1 hour, the next morning, middle of the next day and evening; repeated again the following day, and once more the morning after for a total of 8 water changes over a 72-hour period. During the course of the 72-hour dialysis period, the RSF solution had absorbed water and roughly tripled in volume causing the solution to become more dilute and less viscous.

To remove any contaminants still present within the RSF solution such as remaining silkworm, the solution was centrifuged (Figure 3.1G). Centrifugation of RSF has been previously shown not to have an effect on the shear history of the silk [129]. The RSF solution was transferred out of the dialysis cassette and into a 50 mL conical tube using a syringe and needle. This was then centrifuged (Avanti® J-Series Centrifuge, Beckman Coulter®) at 13,000 G for 20 minutes at 4 °C (Figure 3.1G). After centrifugation, large contaminants had sedimented to the bottom of the conical tube

allowing the RSF solution to be syphoned off. The resulting RSF solution had a concentration between $75 - 85$ mg.mL^{-1}.

To make the solution more concentrated it was dialysed against a 5 wt% poly(ethylene glycol) (PEG) (Av. mol. wt 10,000, Sigma Aldrich, UK), solution (Figure 3.1H). 50 g of PEG was added to 950 mL of dH$_2$O. The silk fibroin solution was transferred to a $0.5 - 3$ mL dialysis cassette (Slide-A-Lyzer™ Dialysis Cassettes, 3.5K MWCO, 3 mL, ThermoFisher Scientific, UK) using a syringe and needle. The cassette was attached to a buoyancy aid (Slide-A-Lyzer™ Cassette Float Buoys for 0.5 to 3 mL Cassettes, ThermoFisher Scientific, UK) and placed into the PEG solution. The RSF solution was concentrated over a period of 20 hours (overnight) after which it had a concentration of around 180 mg.mL^{-1}. This was then diluted down using dH$_2$O to a desired concentration and stored at 4 °C (Figure 3.1I).

A	B	C
Silk Cocoons	Cocoons boiled to remove sericin and release fibres	Silk fibres rinsed and dried

D	E	F
Silk fibres dissolved in 9.3 M LiBr at 70 °C for 3 hours	RSF/LiBr solution added to dialysis cassette	Dialysed against D.I. water for 48 hours

G	H	I
RSF solution centrifuged	RSF solution dialysed against a 10 wt% PEG solution	Concentrated RSF solution stored at 4 °C
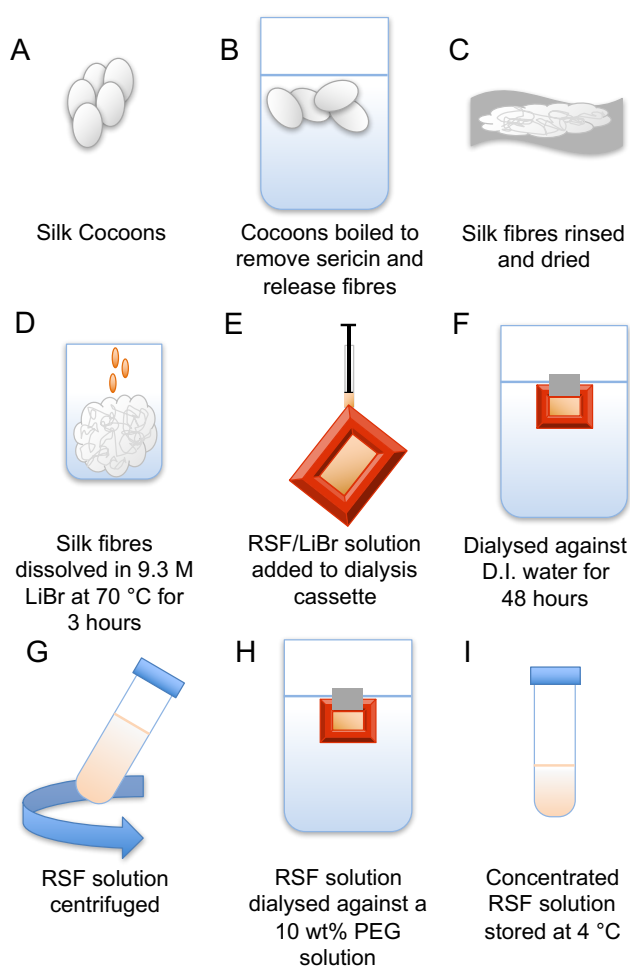
Figure 3.1: Schematic of silk fibroin extraction and concentration

3.2.2 Nano-Hydroxyapatite Synthesis

Nano-hydroxyapatite (nHA) was synthesised using a wet precipitation method based upon the patented Fluidinova process [130]. This method differs from the Fluidinova process as it is a non-continuous method of production. To get non-deficient hydroxyapatite, the molar proportions need to be exact. 4.0827 g of potassium phosphate monobasic (KH_2PO_4) ($\geq$99.0%, powder, Sigma Aldrich, UK), dissolved in 250 mL dH_2O using a magnetic stirrer. 7.3506 g of calcium chloride ($CaCl_2 \cdot 2H_2O$) (USP testing specification, Sigma Aldrich, UK), added to a separate beaker and dissolved in 500 mL dH_2O. A 1 M potassium hydroxide solution (ACS reagent, $\geq$85%, pellets, Sigma Aldrich, UK), was gradually added to the potassium phosphate and calcium chloride solutions to increase their pH. The potassium phosphate solution had its pH increased up to a pH of 13, whilst the calcium chloride solution had potassium hydroxide solution added to it until the solution became continuously cloudy, which occurred at a pH of 12.8.

The KH_2PO_4 solution was poured quickly into the $CaCl_2 \cdot 2H_2O$ solution and mixed with the magnetic stirrer for 1 hour. It was then left to rest for 7 hours, after which the solution had started to separate into a cloudy solution which sank to the bottom of the beaker and a clear solution remaining at the top. The clear solution was syphoned off and the beaker topped up with dH_2O. The solution was placed back on the magnetic stirrer for another 20 minutes before being left to rest for a day. This was repeated twice to neutralise the solution.

After the final wash, the denser cloudy solution at the bottom of the beaker was then either used for printing or analysed for hydroxyapatite content. 1 mL of the solution was weighed using an analytical balance to calculate its density. The density was calculated to be 1.01542 $g.cm^{-3}$.

nHA solution concentration was obtained by performing thermogravimetric analysis (Pyris™ 1 TGA, PerkinElmer). The nHA solution was heated from a starting temperature of 30 °C up to 400 °C at a rate of 10 °C per minute. During heating the sample chamber was purged with nitrogen.

The nHA solution was mixed with RSF solution which had a concentration of 100 mg.mL^{-1}. nHA/RSF ink concentrations were calculated based upon the dry weights of each component solution. Inks were made which had dried weights equivalent to 100 %, 75 %, 50 % and 25 % nHA content. From this point on, each of these inks will be referred to based upon their dried weight nHA content.

3.3 nHA Characterisation

For analysis the nHA solutions were dried in an oven for two days at 70°C. The dried product was ground up in a pestle and mortar until a fine uniform powder was formed. The powder was either left in an unsintered state or placed in a furnace for sintering. To sinter the powder, it was heated at 10 °C/min to 1000 °C and held for 2 hours.

3.3.1 X-Ray Diffraction

To analyse the quality of the nHA powders, X-Ray Diffraction (XRD) was performed. Powders were prepared and attached to acetate discs positioned in metal holders with a thin layer of PVA glue. Enough PVA glue and powder were used to give a thick uniform layer over the acetate disc which upon drying didn't become grainy.

Powder XRD spectra were recorded at room temperature using a diffractometer (STOE STADI P, High Resolution Powder diffractometer, [radiation source Cu K$_\alpha$ = 1.54051 Å]) operating at 40 kV and 35 mA. Data was collected over the range of 3-90° 2θ with a 0.03° incremental step.

3.3.2 Fourier Transform Infrared Spectroscopy with Attenuated Total Reflection

Fourier Transform Infrared Spectroscopy with Attenuated Total Reflection (FTIR-ATR) was used to analyse the purity of the nHA powders. Infrared spectra were collected for nHA sintered and unsintered powers and also RSF and nHA/RSF films. Spectra were collected using a Fourier transform infrared spectrometer (Frontier FTIR, PerkinElmer) equipped with an attenuated total reflectance accessory (Golden

Gate™ Diamond ATR, Specac). For each measurement, 16 scans were co-added with a resolution of 4 cm^{-1}, wavenumbers ranged between 500 – 4000 cm^{-1}.

3.3.3 Transmission Electron Microscopy

Particle morphology was determined using Transmission Electron Microscopy (TEM). Unsintered nHA powder was re-suspended in ethanol at very low concentrations. The solution was placed in an ultra-sound for 15 minutes to disperse the HA. A few drops of the solution were applied to the top of TEM sample mounting discs. A transmission electron microscope (Tecnai G2 Spirit TEM, FEI), operating with an accelerating voltage of 80 kV and emission at 6.75 µA, was used to capture images of the particles. Images were analysed for particle size using ImageJ2 software [131]. Within each image singular particles were measured along their short and long axis.

3.4 Ink Characterisation

3.4.1 Viscosity

Dynamic viscosity measurements were made using a rheometer (Physica MCR 301 Rheometer, Anton Paar). All samples were analysed using a cone and plate geometry (θ = 0.998°; diameter 49.972 mm; gap set to 0.1 mm) at a temperature of 20 °C. The temperature was maintained by a Peltier built into the stage. Viscosity measurements were made in the rotational mode between 0.01 and 10,000 s^{-1}.

3.4.2 Surface Tension

Surface tension measurements were made using the Pendant Drop Method. The equipment for measuring the surface tension comprised of an AL-1000 Programmable Syringe Pump, World Precision Industries, with a syringe attached to a horizontally positioned flat ended needle tip. The syringe pump was programmed to give a low flow rate to give a slow and stable droplet formation.

Droplet formation and detachment from the needle tip were filmed using a camera. The camera comprised of a Macro 10X lens, Computar, and a DCC1545M camera, Thorlabs, which was connected to a computer. Images of the droplet just before

detachment were analysed using a Pendant Drop plugin [132] on open sourced Fiji software [133]. In the software, the image was converted to an 8-bit image and given a scale. A box is drawn around the droplet, with the top of the box aligned with the edge of the needle tip. The Pendant Drop plugin then analyses the surface tension adjusting for any slight angle of the needle tip. During fitting a red line is traced around the droplet. An accurate measurement is only given if the red trace fully matches the outline of the droplet, as seen in Figure 3.2.
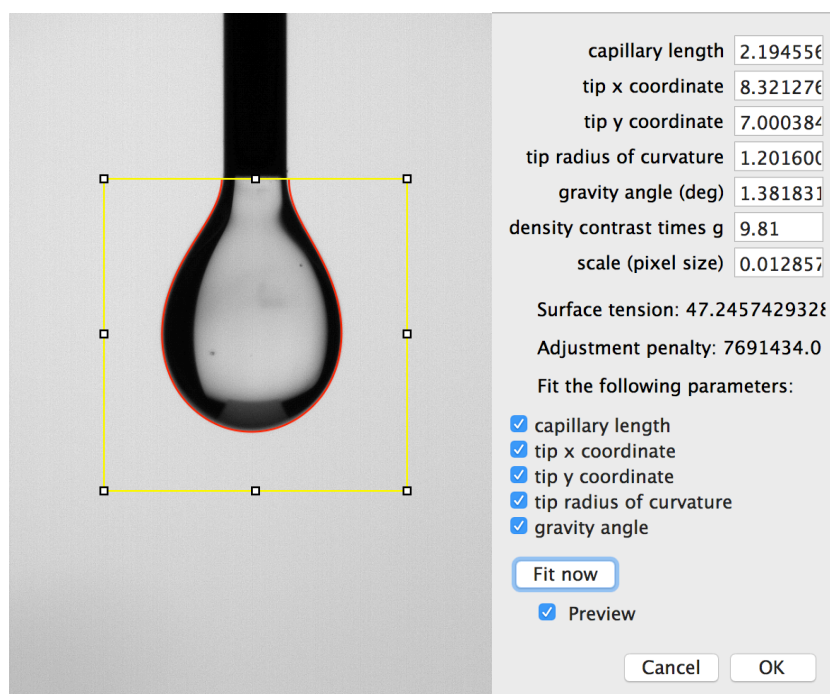
Figure 3.2: Screen shot of 'Pendant Drop' plugin on 'Fiji' software analysing the surface tension of an RSF droplet with a concentration of 100 mg.mL^{-1}

3.5 Film Production

3.5.1 Inkjet Printing

Inkjet printing was performed on a MicroFab drop on demand piezoelectric inkjet printer using JetLab4 software. A piezo printhead with a nozzle aperture of 80 μm was used to print the RSF and RSF/nHA inks; and a 60 μm printhead was used to print methanol (ACS reagent, ≥98%, Sigma Aldrich, UK). Jetting parameters were optimised for each ink to get a stable droplet formation.

Each of the jetting parameters (Table 1 and 2) are used to create a waveform for the piezoelectric actuator. The waveform consists of different voltages: idle voltage, dwell voltage and echo voltage, which are held for determined periods of time; namely dwell time and echo time. Also included are the times taken to reach the dwell voltage from the idle voltage (rise time), the dwell voltage to the echo voltage (fall time), and the echo voltage to the idle voltage (rise time 2). These parameters are graphically displayed in Figure 3.3. Each of these parameters play an important role in producing acoustic waves within the printhead capillary. The acoustic waves need to supply enough energy to expel a droplet from the nozzle, but must also dissipate before the next acoustic wave is produced.
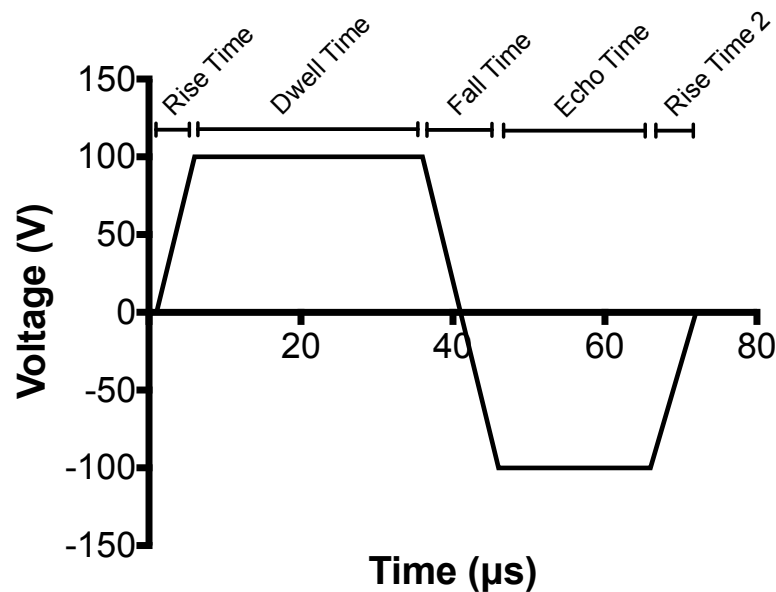
Figure 3.3: Standard waveform for RSF ink at 100 mg.mL^{-1}

Each ink required different printing parameters, which are summarised in Table 1 and Table 2. Printing parameters varied slightly between RSF batches and as the solution aged. After two weeks stored at 4 °C the RSF ink became unreliable and was likely to block the nozzle. Therefore, no inks were used which were over a fortnight old. Laboratory temperature and humidity could also affect droplet propagation and hence waveform parameters. All printing was performed at a frequency of 300 Hz. Samples were printed 'on the fly' meaning that the substrate was in constant motion below the printhead.

Ink	Rise Time (μs)	Dwell Time (μs)	Fall Time (μs)	Echo Time (μs)	Rise Time 2 (μs)	Idle Voltage (V)	Dwell Voltage (V)	Echo Voltage (V)
RSF	6	30	10	20	6	0	100	-100
Methanol	2	120	7	20	4	0	40	-20

Table 2: nHA/RSF ink printing parameters

nHA (wt%)	Rise Time (μs)	Dwell Time (μs)	Fall Time (μs)	Echo Time (μs)	Rise Time 2 (μs)	Idle Voltage (V)	Dwell Voltage (V)	Echo Voltage (V)
100	5	40	6	40	4	0	110	-25
75	5	110	10	110	6	0	110	-90
50	5	110	10	110	6	0	140	-140
25	4	100	7	200	6	0	110	-70

Ratios of RSF to methanol were controlled through droplet spacing and by monitoring droplet sizes. Droplets were photographed using the camera attachment of the MicroFab printer once fully detached from the nozzle and spherical in shape. Droplet volumes were calculated by measuring droplet diameters using ImageJ2 software and using the equation for a sphere:

$$V = \frac{4}{3} \times \pi \times r^3$$

Equation 3

Where 'V' is the droplet volume and 'r' is the droplet radius.

Droplet volumes were then used along with the step size between printed droplets to calculate the volume of ink printed per unit area. Volume per printed area for the RSF ink and the Methanol were compared and step sizes altered to give varying ratios

of printed RSF to Methanol. To ensure that the ratios remained accurate during printing, droplet stability, shape and size were monitored before and after each printed layer. Ratios were recalculated daily due to the necessity to adjust the waveform to compensate for aging of the RSF ink and changes in temperature.

RSF films were produced by printing RSF ink at a concentration of 100 mg.mL^{-1} with a step size (the distance between the centre of each printed droplet) between 0.14 – 0.16 mm and Methanol with a step size between 0.06 and 0.17 mm. Droplets were printed so that they overlapped but did not flood the substrate. Each printed RSF layer was followed by a subsequent layer of printed Methanol. Films were produced by printing alternate layers of RSF ink and Methanol, as demonstrated in Figure 3.4, to a height of 20 RSF layers. The time it took to print each layer of RSF meant that by the time the methanol was printed on top of each RSF layer, the RSF had already dried.
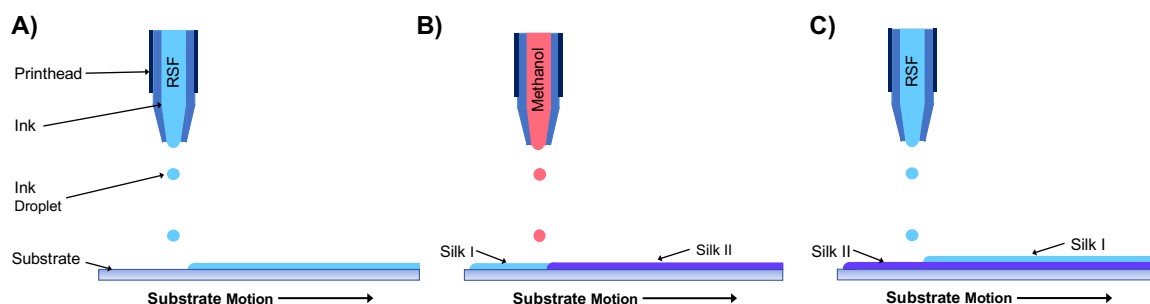
Figure 3.4: Schematic showing the printing of layers to produce an RSF film; A) a layer of RSF is printed, B) followed by a layer of methanol which converts the RSF structure from silk I to silk II, C) the process is repeated, with a layer of RSF printed on top of the previous layer

RSF films were printed onto 13 mm diameter glass coverslips with different volume percentage ratios of RSF ink to methanol. The range of ratios printed were: 1:0, 3:1, 2:1, 1:1, 1:2 and 1:3, whereby a ratio of 3:1 is the equivalent of 300 mg RSF for every 1 mL of methanol, and a ratio of 1:3 is the equivalent of 100 mg RSF for every 3 mL of methanol. This meant that the volume of RSF ink printed equated to: 100 %, 75 %, 66 %, 50 %, 33 % and 25 %, of the total volume of RSF ink and methanol printed to produce the RSF films, and are shown in Table 3. From this point on, the RSF films will be referred to based upon their contributing percentage of RSF ink, whereby RSF

film 100 % represents a 1:0 printed ratio, and an RSF film without any methanol treatment. An RSF film 25 % represents a 1:3 printed ratio, and an equivalent methanol treatment of 100 mg RSF for every 3 mL of methanol. RSF films remained attached to the coverslips for the degradation and cell studies to prevent the films from floating.

Table 3: Proportion of RSF to methanol for each RSF film, whereby RSF film 100 % has had no methanol treatment, and RSF film 25 % consists of 1 part RSF for every 3 parts methanol. (This table is repeated later on for ease of reference)

RSF Film	Ratio RSF: Methanol (100 mg: mL)
100 %	1:0
75 %	3:1
66 %	2:1
50 %	1:1
33 %	1:2
25 %	1:3

3.5.2   Casting RSF Films

RSF films were cast by pipetting 0.5 mL of RSF at 100 mg.mL^{-1} onto glass coverslips. These were left to dry in a laminar flow hood for 48 hours. After this period the RSF films had set. To increase β-sheet content, methanol was poured into a petri dish and the films submerged. The lid was placed onto the petri dish to prevent methanol evaporation and left for four days to induce maximum β-sheet formation [134].

3.6   Film Characterisation

3.6.1   Contact Angle

Wettability of the RSF films was evaluated using the sessile drop method. Contact angle measurements were performed using a camera to capture droplet images positioned on a horizontally level substrate. The camera was composed of a Macro 10X lens, Computar, and a DCC1545M camera, Thorlabs. The camera was positioned level with the plane of the substrate. Droplets were dispensed manually onto the

substrate using a syringe and photos taken after a few seconds once the droplet contact line had stabilised. Photos were analysed using open sourced software ImageJ2 software [131] with the plugin Dropsnake [135]. The Dropsnake plugin allowed the surface of a droplet to be traced. Contact angle measurements were given for both sides of the droplet, and an average of both measurements was recorded. Five repeats were performed for each droplet.

3.6.2 Interferometry

To better characterise surface topography, surface roughness measurements were made using an interferometer (ContourGT, Bruker). Surface parameters were calculated over a 0.6 mm x 0.47 mm area. The average peak to valley distance, which is a measurement of surface area roughness (S_a), was calculated from a mean of 5 measurements.

3.6.3 Fourier Transform Infrared Spectroscopy with Attenuated Total Reflection

FTIR-ATR measurements were made to analyse silk I and silk II content of the films. FTIR-ATR was performed as described in section 3.3.2 Fourier Transform Infrared Spectroscopy with Attenuated Total Reflection.

3.6.4 Fourier Self Deconvolution

Fourier Self Deconvolution (FSD) was performed to determine percentage contribution of secondary protein structure. FSD was performed using OriginPro 2016 software, on the amide I ($1705 - 1595$ cm^{-1}) region of the spectra. FSD was performed based on the methodology explained by X. Hu *et al.* [94]. To resolve hidden peaks, the second derivative of the spectra was calculated and a nine-point Savitsky-Golay smoothing filter was used on the second derivative to reduce noise within the spectra. Hidden peaks of the spectra were shown as minima in the second derivative. The minima were used to position bands during curve fitting of the spectra. Gaussian line shape profiles were used to fit the bands with an accumulative curve fit to the spectra. The OriginPro software used the Levenberg-Marquardt algorithm to fit the spectra. Band positions and baseline were fixed during curve

fitting and each band assigned a maximum value for the full width at half maximum (FWHM). FWHM values of 15, 20, 25 and 30 cm^{-1} were used for each spectrum to ensure that the true fit was established and avoid any artefacts. Differences in percentage contributions between the different FWHM values are represented as error bars where curve fitted data has been displayed.

3.7 Degradation Test

Degradation tests were performed in either phosphate buffered saline (PBS) (Dulbecco's Phosphate Buffered Saline, without calcium chloride and magnesium chloride, Sigma Aldrich, UK), or a buffered solution of Protease XIV (3.5 units/mg, from *Streptomyces griseus,* powder, Sigma Aldrich, UK). Protease XIV consists of a mixture of at least 10 different proteases; five serine-type proteases, two zinc endopeptidases, two zinc leucine aminopeptidases and one zinc carboxypeptidase [136]. Due to the range of proteases included within the mixture, Protease XIV can be used for the complete, or near complete degradation of a protein into its individual amino acid components by breaking down the protein peptide bonds.

The protease solutions were at a concentration of 0.1 mg.mL^{-1} Protease XIV in PBS, as reported by E. M. Pritchard *et al*. [137]. This gave a gradual degradation rate enabling the degradation rates of different films to be observed. RSF films were placed into 24-well plates and submerged in either 1 mL of PBS or 1 mL protease solution and incubated at 37 °C for a maximum period of 8 days. Protease XIV remains active for a period of 24 hours, consequently the PBS and protease solutions were replenished daily [138].

At designated time points, 1, 2, 3, 5, 8 days, a subset (n=3) of the films were removed. The removed films were washed three times by submersion in 1 mL of PBS for 2 minutes. Films were then dried in a drying oven at 60 °C for 1 hour to remove moisture. Films were weighed using an analytical balance prior to and after the degradation test.

3.8   Cell Studies

3.8.1   Film Sterilisation

Silk can be sterilised by a variety of methods, however not all methods preserve the secondary protein structure [139]. UV radiation was chosen to sterilise the samples as it has previously been shown not to affect the protein structure [139]. RSF and nHA/RSF films were placed in 24-well plates (Corning® Costar® Cell Culture Plates, Sigma, UK) and placed in a Class II laminar flow hood with a UV bulb. Plate lids were removed and the hood was closed with the laminar flow switched off. The UV light was then switched on and the samples remained in the hood, under UV light, for 4 hours.

3.8.2   Cell Culture

MG-63 human osteosarcoma cells were maintained in minimum essential medium (α-MEM, Sigma Aldrich, UK), supplemented with 5% (v/v) foetal bovine serum (biosera), 50 μg.mL^{-1} penicillin-streptomycin and 2 mMol L-glutamine. Cells were kept at 37 °C under a humidified atmosphere of 5% CO_2 and 95% air humidity.

For the following experiments, samples were first UV sterilised as described above, before being seeded with 1×10^4 cells in 500 μL of media. These were then incubated and the media replaced every two days.

3.8.3   PrestoBlue® Assay

Viability assays were performed using the PrestoBlue® reagent (PrestoBlue® Cell Viability Reagent, Invitrogen™, Thermo Fisher Scientific). PrestoBlue® is a non-fluorescent resazurin-based solution which permeates cells. PrestoBlue® is reduced by metabolically active cells into resorufin which is a fluorescent compound. PrestoBlue® assays were performed on the samples after 1, 3, 7 and 14 days in culture.

PrestoBlue® was mixed with cell media to a ratio of 1:10. 700 μL of the solution was added to each well and incubated at 37 °C for 1 hour. After incubation, 200 μL

aliquots were taken from each well in triplicate and placed into a 96-well plate. Fluorescence intensity was measured using a fluorescence reader (Tecan Spectrophotometer) at an excitation wavelength of 570 nm and an emission wavelength of 600 nm.

3.8.4   PicoGreen® Assay

To monitor the number of cells, double-stranded DNA (dsDNA) was measured using a PicoGreen® assay kit (Quant-iT™ - PicoGreen® dsDNA assay kit, Invitrogen™, Thermo Fisher Scientific). PicoGreen® dye is a fluorescent nucleic acid stain which when bound to dsDNA in solution will produce an emission at 520 nm which has minimal contribution for either RNA or single-stranded DNA.

After 1, 2 and 3-week time points the samples were washed in PBS three times to remove cells which weren't attached to the film, before being submerged in 1 mL of dH$_2$O and frozen. A freeze thaw cycle was used to lyse the cells, and with every thaw each well was mixed with a 1 mL pipette before being refrozen. On the second freeze thaw cycle, 300 μL of solution was taken from each sample to be used for the PicoGreen® assay.

PicoGreen® assays were performed according to the manufacturer's protocol [140]. In brief, 100 μL of solution from each sample was transferred in triplicate to a 96-well plate. 100 μL of Quant-iT™ PicoGreen® reagent was then added to each well using a multi-pipette to reduce the time of adding the reagent to all of the wells. The well-plate was covered in foil to protect it from light and incubated at room temperature for 4 minutes. Fluorescence was measured at an excitation and emission wavelength of 485 nm and 520 nm respectively using a fluorescence reader (Tecan Spectrophotometer). Results were compared to a standard curve produced using the Lambda DNA standard provided.

3.8.5   Alkaline Phosphatase Assay

Alkaline phosphatase (ALP) activity was analysed using an Alkaline Phosphatase Diethanolamine Activity Kit (Alkaline Phosphatase Diethanolamine Activity Kit, Sigma Aldrich). The kit measures ALP activity by the hydrolysis of para-nitrophenyl phosphate (p-NPP).

Using the same samples used for the PicoGreen® assay, 30 μL of solution was taken from each sample on the third freeze thaw cycle. ALP assays were performed in accordance with the manufacturer's protocol [141]. In brief, a 0.67 Mol solution of p-NPP was prepared with provided reaction buffer as well as an ALP enzymatic control solution with an 0.15 U.mL^{-1} concentration. 10 μL of solution from each sample was transferred to a 96-well plate in triplicate. 230 μL reaction buffer was added to each well containing the sample solutions. A control of 5 μL ALP enzymatic solution with 235 μL reaction buffer was prepared in triplicate, as well as a blank well containing 240 μL of reaction buffer.

Using an absorbance reader (Tecan Spectrophotometer), the 96-well plate was heated up to 37 °C. Using a multi-pipette, 10 μL of p-NPP substrate solution was added to each well. Immediately after, absorbance values were measured at 405 nm every 45 seconds over a period of 10 minutes.

From the resulting graphs a maximum rate of linear increase was recorded for all samples over the same time period, between 1 minute 30 seconds and 4 minutes 30 seconds. This was then used in the following equation provided by Sigma Aldrich in their protocol to calculate units per milligram of solid: [141]

$$\frac{(\Delta A_{405\ nm}/\min Test\ -\ \Delta A_{405\ nm}/\min Blank)(V_F)}{(18.5)(V_E)}$$

Equation 4

Where $\Delta A_{405\,nm}$ is the maximum rate of linear increase, V_F is the volume of the assay, 18.5 is the millimolar extinction coefficient of p-NPP at 405 nm, and V_E is the volume of enzyme used.

3.9 Statistics

Statistical comparisons were performed using a two-way ANOVA test followed by a Tukey's post hoc test (GraphPad Prism version 6.0h for Mac OS X, GraphPad Software, La Jolla California USA) considering a significant difference at the 95% confidence interval. Standard deviations used were at P=0.05 or 0.001 level as mentioned.

Chapter 4: Printability of Silk Fibroin and Silk Fibroin/ Nano-Hydroxyapatite Composite Inks

4.1   Introduction

Droplet formation and stability are key to producing reliable and repeatable experiments with reactive inkjet printing. There are two key factors which influence droplet formation and stability, which are the applied waveform and the rheology of the ink. The waveform of the applied driving voltage causes the piezo' material to change shape, which in turn induces acoustic waves within the printhead which assist in the ejection of droplets. The rheology of an ink affects droplet propagation, ejection and droplet interaction with the substrate. Two important rheological properties for an ink are its surface tension and viscosity, which along with ink density and nozzle diameter can be used to predict printability of an ink in the form of the Z number [122], [142].

This chapter will assess the printability of the regenerated silk fibroin (RSF) and nano-hydroxyapatite (nHA)/RSF inks through their measured surface tensions, viscosities and finally, calculated Z numbers. The chapter is split into two main sections. The first section will focus on the analysis of the RSF inks and the second will provide the analysis of the nHA/RSF inks.

4.2   Results and Discussion

4.2.1   RSF Inks

4.2.1.1   *RSF Ink Surface Tensions*

Surface tension values of the RSF inks were measured using the 'Pendant drop' method [143]. Measurements were made from three RSF batches, with five droplets from each batch used to calculate surface tension values, the results of which are shown in Figure 4.1. The surface tension of an ink is important as it affects the fluid meniscus produced at the nozzle tip and prevents the ink from flooding the nozzle

tip. Surface tension is also linked to droplet stability after ejection which can influence the quality of a print [118].

Surface tension values measured at room temperature were found to lie between $47 - 55$ mN.m^{-1}. The lowest concentrations, between $10 - 50$ mg.mL^{-1}, had the highest surface tensions with an average of 53.5 mN.m^{-1}. Between concentrations of 50 and 70 mg.mL^{-1} the average surface tension dropped by around 10 %. Inks with a concentration of 70 mg.mL^{-1} and higher had an average surface tension of 48.1 mN.m^{-1}. Pure water has a surface tension at room temperature of 72.74 mg.mL^{-1} [144].

Figure 4.1: Surface tensions of RSF with different concentrations measured with the 'pendant drop' method. Standard deviation is shown (n=15)

The slight drop in surface tension might be explained by the work of Yang *et al.* [145]. They modelled the RSF protein at the liquid-air interface and suggested two separate models for high and low RSF concentrations. High concentrations were deemed as solutions higher than 100 mg.mL^{-1} and low concentrations as anything lower. They modelled the RSF molecule as a multi-block amphiphilic macromolecule. At low concentrations the molecules at the liquid-air interface are able to arrange into favourable positions for both hydrophobic and hydrophilic side chains; taking on

helical silk III or β-sheet silk II conformations, which produces a surface with high elasticity. As the concentration of the RSF solutions increases, the air-water interface becomes more crowded with RSF molecules. The crowding of the RSF molecules at the surface forces the surface RSF molecules into a hairpin-like configuration with a large proportion of the RSF molecule protruding from the surface layer, decreasing surface elasticity [145]. The experiment by Yang *et al.* looked at RSF concentrations over a much larger range than those used in this study, however it is suggested that the slight drop in surface tension experienced by the higher concentrated solutions could be the beginning stages of the RSF molecules taking on a hairpin-like conformation.

4.2.1.2 *RSF Viscosity*

The viscosity of the RSF solutions was measured using a rotational rheometer with a cone and plate attachment. Flow curves were produced which compare the apparent viscosities of each ink with increasing shear rates, and are shown in Figure 4.2. Ink viscosity is important to analyse as it is related to drop propagation within the printhead as well as jet stability once the ink has left the nozzle [121].

The RSF solutions appear to be unstable at shear rates below $10\ s^{-1}$, and experienced a non-Newtonian behaviour with pronounced shear thinning up to shear rates of $1000\ s^{-1}$. From a shear rate of $100\ s^{-1}$ and above the solutions began to become shear independent, transitioning into Newtonian behaviour. RSF solutions with a concentration of $40\ mg.mL^{-1}$ or lower have had several data points removed from the final Newtonian plateau as these results showed a rapid increase in viscosity at high shear rates which was caused by the ejection of fluid from between the cone and plate apparatus.
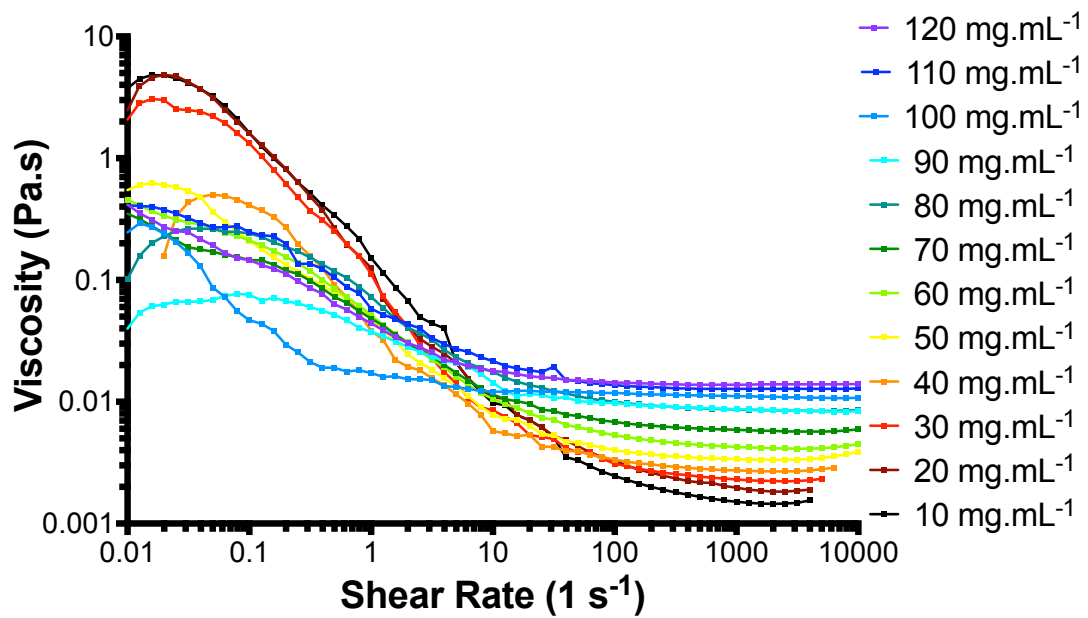
Figure 4.2: Viscosity curve of RSF solutions with different concentrations

Infinite viscosities of the RSF solutions are measured as the viscosity within the Newtonian plateau achieved at high shear. This is where the viscosity has become shear independent and is unlikely to change. Infinite shear viscosities were taken from a shear rate of 2000 s^{-1}, which is within the Newtonian plateau and a mid-range shear rate experienced during printing [146]. The infinite shear viscosities of three batches of RSF ink are compared in Table 4. Infinite viscosities appear to linearly increase with increased concentration.

Table 4: Infinite viscosity values for RSF inks taken from three RSF batches (n=3)

Concentration (mg.mL^{-1})	Infinite Viscosity (mPa.s)	Standard Deviation	Standard Deviation (% of Av.)
10	1.50	0.05	3.36
20	1.88	0.04	2.32
30	2.27	0.03	1.32
40	2.77	0.10	3.43
50	3.44	0.14	4.07
60	4.13	0.03	0.74
70	5.58	0.26	4.65
80	8.68	0.36	4.20
90	8.37	0.60	7.14
100	11.07	0.31	2.76
110	12.73	0.80	6.30
120	14.10	0.35	2.46

4.2.1.3   RSF Z Numbers

The Z number is a dimensionless number which is commonly used in inkjet printing to predict the printability of an ink. If an ink has a Z number between 1 and 10 it is thought to be suitable for reliable inkjet printing [115], [117], [123], [124]. Low Z numbers indicate viscous inks while high Z numbers have an increased likelihood of satellite formation [124]. Z numbers were calculated using the density of each RSF ink, which was calculated by the ratio of RSF to water using the density of pure silk as 1,310 kg.m^{-3} [147] and the density of water as 1000 kg.m^{-3}.

With Newtonian fluids, the zero-shear viscosity is used to calculate the Z number. Most inks used within inkjet printing have Newtonian fluid properties, or, are unlikely to experience significant changes in viscosity over a range of shear rates. However, for a non-Newtonian fluid the viscosity becomes a function of shear, meaning that

the Z number is harder to predict. A non-Newtonian fluid can have a zero-shear viscosity vastly different to that of the infinite viscosity. Thus, the infinite viscosity might be more appropriate to use in the calculation of the Z number for non-Newtonian fluids. As the RSF inks have displayed non-Newtonian characteristics, Z numbers were calculated using infinite shear viscosities collected from a shear rate of 2,000 s^{-1} which is a mid-range shear rate experienced during printing [146]. The Z numbers for each of the RSF inks is shown in Figure 4.3.
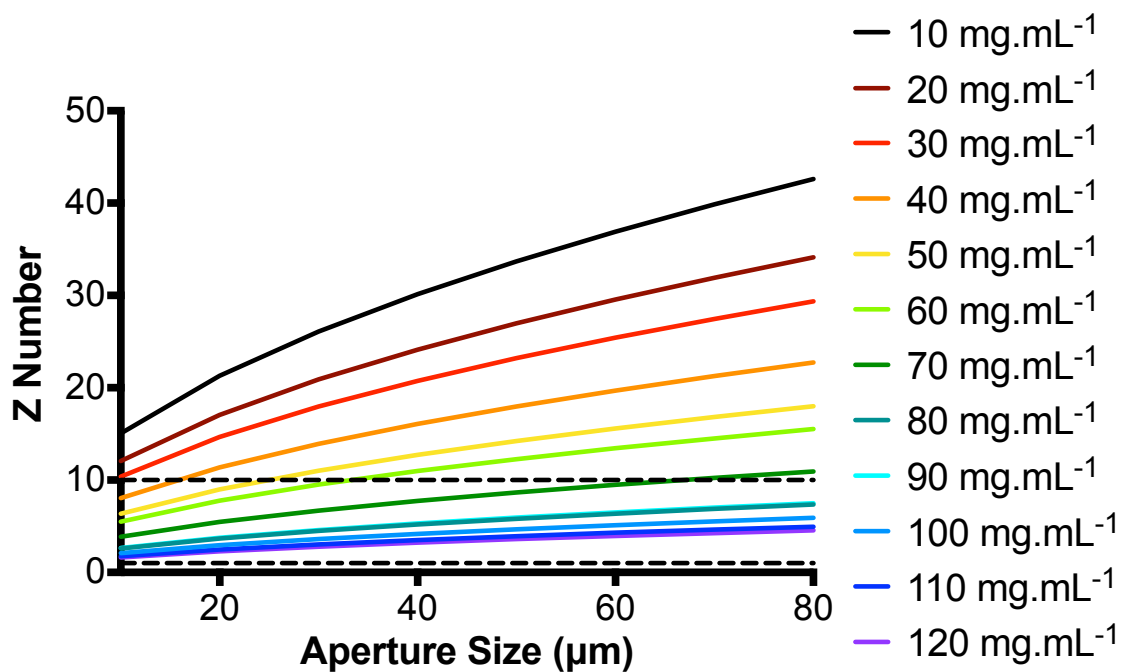
Figure 4.3: Z numbers for RSF inks at different concentrations. Horizontal dashed lines indicate the predicted range for the most printable inks.

Over a range of aperture sizes, the RSF solutions of 80 mg.mL^{-1} and higher consistently gave Z numbers within the predicted stable printing range (Figure 4.3). A concentration of 70 mg.mL^{-1} had a Z number below 10 (hence within the most stable range) up until a nozzle aperture size of 60 μm. Other concentrations; 40, 50 and 60 mg.mL^{-1} began within the stable printing range, however, with increasing aperture sizes their Z numbers increased above 10, suggesting unstable jetting behaviour. The three lowest concentrations; 10, 20 and 30 mg.mL^{-1} did not fall within the stable printing range for any aperture sizes.

All inks with a Z number which predicted stable printing with an 80 μm printhead were loaded into the printer. An 80 μm printhead was chosen to print the inks as it would produce the largest droplets and therefore be the fastest at depositing large quantities of material. Stable drop formation (shown in Figure 4.4) was achieved with all concentrations tested. The highest concentration inks, 110 and 120 mg.mL^{-1}, required the highest driving voltages, which were at the limit of the printer's capability, in order to produce droplets over a sustained period of time. Even though RSF inks with a concentration of 110 and 120 mg.mL^{-1} had Z numbers well within the stable printing range, during printing the nozzle began to crust over, preventing the ejection of droplets. Therefore, an ink concentration of 100 mg.mL^{-1} was chosen as the appropriate ink with which to print the RSF films.
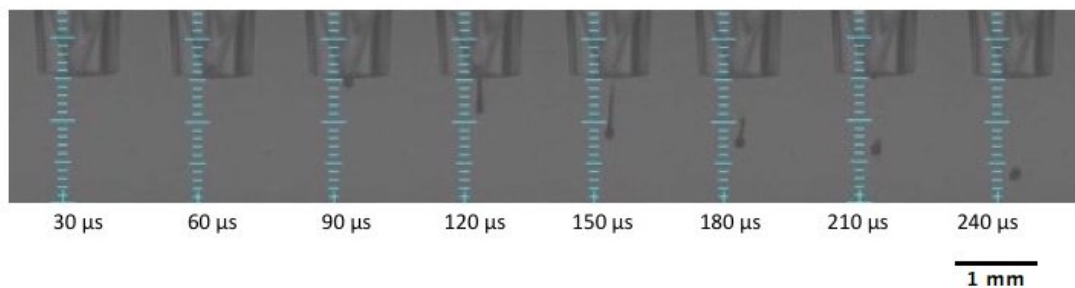
Figure 4.4: Droplet formation of RSF ink at a concentration of 100 mg.mL^{-1} taken at 30 μs intervals

4.2.2 nHA/RSF Inks

A composite ink consisting of nHA and RSF was investigated for inkjet printing. Inks were formulated based upon the dried weight of the nHA and RSF solutions. Inks were produced which had a dried weight content of nHA with: 25 %, 50 %, 75 % and 100 %. From this point on the nHA/RSF inks will be referred to based upon their nHA dried weight content.

4.2.2.1   nHA/RSF Ink Surface Tensions

Surface tensions of the nHA/RSF inks were likely to be different to those of the pure RSF solutions as the nano particles would interact with the droplet surface. It has previously been shown that the inclusion of nanoparticles can cause an increase in surface tension [148]-[150]. Surface tensions were measured using the 'Pendant

drop' method from three separate batches of RSF. The results of the surface tension measurement are shown in Figure 4.5.
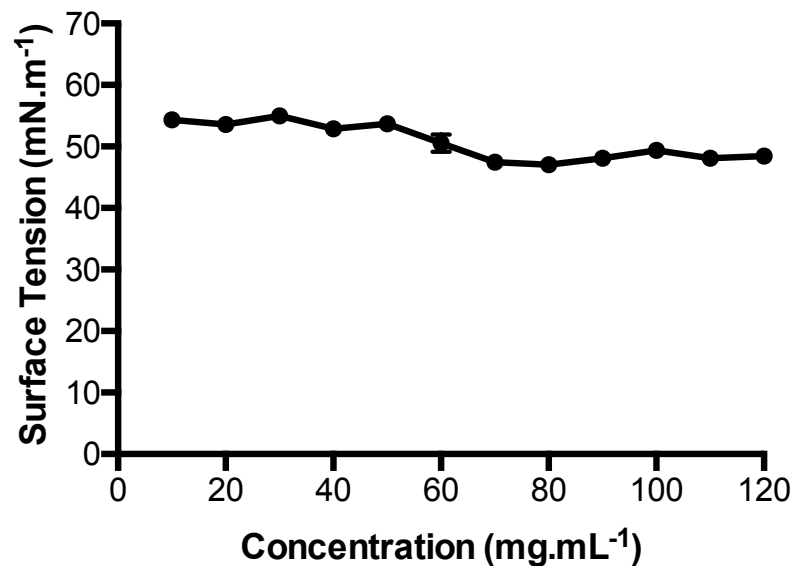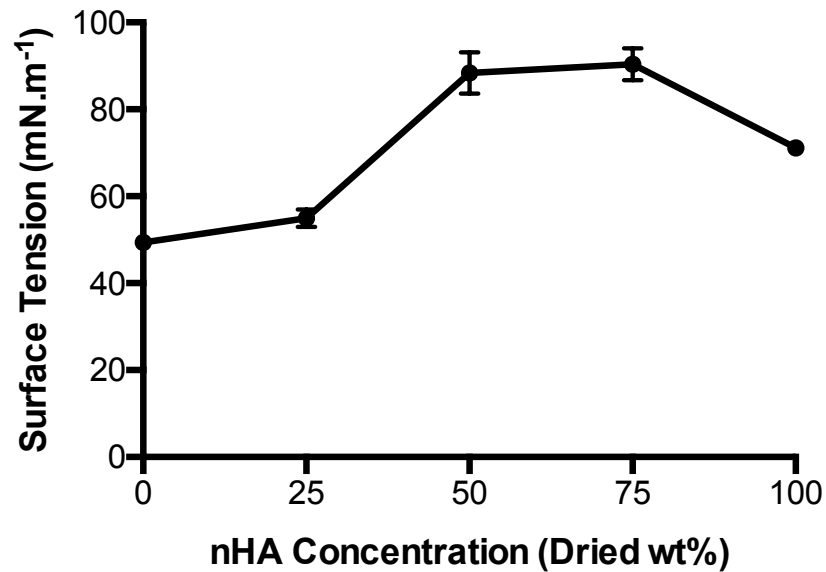

Figure 4.5: Surface tensions of nHA/RSF inks with different concentrations measured with the 'pendant drop' method. Standard deviation is shown (n=15)

The nHA/RSF ink without any RSF content (nHA/RSF ink 100 %), consisting only of nHA and water had a surface tension of 71 $mN.m^{-1}$, similar to pure water which is around 72 $mN.m^{-1}$ at the recorded temperature [144]. nHA has previously been shown to improve the hydrophilicity of composites indicating that nHA is hydrophilic [151], [152]. Hydrophilic particles completely wet (become surrounded by a layer of water) and do not influence the water-air interface [150], which would explain why the highest concentration of nHA particles had only a minor effect on the surface tension of the water base.

Substantial increases in surface tension were measured with the inclusion of nHA to the RSF ink. The nHA/RSF ink 25 % saw an increase of surface tension equivalent to around 10 % of the pure RSF solution (0 wt% nHA). However, the surface tensions for nHA/RSF inks 50 % and 75 % had the highest surface tensions, averaging with 88 and 90 $mN.m^{-1}$ respectively. The surface tensions of the nHA/RSF inks 50 % and 75 % were

not as stable as the other concentrations, and had a greater variation between each batch of ink.

Whereas nHA in water was seen to have a limited effect on surface tension values, the inclusion of both nHA and RSF was seen to be highly influential on the surface tension. The RSF surface could be deforming around the nHA particles at the surface, which therefore causes an increases in surface tension [153]. The more hydrophilic the particles are, the less they will protrude and distort the surface of the droplet. To understand what is causing the significant changes in surface tension, further work would be necessary to investigate the interaction of individual nHA particles with the RSF surface as well as how nHA particle concentration at the RSF surface affected surface tension values.

4.2.2.2   nHA/RSF Viscosity

Viscosities of the nHA/RSF inks were measured using a rotational rheometer to evaluate their suitability for printing. Flow curves for the nHA/RSF inks are shown in Figure 4.6. Viscosities of the nHA/RSF inks appeared to be more stable at low shear rates compared to that of the pure RSF inks, however the nHA/RSF inks took longer to achieve shear independence at high shear rates.
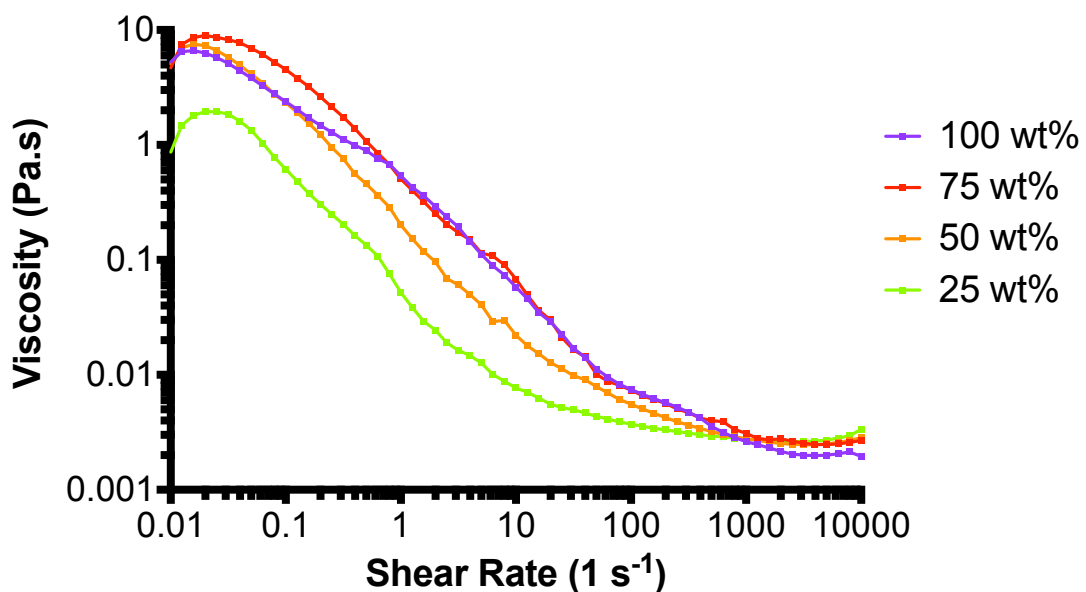
Figure 4.6: Viscosity curves for the nHA/RSF composite inks. Weight percentages shown represent the dried weight nHA content of the inks

The nHA/RSF inks began with an initial shear thickening response for low shear rates which was promptly followed by a mini plateau. A shear thinning response began before a shear rate of 0.1 s^{-1}, which ended in a Newtonian plateau at high shear rates above $1,000$ s^{-1}. Whereas the pure RSF inks had begun to settle into a Newtonian response after a shear rate just over 100 s^{-1}, it took the nHA/RSF inks up until a shear rate of $1,000$ s^{-1} to begin to become shear independent. However, as all of the inks began a Newtonian response around $1,000$ s^{-1}, the inks had become shear independent before reaching a shear rate similar to that induced during printing.

Infinite viscosity values for three batches of nHA/RSF inks taken from a shear rate of $2,000$ s^{-1} are shown in Table 5. All nHA concentrations of the nHA/RSF inks had similar infinite viscosity values despite large differences in the concentration of RSF which was seen to influence viscosity in the pure RSF inks. Infinite viscosity values of the nHA/RSF inks were similar to that of RSF inks with concentrations of $30 - 40$ mg.mL^{-1}.

Table 5: Infinite viscosity values for nHA/RSF inks taken from three separate nHA/RSF ink batches (n=3)

nHA/RSF ink	Infinite Viscosity (mPa.s)	Standard Deviation	Standard Deviation (% of Av.)
25 %	2.66	0.08	2.87
50 %	2.55	0.03	0.99
75 %	2.75	0.08	2.83
100 %	2.16	0.06	2.55

4.2.2.3   RSF Z Numbers

Z numbers were calculated for each of the nHA/RSF inks to compare their predicted printability and are shown in Figure 4.7. Only nHA/RSF inks 25 % and 75 % gave Z numbers below a value of 10, and this was only for printhead aperture size of 10 μm. All of the calculated Z numbers increased with increasing nozzle size, indicating the likelihood of the formation of satellite droplets during printing.
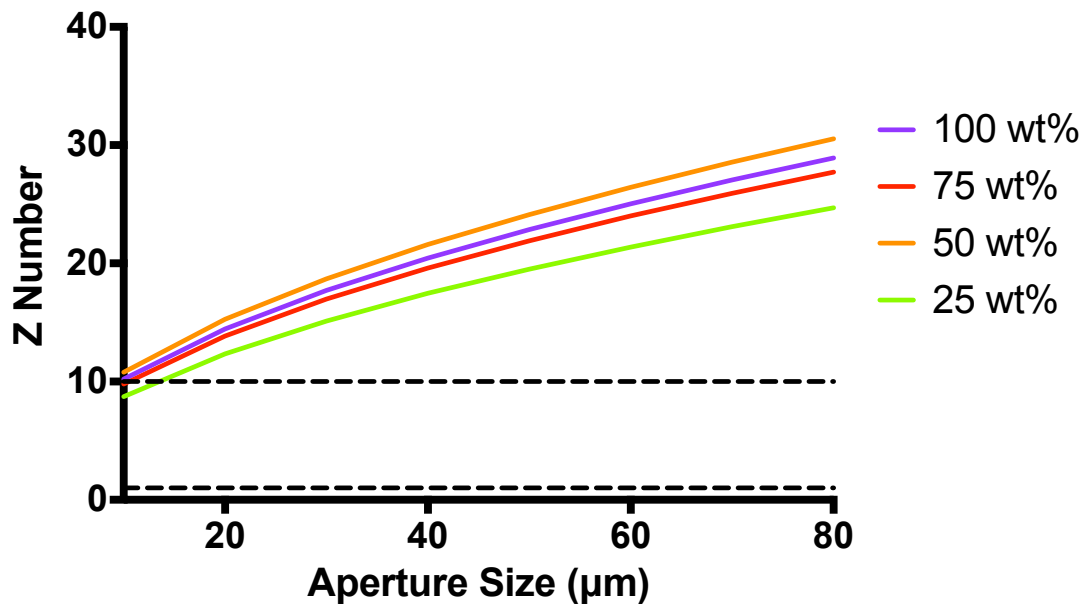
Figure 4.7: Z numbers for nHA/RSF composite inks. Horizontal dashed lines indicate the predicted range for the most printable inks.

Although none of the inks gave a Z number between 1 and 10 for aperture sizes above 10 μm, all inks were loaded into the printer and jetted through a nozzle with an 80 μm diameter to test for droplet stability. All of the inks were able to be printed with a stable droplet formation and without satellites. Usually a high Z number would predict the formation of satellite droplets, however it is possible that the high surface tensions of the nHA/RSF inks prevented this from occurring. As all of the nHA/RSF inks gave a stable droplet formation, all were deemed suitable for printing nHA/RSF films.

4.2.3 Methanol

For this investigation, the conversion of silk I to silk II required the use of printed methanol. Z numbers were calculated for methanol to estimate droplet stability using surface tension and viscosity values at 25 °C taken from the work of Won *et al*. [154].

The calculated Z numbers, shown in Figure 4.8, indicated that satellite droplet formation was highly likely during printing. All of the calculated Z numbers were higher than the most stable Z number range. As before, methanol was loaded into

the printer and jetted through a nozzle with an 80 μm diameter to test for droplet stability. Droplet formation was found to be unstable with the formation of satellite droplets. To improve droplet stability, methanol was printed through a 60 μm diameter printhead, which had a lower Z number. A stable droplet was able to be produced using the smaller printhead and was therefore selected to print the methanol for the RSF and nHA/RSF films.
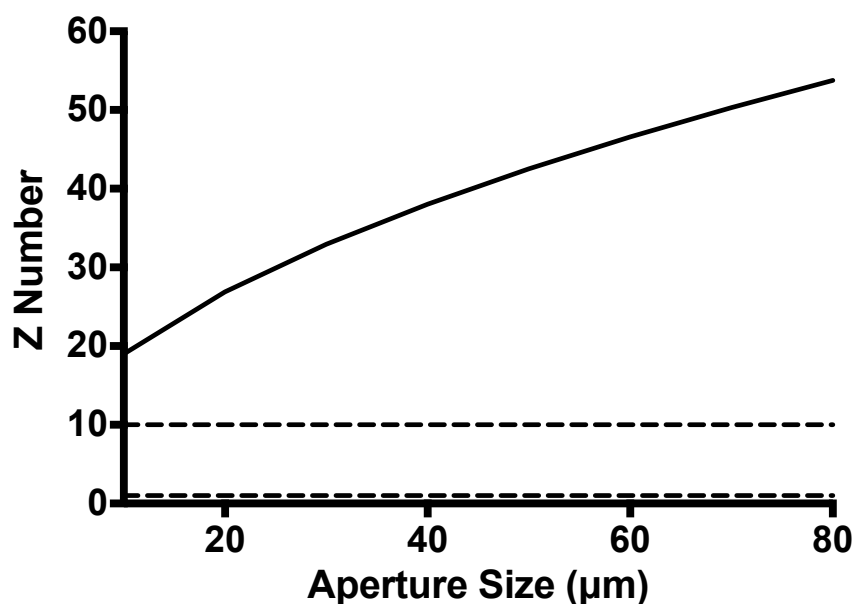
Figure 4.8: Z numbers for methanol. Horizontal dashed lines indicate the predicted range for the most printable inks.

4.3   Summary

This chapter has characterised RSF and nHA/RSF inks through their surface tensions, dynamic viscosities and Z numbers. Surface tensions of the RSF inks were quite stable apart from a slight drop between the range of 50 - 70 mg.mL^{-1}. The low range concentrations had an average surface tension of 53.5 mN.m^{-1} and the high range concentrations had an average surface tension of 48.1 mN.m^{-1}. Differences in the surface tension were attributed to the change in shape of the RSF molecule at the liquid-air interface of the droplet, which at high concentrations protruded out of the droplet surface.

Surface tensions of the nHA/RSF inks was seen to vary considerably. Substantial changes in surface tension were induced by the incorporation of nHA within the RSF solution. There exists lots of conflicting research involving the effect of nanoparticle inclusions on the rheology of a fluid. This relationship is not well understood and requires further work outside the scope of this thesis would to establish the interaction of the nHA particles within the RSF solution.

Apparent viscosities of the RSF inks increased linearly with concentration above a shear rate of 100 s^{-1}. At low shear rates the RSF inks were unstable with relatively high viscosities. As the shear rate increased, the RSF inks experienced shear thinning before becoming shear independent around a shear rate of 100 s^{-1}. Viscosities of the nHA/RSF inks took longer to reach shear independence, although achieved it around a shear rate of 1000 s^{-1}, a shear rate similar to that experienced during printing.

Calculated Z numbers of the RSF inks predicted a higher stability of the most concentrated solutions during printing. As printing of the RSF inks was to be conducted using an 80 μm printhead, inks with a Z number of 10 or less for an aperture size of 80 μm were selected to be tested for printing. Inks with concentrations between 80 – 120 mg.mL^{-1} were jetted and assessed. Although all inks had a stable droplet formation, inks with a concentration of 110 and 120 mg.mL^{-1} were susceptible to crusting over, preventing the ejection of droplets. As RSF ink 100 mg.mL^{-1} was the most concentrated ink with a stable droplet formation, it was chosen as the ideal ink to proceed with.

The Z numbers for the nHA/RSF inks for an aperture size of 80 μm were all well above the Z number predicted stable range. However, all inks were tested for printability by jetting through an 80 μm printhead. All of the inks produced stable droplets without the formation of satellites. Therefore, all nHA/RSF inks were considered suitable for further printing.

The stability of methanol was also evaluated through its Z number. All Z number values were higher than that of the most stable Z number range. When jetted through an 80 μm printhead, droplet formation was seen to be unstable. When printed through a 60 μm printhead which had a lower Z number, droplet formation became stable. Therefore, for the printing of methanol, a 60 μm printhead will be used.

Chapter 5: Inkjet Printing of Regenerated Silk Fibroin Films

5.1 Introduction

This chapter explores the structural changes induced by printing increasing volumes of methanol into RSF films. RSF films will then be degraded in either an enzymatic solution or in a phosphate buffered saline to determine if the structural changes brought on by various volumes of methanol are able to influence degradation rates.

5.2 Results and Discussion

5.2.1 Sericin Removal

Following the procedure outlined in Chapter 3: Materials and Methods, the initial step for RSF preparation is the removal of sericin (a protein glue used to hold the silk fibres together in the form of a cocoon) from the Bombyx Mori silkworm cocoons via a degumming procedure. After degumming, the dried weight of the Bombyx Mori silk cocoons dropped from 5 g to around 3.6 g. This would indicate that roughly 25 – 30% of the cocoon structure is formed of sericin. To ensure the complete removal of sericin from the silk fibres, Fourier transform infrared spectroscopy with attenuated total reflectance (FTIR-ATR) was performed on Bombyx Mori silk worm cocoons before and after the degumming procedure. Sericin has bands positioned at 1650, 1530, 1400 and 1070 cm^{-1}. However, the band positioned at 1400 cm^{-1} is sericin's signature peak [155], as it is positioned away from any silk fibroin bands, making it easy to distinguish. The band at 1400 cm^{-1} is associated with CH and OH bending of the amino acid serine side chain. Serine is present in large quantities in sericin, contributing to around 30 % of the sericin molecule [156] and only 12.1 % of fibroin [81].

Figure 5.1 is the FTIR-ATR spectra for Bombyx Mori silk worm cocoons before and after the degumming procedure. Before degumming there is a large band positioned at 1400 cm^{-1} which disappears in the IR spectra of the silk fibres after degumming. The other bands associated with sericin are difficult to identify as they are positioned within similar areas of the amide I, II and III bands to that of the silk spectra. After

degumming the silk appears to have lost some of its crystallinity with a broadening of the amide I and II bands. The broadening of the bands means that it is only possible to detect the presence of sericin from its signature peak at 1400 cm^{-1}.
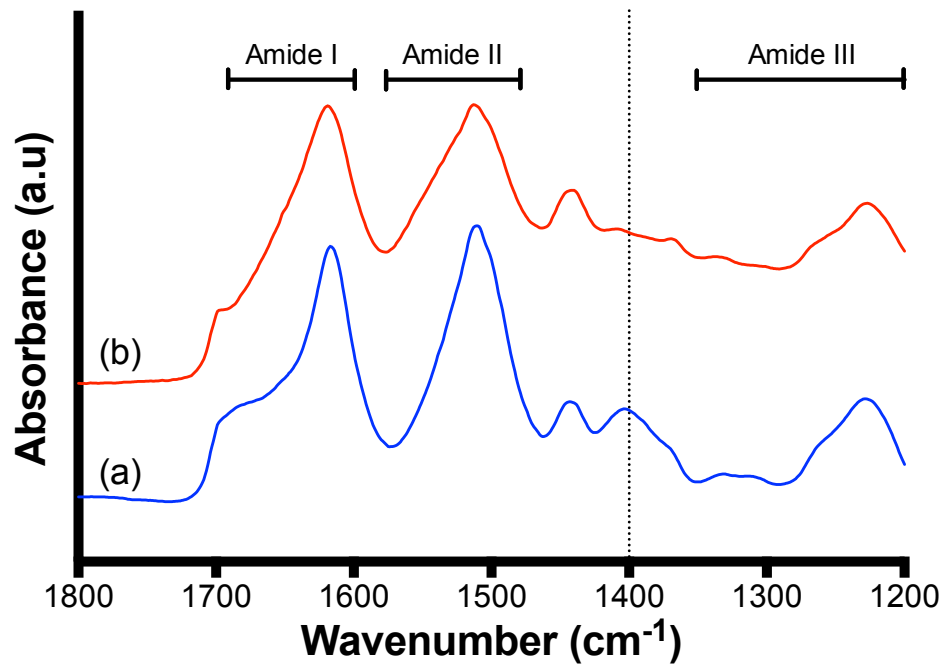
Figure 5.1: FTIR-ATR of amide I, II and III regions for (a) Bombyx Mori silk worm cocoon and (b) silk fibres after the degumming process. The vertical dotted line at 1400 cm^{-1} is positioned at the signature sericin peak

5.2.2 Crystallinity Characterisation

5.2.2.1 RSF Film FTIR-ATR

To determine if the transition of unordered silk fibroin (silk I) to silk II could be controlled in a graduated manner through reactive inkjet printing, RSF films were printed with different volumes of RSF to methanol, the proportions of which are shown in Table 6. Figure 5.2 is the FTIR-ATR spectra for these films, along with the spectra of cast films without any methanol treatment, cast films which have been submerged in methanol for 4 days, and unprocessed B. Mori silkworm cocoons. The cast films demonstrate the extremes of crystallinities achievable through methanol treatments.

RSF Film	Ratio RSF: Methanol (100 mg: mL)
100 %	1:0
75 %	3:1
66 %	2:1
50 %	1:1
33 %	1:2
25 %	1:3

Figure 5.2: FTIR-ATR spectra of silk films printed with different volumes of RSF ink to methanol, whereby RSF film 25 % consists of 1 part RSF for every 3 parts methanol. Also shown are the spectra for cast RSF (NP), cast with 4-day methanol treatment (NP+M) and for native Bombyx Mori silkworm cocoon (SC).

Figure 5.2 shows several characteristic infrared absorption bands produced by the polypeptide chain of silk called the amide A, B, I, II and III. The amide A and B regions range between $2800 - 3600$ cm^{-1} and are formed from NH stretching vibrations [157], [158]. Regions which represent NH stretching give an indication of intra-sheet and

inter-chain bonding between NH and C=O groups. Band intensities are sensitive to the formation and strength of hydrogen bonds made during inter-sheet bonding [158]. Each RSF film has a peak at 3275 cm^{-1} which becomes narrower and more prominent with increasing methanol treatment. Band intensities at 3275 cm^{-1} for each of the RSF films was compared to that of the silk cocoon, and are shown in Table 7.

Table 7: Change in absorbance values for the Amide A band at 3275 cm^{-1} in comparison to the unprocessed silk cocoon as a standard, with increasing volumes of methanol. Where 100 % equals RSF without any methanol addition and 75 % being three-parts RSF with one-part methanol. It can be seen that the ratio increases with increasing methanol addition. Results shown from singular spectrum (n=1)

RSF Film	$A_{3275}/A_{Standard}$
NP	0.72
100 %	0.70
75 %	0.75
66 %	0.70
50 %	0.77
33 %	0.79
25 %	0.99
NP+M	1.08

The ratios show a general trend where increasing volumes of methanol produce larger band intensities at 3275 cm^{-1}, hence denser packing of β-sheet stacks. However, the RSF film 75 % (three parts RSF to one-part methanol) was the only spectrum to break this trend, having a higher ratio than that of RSF film 66 %. Film NP+M had the highest ratio of 1.08, which shows a higher density packing of β-sheet stacks than that of the unprocessed cocoon. Increased intensities and a narrowing of the amide A band due to increased volumes of printed methanol is indicative of the RSF films becoming more crystalline and ordered.

All of the RSF films have a shoulder on the 3275 cm^{-1} band which is of consistent shape and size, occurring at 3500 cm^{-1}. The shoulder is not present in the spectrum

of the unprocessed silk cocoons and is suggestive of water absorption [159]. It is possible that some water remains trapped in the RSF structure after setting.

Some of the films have an additional band positioned around 2400 cm^{-1} that is caused by an asymmetric stretch of CO_2 [160]. CO_2 could have been absorbed during the printing process or be an artefact arising from the atmosphere of the laboratory when recording the FTIR-ATR spectra.

Figure 5.3 is an enlargement of the spectra shown in Figure 5.2 focusing on the amide I (1600 – 1700 cm^{-1}), amide II (1480 – 1570 cm^{-1}) and amide III (1200 – 1350 cm^{-1}) regions. Peaks between 1340 and 1456 cm^{-1} are attributed to vibrational modes of the amino acid residues [161]. The largest of the residual vibrations, at 1445 cm^{-1}, is produced via CH_2 scissoring mode vibrations. The amide I band arises from carbonyl C=O stretching vibrations with small contributions from out of phase CN stretching and CNH in plane bending [162]. Due to the significant contribution of polypeptide backbone vibrations, the amide I region is most commonly used to determine protein secondary structure, however the amide II and III regions have also been used [163]. The amide II band is formed from CN stretching and NH out of phase in plane bending vibrations of the polypeptide backbone, and the amide III band, between 1200 – 1400 cm^{-1}, is produced from an in phase combination of NH bending, CN stretching and contributing side chains [163]. Bands centred around 1620 cm^{-1} (amide I), 1515 cm^{-1} (amide II) and 1260 cm^{-1} (amide III) are indicative of silk II (represented as a dotted vertical line in Figure 5.3), whilst bands centred around 1640 cm^{-1} (amide I), 1535 cm^{-1} (amide II) and 1235 cm^{-1} (amide III) are indicative of silk I (represented as a solid black vertical line in Figure 5.3).
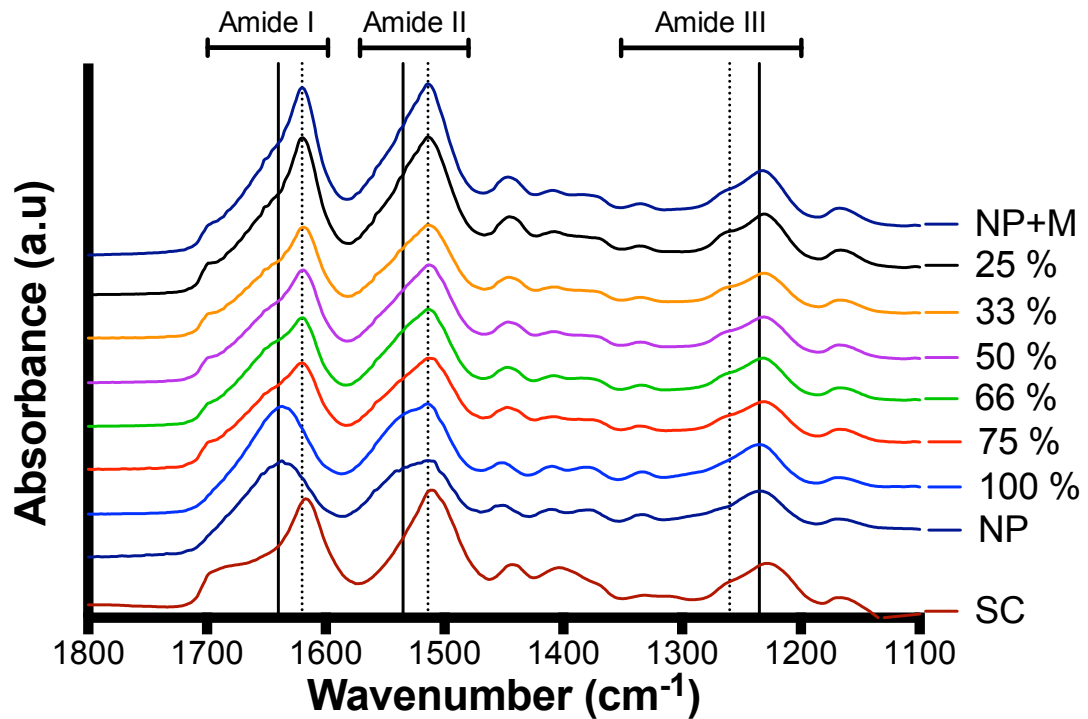
Figure 5.3: FTIR-ATR spectra of the amide I, II and III regions for silk films printed with different concentrations of RSF ink (100 mg.mL^{-1}) and methanol (1 mL), whereby 25 % represents one part RSF for every 3 parts methanol. Also shown are the spectra for cast (NP), cast with methanol treatment (NP+M) and for a Bombyx Mori silkworm cocoon. Solid vertical lines mark the position of silk I bands and dotted vertical lines mark the position of silk II bands.

A comparison of RSF films NP and 100 % show that β-sheet formation has not been induced by printing. Each spectrum is similar in shape and have amide I band peaks centred around the silk I band position. The amide I region has no peak at 1620 cm^{-1} (silk II band position) suggesting that each film has a highly unordered structure. As RSF film NP hadn't had any methanol treatment to induce β-sheet formation, it can be assumed that the film is in its least ordered state. Both spectra have an amide II band which covers both silk I and silk II peaks positions, although the silk II peak is slightly more prominent. Due to the high shear rates produced during printing, there was the possibility that printing might induce β-sheet formation. However, after comparing the spectrum of the printed and cast films, it is shown that the shear induced by printing through an 80 μm nozzle at 300 Hz is not enough to induce a structural transformation. The slight prominence of the silk II peak within the amide II band appears to be inherent, and not caused by the printing process. Therefore, any changes in band positions and intensities can be attributed to the methanol treatment and not the process of printing alone.

Between RSF films 100 % and 75 % there occurs a shift in peak position within the amide I band. RSF films without any methanol treatment have an amide I band peak positioned around 1640 cm^{-1} which moves to 1620 cm^{-1} for RSF film 75 %, showing that the lowest concentration of printed methanol induces a primarily silk II RSF structure. With increasing volumes of printed methanol, the intensity of the silk II band increases whilst the intensity of the silk I band decreases, signifying increasing concentrations of silk II.

A comparison of the silk I and silk II bands within the amide I region is shown in Table 8. Intensities of silk I bands are the most dominant within the amide I region for RSF films; NP and 100 %, which have had no methanol treatment. As soon at the RSF films are exposed to methanol the band around 1620 cm^{-1} consistently has the highest intensity. The presence of a band at 1620 cm^{-1} is instantaneous with the addition of methanol, as can be seen by comparing the bands of RSF films NP and 100 % to that of RSF film 75 %. Increasing the volume of methanol caused an increase of intensity around 1620 cm^{-1} with a drop in intensity observed for the band at 1640 cm^{-1}. The ratio of silk II to silk I continues to rise with every increase of methanol. RSF films 75 % and 66 % which were subjected to the lowest volumes of methanol had similar ratios of silk II to silk I, suggesting that although the addition of methanol has an immediate effect in transforming silk I to silk II, larger volumes are required to transform a greater proportion of the structure. The ratio of silk I to silk II for that of native Bombyx Mori cocoons had the highest ratio of 1.85.

Table 8: Ratio of silk II to silk I band intensities within the amide I and amide II regions. It can be seen that the ratio increases with increasing methanol addition. Results shown from singular spectrum (n=1)

RSF Film	A_{1620}/A_{1640} Silk II/ Silk I	A_{1515}/A_{1535} Silk II/ Silk I
NP	0.83	1.08
100 %	0.79	1.11
75 %	1.24	1.22
66 %	1.25	1.22
50 %	1.36	1.27
33 %	1.41	1.26
25 %	1.53	1.31
NP+M	1.58	1.34
SC	1.85	1.76

The amide II band is not as sensitive as the amide I band for detecting changes to the secondary structure, however the band at 1515 cm^{-1} is produced via secondary NH bending, giving an indication of β-sheet stacking densities. All of the RSF films have a peak positioned at 1515 cm^{-1} which shows that even the least crystalline films have some β-sheet structure. RSF films NP and 100 % have a broad peak spread over band positions for both silk I and silk II. As the volume of methanol increases, the silk I peak at 1535 cm^{-1} disappears and the silk II peak at 1515 cm^{-1} becomes more intense. An increased intensity of the band at 1515 cm^{-1} is matched with intensity increases at 3275 cm^{-1} demonstrating an increase of NH group bonding.

The ratio of silk II to silk I band intensities within the amide II region are compared in Table 8, as mentioned earlier. The ratios give a comparison of crystal density of the RSF films. A steady increase in the ratio of band intensities consistently increased with increasing volumes of methanol. Similar to the amide I region, there was no difference in the ratio of silk II to silk I band intensities between RSF films 75 % and 66 %. Similar ratios of RSF films 75 % and 66 % help to reinforce the notion that although a small volume of methanol will induce silk II formation, in order to induce a larger proportion of the silk I to transform, larger volumes of methanol are

required. Also similar to the amide I region, the silk cocoon had a significantly higher ratio of silk II to silk I.

The peak at 1515 cm^{-1} has also been attributed to the ring CC stretch and CH bend of Tyrosine [164]. Tyrosine forms part of a Gly-Tyr ~ Gly-Tyr sequence which appears within crystalline segments of the amino acid sequence. According to Sung-Won Ha *et al.*, these sequences act as turns in the β-sheet structure [86]. The tyrosine residues are observed to affect the intermolecular chain arrangements which have an effect on the long range packing in the semi-crystalline regions of silk II [165]. It has also been shown that the tyrosine residues prefer a random coil conformation in silk I and a β-sheet conformation in silk II [166]. Therefore, as the tyrosine residues are linked to turns in the β-sheet structure and consequently the long range packing of the semi-crystalline regions, changes in the tyrosine band at 1515 cm^{-1} can be used to monitor changes in the conformational freedom of the polypeptide molecule [167]. As the intensity of the peak at 1515 cm^{-1} progressively increases as the volume of printed methanol becomes larger, this suggests a lower conformational freedom of the β-strands, and therefore a denser packing of the β-sheet crystals.

The amide III region was used as one of the earliest methods of calculating silk crystallinity before the invention of more advanced FTIR machines. Crystallinity is calculated using the following equation: [87], [168]

$$Degree\ of\ Crystallinity\ (\%) = \frac{A_{1256}}{(A_{1256} + A_{1235})} \times 100$$

Equation 5

Where A_{1256} is the absorbance at 1256 cm^{-1} (a silk II band), and A_{1235} is the absorbance at 1235 cm^{-1} (a silk I band). The result of the calculations are shown in Table 9. According to the amide III region, the degree of crystallinity for all RSF films is around 44 %. For the native Bombyx Mori cocoon, a crystallinity value of 35 % was calculated. This value is contradictory to what has been observed for the amide I and II regions which consistently showed that the unprocessed silk cocoons were the most

crystalline. However, this value could be caused by the presence of sericin in the unprocessed silk cocoons. Sericin is a non-crystalline protein which presents a peak at an α-helix band within the amide III region, positioned at 1230 cm^{-1} [169]. As the amide III region appears to have little sensitivity to the structural content of the RSF films, further analysis will only be performed on the amide I and II regions of the spectra.

Table 9: Degree of crystallinity according to the amide III region for RSF films with different methanol treatments. It can be seen that there are no changes to crystallinity according to the amide III region with increasing methanol addition. Results shown from singular spectrum (n=1)

RSF Film	Crystallinity degree (%)
NP	45
100 %	45
75 %	44
66 %	44
50 %	44
33 %	44
25 %	44
NP+M	44
SC	35

5.2.2.2 RSF Film FSD

To better quantify the changes observed in the FTIR-ATR spectra, Fourier self-deconvolution (FSD) was performed on the amide I region of the RSF films. FSD is used to calculate individual bands which contribute to form the overall amide I band, and hence calculate the proportion of secondary structure components; β-sheet, α-helix and random coils, β-turns and side chains. An example of FSD performed on RSF film 25 % is shown in Figure 5.4.The peak absorption bands, as determined by Xiao Hu *et al.*, were assigned as follows: 1616 – 1637 cm^{-1} and 1697 – 1703 cm^{-1} for β-sheet, 1656 – 1662 cm^{-1} for α-helix, 1638 – 1655 cm^{-1} for random coils, 1663-1696 cm^{-1} for β-turns and 1600 – 1615 cm^{-1} for side chains [94]. Due to the convolution of peaks associated with α-helix and random coils they are combined into a single

contributing structure. However, it should be noted that there is a higher proportion of random coils to α-helix calculated for all of the RSF films. This high proportion can be linked to the method of synthesizing the RSF solution. Using a concentrated inorganic salt solution to dissolve the silk fibres has been reported to produce a random coil structure [87].
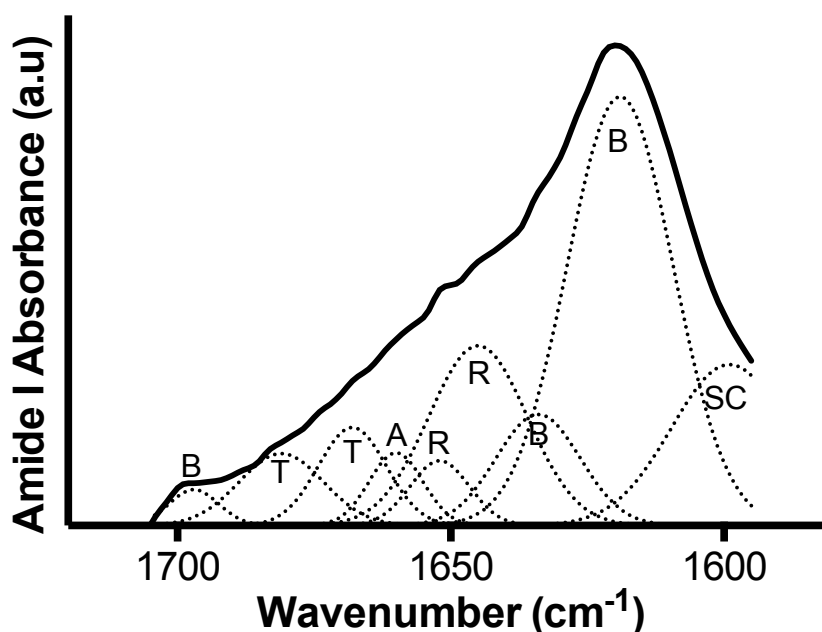
Figure 5.4: FSD of RSF film 25 % amide I region. Peaks are assigned to (B) β-sheet, (A) α-helix, (R) random coils, (T) β-turns and (SC) side chains.

The FSD results are shown in Figure 5.5. The FSD data confirms that crystallisation is not induced during printing. RSF films NP and 100 % had similar amounts of each secondary structure, which was predominantly non-crystalline. The addition of a small volume of methanol was enough to have a substantial effect on RSF crystallinity. The amount of β-sheet increases from an average of ~20 % to ~44 % between RSF films 100 % and 75 %. Likewise, there was a similar drop in the percentage of α-helix and random coil contributing to the structure, dropping from ~46 % to ~27 %.
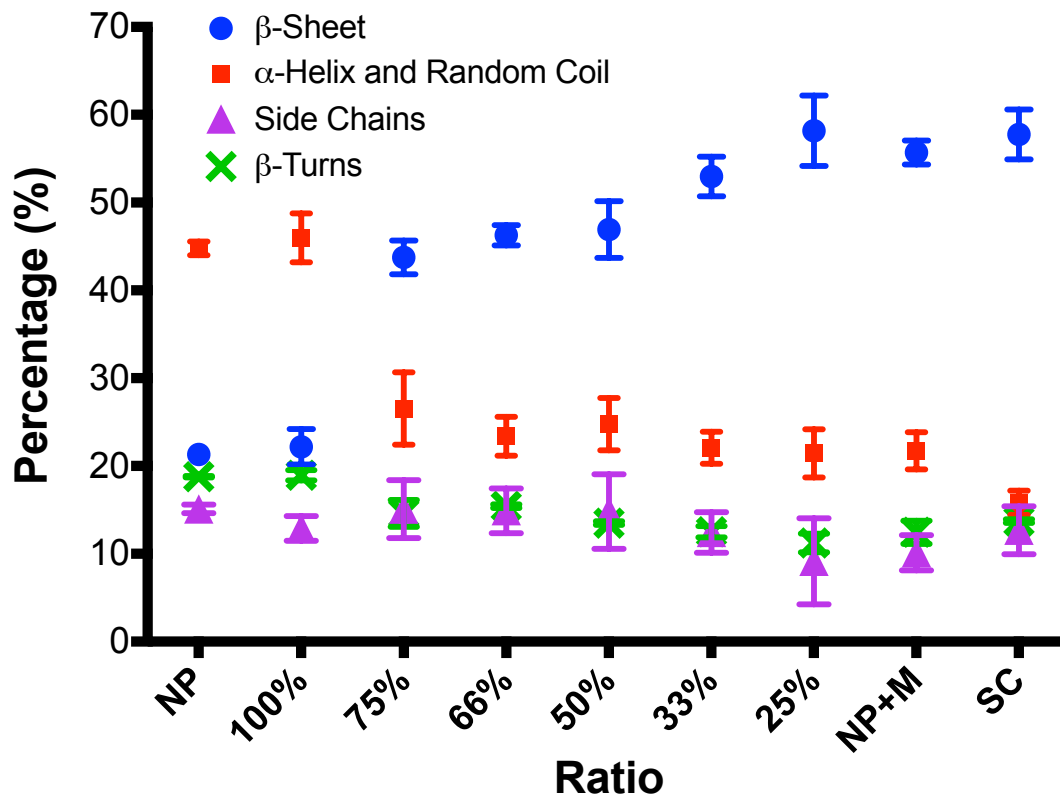
Figure 5.5: Percentage contribution of protein structure of the different silk films. RSF films are described by their RSF ink concentration, where RSF film 25 % is one part RSF ink to 3 parts methanol. (n=4)

Between RSF films of 75 %, 66 % and 50 % there are no significant differences between secondary structure contributions. However, after RSF film 50 %, each incremental increase in the volume of methanol printed induced a significant increase in the percentage of β-sheet for each sequential increment. β-sheet crystallinity increased by 6% between RSF films 50 % and 33 % (p<0.001), and 5% between RSF films 33 % and 25 % (p<0.01). Significant differences were not observed for α-helix, random coil and β-turns between RSF films 50 %, 33 % and 75 %.

There was no significant difference of β-sheet content between RSF films 25 %, NP+M and that of the unprocessed silk cocoon (SC) which had average crystallinities of ~58 %, ~56 % and ~58 % respectively. NP+M had the same crystallinity as that observed previously by Xiao Hu *et al.* confirming maximum β-sheet crystallinity via a methanol treatment [134].

The FSD data in Figure 5.5 show that small volumes of methanol are able to affect the RSF structure significantly by inducing a crystalline structure. The crystallinity of the RSF structure is gradually increased with increasing volumes of methanol until maximum β-sheet content has been achieved, similar to that of unprocessed Bombyx Mori silk cocoons. These observations are obtained with an average volume of 12 μL of RSF printed per square centimetre, or 1.2 mg of silk fibroin per square centimetre, for each layer of RSF. Similar ratios with different volumes of RSF solution printed per layer could change the influence of methanol on the RSF structure.

5.2.3 RSF Film Topography

5.2.3.1 Light Microscopy

Light microscopy photos at a high magnification were taken for each RSF film and are shown in Figure 5.6. A composite photo has been produced to show the entirety of each film which is accompanied by a higher magnification photo of the film surface to highlight the film topography.

Each film appears to be highly textured. There are clear troughs and peaks visible in RSF films 75 % and 66 % (Figure 5.6B and C) which have been produced by the deposition of droplets along the direction of printing. Lines of droplets are less visible in RSF films 50 %, 33 % and 25 % (Figure 5.6D, E and F), although peaks and troughs are still seen as light and darks patches. The peaks and troughs are caused by the spacing of the silk droplets. The initial spacing of the droplets was chosen to prevent flooding of the glass coverslip substrates, whilst still allowing for all of the droplets to touch and therefore create a film. As the film thickness built up, the RSF droplets were no longer interacting with the glass coverslip and were instead interacting with dried RSF film. As lines of droplets are visible on the surface of the films, it would indicate the RSF films were slightly more hydrophobic than that of the glass coverslips, causing the droplets to spread over a smaller area. The only film where no droplets were visible was on RSF film 100 % (Figure 5.6A) which had had no methanol treatment. No visible droplets on the surface of RSF film 100 % could be an indication that the methanol treatment was causing the films to become more

hydrophobic, which makes sense when one considers that the addition of methanol results in the production of insoluble silk II.
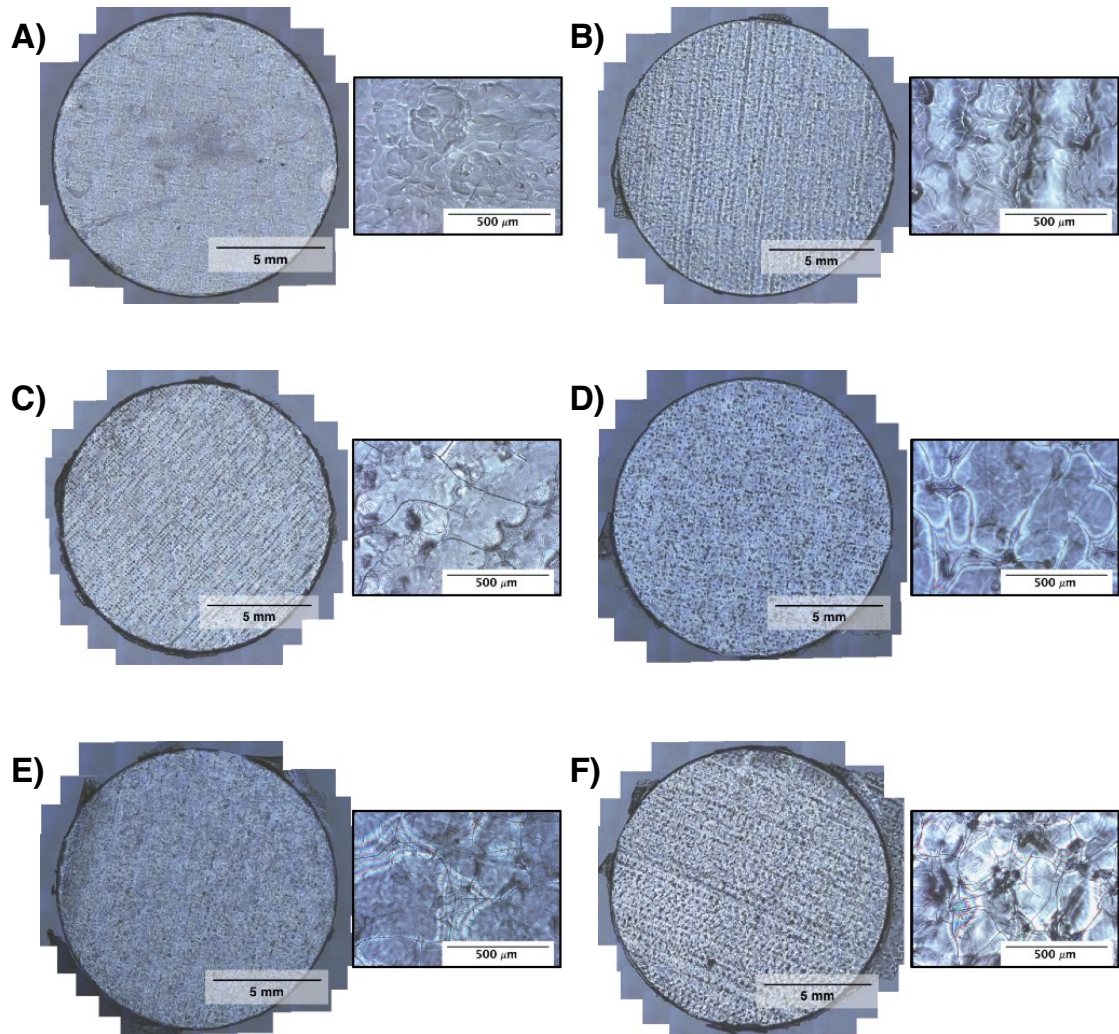
Figure 5.6: Light microscopy photos of the RSF films: A) 100 %, B) 75 %, C) 66 %, D) 50 %, E) 33 % and F) 25 %. Next to each film is a photo of the film at a higher magnification.

When observing the higher magnification photos, cracks begin to appear on the films which increase in size and density with increasing methanol treatment. Significant cracks begin to form on RSF film 66 % which become larger and more frequent up until RSF film 25 %. No cracking is visible on RSF film 100 %. The cracking of the films could have been the result of rapid dehydration of the RSF caused by methanol. Larger volumes of methanol would have had a greater effect on the films and therefore caused greater crack propagation.

Roughness of the surface topography was measured using interferometry and was calculated from an area ~0.28 mm^2. Roughness values for the RSF films are shown in Figure 5.7. The four RSF films with the lowest crystallinity values had no significant differences between their roughness values (RSF films 100 %, 75 %, 66 % and 50 %), despite a higher average roughness for RSF film 50 % which was around 0.6 μm higher than that of RSF film 100 %. Generally, as the crystallinity of the films increased, the variation in surface roughness measured at different points on the film became larger. The only significant difference measured between consecutive increases in crystallinity were between RSF films 50 % and 33 % with a significance of p<0.05. RSF films 33 % and 25 % had significantly higher roughness values than RSF films 100 %, 75 % and 66 % by a significance of p<0.01 or greater.
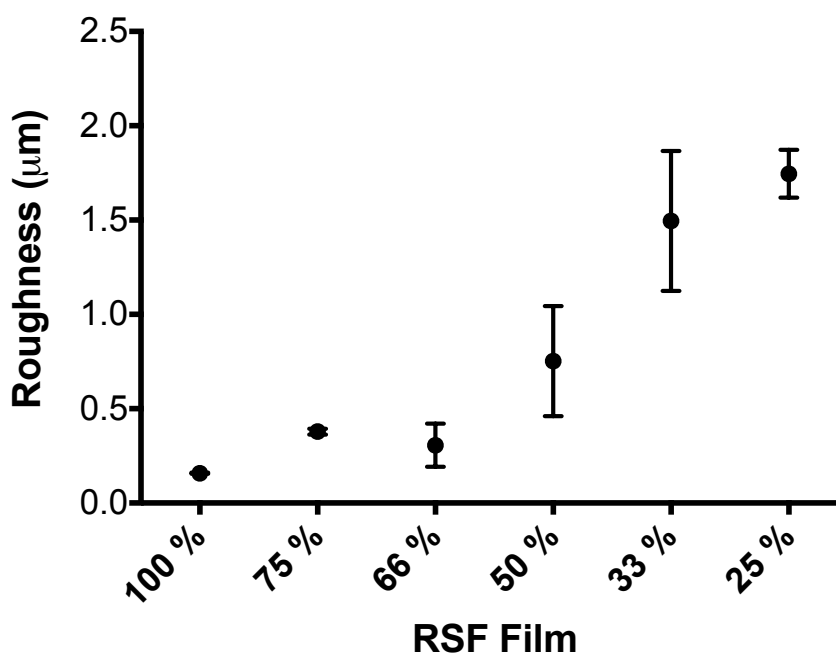
Figure 5.7: Surface roughness of the RSF samples measured using interferometry. Standard deviation over 3 measurements is shown

Overall, films which had had larger volumes of methanol printed between layers of RSF had the roughest surfaces. Increasing the volume of methanol caused larger, deeper and more frequent cracking to occur and could be observed visually in Figure 5.6, which caused the roughness values of the RSF films to increase. The cracking of

the films was most likely caused by the rapid dehydration of the RSF and was proportional to the volume of methanol printed.

5.2.3.3 Contact Angle Measurements

Crystallinity of the RSF films should influence water droplet contact angle measurements [86]. When the RSF is in an amorphous state, polar groups along the molecule have a random orientation, which produces a high surface energy and thus a more hydrophilic surface. During crystallisation, the polar groups are used for hydrogen bonding to produce a β-sheet structure [86]. As the polar groups are positioned within the β-sheet layers the surface energy is reduced, increasing hydrophobicity. Therefore, it would be expected that increasing amounts of β-sheet structure within the RSF films would contribute to more hydrophobic films. A droplet of water is, therefore, expected to exhibit higher contact angles as the β-sheet content increases.

Contact angles were measured for water droplets on each of the RSF films as well as for controls of PLLA and glass coverslips. Contact angles were measured for five different droplets on three different samples of each film, the results of which are shown in Figure 5.8. Measurements of contact angles on roughened surfaces can be a problem due to pinning of the contact line, however, in this study all of the droplets formed circular contact lines on each film tested. Contact angles were unable to be recorded for RSF films which had not been exposed to a methanol treatment as they were still water soluble. Contact angles for RSF film NP+M were also not measured as during the methanol treatment the films became warped and no longer flat, making it difficult to collect a correct measurement.
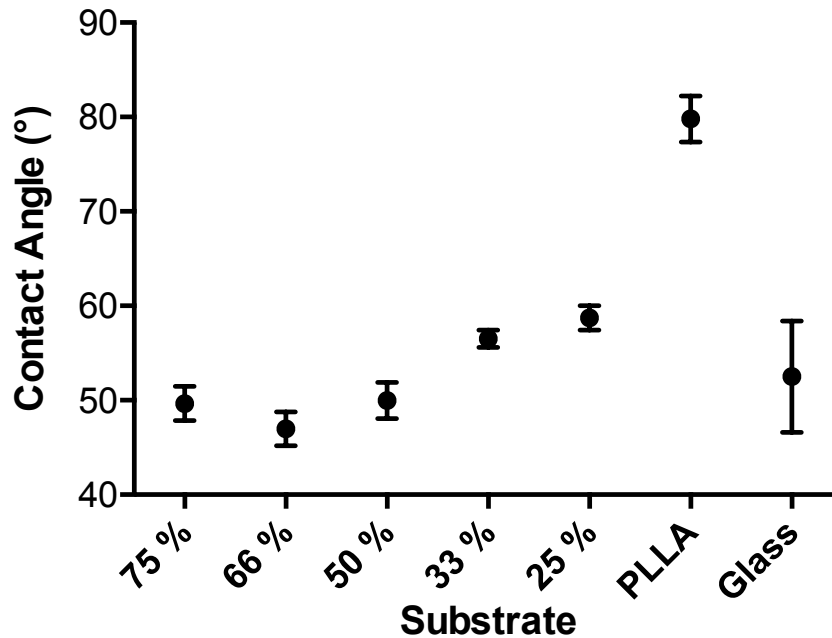
Figure 5.8: Contact angle measurements for the RSF films and that of controls PLLA and glass. Standard deviation over 5 measurements is shown.

The average contact angle for each of the RSF films became larger with increasing crystallinities after RSF film 66 %. Average contact angles were 49.7°, 47°, 50°, 56.6°and 58.7° for RSF films 75 %, 66 %, 50 %, 33 % and 25 % respectively. The three RSF films with the lowest crystallinity (RSF films 75 %, 66 % and 50 %) had no significant differences between them. RSF films with the highest crystallinity (RSF films 33 % and 25 %) were both significantly higher than the lower crystallinity films ($p \leq 0.01$), but were not significantly different between each other. The only significant difference between individual incremental increases of methanol printed, was between RSF films 50 % and 33 % ($p \leq 0.01$). Overall there is a significant difference between the lowest contact angle, measured for RSF film 66 %, and the largest, for RSF film 25 % ($p \leq 0.0001$).

RSF film 66 % was the only RSF film to be significantly different to that of the glass coverslip ($p \leq 0.05$), which had an average contact angle of 53°. All of the RSF films had significantly lower contact angles than that of the PLLA with a contact angle of 80° ($p \leq 0.0001$).

5.2.4 Degradation Studies

5.2.4.1 Mass Loss

Degradation of the RSF films were studied and compared by immersing them in either an enzymatic solution of protease XIV or in a phosphate buffered saline (PBS) over an 8-day period (Figure 5.9 and Figure 5.10). Studying the degradation of the films helps to predict how the films will perform when in vivo. The enzymatic solution should facilitate the breakdown of the fibroin structure and therefore produce faster degradation rates. PBS solutions are commonly used as a control comparison when degrading RSF films with a protease. Therefore, to provide a more direct comparison to similar studies, degradation studies were also performed in PBS solution. Degradation within the PBS solutions show what proportion of the RSF films are being actively broken down by enzymatic activity and how much RSF is lost simply due to dissolution of the water-soluble structures.

5.2.4.1.1 Enzymatic Degradation Mass Loss

Films degraded in an enzymatic solution (Figure 5.9) experience the largest mass loss over the initial 24-hour period. Initial mass loss was related to RSF film crystallinity. RSF films which were exposed to the smallest volumes of methanol (therefore less crystalline) experienced the largest mass loss. The RSF film which had had no methanol treatment (RSF film 100 %) experienced a similar mass loss to that of the RSF film printed with the smallest volume of methanol (RSF film 75 %), both dropping to around 30 % of their initial mass. RSF films 66 % and 50 %, which have been shown to have a similar level of crystallinity (Figure 5.5), experienced similar mass losses, dropping to 55 % and 58 % of their initial mass. RSF film 33 % which had the second highest crystallinity, experienced a mass loss of 21 %. RSF film 25 % which had the highest crystallinity lost the least amount of mass, losing 12 % of its initial mass. Using Tukey's analysis, RSF films 100 % and 75 % had similar mass losses, as did RSF films 66 % and 50 %, and RSF films 33 % and 25 %.
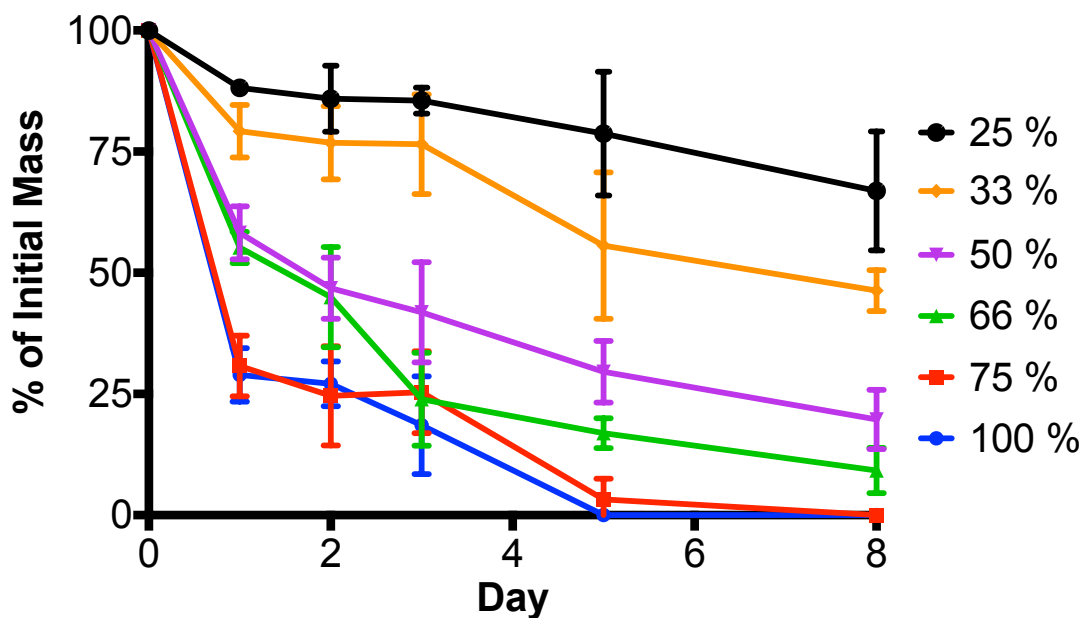
Figure 5.9: Degradation mass loss for RSF films printed with different volumes of RSF ink (100 mg.mL^{-1}) and methanol (1 mL), where RSF film 25 % is one part RSF to 3 parts methanol, degraded in a protease XIV solution. Standard deviation over 3 measurements is shown.

After 1 day within an enzymatic solution, the degradation rate of the RSF films had rapidly slowed. RSF film 100 % had the smallest mass loss between days 1 and 2, losing an average or 1 % of its initial mass. RSF films 66 % and 50 % had the largest mass loss, losing 10 % and 11 % respectively of their initial mass. None of the RSF films experienced a statistically significant difference in mass between days 1 and 2. Similarly as observed over the first 24 hours, by day 2, RSF films 100 % and 75 % had similar mass losses, as did RSF films 66 % and 50 %, and RSF films 33 % and 25 %.

By the third day, RSF film 66 % was the only film to have a significant reduction in its mass (p≤0.01) between days 2 and 3, losing 21 % of its initial mass. This brought RSF film 66 % closer to RSF films 100 % and 75 % with the proportion of their mass lost. Therefore, after 3 days degraded in a protease XIV solution, RSF films 100 %, 75 % and 66 % had accumulatively lost similar proportions of their initial mass. RSF films 33 % and 25 % remained with similar masses to that recorded on day 2, each losing less than 0.5 % of their initial mass between days 2 and 3.

After 5 days degraded in an enzymatic solution, RSF film 100 % had completely degraded. RSF film 75 % had almost completely degraded with only 3 % of its initial mass remaining. Between days 3 and 5, RSF films 66 % and 50 % had lost 7 % and 12 % respectively of their initial masses. RSF film 33 % had experienced a significant reduction of mass, losing 21 % of its initial mass between days 3 and 5. Between days 3 and 5, RSF film 25 % had lost 7 % of its initial mass. Despite a substantial average mass loss for RSF film 33 %, it had a large variation in the amount of mass lost between each sample at this time point, therefore, RSF films 33 % and 25 % remained similar.

By day 8, RSF film 75 % had completely degraded within the enzymatic solution. Of the RSF films which remained on the eighth day, overall mass loss was related to RSF crystallinity. Films with the smallest to highest remaining masses were as follows, RSF films 66 % < 50 % < 33 % < 25 %, each losing around 90 %, 80 %, 55 % and 35 % respectively of their initial mass.

5.2.4.1.2 PBS Degradation Mass Loss

Degradation profiles of the RSF films degraded in PBS differed from those degraded in an enzymatic solution (Figure 5.10). Over the initial 24-hour period, RSF films 100 % and 75 % were the only films to experience a significant decrease in mass. RSF film 100 % lost almost 70 % of its initial mass, similar to the first 24 hours in the protease XIV solution. RSF film 75 % lost 20 % of its initial mass, which is considerably less than its enzymatic degradation mass loss. The remaining RSF films had no significant mass loss.
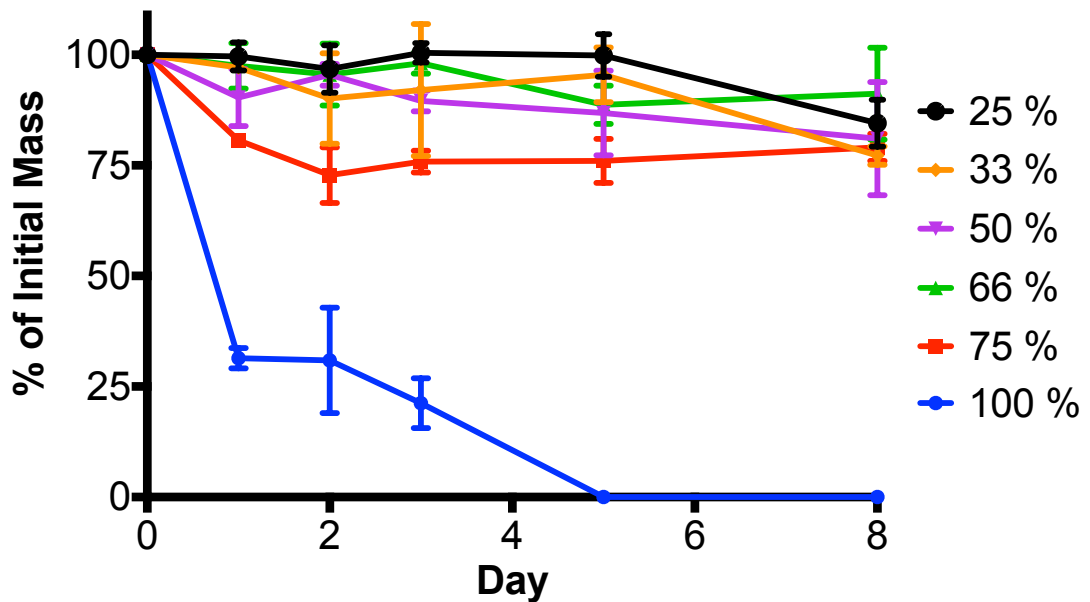
Figure 5.10: Degradation mass loss for RSF films printed with different volumes of RSF ink (100 mg.mL^{-1}) to methanol (1 mL), where RSF film 25 % is one part RSF to 3 parts methanol, degraded in a PBS solution. Standard deviation over 3 measurements is shown.

Between days 1 and 5 there were no significant changes in mass between the RSF films when degraded in PBS, apart from RSF film 100 %. RSF film 100 % had a similar degradation profile in PBS as it did in the enzymatic solution, plateauing out between days 1 and 2, before its average mass began to drop by day 3 and completely degrading by day 5. On day 8, the remaining RSF films had experienced similar mass losses to each other. Unlike RSF films degraded with protease XIV, the remaining mass was not related to film crystallinity. Films with the smallest to highest remaining masses were as follows, RSF film 33 % < 75 % < 50 % < 25 % < 66 %, each losing around 23 %, 21 %, 19 %, 15 % and 9 % respectively of their initial mass.

RSF film degradation rate was shown to be proportional to RSF crystallinity when degraded with protease XIV. After the first 24 hours, all RSF films experienced a significant mass loss, after which, the degradation rate slowed down. It is possible that within the first 24 hours all of silk I and the non-crystalline silk structures were degraded, leaving only a silk II, β-sheet crystal structure. Over the remaining days the degradation rate slowed down due to the difficulty of protease XIV in breaking down the β-sheet crystals.

5.2.4.1.3 Mass Loss Discussion

The initial 24-hour period should have yielded the largest mass loss for RSF films degraded in PBS due to the dissolution of water soluble, unordered silk I structures. However, it was only the films degraded with protease XIV which experienced a significant mass loss related to film crystallinity. RSF film 100 %, which had had no methanol treatment, was the only RSF film to have similar degradation profiles in both solutions.

A potential reason for the methanol treated RSF films having different degradation profiles could be due to the manner in which they are produced. During printing, each layer of RSF solution printed is very thin, and it is therefore necessary to print multiple layers in order to build up RSF film mass. A layer-by-layer approach to producing the films meant that layers of methanol were printed between sequential layers of RSF solution. Printing methanol between layers of RSF could have produced a film with a non-uniform structure, whereby layers of unordered silk I were encapsulated under layers of silk II. Films exposed to larger volumes of methanol had higher crystallinities which could represent thicker layers of silk II. Larger volumes of methanol would require longer to evaporate off of the substrate. The longer evaporation times would increase the RSF exposure to methanol, enabling it to penetrate further into the RSF film, converting unordered silk I into silk II. Therefore, films which have had a longer exposure to methanol would have thicker layers of silk II with denser crystal packing, encapsulating the unordered silk I beneath.

RSF films degraded in protease XIV solution could have had holes formed in the silk II layers due to enzymatic degradation. Holes in the silk II layers would expose the water-soluble unordered silk I which consequently dissolved/ degraded in the surrounding solution. Films which were degraded in PBS kept an outer silk II protective layer, as there were no enzymes to degrade the RSF. Subsequently, the unordered silk I could have remained within the films. It was only RSF film 100 %, printed without methanol, which had no outer silk II layer to protect it, and fully degraded. To test this theory further, FTIR-ATR is required to examine the RSF structure.

5.2.4.2 Degradation FTIR-ATR

This section begins with a commentary of the obtained results, before concluding with a discussion. Control over the crystallinity of the RSF films was proven via FTIR-ATR and FSD. RSF film crystallinity was shown to influence degradation rates when the films were submerged in an enzymatic solution, although this was not seen to affect mass loss when submerged in PBS. By performing FTIR-ATR on the RSF films at each degradation time point (Figures 29 – 34), silk I and silk II structural changes can be observed which may reveal patterns to the degradation profiles. Intensities of the silk I and silk II peaks were compared within the amide I region for RSF films degraded with protease XIV (in Table 10), and for RSF films degraded in PBS (in Table 12). Peak intensities are also compared within the amide II region for RSF films degraded in an enzyme (in Table 11), and for RSF films degraded in PBS (in Table 13). RSF films 100 % and 75 % degraded in protease, and RSF film 75 % degraded in PBS, have no ratios for days 3, 5 and 8 as there was not enough material to create an accurate FTIR measurement.

Table 10: Ratio of silk II to silk I bands (A_{1620} / A_{1640}) within the amide I region for films degraded in protease XIV, where RSF film 100 % equals an RSF film without any methanol addition and RSF film 75 % being three-parts RSF with one-part methanol.

RSF Film	A_{1620}/ A_{1640} (on day)					
	0	1	2	3	5	8
100 %	0.79	1.34	1.25			
75 %	1.24	1.30	1.26			
66 %	1.25	1.53	1.46	1.35	1.44	1.27
50 %	1.36	1.44	1.29	1.13	1.10	1.20
33 %	1.41	1.45	1.55	1.32	1.30	1.29
25 %	1.53	1.54	1.50	1.62	1.45	1.43

Table 11: Ratio of silk II to silk I bands (A_{1515} / A_{1535}) within the amide II region for films degraded in protease XIV, where RSF film 100 % equals an RSF film without any methanol addition and RSF film 75 % being three-parts RSF with one-part methanol.

RSF	A_{1515}/ A_{1535} (on day)					
Film	0	1	2	3	5	8
100 %	1.11	1.12	1.08			
75 %	1.22	1.11	1.13			
66 %	1.22	1.18	1.13	1.14	1.12	1.11
50 %	1.26	1.11	1.12	1.11	1.08	1.13
33 %	1.26	1.17	1.16	1.06	1.15	1.09
25 %	1.31	1.17	1.14	1.23	1.14	1.17

5.2.4.2.1 Protease Degradation of RSF Films 100 % and 75 %

The results of this section are of interest since they discuss the difference between an RSF film that has had no methanol treatment (RSF film 100 %), which can be thought of as the control, and RSF film 75 %, which has had the smallest volume of methanol added. As can be concluded from the earlier results, the addition of a small volume of methanol has a significant effect on silk II content.

RSF film 100 % begins with a predominantly silk I structure (Figure 5.11A). On day 0, within the amide I region, there is a peak centred at 1640 cm^{-1} (silk I). After 24 hours in the protease solution, a sharp peak has formed around 1620 cm^{-1} with a shoulder at 1640 cm^{-1}. The spectrum also develops a peak at 1697 cm^{-1} which is another indication of silk II structure and the formation of β-sheets. The intensity of both peaks has dropped by day 2, possibly due to a reduction to the amount of material available to perform FTIR-ATR on. Ratios of band intensities within the amide I region show a large increase of silk II after 1 day (Table 10). An increase in the ratio of around 70 % is calculated on the first day, rising from 0.79 to 1.34, which drops slightly by the second day to 1.25. On day 0 the amide II band has a rounded shaped, split between the silk I and silk II bands positions, with a slightly larger peak positioned at 1515 cm^{-1}. On day 1 the amide II band is of a similar shape, but on the second day

the protruding peak at 1515 cm^{-1} is no longer visible. The ratio of silk I to silk II within the amide II region remains steady, averaging around 1.10 (Table 11).

Figure 5.11: FTIR-ATR of of RSF films A) 100 % and B) 75 % degraded in a protease XIV solution. Brackets represent the degradation time point in days. Solid vertical lines mark the position of silk I bands and dotted vertical lines mark the position of silk II bands.

RSF film 75 % on day 0, had silk II peaks positioned around 1620 cm^{-1} and 1697 cm^{-1}, within the amide I region, (Figure 5.11B). The peak at 1620 cm^{-1} had a small shoulder at 1640 cm^{-1}. By day 1 the intensities of all peaks dropped slightly to produce a flatter spectrum and the shoulder at 1640 cm^{-1} became less pronounced. The spectrum of day 2 was similar to that of day 1. Ratios of the silk I and silk II bands within the amide I region showed a small increase of silk II between days 0 and 1, which then dropped back down again by day 2 (Table 10). Within the amide II region, the peak at 1515 cm^{-1} is the most prominent on day 0, and remains so for the remaining days, however it drops in intensity and becomes flatter by day 1. A drop of intensity for the peak at 1515 cm^{-1} is reflected in the ratio between silk I and silk II bands, which shows a drop of silk II between days 0 and 1 (Table 11).

5.2.4.2.2 Protease Degradation of RSF Film 66 % and 50 %

The results of this section will compare the mid-ranged methanol treated films. Earlier it was discussed that the RSF structure had only minor differences between films which had been exposed to the smallest volumes of methanol. RSF films 66 % and 50 % had similar degradation profiles, however, RSF film 50 % consistently had a higher average mass. Therefore, any differences between their structures will have caused different degradation rates and may become highlighted in their degradation FTIR-ATR spectra.

The amide I region for RSF film 66 % changed considerably over the first 24 hours when the film was degraded in an enzymatic solution (Figure 5.12A). Silk II peaks were present at both 1697 cm^{-1} and at 1620 cm^{-1} on day 0. A shoulder to the silk II peak at 1640 cm^{-1} indicated the presence of silk I. After 1 day, both of the silk II peaks grew in intensity, whilst the silk I peak at 1640 cm^{-1} significantly reduced in size. By day 2, the intensity of the silk II peak at 1620 cm^{-1} was at its largest, however the shoulder at 1640 cm^{-1} had returned. The peak at 1697 cm^{-1} remained in shape and size after day 1. By day 3 the peak at 1620 cm^{-1} had reduced in size to produce a flatter band, but by day 5 the intensity of the peak had increased in size again. On the final day, the amide I region had a similar shape to day 3.

Although there were significant fluctuations in the size of the 1620 cm^{-1} peak, the ratio between the silk I and silk II bands was more stable (Table 10). Day 0 and 8 had the least silk II content according to the ratio of silk I and II peak intensities within the amide I region. The first day had the highest ratio of silk II to silk I which progressively became smaller at each time point, except for day 5 which had a similar ratio as on day 2. The amide II band became more rounded over the course of the degradation test, which was reflected by a steady decline in the ratio of silk II to silk I bands within the amide II region, seen in Table 11.
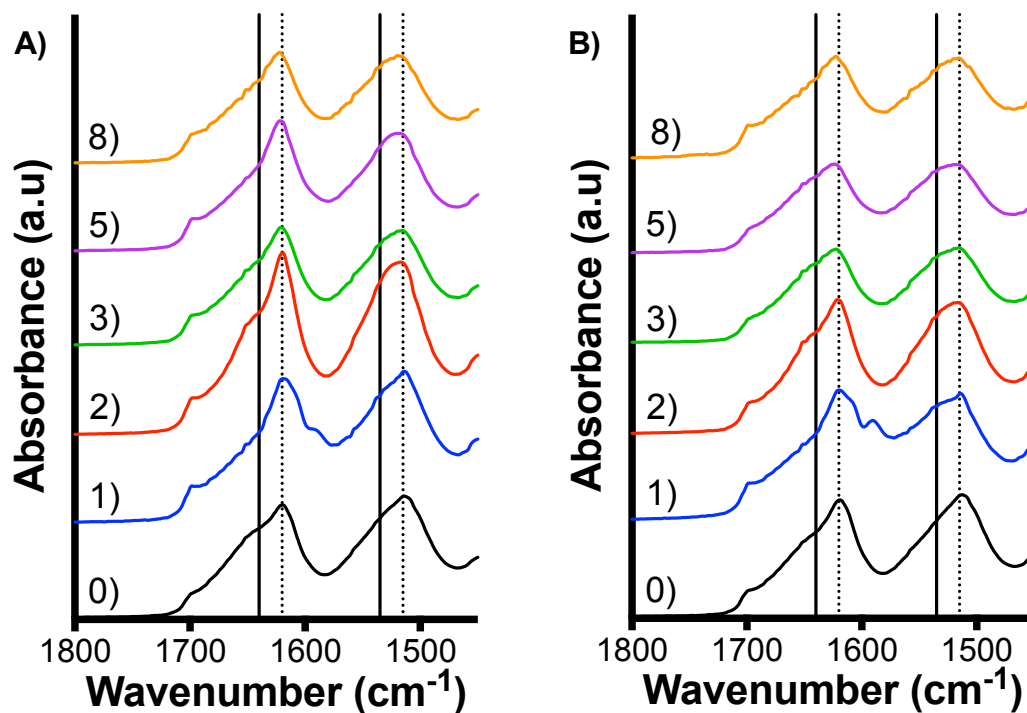
Figure 5.12: FTIR-ATR of of RSF films A) 66 % and B) 50 % degraded in a protease XIV solution. Brackets represent the degradation time point in days. Solid vertical lines mark the position of silk I bands and dotted vertical lines mark the position of silk II bands.

RSF film 50 % had a slightly larger silk II peak positioned at 1620 cm^{-1} in comparison to RSF film 66 %, but with similar sized peaks at 1640 cm^{-1} and at 1697 cm^{-1}. By day 1, the peak at 1620 cm^{-1} grew in intensity whilst the silk I peak at 1640 cm^{-1} dropped (Figure 5.12B). By day 2, the peak at 1620 cm^{-1} remained at a similar size, however the silk I band at 1640 cm^{-1} became more prominent. By day 3 the peak at 1620 cm^{-1} had reduced in intensity. Between days 3, 5 and 8, the amide I spectra kept a similar shape. Ratios of the silk II to silk I band intensities showed that there was an initial increase of silk II after 1 day (Table 10). After which, the amount of silk II slowly declined until day 8 when there was a slight increase. As observed with RSF film 66 %, the amide II band became more rounded over the course of the degradation test. Day 0 and 1 had a sharp peak positioned at 1515 cm^{-1} which had disappeared by day 2. The ratio of silk II to I within the amide II band dropped after 1 day from 1.26 to 1.11 (Table 11). It remained around this ratio for the remaining days.

5.2.4.2.3 Protease Degradation of RSF Films 33 % and 25 %

This section will compare the RSF films with the highest crystallinity. β-sheet content has been shown to significantly increase between RSF films 33 % and 25 %. Both films lost significantly less mass than the other RSF films when degraded with protease XIV. Whereas the lower crystallinity films gained strong peaks at silk II band positions due to the dissolution of silk I, RSF films 33 % and 25 % already had a large proportion of silk II contributing to their structure.

RSF film 33 % has a significant silk II peak at 1620 cm^{-1} and a small silk II peak at 1697 cm^{-1} within the amide I region (Figure 5.13A). The silk II peak at 1620 cm^{-1} has a shoulder at 1640 cm^{-1}. After 1 day degraded in an enzymatic solution, both silk II peaks have increased in intensity whist the silk I peak at 1640 cm^{-1} has reduced. The spectra at days 1 and 2 have a similar shape and intensity, however by day 3 the silk II band at 1620 cm^{-1} has begun to decrease in intensity, whist the silk I band at 1640 cm^{-1} has grown in size. The intensity of these peaks continues to decline until day 8. Ratios of the silk II to silk I bands within the amide I region, show that the amount of silk II increases until day 2, after which, there is a significant drop from 1.55 to 1.32 and the ratio remains similar between days 3, 5 and 8 (Table 10). The amide II band is more prominently positioned at 1515 cm^{-1} between days 0 and 2, and then between days 3 and 8, the intensity of bands at 1515 cm^{-1} and 1535 cm^{-1} are similar in size. The ratio of intensities of the silk I and silk II bands show a decline in silk II after 1 day (Table 11). The ratio of silk II to silk I remains similar for days 1 and 2, drops from 1.16 to 1.06 between days 2 and 3, increases again between days 3 and 5 to 1.15, before finally finishing at 1.09 on the final day.
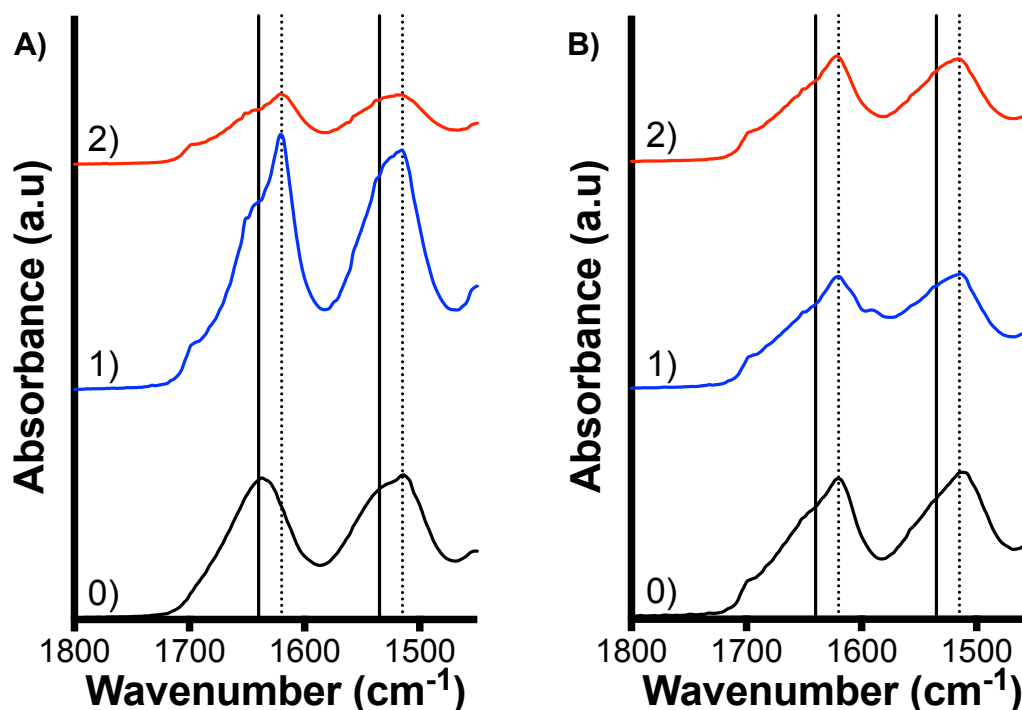
Figure 5.13: FTIR-ATR of of RSF films A) 33 % and B) 25 % degraded in a protease XIV solution. Brackets represent the degradation time point in days. Solid vertical lines mark the position of silk I bands and dotted vertical lines mark the position of silk II bands.

The most crystalline film, RSF film 25 %, had a similarly shaped spectra for days 0, 1 and 2 within the amide I region when degraded with protease XIV (Figure 5.13B). It had prominent silk II peaks positioned at 1620 cm^{-1} and at 1697 cm^{-1} with a small silk I peak at 1640 cm^{-1}. By day 3 the intensity of both peaks positioned at 1640 cm^{-1} and 1620 cm^{-1} had reduced in intensity. The intensity of the silk I peak at 1640 cm^{-1} had reduced more significantly than the silk II peak. By day 5 the silk II peak at 1620 cm^{-1} remained with a similar intensity, whilst the silk I peak at 1640 cm^{-1} had become more prominent. By day 8, the peak at 1620 cm^{-1} continued to reduce in size. The ratio between the silk I and silk II bands showed little difference between days 0 and 1 (Table 10). There is a slight drop in the ratio between days 1 and 2, from 1.54 to 1.50. By day 3 there is a large increase in silk II as the ratio rises to 1.62, the largest ratio achieved for any of the RSF films. This ratio then drops to 1.45 for day 5 and then 1.43 for day 8. The amide II band begins on day 0 with a sharp peak positioned at 1515 cm^{-1} (Table 11). By day 1 the band at 1515 cm^{-1} and a small shoulder appears at 1535 cm^{-1}. The amide II band remains a similar shape between days 1 and 5, but reduces in intensity by day 8.

5.2.4.2.4 PBS Degradation of RSF Films 100 % and 75 %

RSF film 100 % was the only RSF film to have a similar degradation profile in both the proteolytic solution as well as in PBS. This section will compare the structural changes of the control without any methanol treatment (RSF film 100 %), and that of the RSF film with the smallest volume of methanol (RSF film 75 %).

Table 12: Ratio of silk II to silk I bands (A_{1620} / A_{1640}) within the amide I region for films degraded in PBS, where RSF film 100 % equals an RSF film without any methanol addition and RSF film 75 % being three-parts RSF with one-part methanol.

RSF Film	A_{1620}/ A_{1640} (on day)					
	0	1	2	3	5	8
100 %	0.79	0.93	1.23			
75 %	1.24	1.01	0.91	0.89	0.91	0.93
66 %	1.25	1.26	1.02	1.03	1.08	1.09
50 %	1.36	0.84	0.97	1.27	1.42	1.27
33 %	1.41	1.01	1.38	1.34	1.56	1.33
25 %	1.53	1.18	1.28	1.38	1.35	1.66

Table 13: Ratio of silk II to silk I bands (A_{1515} / A_{1535}) within the amide II region for films degraded in PBS, where RSF film 100 % equals an RSF film without any methanol addition and RSF film 75 % being three-parts RSF with one-part methanol.

RSF Film	A_{1515}/ A_{1535} (on day)					
	0	1	2	3	5	8
100 %	1.11	1.03	1.14			
75 %	1.22	1.06	1.04	1.06	1.05	1.05
66 %	1.22	1.14	1.06	1.08	1.11	1.10
50 %	1.26	1.05	1.08	1.16	1.20	1.20
33 %	1.26	1.07	1.18	1.16	1.25	1.16
25 %	1.31	1.13	1.14	1.18	1.20	1.28

RSF film 100 % when degraded in PBS showed a flattening of the amide I band between days 0 and 1 (Figure 5.14A). The band positioned at 1640 cm^{-1} reduced in size, revealing a band positioned at 1620 cm^{-1}, which had a similar intensity to that

of the band at 1640 cm^{-1}. By day 2, the band at 1640 cm^{-1} had reduced even further and the band at 1620 cm^{-1} remained a similar size. The ratio of the silk II to silk I bands within the amide I region show a continuous increase of silk II after each day (Table 12). The amide II region began with a sharp peak at 1515 cm^{-1} and a broad peak at 1535 cm^{-1} on day 0. By day 1 the band has lost its prominent sharp peak at 1515 cm^{-1}, and has instead flattened out with level peaks at 1515 cm^{-1} and 1535 cm^{-1}. By day 2 the peak at 1535 cm^{-1} has reduced, leaving the peak at 1515 cm^{-1} with a similar intensity to day 1. Ratios of the silk II to silk I bands show a drop of silk II between days 0 and 1, before recovering to a similar amount on day 2 as for day 0 (Table 13).

Figure 5.14: FTIR-ATR of of RSF films A) 100 % and B) 75 % degraded in PBS. Brackets represent the degradation time point in days. Solid vertical lines mark the position of silk I bands and dotted vertical lines mark the position of silk II bands.

After the first 24 hours degraded in PBS, the amide I band of RSF film 75 % flattened out due to a massive increase in size of the silk I band positioned at 1640 cm^{-1} (Figure 5.14B). The silk II peak at 1620 cm^{-1} remained a similar intensity. By day 2, the band at 1620 cm^{-1} had reduced in size causing the amide I band to appear more rounded. By day 3, the band at 1620 cm^{-1} had reduced further, causing the band to shift towards the silk I band at 1640 cm^{-1}. The amide I remained a similar shape on day 5,

however both 1620 cm^{-1} and 1640 cm^{-1} bands increased in size. By the final day the amide I band had become flat with both peaks at 1620 cm^{-1} and 1640 cm^{-1} having a similar intensity. Ratios of the silk I and silk II bands show a large drop of silk II between days 0 and 1 (Table 12). The ratio drops from a starting value of 1.24 to 1.01. By the following day the ratio of silk II to silk I has reduced further to 0.91, and remains around this value for the remaining days. The amide II band initially has a predominant peak at 1515 cm^{-1}. By day 1, the peak at 1515 cm^{-1} has remained in intensity, however it has formed a large shoulder of a similar intensity at 1535 cm^{-1}. The amide I region remains a similar shape for the remaining days, but with a slightly larger intensity on day 5. The ratio of silk II to silk I within the amide II region shows a substantial decrease of silk II over the first 24 hours (Table 13). The ratio of silk II to silk I bands drops from 1.22 to 1.06 by day 1 and then remains at this level.

5.2.4.2.5   PBS Degradation of RSF films 66 % and 50 %

This section will compare the mid-ranged methanol treated RSF films. During degradation RSF films 66 % and 50 % experienced minimal mass loss when degraded in PBS despite beginning with a large proportion of unordered, water-soluble silk within their structure.

RSF film 66 % had an increase of intensity for both silk I and silk II bands within the amide I region over the first 24 hours in PBS (Figure 5.15A). The peak at 1620 cm^{-1} had the most significant increase. By the following day, the silk I band at 1640 cm^{-1} had increased further to a similar intensity to the peak at 1620 cm^{-1}. By day 3, the peak at 1620 cm^{-1} had increased slightly to give a sharper peak to the amide I band. Between days 3 and 5 the peak at 1640 cm^{-1} decreased slightly before slightly increasing between days 5 and 8. Ratios between the silk I and silk II bands within the amide I region, show a similar ratio between days 0 and 1 (Table 12). This then drops with an increase of silk I from 1.26 to 1.02. The ratio of silk II to silk I remains similar between days 2 and 3, before increasing to 1.08 and 1.09 for days 5 and 8 respectively. After 24 hours in PBS the 1515 cm^{-1} band within the amide II region begins to form a shoulder at 1535 cm^{-1}. The shoulder grows and becomes more pronounced by day 2, after which, the amide II band remains a similar shape. The

ratio of silk II to silk I within the amide II region show a gradual reduction in the prevalence of silk II over the first 2 days (Table 13). The ratio of silk II to silk I remains steady for the remaining days.
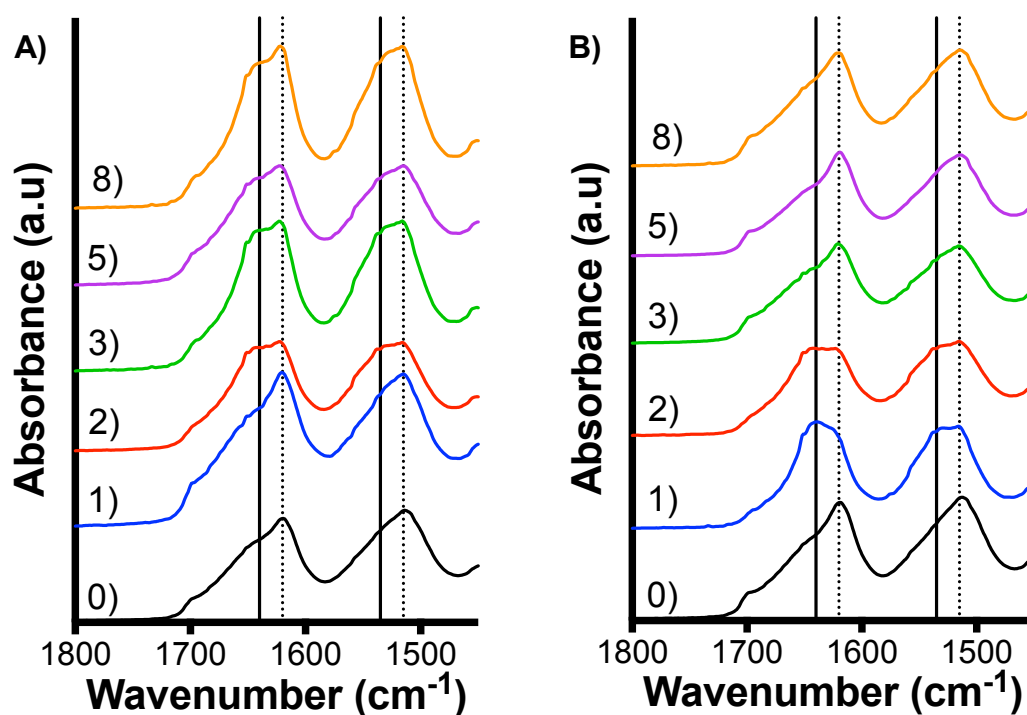
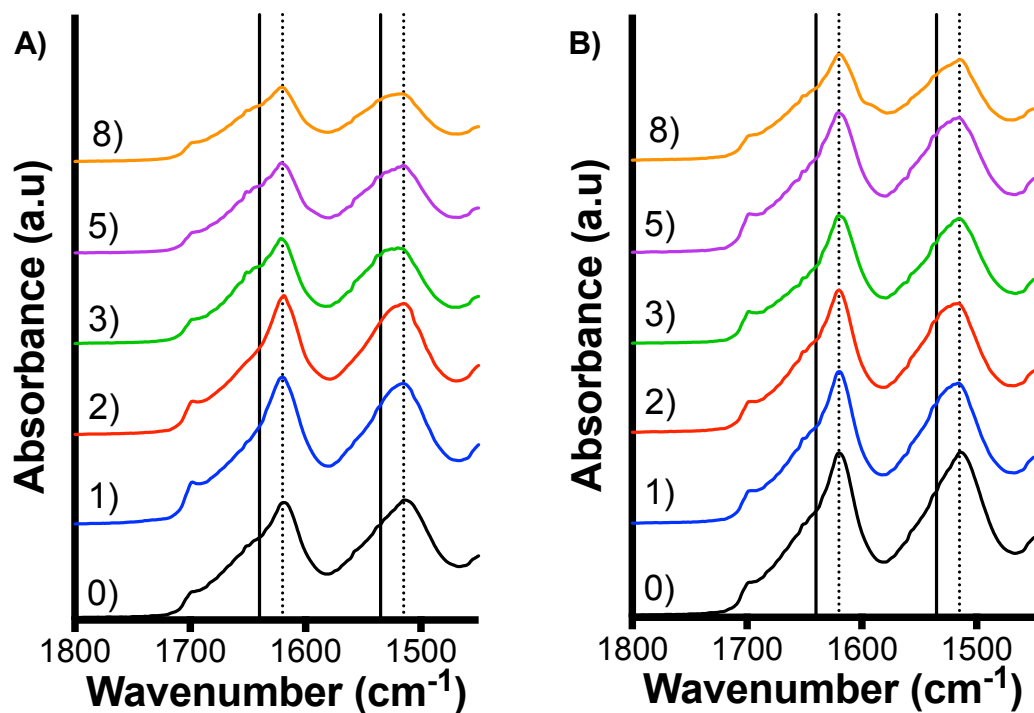*Figure 5.15: FTIR-ATR of of RSF films A) 66 % and B) 50 % degraded in PBS. Brackets represent the degradation time point in days. Solid vertical lines mark the position of silk I bands and dotted vertical lines mark the position of silk II bands.*

RSF film 50 %, when degraded in PBS has a significant increase of silk I over the first 24 hours (Figure 5.15B). By the first day, a peak of high intensity has formed at 1640 cm^{-1} causing the amide I band to shift to a predominantly silk I position. By day 2, the band at 1640 cm^{-1} has reduced in intensity to a similar size to the peak at 1620 cm^{-1} creating a flat amide I band. Between days 3, 5 and 8 the 1640 cm^{-1} continues to decrease in size. The ratio of silk II to silk I within the amide I region, show a massive decrease over the first day, decreasing from 1.36 to 0.84 (Table 12). The ratio then begins to steadily increase between days 1 to 5 before reaching its highest ratio of 1.42. By the final day the ratio has reduced to 1.27. Within the amide II region, there is also a significant increase of silk I over the first 24-hour period. By day 1 a peak has developed at 1535 cm^{-1} which has a similar intensity to the peak at 1515 cm^{-1}. Both peaks remain a similar size on day 2. By day 3, the peak at 1535 cm^{-1} has begun to

reduce, and continues to do so until the final day. The ratio of silk II to silk I shows an initial drop from 1.26 to 1.05 on day 1 (Table 13). The ratio remains similar between days 1 and 2. By day 3 the ratio has increased to 1.16, and by the fifth day 1.20 where it remains for the final day as well.

5.2.4.2.6   PBS Degradation of RSF films 33 % and 25 %

The results of this section will compare the FTIR-ATR spectra for the RSF films with the highest crystallinity. These films had similar degradation profiles to the other RSF films when degraded in PBS, even though they had a higher crystallinity, hence less water soluble silk content, to begin with.

After 24 hours degraded in PBS, RSF film 33 % there was a significant increase of silk I (Figure 5.16A). Within the amide I region the peak at 1640 cm^{-1} increased in intensity to a similar size to the peak 1620 cm^{-1}. By day 2, the peak at 1640 cm^{-1} had reduced, and the peak at 1620 cm^{-1} had increased in size. Day 2 and 3 had a similarly shaped amide I band. Between days 3 and 5, the band at 1640 cm^{-1} reduced in size, however by day 8 had significantly increase in size. The ratio of the silk I and silk II bands within the amide I region, show a substantial drop in the proportion of silk II, as the ratio decreased from 1.41 to 1.01 over the first 24 hours (Table 12). The proportion of silk II significantly increased the following day as the ratio rose to 1.38. It remained at this level for days 2, 3 and 8, with an increase of silk II on day 5 when the ratio increased to 1.56. Within the amide II region, the peak at 1515 cm^{-1} formed a shoulder at 1535 cm^{-1} by the first day, however the shoulder disappeared by day 2 and didn't reappear on the following days. The ratio of silk II to silk I bands within the amide II region show a decrease from 1.26 to 1.07 over the first 24 hours, after which the ratio increases 1.18 and remains around this value for the remaining days (Table 13).
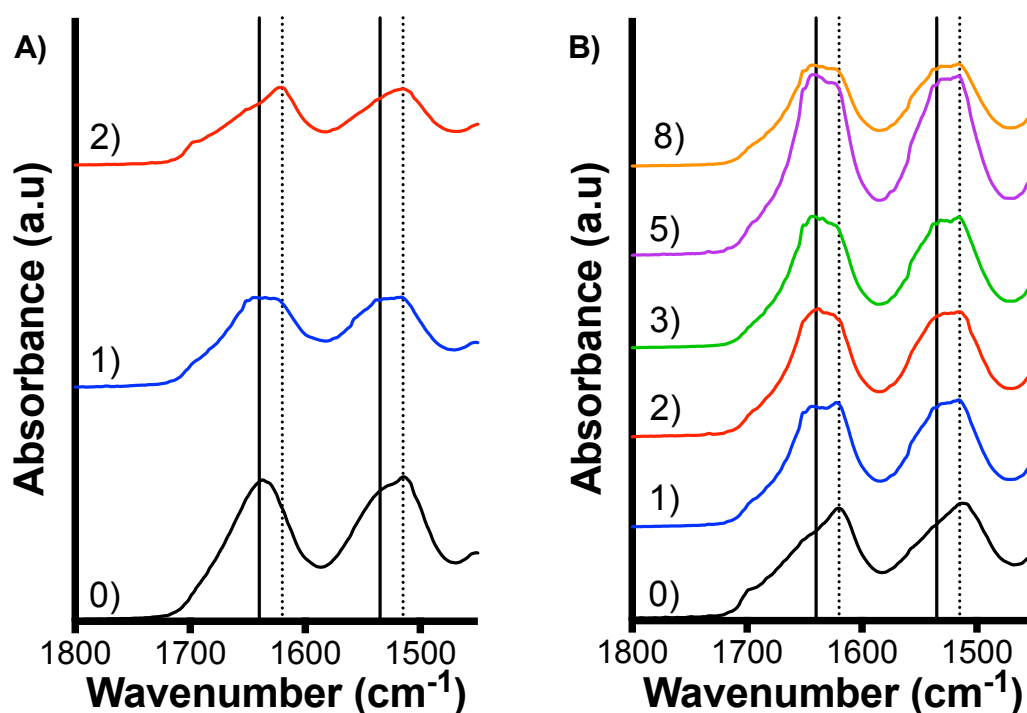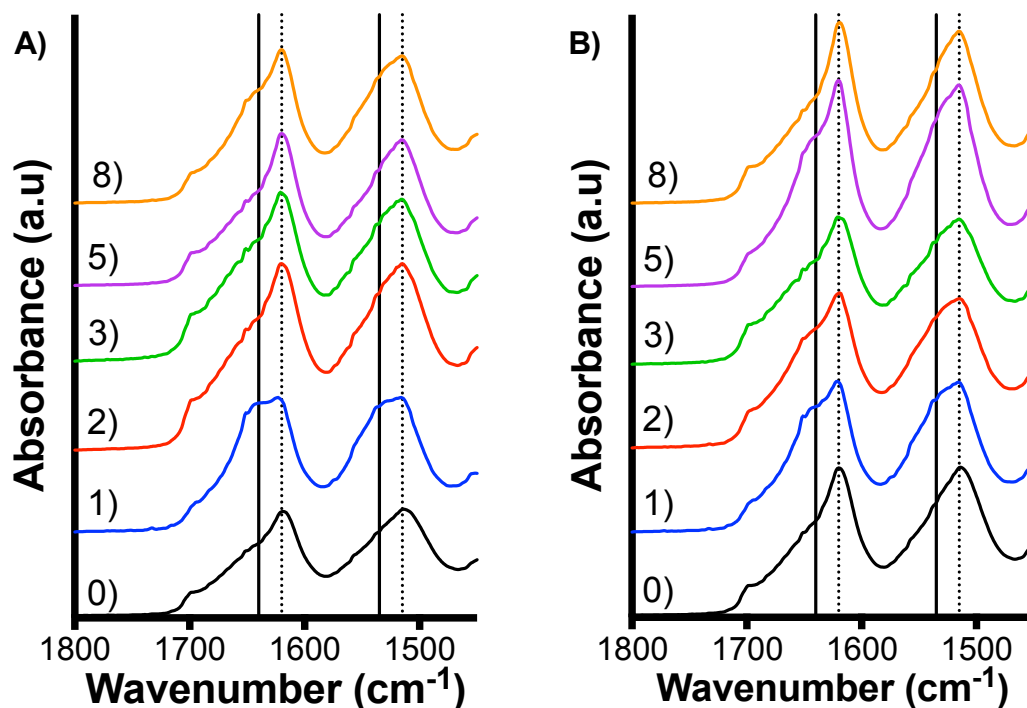
Figure 5.16: FTIR-ATR of of RSF films A) 33 % and B) 25 % degraded in PBS. Brackets represent the degradation time point in days. Solid vertical lines mark the position of silk I bands and dotted vertical lines mark the position of silk II bands.

RSF film 25 % showed an increase in the silk I band intensities over the first 24 hours in PBS (Figure 5.16B). Within the amide I region, the band at 1640 cm^{-1} increases in intensity by day 1 to produce a shoulder on the band at 1620 cm^{-1}. Between days 1 and 3, the band at 1640 cm^{-1} gradually decreases before increasing again on day 5. By day 8 the band at 1640 cm^{-1} had decreased in size, whilst the band at 1620 cm^{-1} had a significant increase of intensity. The ratios of silk II to silk I for the amide I region, show a substantial drop from 1.56 to 1.18 by day 1 (Table 12). By day 2 the ratio increases to 1.28, and continues to rise on day 3 to 1.38. Day 5 has a similar ratio to day 3. Day 8 has the highest ratio of silk II to silk I than any of the other RSF films at any time point, when degraded in either PBS or protease XIV. Within the amide II region, by the first day the band at 1515 cm^{-1} has developed a shoulder at 1535 cm^{-1}. This gradually decreases over the remaining days. The ratio of silk II to silk I within the amide II region show an initial drop in the proportion of silk II, as the ratio decreases from 1.31 to 1.13 (Table 13). Over the following days the ratio gradually increases, until on the final day a ratio of 1.28 is achieved.

5.2.4.2.7 Discussion of the Degradation FTIR-ATR Results

RSF films degraded with protease XIV increased in silk II content over the first few days of degradation, even RSF films with the highest crystallinity experienced a slight increase. This was caused by the degradation of silk I as the protease XIV degraded the less dense regions of fibroin first [98]. Over longer degradation times, the intensity of the silk II peaks reduced, signifying the digestion of silk II β-sheet crystals by the enzymes.

Conversely, many of the RSF films degraded in PBS developed a strong silk I band positioned around 1640 cm^{-1}, whilst the silk II peak at 1620 cm^{-1} remained fairly consistent. When the films were submerged in PBS they became hydrated. Hydration of the films occurs with van de Waals interactions, hydrogen bonding and interactions with amino acid side chains, between the fibroin and water molecules. Water molecules are able to affect intermolecular cohesive forces, thereby improving mobility of the non-crystalline regions and loosening the less dense crystalline regions [167]. An increase in the silk I band intensities could be reflective of improved conformational freedom of the β-strands.

Degradation of the RSF films in a proteolytic solution and in PBS supports the theory that the RSF films have multiple structural layers. RSF films degraded with protease XIV quickly lost silk I content, before silk II content was broken down by enzymatic activity. This could be reflective of the enzymes breaking through the silk II layers enabling silk I to be dissolved/ degraded. RSF films degraded in PBS did not experience an initial loss of silk I, and instead increased in silk I content. This could be the result of the hydration of the RSF films when submerged in PBS, which loosened the less dense crystalline regions. As the silk I content did not dissolve into the surrounding solution, because it was trapped beneath the silk II layers, the RSF structure appeared less crystalline.

5.2.4.3 Degradation FSD

This section will begin with a written commentary of the results obtained through Fourier self deconvolution (FSD), which will be followed by a discussion of the results.

The FTIR-ATR spectra had shown that the RSF structures had experienced different structural changes when degraded with a proteolytic solution or in PBS. The spectra show low crystallinity RSF films becoming more crystalline when degraded with protease XIV, which developed strong silk II bands. However, when degraded in PBS, they appear to become less crystalline, developing large silk I bands. FSD was performed on the FTIR-ATR spectra of RSF films degraded in either enzymatic solution or PBS to calculate changes in secondary structural contributions (Figures 35 – 40).

5.2.4.3.1 Protease Degradation

Over the initial 24-hour period RSF film 100 % had a significant increase in crystallinity when degraded in the protease XIV solution (p≤0.0001) (Figure 5.17A). β-sheet content increased 30 % which was accompanied by a 19 % loss of α-helix and random coil content. By the following day β-sheet content reduced by 5 %, whilst the proportion of α-helix and random coil remained similar with no significant difference between days.

Figure 5.17: FSD data showing percentage of secondary structures components for RSF films A) 100 % and B) 75 % degraded in protease XIV at different degradation time points. Standard deviation of measurements made over four different FWHM values is shown.

RSF film 75 % had no significant changes in β-sheet content over the first 2 days when degraded in an enzymatic solution, increasing by 2 % after 24-hours and then remaining at this concentration (Figure 5.17B). α-helix and random coil content

experienced more significant changes. An initial drop of 8 % (p≤0.0001) was followed by a 5 % (p≤0.01) increase the subsequent day.

After 48-hours in the enzymatic solution, RSF film 66 % (Figure 5.18A) had a slight increase in β-sheet content, increasing by a total of 6 %; 3 % (p≤0.05) on each consecutive day. Over the final three time points, β-sheet content fluctuated. On day 3 β-sheet content dropped by 3 % (p≤0.05), followed on day 5 with a 5 % increase (p≤0.0001) and finally on day 8 there was a 7 % decrease (p≤0.0001). The percentage of α-helix and random coil structures within the films fluctuated around an average of 22%. After 8 days degraded with protease XIV, there was no significant difference between the starting secondary structural content and that which remained on the final day.

Figure 5.18: FSD data showing percentage of secondary structures components for RSF films A) 66 % and B) 50 % degraded in protease XIV at different degradation time points. Standard deviation of measurements made over four different FWHM values is shown.

β-sheet content of RSF film 50 % (Figure 5.18B) remained similar over the first 48-hour period, although the average on day 2 was lower than days 1 and 0. Between days 2 and 3 there was a 4 % drop in β-sheet content (p≤0.05), however there was no other significant differences between consecutive time points. α-helix and random coil content initially dropped over the first 24-hours by 5 % (p≤0.01), which was followed by a 9 % increase (p≤0.0001) the following day. The subsequent time

points had similar α-helix and random coil content. By the final day, all secondary structural contributions were similar to secondary structure content on day 0.

β-sheet content for RSF film 33 % (Figure 5.19A) gradually reduced over the 8-days degraded in an enzymatic solution. Between consecutive days there were no significant differences, however, by the eighth day there had been an overall 8 % reduction (p≤0.0001) in β-sheet content from the starting concentration. α-helix and random coil content remained stable over the first 48-hour period. Between days 2 and 3, α-helix and random coil content increased by 9 % (p≤0.0001), which then reduced by 7 % (p≤0.05) between days 3 and 5, and increased by 6 % (p≤0.01) between days 5 and 8. The final α-helix and random coil content was 8 % (p≤0.0001) higher than the initial concentration.
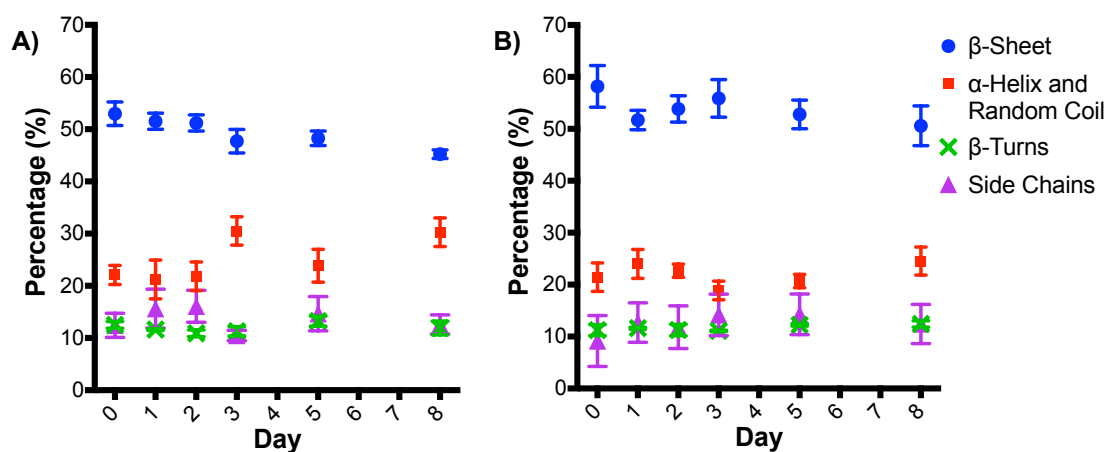
Figure 5.19: FSD data showing percentage of secondary structures components for RSF films A) 33 % and B) 25 % degraded in protease XIV at different degradation time points. Standard deviation of measurements made over four different FWHM values is shown.

RSF film 25 % (Figure 5.19B), had after the first 24 hours in an enzymatic solution, a drop of β-sheet content by 6 % (p≤0.0001). Between days 1 and 3, β-sheet content gradually increased before dropping by 3 % (p≤0.05) between days 3 and 5 and remained around this concentration. α-helix and random coils contributed to between 19% and 25% of the film structure over the 8-day period. Significant changes in concentration occurred between days 2 and 3 with a 4 % decrease (p≤0.01), and between days 5 and 8 with a 4 % increase (p≤0.01). Over the 8-day

period, β-sheet content decreased by 8 % (p≤0.0001) and α-helix and random coil content increased by 3 % (p≤0.05).

5.2.4.3.2 PBS Degradation

RSF film 100 %, when degraded in PBS (Figure 5.20A) experienced a significant increase in β-sheet content over the first 24-hour period of 15 % (p≤0.0001). However, this is around half the β-sheet content increased by when the film was degraded in an enzymatic solution. β-sheet content remained at this concentration by the following day. α-helix and random coil content decreased by 14 % (p≤0.0001) over the first 24-hours and a further 5 % (p≤0.0001) the following day.
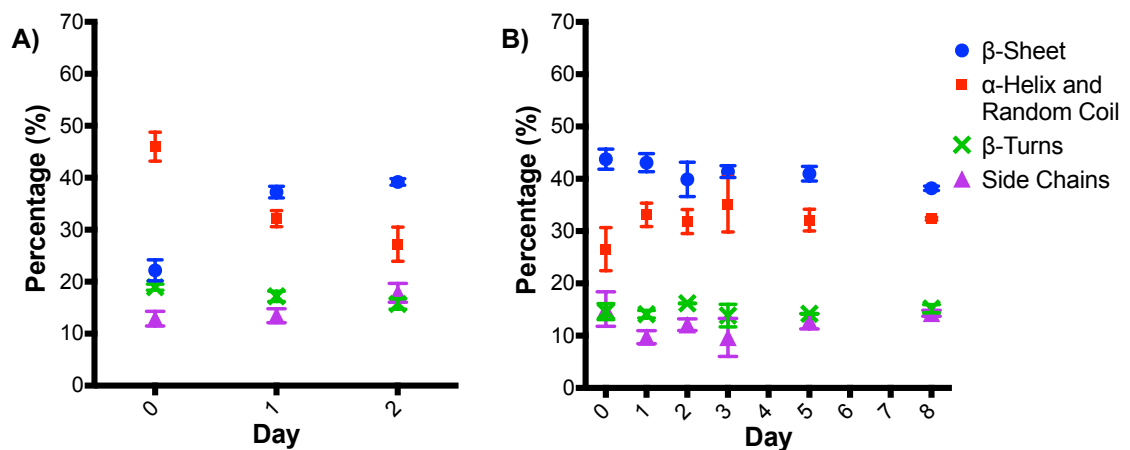
Figure 5.20: FSD data showing percentage of secondary structures components for RSF films A) 100 % and B) 75 % degraded in PBS at different degradation time points. Standard deviation of measurements made over four different FWHM values is shown.

β-sheet content remained relatively steady for RSF film 75 % in the PBS solution (Figure 5.20B). Between sequential time-periods there were no significant reductions in β-sheet content, however, there was a consistent downward trend resulting in a significant difference between the starting concentration and the concentration on the final day. By day 8, β-sheet content had reduced by 6 % (p≤0.01). α-helix and random coil content experienced a significant increase after 1 day in PBS, increasing by 7 % (p≤0.001). For the remaining 7 days, α-helix and random coil content remained around this concentration, finishing with a concentration of 32 % which was significantly higher than the starting concentration (p≤0.01).

RSF film 66 % when degraded in PBS (Figure 5.21A), experienced an initial drop in β-sheet content over the first day by 7 % (p≤0.0001). Between days 1 and 2 there was no significant change in β-sheet content, which then began to fluctuate over the remaining days. Between days 2 and 3 there was a 3 % increase (p≤0.05), between days 3 and 5 a 4 % decrease (p≤0.01), and between days 5 and 8 an 8 % increase (p≤0.0001). Over the first 48-hours in PBS, α-helix and random coil content steadily increased by 4 % (p≤0.01) by day 1, and a further 6 % (p≤0.0001) by day 2. By day 3 there was a 4 % (p≤0.05) drop in α-helix and random coil content, and no significant differences between days 3, 5 and 8. Overall, after 8 days in PBS, there was no significant changes in β-sheet content and a 4 % increase (p≤0.01) in α-helix and random coil content between the starting and finishing concentrations.
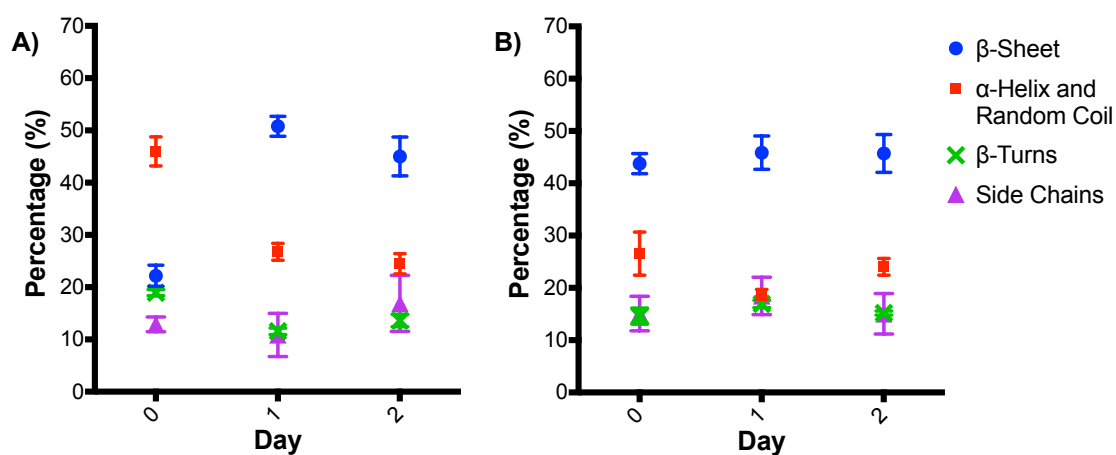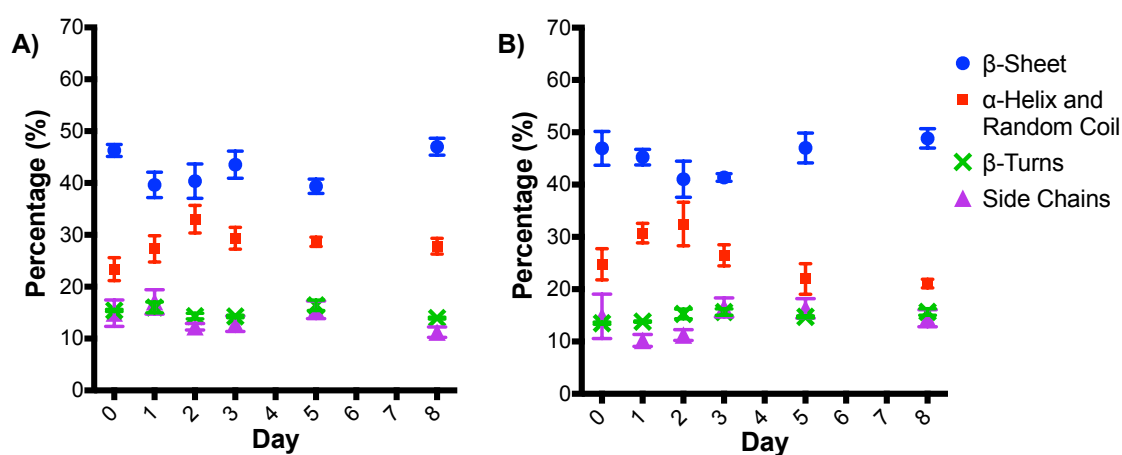

Figure 5.21: FSD data showing percentage of secondary structures components for RSF films A) 66 % and B) 50 % degraded in PBS at different degradation time points. Standard deviation of measurements made over four different FWHM values is shown.

β-sheet content for RSF film 50 % (Figure 5.21B) remained similar after 1 day in PBS. By day 2, there was a 4 % decrease (p≤0.05) in β-sheet content and remained at this concentration up until day 5, where between days 3 and 5, there was a 6 % increase (p≤0.001). There was no significant difference of β-sheet concentration between days 5 and 8. α-helix and random coil content increased significantly after 1 day in PBS, rising by 6 % (p≤0.001). Between days 1 and 2 there was no significant difference in α-helix and random coil content. Between days 2 and 5 there were two consecutive losses of α-helix and random coil content, a 6 % reduction (p≤0.001)

between days 2 and 3, and a 5 % (p≤0.01) loss between days 3 and 5. By the final day in PBS, all secondary structural contributions were similar to secondary structure content on day 0.

RSF film 33 % degraded in PBS (Figure 5.22A) experienced a significant drop in β-sheet content over the first 24 hours with a 13 % (p≤0.0001) loss which was followed by a 5 % increase (p≤0.01) by day 2. No significant differences were measured until the final day, where between days 5 and 8 there was a 5 % (p≤0.01) decrease of β-sheet content. α-helix and random coil content experienced similar significant changes over the first 2 days in PBS. By the first day there had been an 11 % increase (p≤0.0001) of α-helix and random coil content followed by an 11 % (p≤0.0001) decrease between days 2 and 3. No significant differences were measured until the final day, where between days 5 and 8 there was a 6 % (p≤0.001) increase. Overall there was a 7 % decrease (p≤0.0001) in β-sheet content and a 5 % increase (p≤0.01) in α-helix and random coil content by the final day.

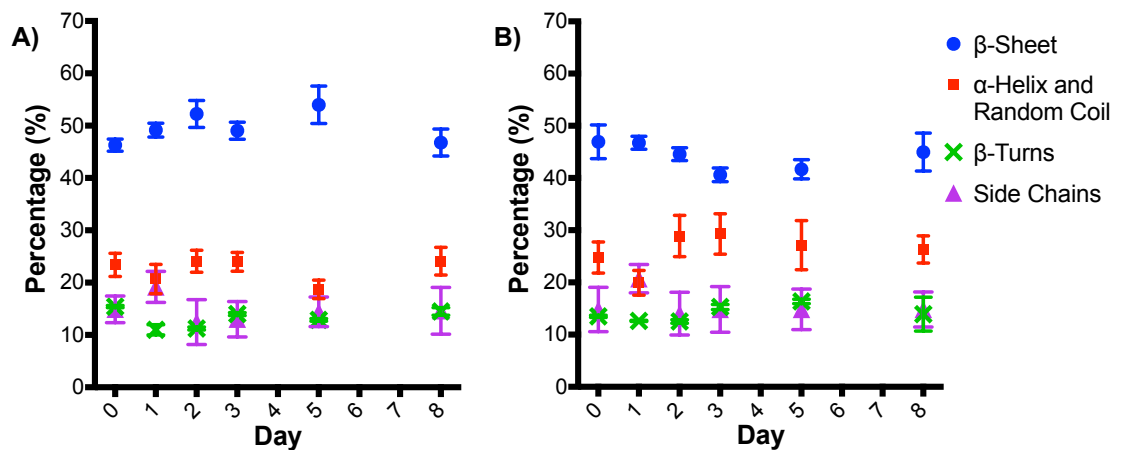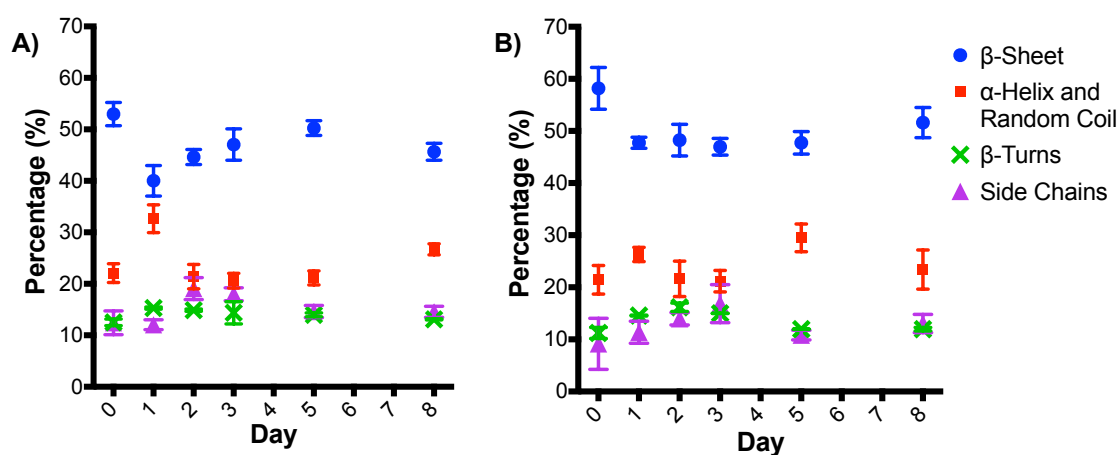*Figure 5.22: FSD data showing percentage of secondary structures components for RSF films A) 33 % and B) 25 % degraded in PBS at different degradation time points. Standard deviation of measurements made over four different FWHM values is shown.*

There is an initial drop in β-sheet content of 10 % (p≤0.0001) for RSF film 25 % after 24 hours in PBS (Figure 5.22B). β-sheet content remains around this concentration with no significant differences between the remaining days. α-helix and random coil content increased by 5 % (p≤0.05) over the first 24 hours and then dropped by 5 %

(p≤0.05) by day 2. α-helix and random coil content remained similar between days 2 and 3, after which it increased by 8 % (p≤0.0001) between days 3 and 5, and then decreased by 6 % (p≤0.01) between days 5 and 8. By the final day, β-sheet content had decreased by 7 % (p≤0.001) and there was no significant difference of α-helix and random coil content between day 8 and day 0.

5.2.4.3.3 Discussion of the FSD Results

FSD data for the RSF films degraded with protease XIV showed small fluctuations in β-sheet, α-helix and random coil content. RSF film 100 % was the only RSF film degraded with protease XIV to experience a substantial increase in β-sheet content and a loss of α-helix and random coil content over the first few days of degradation. Large changes in RSF film 100 % structure could be attributed to its large mass loss, and the dissolution of unordered silk I structures. Fluctuations in β-sheet, α-helix and random coil content of the other RSF films could support the notion that the scaffolds have a layered structure, comprising of silk II layers encapsulating layers of unordered silk I. Enzymes are only able to degrade the surface of the films and unable to penetrate into the structure. Therefore, each individual layer of silk II would have to degrade to expose the unordered silk I. Consequently, small amounts of silk I remained trapped beneath the layers of silk II, which prevented a complete loss of silk I within the first day of degradation.

RSF films 100 %, 75 %, 66 % and 50 % all experienced a drop in average α-helix and random coil content over the first 24 hours, which could be linked to the large mass loss experienced by these samples. Qiang Lu *et al.* discovered that the hydrophilic non-crystalline regions of the RSF films were the first to degrade followed by the degradation of the hydrophobic crystalline region. However, as the hydrophilic regions of fibroin degraded they released the hydrophobic crystalline blocks which moved rather than degraded into the surrounding solution [71]. This might help to explain any fluctuations of the β-sheet content and the relatively stable proportions β-sheet to α-helix and random coil content.

Films degraded in PBS showed greater fluctuations in crystallinity. These fluctuations could be the result of amorphous regions of the silk II structure hydrolysing and secreting β-sheet crystals into the surrounding solution. RSF film 100 % increased in crystallinity by 17 % when degraded in PBS, probably caused by the dissolution of unordered silk I content. All of the methanol treated RSF films experienced an increase of α-helix and random coil content over the first 24 hours, which could be related to the hydrolysis of the less dense crystalline regions caused by hydration of the RSF films [167].

5.3 Summary

Printing methanol into the RSF films was shown to induce a gradual structural transition of silk I to silk II. By increasing the volume of methanol printed, a greater proportion of the RSF films became crystalline, until a maximum crystallinity was achieved with RSF film 25 % (1 part RSF ink to 3 parts methanol). As the level of crystallinity achieved for RSF film 25 % was similar to that of the unprocessed silk cocoon and that of an RSF film which had been submerged in methanol for 4 days, it can be concluded that the maximum crystallinity attainable through methanol treatment was achieved. It was also shown, by comparing unprinted RSF with that of printed RSF without methanol treatment, that the printing conditions used did not cause any shear induced structural changes to the RSF.

FTIR-ATR spectra of the RSF films showed a characteristic shift of absorption intensities from a silk I structure to a silk II structure with the addition of methanol. Absorbance wavenumbers within the amide I and II regions moved from higher to lower positions. From previous studies it has been determined that the higher wavenumbers (1648 – 1654 cm^{-1} and 1535 – 1542 cm^{-1}) are representative of α-helix and a silk I structure, whereas the lower wavenumbers (1610 – 1630 cm^{-1} and 1510 – 1520 cm^{-1}) are representative of β-sheet and a silk II structure [94]. To compare the shift of absorbance peak position, intensity ratios were made for absorbance intensities at 1620 and 1640 cm^{-1} within the amide I region, and at 1515 and 1535 cm^{-1} within the amide II region. Ratios within both the amide I and II regions showed

a dependence upon the volume of methanol printed. Larger volumes of methanol produced higher ratios of silk II to silk I.

FSD (Fourier self-deconvolution) performed on the amide I region of the RSF films confirmed that increasing the volume of methanol printed had a gradual effect of converting silk I to silk II. The smallest volumes of methanol had similar proportions of β-sheet content, however, as the volume of methanol increased above a ratio of 1:1 RSF to methanol (RSF film 50 %), significant increases of β-sheet content began to be observed. The large increase in crystallinity was reflected by a significant increase in water droplet contact angle between RSF films 50 % and 33 %. Topography of the films also changed as a result of the methanol treatment. Cracks on the surface of the films, along with increased roughness values were shown to be proportional to the volume of methanol used.

Degradation of the RSF films within a protease XIV solution was shown to be dependant on RSF film crystallinity. The most significant mass loss was observed over the first 24-hour period, after which degradation slowed down and kept to a similar degradation rate for the remainder of the test. Films degraded in a PBS solution should have also experienced an initial mass loss related to silk I content. However, this was not the case, as all films exposed to methanol had experienced similar mass losses by the final day when submerged in PBS. A potential reason for this could be down to the method in which the RSF films were produced. The RSF films were produced layer by layer, where each layer of RSF was followed by a layer of methanol. This could have produced a non-uniform structure which had multiple layers of silk II encapsulating layers of silk I. The silk II could have acted as a protective layer, preventing the silk I from dissolving into the surrounding PBS solution.

The large mass loss over the first day, experienced by the RSF films in an enzymatic solution, was initially related to the dissolution of the water soluble silk I within the films. However, FSD of the films did not show a large drop of α-helix and random coil structure in proportion to the mass lost. A potential reason for this could be that as the amorphous regions of the silk fibroin were dissolved and digested by the

enzymes, they released large quantities of β-sheet crystals into the surrounding solution. Hence the mass loss was related to silk I content of the RSF films, however structural content of the films remained alike between days due to similar amounts of β-sheet, α-helix and random coil structure being released into the surrounding solution.

By reactively inkjet printing RSF with methanol, the structure of RSF films has been controlled. Gradual increases in the volume of methanol printed between layers of RSF has been shown to directly correlate with an increased β-sheet crystal content, which in turn has influenced degradation rates of the RSF films. Reactive inkjet printing has also been shown to offer a faster transition of silk I to silk II than that of submerging RSF films in methanol. RSF films submerged in methanol, as is currently done to improve RSF film properties, can take up to 4 days to induce maximum β-sheet content within the RSF films [134]. Thus, producing RSF films via reactive inkjet printing offers a more efficient transition of inducing β-sheet as well as control over crystal content and degradation rates which can be desirable for the design of dental barrier membranes.

Chapter 6: Inkjet Printing of Nano-Hydroxyapatite / Regenerated Silk Fibroin Composite Films

6.1   Introduction

This chapter will explore the inclusion of nano hydroxyapatite (nHA) within the RSF (regenerated silk fibroin) films. Hydroxyapatite has been synthesised to a nano-scale for ease of printing, improved osteoinduction as well as closer replication of biological apatite [170]. The nHA was added into the RSF ink, this made it necessary to investigate if the presence of nHA would affect the transition of silk I into a silk II. The inclusion of nHA within the RSF structure could change film degradation rates. As the films degrade it is expected that the nHA crystals will be released by the film, thereby increasing the surface area of the RSF. A larger surface area could increase the degradation rate of the films when degraded with a protease, as the proteolytic enzymes are only able to work on the surface of the films.

By using an inkjet printer to produce the dental barrier membranes, it is possible to produce a graduated structure, and therefore, a film which is predominantly nHA on one side to interface with the bone, and predominantly RSF on the other to interact with the gingiva. The inks used for this experiment were produced with a dried weight composition of 100 %, 75 %, 50 % and 25 % nHA. These concentrations have been chosen to represent the extremes of surface nHA concentrations (and would only represent the surface on one side of the barrier membrane) to determine which would be most suited for promoting bone growth. RSF has also been used previously to improve mechanical strength and brittleness to biphasic calcium phosphate scaffolds [171]

6.2   Results and Discussion

The following section will begin by reporting the results of the nHA synthesis which will be followed by the characterisation of the nHA/RSF films and then a discussion of the obtained data.

6.2.1 nHA Characterisation

6.2.1.1 nHA X-Ray Powder Diffraction (XRD)

X-ray powder diffraction (XRD) was performed on dried wet precipitated nHA before and after sintering. For printing nHA was used in its pre-sintered form, as during sintering the nHA particles will fuse together. Analysing both the sintered and unsintered nHA enables a comparison of the quality of the nHA, the diffractograms for both forms are shown in Figure 6.1. In both samples only HA reflections were detected as confirmed with JCPDS file number 09-432. The unsintered nHA had broad diffraction peaks which became sharper after sintering which indicates an improvement of crystallinity and crystallite size [172].
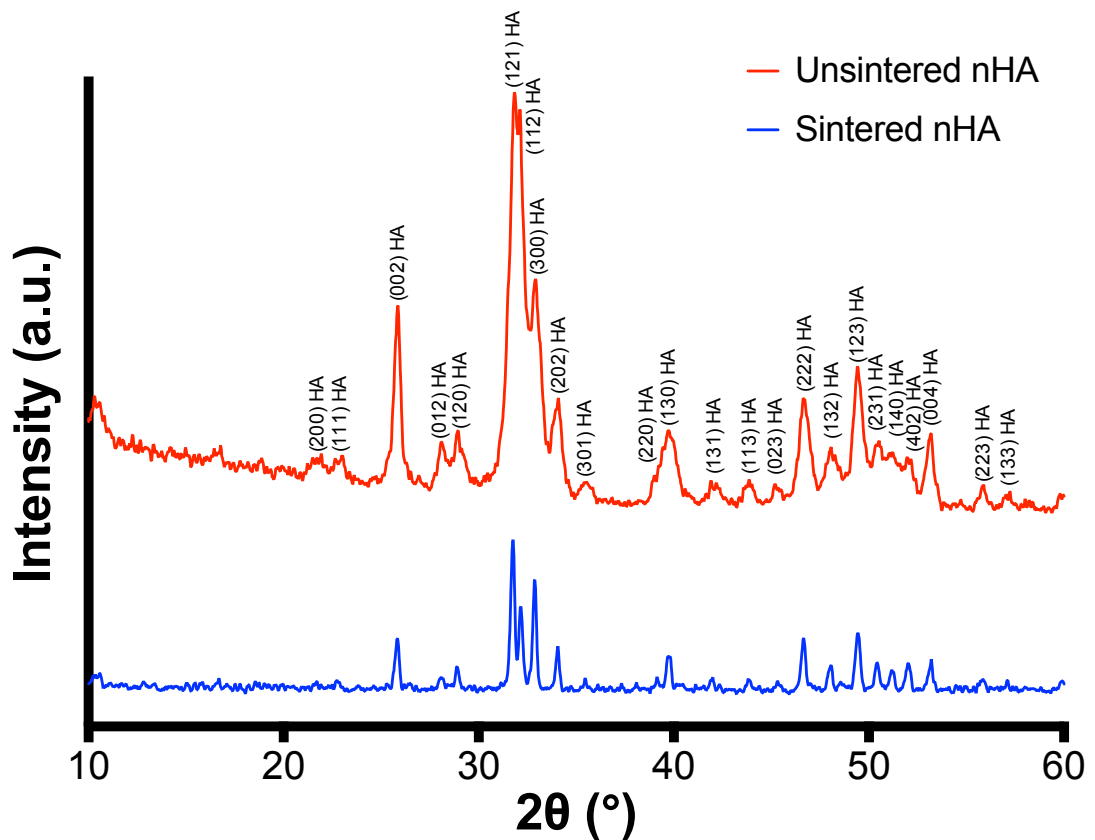
Figure 6.1: Diffractogram of wet precipitated nHA before sintering and after sintering

6.2.1.2 nHA Fourier Transform Infrared Spectroscopy (FTIR)

Fourier transform infrared spectroscopy with attenuated total reflectance (FTIR-ATR) was performed on the nHA before and after the sintering process, and is shown in

Figure 6.2. By comparing the FTIR-ATR spectra before and after sintering, the purity of the unsintered samples can be analysed. During sintering, between temperatures of 450 – 950 °C, impurities such as CO_3^{2-} are removed from the surface of the nHA crystals which would otherwise show up in the unsintered sample [173]. Hence by sintering, any impurities included within the HA crystal lattice will become apparent.

A big difference between the two spectra is the broad band, which is between 2500 – 3700 cm^{-1} present for the unsintered nHA sample. This band is indicative of a hydrated structure, which has an additional characteristic peak at 1639 cm^{-1} [174], [175]. In comparison, the sintered spectrum has no peaks as the water has most likely evaporated during sintering.
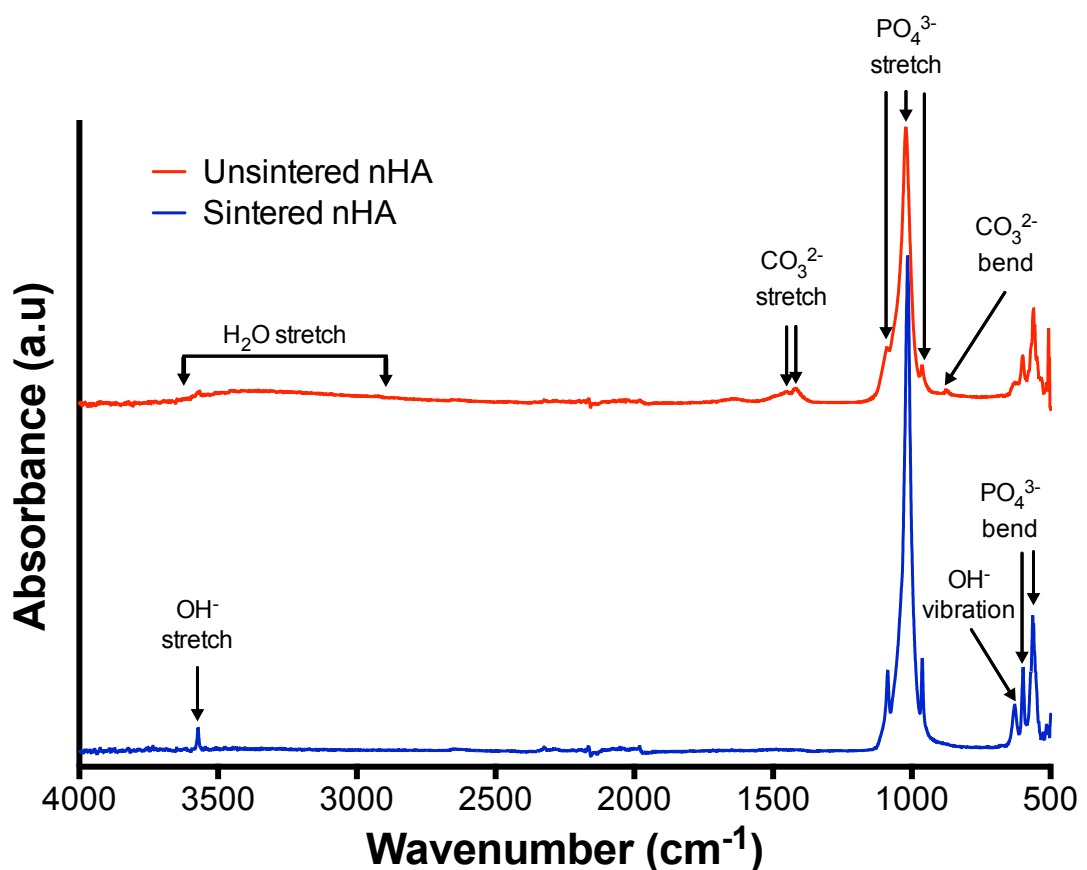
Figure 6.2: FTIR-ATR of unsintered and sintered nano-hydroxyapatite

A sharp peak present at 3571 cm^{-1}, caused by a hydroxyl stretch, was present for both samples [176]. The peak was more prominent in the sintered sample, as the peak at

3571 cm^{-1} in the unsintered sample was partially hidden by the broad water band between 2500 cm^{-1} and 3700 cm^{-1}. Another hydroxyl peak, formed from libration mode OH$^-$ vibrations occur at 634 cm^{-1} and was smallest in the unsintered sample. A reduction of OH$^-$ vibration in the unsintered sample could have been caused by the positioning of CO_3^{2-} ion substitutions within the lattice [176].

Carbonate bands appear in the unsintered nHA sample at 1420 cm^{-1} and 1457 cm^{-1} which are produced via asymmetric stretching ν_3 vibrational mode, and a further band at 870 cm^{-1} which is caused by out of plane bending ν_2 vibrational mode of CO_3^{2-} groups [176], [175]. Carbonate bands between 1300 cm^{-1} and 1650 cm^{-1} are produced by surface carbonate ions and do not originate from inside the crystal lattice [176]. The peaks at 1420 cm^{-1} and 1457 cm^{-1} are likely to originate from CO_2 dissolved from the atmosphere during synthesis due to the high alkalinity of the nHA precipitate solution. The precipitate solution would have plenty of OH$^-$ ions with which the CO_2 could react with [174].

Both spectra have three prominent phosphate bands positioned at 963 cm^{-1}, ~1020 cm^{-1} and ~1090 cm^{-1}. Peaks around 1020 cm^{-1} and 1090 cm^{-1} are formed via ν_3 PO anti-symmetric stretch vibrations, and the peak at 963 cm^{-1} is produced by ν_1 mode symmetric stretching vibration of PO [176]. The most intense absorption peak for both samples occurs around 1020 cm^{-1}. Other phosphate bands appear at 561 cm^{-1} and 601 cm^{-1} and are formed from ν_4 OPO bending mode [176].

Overall the unsintered nHA sample exhibited the characteristic bands of a partially carbonated, hydrated hydroxyapatite. A lack of bands positioned between 700 – 750 cm^{-1} is an indication that no calcium carbonates have formed [174]. The sintered nHA sample had the characteristic spectra of a highly pure and crystalline hydroxyapatite. Therefore, the nHA has been synthesised to a high level of purity.

6.2.1.3   nHA Transmission Electron Microscopy

Images were taken of the unsintered nHA using transmission electron microscopy to approximate morphology and size of the precipitated particles (Figure 6.3). The nHA

had a mixture of rod-like and rounded morphologies, however, the majority of the particles were mainly rod shaped with a long and a short axis. The average length of the long axis was 31 nm (± 9 nm std. deviation) and the average length of the short axis was 12 nm (± 3 nm std. deviation). Sizes ranged from 13 nm to 55 nm along the long axis and 3 nm to 24 nm along the short axis. The size of the particles is sufficiently small enough to prevent blockages from occurring during printing.
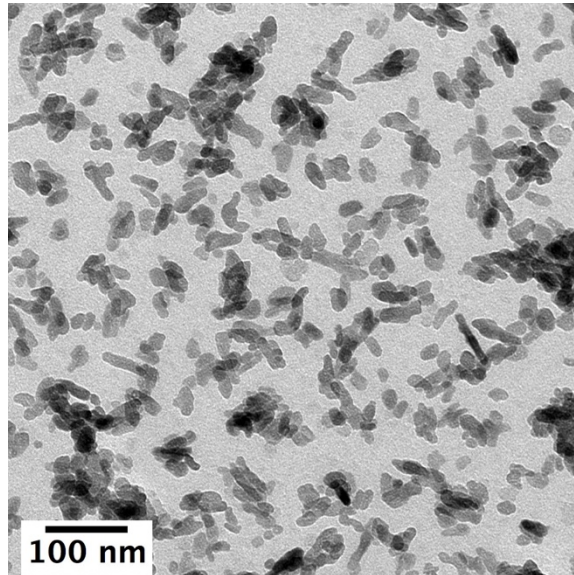
Figure 6.3: TEM image of unsintered nano-hydroxyapatite

6.2.2   nHA/RSF Film Characterisation

High density nHA scaffolds have been used to induce bone growth, however they suffer from poor mechanical properties [177]. Including nHA within the RSF film structure could provide a more durable osteoinductive film which has a controllable degradation rate. This results section will evaluate the effect of the inclusion of nHA within the RSF ink. It will begin by investigating if the presence of nHA affects the transition of silk I to silk II, which will be followed by an analysis of the relationship between nHA concentration and degradation rate of the nHA/RSF films.

6.2.2.1   *nHA/RSF Film FTIR-ATR*

nHA/RSF films were produced with different dried weight concentrations of nHA; namely 100 %, 75 %, 50 % and 25 %, where 100 % is pure nHA. From this point on, each film will be referred to based upon its nHA content, e.g. nHA/RSF film 100 %.

Films were printed with a 1:1 vol% ratio of RSF to methanol (equivalent to RSF film 50 %). A ratio of 1:1 RSF to methanol was chosen as it gave a suitable baseline with which to compare any changes brought on by the inclusion of nHA. In the previous chapter (Chapter 5: Inkjet Printing of Regenerated Silk Fibroin), RSF film 50 % had a mid ranged crystallinity compared to the other RSF films as well as losing a large proportion of mass without completely degrading during the degradation study. FTIR-ATR was performed on the nHA/RSF films to determine if the inclusion of nHA within the RSF ink had affected the transformation of silk I to silk II. The FTIR spectra for RSF film 50 % (Chapter 5: Inkjet Printing of Regenerated Silk Fibroin Films) has been used as a comparison to the nHA/RSF films and will be referred to as nHA/RSF film 0 %.

The FTIR-ATR spectra showed characteristic peaks for hydroxyapatite, however, not all the peaks were observable as they were hidden behind bands associated with silk fibroin. All of the nHA/RSF films had a broad band between $2500 - 3700$ cm^{-1} indicating the presence of water, and hence a hydrated structure. The hydroxyl stretch at 3571 cm^{-1} was largely hidden by the water bands as well as by the amide A and B bands of silk fibroin. The most prominent hydroxyapatite bands were the phosphate bands, positioned around 1090 cm^{-1}, 1020 cm^{-1} and 960 cm^{-1}.

The spectra had prominent amide A and B bands ($2800 - 3600$ cm^{-1}), as well as amide I ($1600 - 1700$ cm^{-1}), amide II ($1480 - 1570$ cm^{-1}) and amide III ($1200 - 1350$ cm^{-1}) bands associated with the RSF. The amide A and B bands, formed from NH stretching, had a similar shape with a prominent peak centred at 3275 cm^{-1} for all of the nHA/RSF films that included RSF within the film (nHA/RSF films 75 %, 50 %, 25 % and 0 %).

Figure 6.4 is a select region of the FTIR spectra focusing on the most well defined regions of interest, including the amide I, II and II regions of the silk as well as the most prominent HA phosphate bands. For the nHA/RSF films which included nHA (all except nHA/RSF film 0 % which was pure RSF), the amide I band was centred on a peak of 1640 cm^{-1} which is associated with a non-crystalline silk I structure. There

was no peak positioned at 1620 cm^{-1} which would have indicated the presence of β-sheet and a silk II structure. The amide II band had peaks at both 1535 cm^{-1} and 1515 cm^{-1}, although was slightly inclined towards the silk II peak. The silk II peak at 1515 cm^{-1} was the most prominent for nHA/RSF film 0 %. The presence of both peaks indicate that both silk I and silk II structures were present with a slight prevalence of silk II structure. The band at 1515 cm^{-1} is associated to a the ring CC stretch and CH bend of Tyrosine [164], which, as discussed in the previous chapter (Chapter 5: Inkjet Printing of Regenerated Silk Fibroin Films, **page 78**), is an indication of β-strand packing density. As the β-strand packing becomes more dense, a lack of chain mobility causes an increase of the band at 1515 cm^{-1} [166]. As this band has a similar absorbance intensity to that of the peak at 1535 cm^{-1} it shows that the RSF molecules have plenty of mobility. As the films were printed with a 1:1 vol% ratio of RSF to methanol it would be expected that the RSF would have a largely silk II structure as seen in nHA/RSF film 0 %, however this has not been observed with the other nHA/RSF films. The presence of nHA within the RSF solution could be acting as a barrier between the methanol and the RSF, by limiting the methanol interaction with the RSF before the methanol evaporates.
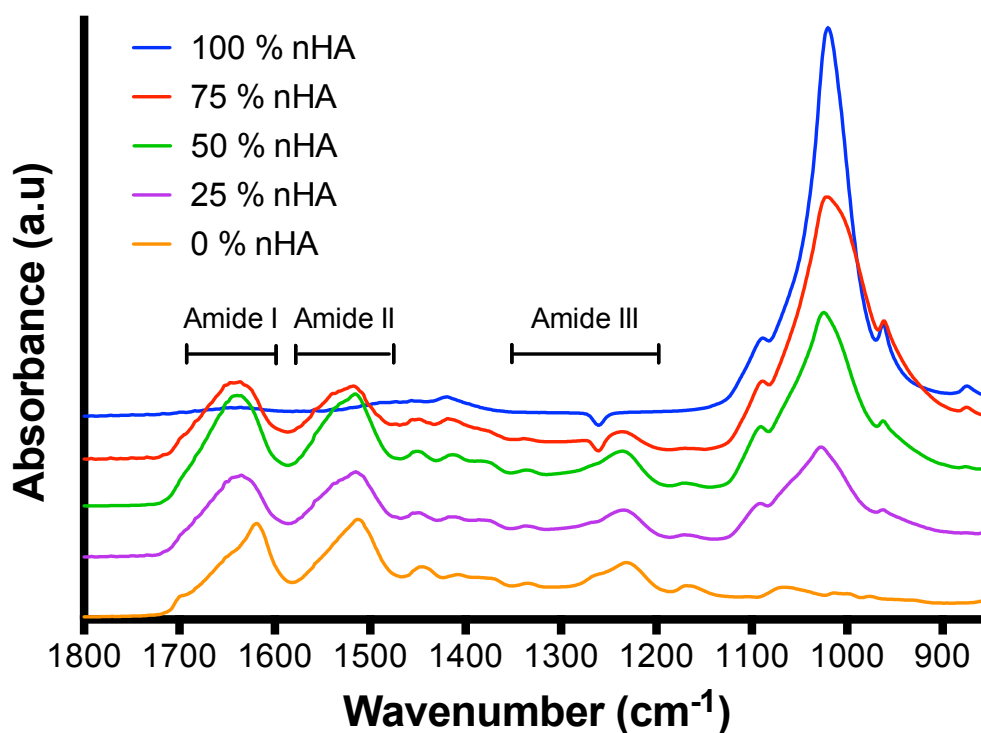
Figure 6.4: FTIR-ATR spectra of nHA/RSF films with different concentrations of nHA

Within the amide III band there appears a negative band positioned at 1260 cm^{-1} for nHA/RSF films with a high content of nHA (nHA/RSF films 100 % and 75 %). The negative band prevents a comparison between the silk I band (positioned at 1256 cm^{-1}) to the silk II band (positioned at 1235 cm^{-1}) within the amide III region. However, all nHA/RSF films with RSF content (nHA/RSF films 75 %, 50 %, 25 % and 0 %) have a peak positioned at 1235 cm^{-1} indicating the presence of an unordered silk I structure.

Ratios of the silk I (1640 cm^{-1} and 1535 cm^{-1}) and silk II (1620 cm^{-1} and 1515 cm^{-1}) absorbance peak intensities were calculated and are compared in Table 14. The ratio of silk II to silk I within the amide I region show that nHA/RSF films 75 % and 50 % had a similar structure, whilst nHA/RSF film 25 % had a slightly higher content of silk II. Within the amide II region there is a gradual increase of the silk II band with decreasing concentration of nHA, which would indicate that the RSF molecules were becoming more densely packed. However, nHA/RSF film 0 % consistently had a larger proportion of silk II than the other nHA/RSF films.

Table 14: Ratio of silk II to silk I band intensities within the amide I and amide II region for nHA/RSF films

% nHA	A_{1620}/A_{1640} Silk II/ Silk I	A_{1515}/A_{1535} Silk II/ Silk I
75	0.80	1.08
50	0.80	1.12
25	0.86	1.14
0	1.36	1.27

The RSF content of the nHA/RSF films appears the have a predominantly unordered silk I structure, contrary to what would be expected when printing with a 1:1 RSF to methanol vol% ratio, as seen with nHA/RSF film 0 %. Thus, an unordered RSF structure could be an indication that the presence of nHA was disrupting the transition of silk I to silk II, possibly by obstruction, preventing the methanol from infiltrating the RSF structure before it evaporated.

To determine what the RSF secondary protein structure was comprised of, Fourier self-deconvolution (FSD) was performed on the amide I region of the nHA/RSF films. Figure 6.5 shows the FSD data for the nHA/RSF films as well as for comparison, pure RSF films 100 % and 50 % which had a 1:0 and 1:1 vol% ratio of RSF to methanol. As the RSF within the nHA/RSF films was seen to be mainly unordered silk I (even though it had been exposed to methanol), the structural contributions of the fibroin protein secondary structures may differ from the primarily silk I structure of RSF film 100 %, and a ratio of 1:0 (i.e. the film that had had no methanol treatment).
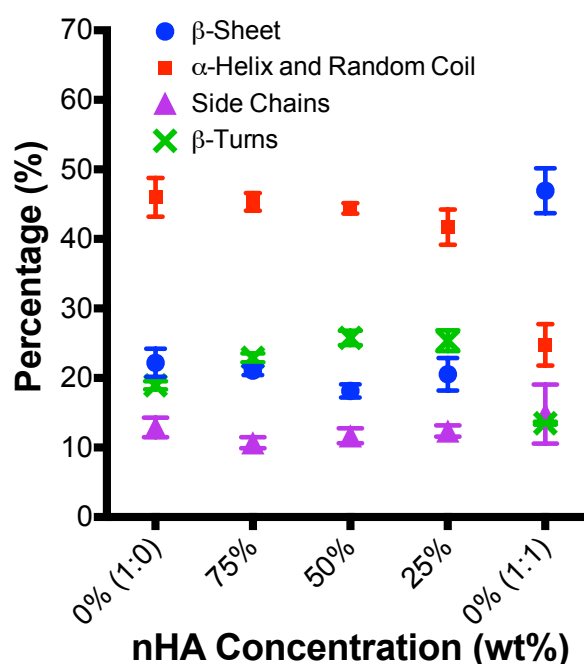
Figure 6.5: FSD data of amide I protein secondary structures for nHA/RSF films. Films of 0 % are representative of pure RSF films, whereby 0 % (1:0) is RSF film 100 %, and 0 % (1:1) is RSF film 50 %. Standard deviation of measurements made over four different FWHM values is shown.

As can be seen from Figure 6.5, β-sheet content remained around 20 % for all of the nHA/RSF films, similar to that of RSF film 100 % which has had no methanol exposure. All films were shown to have a very unordered RSF structure with a high proportion of α-helix, random coil and β-turns. Although visually the proportion of α-helix appears to decrease with decreasing percentages of nHA, there were no significant differences of α-helix between the nHA/RSF films. The amount of β-turns within the

RSF structure was significantly higher for all of the nHA/RSF films in comparison to RSF films 100 % and 50 % (nHA/RSF films 0 % 1:0 and 1:1). Previously, Yamane *et al.,* suggested that β-turns are a precursor to β-sheet structure formation and that the transition can occur more readily in a hydrated structure due to a higher mobility and relaxation of the β-turns [178]. This is supported by Wilson *et al.* who created a model amorphous fibroin peptide chain, which, when exposed to methanol, gradually transitioned into a crystalline silk II structure. During the transition, an intermediate state appeared which consisted of a high proportion of β-turns [88]. This could suggest that although the methanol did not induce a complete transition of the silk I into silk II, a partial transition occurred.

In the previous chapter (Chapter 5: Inkjet Printing of Regenerated Silk Fibroin Films, **page 81**) it was observed that even the smallest volume of methanol would cause a significant transformation of the RSF structure. RSF film 100 % had a β-sheet content of 22 %, which increased to 44 % with the addition of the smallest volume of methanol, as seen for RSF film 75 %, and remained around this concentration up until a higher methanol concentration of RSF film 50 %. No transition occurred for any of the nHA/RSF films even though they had been produced with an RSF to methanol vol% ratio of 1:1 (equivalent to RSF film 50 %). As none of the nHA/RSF films developed a crystalline structure, it is most likely that it is the presence of the nHA within the ink, rather than different volumes of methanol, which has prevented the transition of silk I to silk II.

6.2.2.3   nHA/RSF Film Topography

The surface roughness of the nHA/RSF films was measured using interferometry to determine if the concentration of the nHA affected the surface topography. nHA/RSF film roughness values are shown in Figure 6.6. No significant differences were measured between any of the nHA/RSF films, although the average roughness values for nHA/RSF films 25%, 50 %, 75 % and 100 %, were lower than that of the pure RSF film (nHA/RSF film 0%). Therefore, increasing the amount of nHA within the films does not affect the film micro-topography.
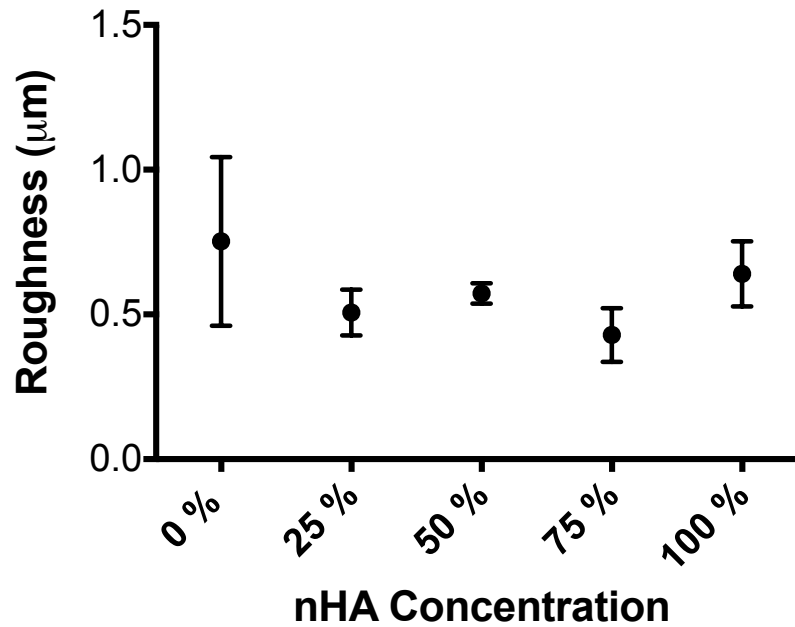
Figure 6.6: nHA/RSF film surface roughness values. Significant differences of three measurements is shown

6.2.3 Degradation Studies

6.2.3.1 *Mass Loss*

The degradation behaviour of the nHA/RSF films was studied and compared in either an enzymatic solution of protease XIV or in a phosphate buffered saline (PBS) solution over an 8-day period, the results of which are shown in Figure 6.7 and Figure 6.8. Investigating the degradation of the nHA/RSF films will help to determine if the addition of nHA has changed the degradation rate.

6.2.3.1.1 Protease Degradation Mass Loss

nHA/RSF film 100 % had initially no significant mass loss over the first two days degraded in a protease XIV solution (Figure 6.7). Between days 2 and 3 the film lost the equivalent of 21 % ($p<0.0001$) of initial mass, followed by a 14 % loss ($p<0.05$) between days 3 and 5, and finally 27 % ($p<0.0001$) lost between days 5 and 8. As nHA/RSF film 100 % had no RSF incorporated within the film, it is likely that any degradation was due to the nHA being washed off into the surrounding solution rather than related to protease activity.
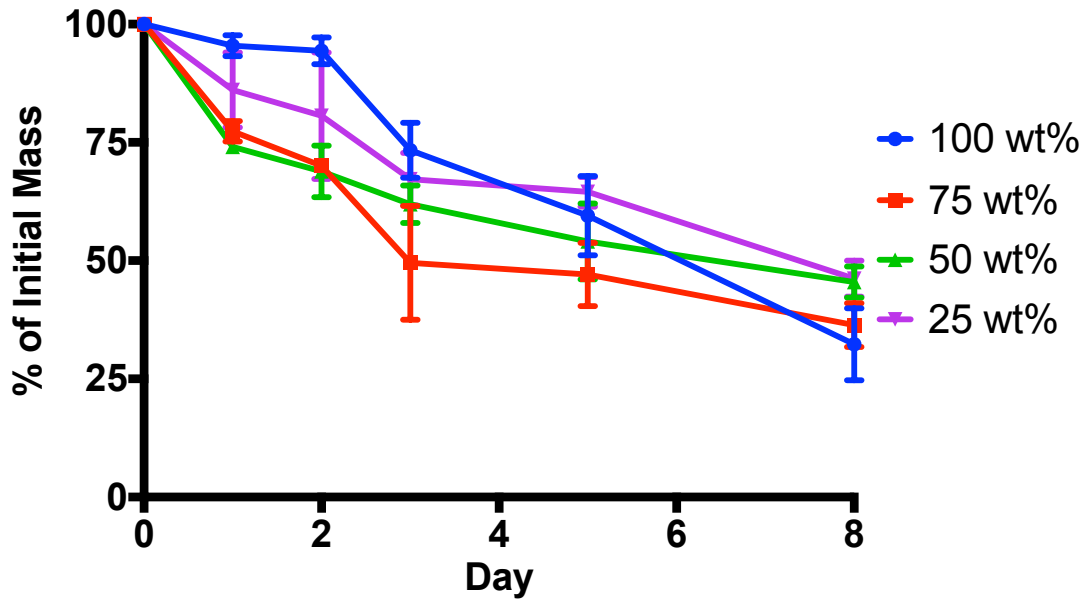
Figure 6.7: Degradation mass loss for nHA/RSF films with different concentrations of nHA degraded in a Protease XIV solution over an 8-day period. Standard deviation of three measurements is shown.

A significant mass loss was observed for nHA/RSF film 75 % over the first 24 hours when degraded in protease XIV (Figure 6.7). By the first day, nHA/RSF film 75 % had lost 23 % ($p<0.0001$) of its initial mass. Between days 1 and 2 there was no significant change in mass despite its average mass dropping by a further 7 % of its initial mass. Between days 2 and 3 there was a significant reduction as the film lost 20 % ($p<0.001$) of its initial mass. This reduction was followed by no significant differences of mass lost between sequentially remaining time points. Between days 3 and 5, there was a 2 % mass loss, and between days 5 and 8, there was an 11 % mass loss.

nHA/RSF film 50 % experienced its largest mass loss over the first 24-hour period (Figure 6.7). By the first day, the film had lost 26 % ($p<0.0001$) of its initial mass. After the first day, the degradation rate of the film slowed down so that between sequential time points there was no significant difference in mass loss. Between day 1 and 2 there was a 5 % mass loss, followed by a 7 % mass loss between days 2 and 3, an 8 % mass loss between days 3 and 5, and finally a 9 % mass loss between days 5 and 8.

After 1 day degraded with protease XIV, nHA/RSF film 25 % had lost 14 % (p<0.05) of its initial mass (Figure 6.7). By day 2 there had been no significant change in mass with an average mass loss of 5 %. Between days 2 and 3, the equivalent of 13 % (p<0.05) of its initial mass was lost. Between days 3 and 5 there was no significant change in mass, followed by a mass loss of 18 % (p<0.01) between days 5 and 8.

After 8 days degraded in a protease XIV solution, all nHA/RSF films had lost a significant proportion of their initial mass. All of the nHA/RSF films had similar masses, apart from nHA/RSF film 100% which had a significantly lower mass than the nHA/RSF films 50 % and 25 % (p<0.05). Films with the highest to lowest masses were as follows: nHA/RSF film 25 % > 50 % > 75 % > 100 %, with equivalent masses proportional to their initial weight of 46 %, 45 %, 36 % and 32 % respectively, the potential reasons for this behaviour will be discussed shortly.

6.2.3.1.2   PBS Degradation Mass Loss

nHA/RSF film 100 %, when degraded in PBS, lost 27 % (p<0.0001) of its initial mass over the first 3 days, however had no significant difference between sequential time point, losing 5 % between day 0 and day 1, 8 % between days 1 and 2, and 14 % between days 2 and 3 (Figure 6.8). Between days 3 and 5 the mass remained relatively stable with no significant changes. The largest mass loss occurred between days 5 and 8 where the nHA/RSF film lost 35 % (p<0.0001) of its initial mass.
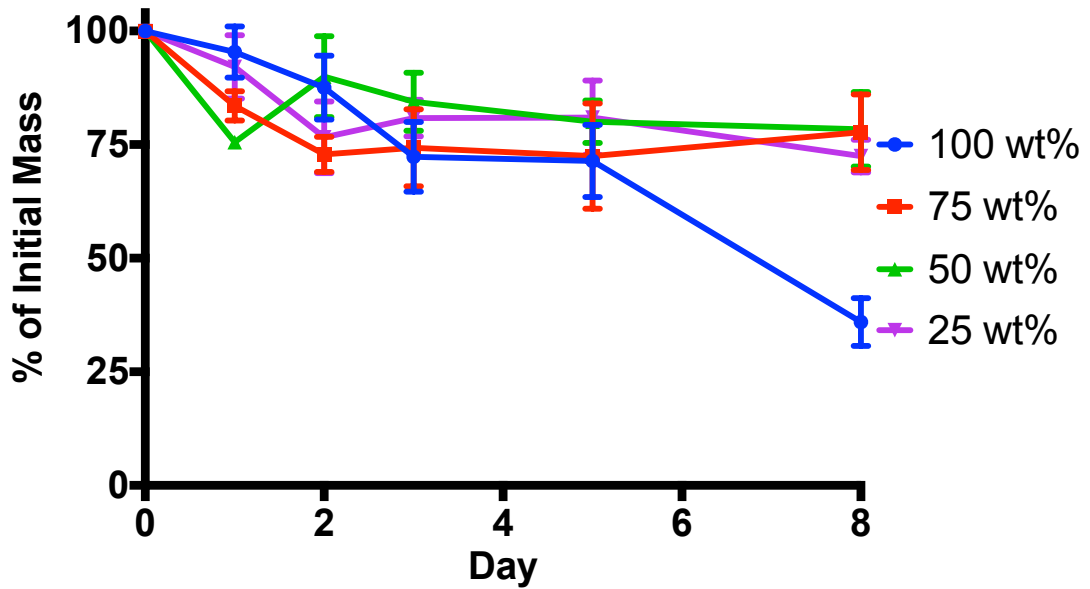
Figure 6.8: Degradation mass loss for nHA/RSF films with different concentrations of nHA degraded in a PBS solution over an 8-day period. Standard deviation of three measurements shown.

After 1 day degraded in PBS, nHA/RSF film 75 % had lost 16 % (p<0.05) of its initial mass. After the first day it had no significant changes in mass between sequential time points. Between days 1 and 2, the average mass decreased by a further 11 % of the initial mass. Between days 2 and 8 there were minor fluctuations in the average mass of the films which accumulated in an average increase of 4 % mass. Overall the film lost a total of 22 % (p<0.01) of its initial mass over the 8-day period.

nHA/RSF film 50 % lost 24 % (p<0.001) of its initial mass over the first 24-hour period. This was followed by a 14 % increase between days 1 and 2. There was no significant differences between the following sequential time points which experienced a gradual mass loss of 6 % between days 2 and 3, 4 % between days 3 and 5, and 2 % between days 5 and 8.

There was no significant mass loss observed for nHA/RSF film 25 % over the initial 24 hours degraded in PBS (Figure 6.8). By the first day the film had lost 8 % of its initial mass, followed by a further 16 % (p<0.05) between days 1 and 2. Between days 2 and 3 there was a slight increase of 4 %, no change in mass between days 3 and 5, and finally an 8 % mass loss between days 5 and 8.

Overall, the nHA/RSF films degraded in PBS lost significantly less mass compared to nHA/RSF films degraded with protease XIV. nHA/RSF film 100 % was the only nHA/RSF film to experience similar mass losses when degraded in either solution. nHA/RSF film 100 % exhibited different degradation behaviour to that of the other nHA/RSF films when degraded in PBS, which could be because the film was formed from pure nHA whereas the other nHA/RSF films contained RSF. The RSF within the films acts as a binder, preventing the nHA from being washed away by the degradation solution and by PBS washes. nHA/RSF films 75 % and 50 % experienced the smallest mass loss, both finishing with an overall mass loss of 22 % (p<0.01). nHA/RSF film 25 % lost 28 % (p<0.0001) of its initial mass.

6.2.3.1.3   Mass Loss Discussion

As expected, the nHA/RSF films which included RSF within their structure, all experienced larger mass losses when degraded in the protease solution compared to the PBS solution. As observed in the previous chapter; Chapter 5: Inkjet Printing of Regenerated Silk Fibroin Films, RSF films exposed to the protease XIV solution were gradually degraded after an initially large mass loss experienced over the first 24 hours. Due to the nHA/RSF films having been shown to have a predominantly unordered structure through FTIR-ATR spectra and FSD, it was expected that the films would degrade with a similar rate to that of RSF film 100 %.

As the nHA/RSF films had a largely unordered water soluble silk I structure, they should have experienced substantial mass losses within the first 24 hours related to their RSF content. nHA/RSF film 25 %, which had the highest RSF concentration and hence the largest mass of unordered silk I, experienced a lower average mass loss within the first 24 hours than that of nHA/RSF films 50 % and 75 % (films with a lower RSF content and therefore less water soluble silk I structure).

After 8 days degraded with protease XIV, it appeared that films with the highest RSF content had the lowest degradation rates. Films with a higher nHA content would have been less susceptible to proteolytic degradation, yet experienced the largest

mass losses. Potentially the higher degradation rates of nHA/RSF films 50 % and 75 % could have been caused by the degradation of the RSF binding the nHA together. As the RSF degraded, it released the nHA embedded within it. The RSF of the nHA/RSF films had been shown to have similar levels of crystallinity, and would therefore have similar degradation rates. However, the more concentrated nHA films could have released larger quantities of nHA particles into the surrounding solution, which resulted in larger mass losses.

nHA/RSF films which had RSF within their structure, when degraded in PBS, experienced significantly lower mass losses that that of the nHA/RSF films degraded with a protease. Unlike RSF film 100 % (Chapter 5: Inkjet Printing of Regenerated Silk Fibroin Films, **page 88**), which was also shown to have a predominantly unordered structure, none of the nHA/RSF films completely dissolved/ degraded over the 8-day period. nHA/RSF film 100 %, which had no RSF within its structure, experienced the largest mass loss. As there was no RSF within the structure, there was nothing binding the nHA crystals together, which, during the washing of the films, could have been released into the solution.

The relative mass losses of the nHA/RSF films degraded in either a protease XIV or PBS solution, show, that although the initial RSF structure was mainly comprised of water soluble silk I, degradation did not occur similarly to a pure RSF film with a similar structure. This would either indicate that there was a higher proportion of non-water soluble silk present within the films, or, that the presence of nHA within the RSF was affecting degradation rates.

6.2.3.2 *Degradation FTIR-ATR*

Because the nHA/RSF films had not completely degraded over the course of the degradation study, the RSF within the films may not have had an entirely unordered and water soluble structure as suggested by the FTIR-ATR spectra on day 0. To determine how the RSF structure changed during the course of the degradation study, FTIR-ATR was performed on the nHA/RSF films at each time point. As this section is investigating RSF structural changes due to degradation, the results of this

section are focused on nHA/RSF films 75 %, 50 % and 25 %, which contained RSF. This section will begin with a commentary of the different spectra before concluding with a discussion of the results.

6.2.3.2.1 Protease Degradation

The results of this section are of interest because the FTIR-ATR spectra of the RSF within the nHA/RSF films will highlight any structural changes which may offer an explanation as to the lower degradation rates experienced by the films when degraded in a proteolytic solution. To measure the changing proportions of RSF silk I and silk II structure, ratios of the silk II to silk I absorbance peak intensities are recorded and compared in Table 15 and Table 16. These two tables are presented below and will be referred to when discussing each of the degradation FTIR spectra in Figures 49, 50 and 51.

Table 15: Ratio of silk II to silk I bands (A_{1620} / A_{1640}) within the amide I region for nHA/RSF films degraded in protease XIV, where 75 % represents an nHA/RSF film which has a starting concentration of 75 % nHA and 25 % RSF

nHA/RSF	A_{1620}/A_{1640} on Day					
Film	0	1	2	3	5	8
75 %	0.82	1.32	1.43	1.38	1.34	1.34
50 %	0.82	1.17	1.09	1.21	1.10	1.14
25 %	0.88	1.38	1.48	1.43	1.33	1.44

Table 16: Ratio of silk II to silk I bands (A_{1515} / A_{1535}) within the amide II region for nHA/RSF films degraded in protease XIV, where 75 % represents an nHA/RSF film which has a starting concentration of 75 % nHA and 25 % RSF

nHA/RSF	A_{1515}/A_{1535} on Day					
Film	0	1	2	3	5	8
75 %	1.08	1.17	1.24	1.23	1.15	1.15
50 %	1.12	1.12	1.07	1.11	1.08	1.12
25 %	1.14	1.18	1.20	1.21	1.16	1.16

On day 0, the amide I region for the nHA/RSF film 75 %, was centred on a silk I peak of 1640 cm^{-1} (Figure 6.9). After 24 hours in a protease solution the silk I band

positioned at 1640 cm^{-1} reduced in intensity and the entire amide I band shifted towards a silk II peak position of 1620 cm^{-1}. Another indication of a silk II structure is the formation of a band at 1697 cm^{-1} which is related to a β-sheet structure. By day 2 the intensity of the band at 1620 cm^{-1} had increased to its highest intensity, and continued to decrease in size over the remaining time points. The ratio of the silk II to silk I peak intensities show a large increase of silk II over the first 24 hours, with an increase in ratio from 0.82 to 1.32, followed by an increase up to 1.43 by day 2 (Table 15), suggesting that the RSF became more crystalline. The ratio gradually reduces between days 2 and 5, and remains at a ratio of 1.34 for days 5 and 8.

Figure 6.9: FTIR-ATR of nHA/RSF films 75 %, within the amide I and II regions, degraded in a solution of protease XIV. Brackets represent the degradation time point in days. Solid vertical lines mark the position of silk I bands and dotted vertical lines mark the position of silk II bands.

The amide II region of nHA/RSF film 75 %, on day 0, consists of a broad band with peaks positioned at 1535 cm^{-1} and 1515 cm^{-1}, with a slightly higher intensity for the silk II peak at 1515 cm^{-1}. After 24 hours degraded with protease XIV, the silk I band has reduced in size giving the amide II band a predominantly silk II shape. Over the course of the remaining days, the amide II band remains in a similar shape, reducing in intensity proportionally to the amide I band. Ratios of the silk II to silk I band

intensities within the amide II region show a gradual increase of silk II between days 0 and 2, from 1.08 to 1.24 (Table 16). This shows that the RSF was becoming more crystalline with denser β-sheet stacking. Between days 2 and 3 the ratio remained similar before reducing to 1.15 for days 5 and 8, indicating that the RSF crystal structure had become slightly less dense.

nHA/RSF film 50 % on day 0, had an amide I band centred around 1640 cm^{-1} showing that the RSF had mainly a silk I structure (Figure 6.10). By day 1, the amide I band had shifted with the formation of a predominant peak at 1620 cm^{-1}, whilst the band at 1640 cm^{-1} had reduced in intensity. A small band has also formed at 1697 cm^{-1} and remained at a consistent size over the course of the degradation study. Over the remaining days, the silk II band decreased in proportion to the silk I band.

Figure 6.10: FTIR-ATR of nHA/RSF films 50 %, within the amide I and II regions, degraded in a solution of protease XIV. Brackets represent the degradation time point in days. Solid vertical lines mark the position of silk I bands and dotted vertical lines mark the position of silk II bands.

The ratio of silk II to silk I band intensities for nHA/RSF film 50 %, within the amide I region, show the transition of a predominantly silk I to silk II structure between days 0 and 1 (Table 15). However, the ratio of silk II to silk I remains relatively low in

comparison to the other nHA/RSF films degraded in protease at each time point. This shows that although the structure has become more crystalline, there is still a high proportion of unordered silk within the RSF structure. The amide II band at all time points had bands positioned for silk I at 1535 cm^{-1} and for silk II at 1515 cm^{-1}. The ratio of silk II to silk I within the amide II region shows that the RSF molecules had a similar mobility at each time point with a relatively consistent crystal density.

The FTIR-ATR spectra for nHA/RSF film 25 %, when degraded with protease XIV shows a transition from a predominantly silk I structure to a predominantly silk II structure over the first 24 hours (Figure 6.11). On day 0 the amide I band is centred around 1640 cm^{-1}, which by the first day, has reduced in intensity whilst a large band has formed at 1620 cm^{-1}, as well as a small peak at 1697 cm^{-1}. The silk II band at 1620 cm^{-1} continues to grow larger between days 1 and 2 before gradually reducing in intensity over the remaining time points.
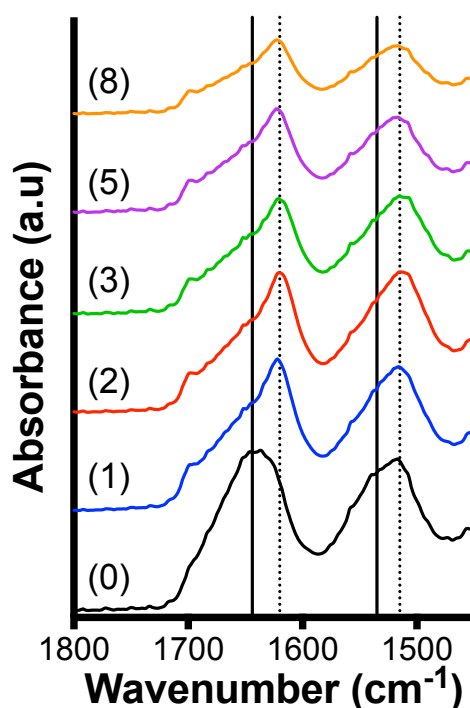

Figure 6.11: FTIR-ATR of nHA/RSF films 25 %, within the amide I and II regions, degraded in a solution of protease XIV. Brackets represent the degradation time point in days. Solid vertical lines mark the position of silk I bands and dotted vertical lines mark the position of silk II bands.

Ratios of the silk II to silk I peak intensities show a significant increase over the first 24 hours, which continues to increase until day 2, reaching a maximum ratio of 1.48 (Table 15). The ratio steadily reduces between days 2 and 5, before increasing significantly again on day 8. The amide II region had a gradual increase of the silk II band at 1515 cm^{-1} between days 0 and 1, and remains a similar shape until day 8, where the intensity of the entire amide II band reduces. An initial increase of crystallinity within the amide II region occurs over the first 24 hours is shown by an increase in the ratio of silk II to silk I band intensities (Table 16).

6.2.3.2.2 PBS Degradation

The nHA/RSF films degraded in PBS experienced a small mass loss over an 8-day period compared to the dissolution of the pure RSF film with a similar structure (RSF film 100 %) which had completely dissolved. Instead the nHA/RSF films had similar degradation profiles to that of RSF films which had been exposed to methanol (as had the nHA/RSF films) despite initially having a largely silk I structure. Changes to the RSF structure during degradation could show why the films only lost a small amount of mass. Absorbance intensity ratios of the silk II to silk I peaks for films degraded in PBS are shown in Table 17 and Table 18 and will be referred to when discussing each of the degradation FTIR spectra in Figures 52, 53 and 54.

Table 17: Ratio of silk II to silk I bands (A_{1620}/ A_{1640}) within the amide I region for nHA/RSF films degraded in PBS, where 75 % represents an nHA/RSF film which has a starting concentration of 75 % nHA and 25 % RSF

nHA/RSF Film	A_{1620}/A_{1640} on Day					
	0	1	2	3	5	8
75 %	0.82	1.25	1.27	1.33	1.14	1.21
50 %	0.82	0.92	1.17	1.09	1.04	1.12
25 %	0.88	1.45	1.40	1.37	1.26	1.43

nHA/RSF	A$_{1515}$/A$_{1535}$ on Day					
Film	0	1	2	3	5	8
75 %	1.08	1.14	1.19	1.17	1.18	1.17
50 %	1.12	1.12	1.12	1.13	1.09	1.14
25 %	1.14	1.22	1.21	1.20	1.15	1.18

nHA/RSF film 75 % degraded in PBS, had by the first day developed silk II peaks positioned at 1620 cm^{-1} and at 1697 cm^{-1} (Figure 6.12) whilst the silk I peak had reduced in intensity. By day 2, the silk II peak had grown larger, whilst the silk I peak intensity remained similar. Over the remaining days, both peaks became smaller and less pronounced. The ratio of silk II to silk I peak intensities of the amide I region show that there is a large increase in silk II by the first day, which continues to increase until day 3, with a ratio of 1.33 (Table 17). Between days 3 and 5 the ratio dropped to 1.14, before rising again to 1.21 on day 8.
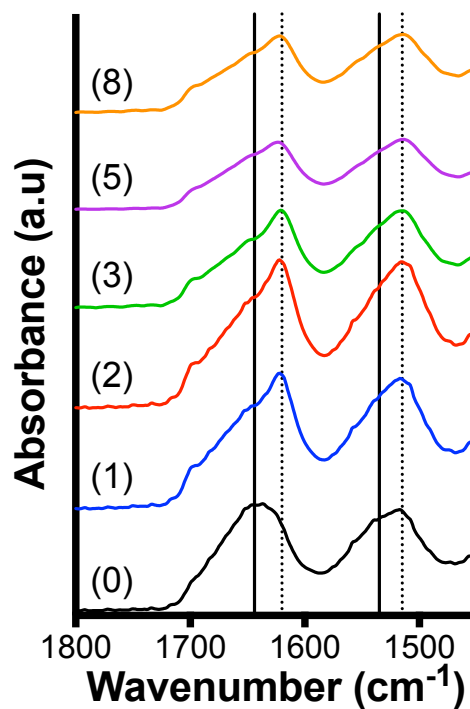
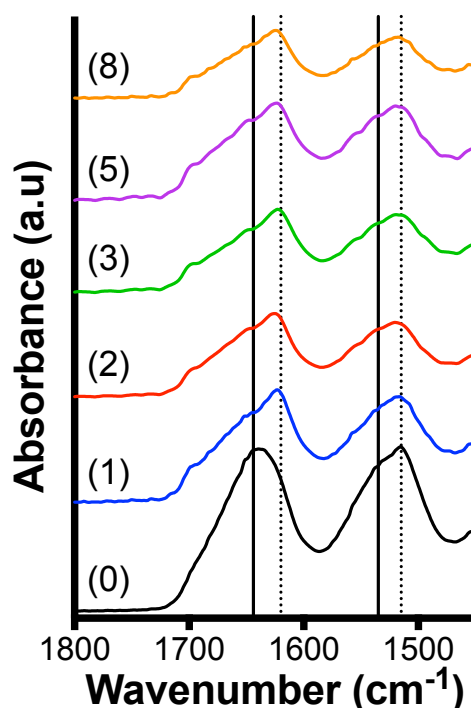*Figure 6.12: FTIR-ATR of nHA/RSF films 75 %, within the amide I and II regions, degraded in PBS. Brackets represent the degradation time point in days. Solid vertical lines mark the position of silk I bands and dotted vertical lines mark the position of silk II bands.*

Within the amide II region of nHA/RSF film 75 %, on day 0, had silk I and II peaks positioned at 1535 cm^{-1} and 1515 cm^{-1} respectively (Figure 6.12). The intensity of the silk II peak is slightly higher. By the first day, the intensity of the silk II peak had slightly increased so that the amide II band was prominently positioned around the 1515 cm^{-1} peak. The amide II region had a similar shape for days 1, 2 and 3, and then began to reduce in intensity for days 5 and 8. Ratios of the silk II to silk I peaks within the amide II region show that over the first 24 hours there was a slight increase in crystallinity which remained at a similar ratio for the remainder of the degradation test (Table 18).

The amide I band for the nHA/RSF film 50 % degraded in PBS, saw a more gradual propagation of the silk II band positioned at 1620 cm^{-1} (Figure 6.13). On day 0, the amide I band had a predominantly silk I shape. By day 1, the amide I band was split between bands positioned at 1648 cm^{-1} (representative of silk I structure) and 1620 cm^{-1}, which were of a similar intensity, and gave the amide I band a flat top. By day 2 the silk II peak had grown, so that the amide I band shows a mainly silk II structure. Over the remaining days the silk II peak becomes less intense, but remains more prominent than the silk I peak.

Ratios of the silk II to silk I band intensities of nHA/RSF film 50 % show a gradual increase of silk II. nHA/RSF film 50 % is the only nHA/RSF film to have a higher proportion of silk I than silk II after one day degraded in PBS (Table 17). The ratios increase from 0.82, on day 0, to 0.92 on day 2, and reaches the highest ratio on day 3 with a ratio of 1.17. The ratio then reduces between days 2 and 5 to 1.04, before increasing to 1.12 on day 8. The amide II band has a slightly higher silk II peak at 1515 cm^{-1} than that of the silk I peak at 1535 cm^{-1} for all time points, and remains a similar shape for the duration of the degradation study. The ratio of the silk II to silk I peak intensities remains similar to the day 0 value of 1.12 for all time points (Table 18).

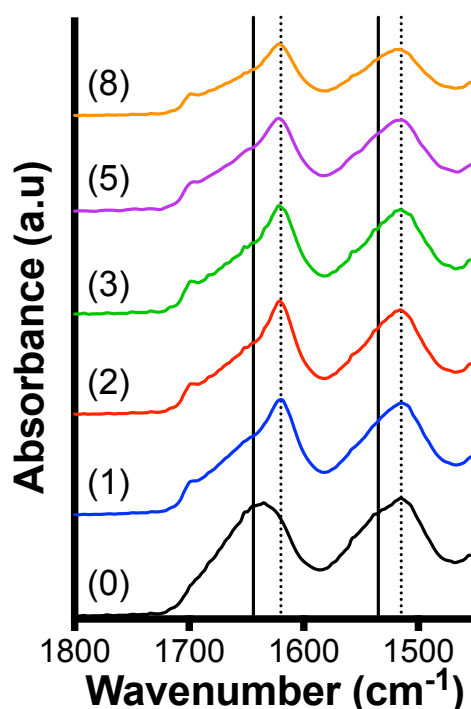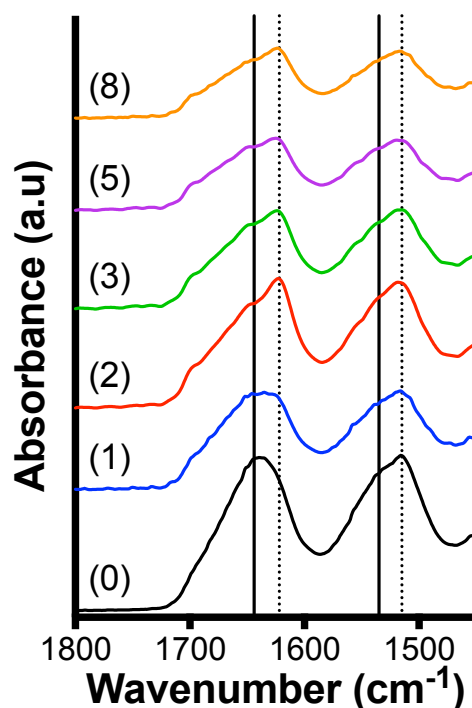*Figure 6.13: FTIR-ATR of nHA/RSF films 50 %, within the amide I and II regions, degraded in PBS. Brackets represent the degradation time point in days. Solid vertical lines mark the position of silk I bands and dotted vertical lines mark the position of silk II bands.*

nHA/RSF film 25 % developed a large silk II peak at 1620 cm^{-1} within the amide I region over the first 24 hours degraded in PBS (Figure 6.14). The silk II band gradually decreased in intensity over the remaining days. The silk I band positioned around 1640 cm^{-1} remained a similar shape for the duration of the degradation study. The ratio of silk II to silk I show that the nHA/RSF film rose from 0.88 to 1.45 over the first 24 hours (Table 17). The ratio gradually reduced to 1.26 by day 5, however by day 8 the ratio increased to 1.43. The amide II region saw an increase of the silk II peak positioned at 1515 cm^{-1} over the first 24 hours and remained a similar shape for the remaining time points. The ratio of silk II to silk I within the amide II region show an increase from 1.14 to 1.22 between day 0 and day 1, and remains around this ratio up until day 5 where the ratio drops to 1.15, and increases slightly to 1.18 by day 8 (Table 18).
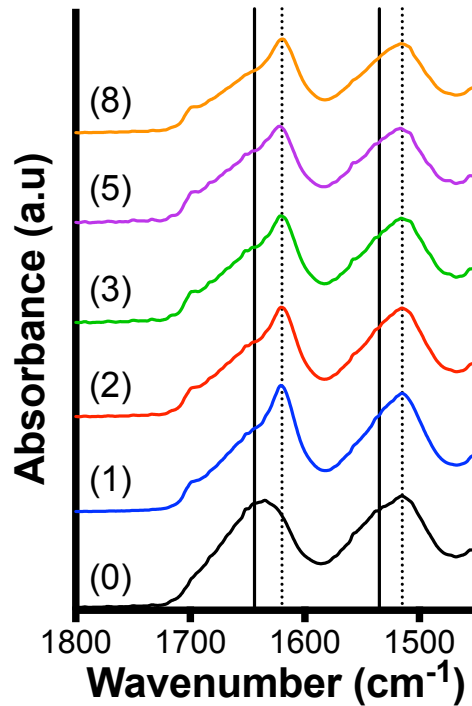
Figure 6.14: FTIR-ATR of nHA/RSF films 25 %, within the amide I and II regions, degraded in PBS. Brackets represent the degradation time point in days. Solid vertical lines mark the position of silk I bands and dotted vertical lines mark the position of silk II bands.

6.2.3.2.3 Discussion of the Degradation FTIR-ATR Results

During degradation in both protease XIV solution and in PBS, the FTIR-ATR spectra showed that the RSF within the nHA/RSF films became more crystalline by day 1. The films developed strong absorption bands for silk II within the amide I and II regions, which reached a maximum intensity within the first few days. Increased intensity of the peak 1515 cm^{-1} suggests that the RSF molecules were becoming more densely packed, or that the less dense crystalline regions were being degraded first.

nHA/RSF films degraded with protease XIV, had after the first day of degradation, similar spectra to that of RSF films exposed to methanol, despite initially showing a predominantly unordered structure. However, not all of the nHA/RSF films showed similar degradation FTIR-ATR spectra to the crystalline RSF films when degraded in PBS. nHA/RSF films 75 % and 25 % had similar FTIR-ATR spectra to that of the more crystalline RSF films, yet nHA/RSF film 50 % had a similar FTIR-ATR spectra to that of RSF film 100 % over the first 2 days of degradation (Chapter 5: Inkjet Printing of Regenerated Silk Fibroin Films, **page 94**).

Overall, nHA/RSF film 50 % was shown to have the lowest average silk II content of all the nHA/RSF films when degraded in either proteolytic or PBS solutions, whilst nHA/RSF film 25 % was shown to the highest average silk II content. This shows that the inclusion of nHA within the RSF films had made the crystal content of RSF unpredictable.

6.2.3.3   Degradation FSD

Fourier self-deconvolution (FSD) was performed on the amide I region for the FTIR-ATR spectra of the nHA/RSF films at each time point of the degradation study. The initial structural state of the RSF was comprised of a low percentage of β-sheet but with a higher proportion of β-turns in comparison to the pure RSF films. The β-turns may have been a precursor to β-sheet formation. During degradation the RSF within the nHA/RSF films was shown to transform from a largely silk I structure to a silk II structure. By performing FSD on the spectra the crystallinity of the films can be more precisely compared as well as changes in the proportion of β-turns. This section is written as a commentary followed by a discussion of the results.

6.2.3.3.1   Protease Degradation

nHA/RSF film 75 %, when degraded in protease rapidly increased in β-sheet content over the first two days (Figure 6.15), by 19 % after 1 day ($p<0.0001$); from 21 % to 40 %, to 49 % by day 2($p<0.0001$). β-sheet content then dropped by 4 % ($p<0.05$) between days 2 and 3, and then had no significant differences between the remaining days.

Figure 6.15: FSD data of amide I protein secondary structures for nHA/RSF film with 75 % nHA concentration, when degraded in a protease XIV solution for 8 days. Standard deviation of measurements made over four different FWHM values is shown.

The increase of β-sheet content for nHA/RSF film 75 %, over the first 2 days was accompanied by a decrease in α-helix and random coil structural content. By the first day there had been a decrease of 18 % ($p < 0.0001$) in the α-helix and random coil content, and a further 3 % decrease by day 2. Between days 2 to 8 there was no significant difference in α-helix and random coil structural content. The amount of β-turns also reduced over the first 2 days, dropping by 4 % ($p < 0.01$) by the first day, and by 3 % ($p < 0.05$) by the second day. After day 2 there were no significant differences in the amount of β-turns within the RSF structure. During 8 days of degraded in an enzymatic solution, nHA/RSF film 75 % increased in β-sheet content by 24 % ($p < 0.0001$), α-helix and random coil decreased by 18 % ($p < 0.0001$), β-turns decreased by 6 % ($p < 0.0001$), and side chain contributions remained consistent.

After 24 hours degradation with protease XIV, nHA/RSF film 50 % had increased in β-sheet content by 22 % ($p < 0.0001$) (Figure 6.16). Between days 2 and 5, there was a continuous drop in β-sheet content, accumulating to a total loss of 5 % ($p < 0.01$), which was followed by a 4 % ($p < 0.01$) increase between days 5 and 8.

Figure 6.16: FSD data of amide I protein secondary structures for nHA/RSF film with 50 % nHA concentration, when degraded in a protease XIV solution for 8 days. Standard deviation of measurements made over four different FWHM values is shown.

α-helix and random coil structural content, for nHA/RSF film 50 % decreased by 17 % (p<0.0001) over the first 24 hours, after which, there were no significant differences between each time point. There was a loss of structural contributions from β-turns by 8 % (p<0.0001) over the first 24 hours, with no significant difference between sequential time points for the remaining days. After 8 days being degraded in an enzymatic solution, β-sheet content had increased by 24 % (p<0.0001), α-helix and random coil structural content had decreased by 17 % (p<0.0001), β-turns had reduced by 8 % (p<0.0001), and there were no significant differences between side chain contributions.

nHA/RSF film 25 % when degraded in a protease XIV solution gained the largest proportion of β-sheet content by the first day (Figure 6.17). Over the first 24 hours, the amount of β-sheet content increased from 21 % to 48 % of the RSF secondary structure (p<0.0001). β-sheet content then decreased by 7 % (p<0.001) between days 1 and 2, increased by 5 % between days 2 and 3, and then remained similar over the remaining days.
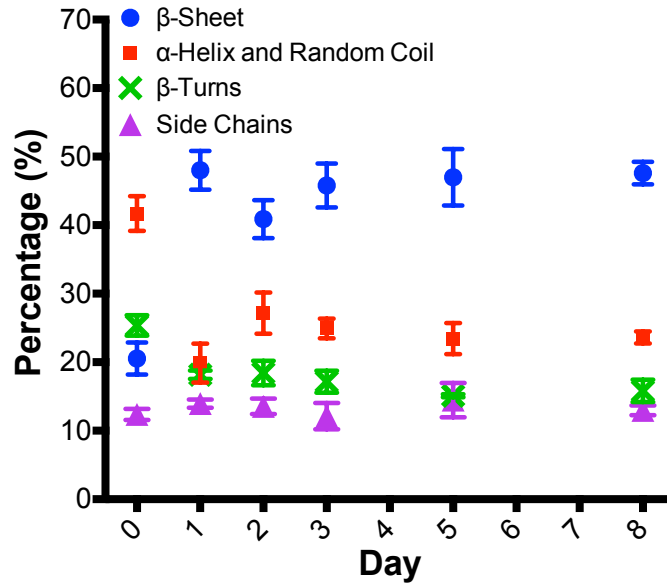
Figure 6.17: FSD data of amide I protein secondary structures for nHA/RSF film with 25 % nHA concentration, when degraded in a protease XIV solution for 8 days. Standard deviation of measurements made over four different FWHM values is shown.

α-helix and random coil structural content for nHA/RSF film 25 % decreased by 22 % (p<0.0001) over the first 24 hours, increased by 7 % (p<0.001) between days 1 and 2, and then remained similar between the following time points. β-turns reduced by 8 % (p<0.0001) by the first day and then remained similar between the remaining time points. There was no significant difference between side chain content at any of the time points. By the final day there had been an overall increase of β-sheet content by 27 % (p<0.0001), a loss of α-helix and random coil structural content of 18 % (p<0.0001) and a drop in β-turns by 10 % (p<0.0001).

6.2.3.3.2 PBS Degradation

nHA/RSF film 75 % when degraded in PBS had a significant increase of β-sheet content over the first 24 hours of 26 % (p<0.0001) (Figure 6.18). Between the following sequential days there were no other significant differences of β-sheet content.
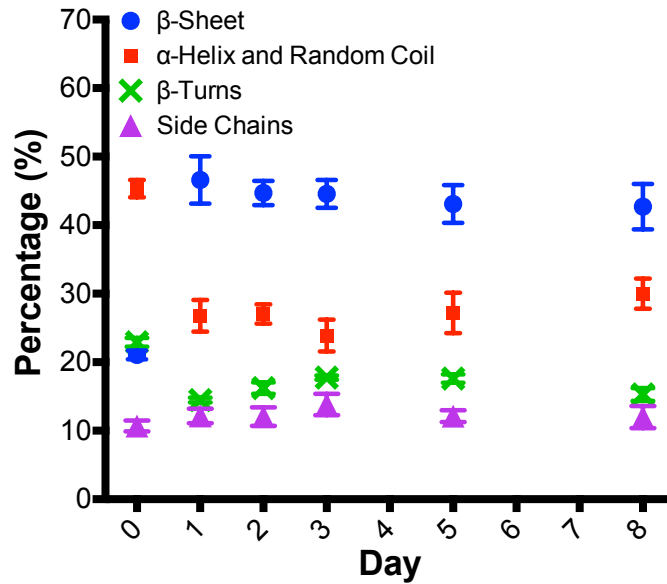
Figure 6.18: FSD data of amide I protein secondary structures for nHA/RSF film with 75 % nHA concentration, when degraded in PBS for 8 days. Standard deviation of measurements made over four different FWHM values is shown.

After the first day degraded in PBS, nHA/RSF film 75 % had α-helix and random coil structural content decrease by 19 % (p<0.0001). There was no significant difference in α-helix and random coil structural content between days 1 and 2, however between days 2 and 3 there was a 3 % (p<0.05) loss, followed by an increase of 3 % between days 3 and 5. There was no significant difference between days 5 and 8. β-turns reduced by 8 % (p<0.0001) by the first day and then remained similar between the remaining sequential time points. During the 8 day degradation in PBS, β-sheet content had increased by 22 % (p<0.0001), α-helix and random coil structural content had reduced by 15 % (p<0.0001) and β-turns had dropped down by 8 % (p<0.0001).

β-sheet content of nHA/RSF film 50 % fluctuated over the 8 days when degraded in PBS (Figure 6.19). Over the first two days β-sheet content continuously increased; by 18 % (p<0.0001) by day 1, and then by a further 9 % (p<0.0001) between days 1 and 2. Between days 2 and 3 there was a reduction in β-sheet content by 8 % (p<0.0001), increased by 5 % (p<0.01) between days 3 and 5, and no significant difference occurred between days 5 and 8.
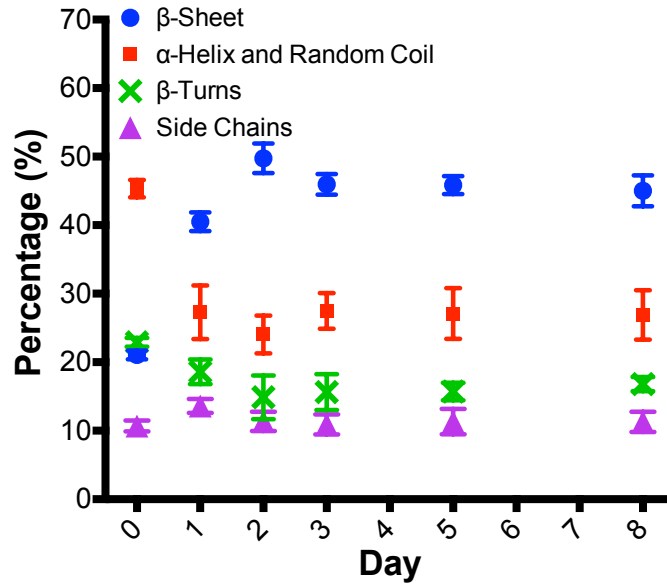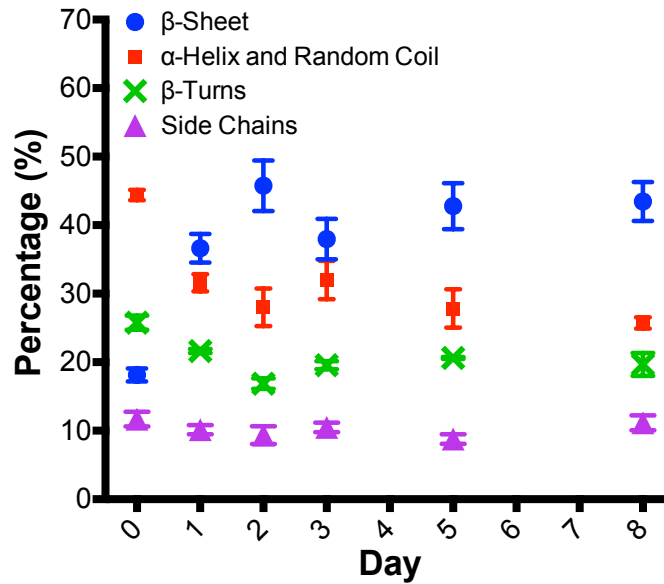
Figure 6.19: FSD data of amide I protein secondary structures for nHA/RSF film with 50 % nHA concentration, when degraded in PBS for 8 days. Standard deviation of measurements made over four different FWHM values is shown.

α-helix and random coil structural content for nHA/RSF film 50 %, experienced a continuous decrease over the first 2 days, by 13 % ($p<0.0001$) over the first day and by 4 % ($p<0.05$) on the following day. Between days 2 and 3, α-helix and random coil content increased by 4 % ($p<0.05$), decreased by 4 % ($p<0.05$) between days 3 and 5, and remained similar between days 5 and 8. Similar to the α-helix and random coil content, β-turns continually reduced over the first 2 days. Over the first 24 hours β-turns reduced by 4 % ($p<0.01$), and then by 5 % ($p<0.01$) between days 1 and 2. There were no more significant differences between sequential time points for β-turns. After 8 days degraded in PBS, nHA/RSF film 50 % had overall gained 25 % ($p<0.0001$) β-sheet content, lost 19 % ($p<0.0001$) α-helix and random coil structural content, β-turns had reduced by 6 % ($p<0.0001$), and there were no significant differences in side chain content.

nHA/RSF film 25 %, when degraded in PBS, had an increase of β-sheet content by 24 % ($p<0.0001$) over the first 24 hours (Figure 6.20). β-sheet content then remained similar between days 1 and 5, before experiencing a further increase by 10 % ($p<0.0001$) between days 5 and 8.
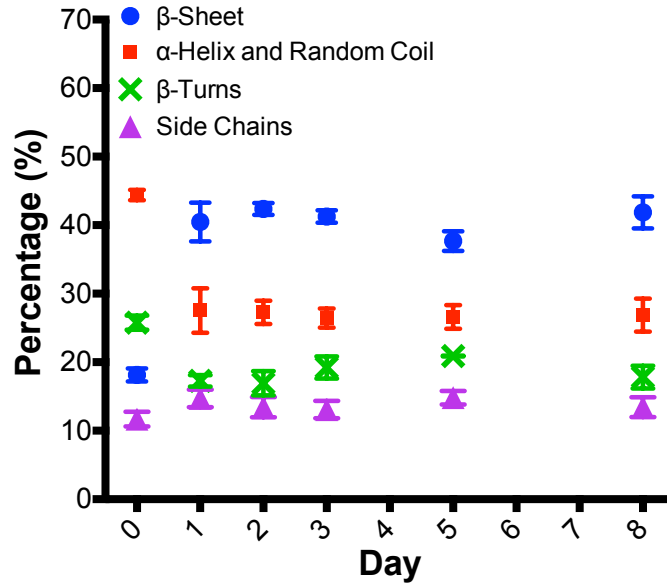
146
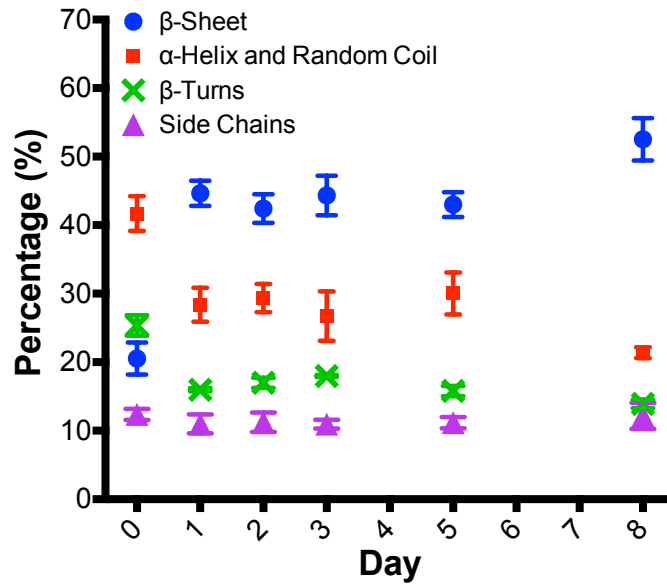
Figure 6.20: FSD data of amide I protein secondary structures for nHA/RSF film with 25 % nHA concentration, when degraded in PBS for 8 days. Standard deviation of measurements made over four different FWHM values is shown.

α-helix and random coil content for nHA/RSF film 25 % decreased by 13 % (p<0.0001) over the first 24 hours, and then remained similar between sequential time points until day 8, when there was a loss of 9 % (p<0.0001) between days 5 and 8. β-turns had reduced by 9 % (p<0.0001) by the first day, and had no significant differences between sequential time points. Overall, after 8 days degraded in PBS, nHA/RSF film 25 % had gained 32 % (p<0.0001) β-sheet content, lost 20 % (p<0.0001) α-helix and random coil structural content, β-turns had reduced by 11 % (p<0.0001), and there were no significant differences in side chain content.

6.2.3.3.3 Discussion of the Degradation FSD Results

Although the RSF within the nHA/RSF films began with a structure similar to RSF film 100 %, which had had no methanol treatment, the RSF rapidly turned crystalline, and, unlike the RSF film 100 %, did not fully degrade after 8 days in either a PBS or a protease XIV solution. Over the first 24 hours, all the films experienced their largest increase in β-sheet content accompanied by a significant reduction in α-helix, random coil and β-turns, representative of the dissolution of silk I.

Final crystallinities of the nHA/RSF films degraded with protease XIV were 45 %, 42 % and 48 % for nHA/RSF films 75 %, 50 % and 25 % respectively. nHA/RSF films finished with similar crystallinities to that of the RSF films 66 %, 50 % and 33 % which ended up with crystallinities between 45 - 47 % when degraded with protease XIV.

Final crystallinities of the films degraded in PBS were 43 %, 44 % and 53 % for nHA/RSF films 75 %, 50 % and 25 % respectively. nHA/RSF films 75 % and 50 % finished with crystallinities similar to RSF films 66 % and 33 % which finished with crystallinities of 47 % and 46 % respectively when degraded in PBS. nHA/RSF film 25 % finished with a similar crystallinity to that of RSF film 25 %, which was the most crystalline of the RSF films, ending with a crystallinity of 52 %.

Even though nHA/RSF films 75 %, 50 % and 25 % had similar degradation profiles, each had different proportions of protein secondary structures. Each film started with an unordered structure and a larger β-turn concentration than that of the RSF films. Over the course of the degradation study the RSF rapidly became crystalline, and, unlike the non-methanol treated RSF films, lasted the entirety of the degradation study. The slower degradation rate of the nHA/RSF films in comparison to the non-methanol treated pure RSF film 100 %, could be related to having a higher β-turn concentration. β-turns are associated with a water-soluble silk I structure, however it has previously been shown that RSF films with a high β-turn content are water insoluble [179]. Therefore, the initially high silk I content of the nHA/RSF films, shown by the FTIR-ATR, could be partially attributed to a high β-turn concentration, which has a lower solubility than that of the other silk I structures. This meant that the films did not degrade similarly to the RSF film 100 % which appeared to have a comparable silk I content.

Unlike the low crystallinity RSF films degraded in PBS, the nHA/RSF films did not develop large silk I absorption bands within the amide I region. In the previous chapter (Chapter 5: Inkjet Printing of Regenerated Silk Fibroin Films) it was hypothesised that by printing a layer of the RSF ink followed by a layer of methanol

and so on, produced a layered structure of water soluble silk I encapsulated by non-water soluble silk II. When the RSF films were submerged in PBS they became hydrated, which resulted in a greater mobility of the non-crystalline silk I structures and a breakdown of the less dense crystalline fibroin regions [167]. The silk II layers prevented the dissolution of the silk I structure, which along with the breakdown of the less dense crystalline regions caused an increase in silk I absorption bands. It is possible that the nHA/RSF films didn't develop larger silk I absorption bands, caused by greater mobility of the RSF molecules, as the nHA produced holes within the silk II layers. As there were holes within the layers of silk II, the encapsulated silk I was able to be dissolved. This would explain the mass loss and the increased crystallinity of the nHA/RSF films degraded in PBS when compared to the pure RSF films.

6.3   Summary

Using a methodology based upon the patented Fluidinova process, pure nano-hydroxyapatite (nHA) was produced, as proven by XRD and FTIR. The nHA used for printing had a hydrated structure and was less crystalline than the sintered samples. The unsintered nHA had a rod like morphology with an average length of 31.7 nm; this size of nHA did not cause any blockages of an 80 μm printhead when incorporated into an RSF ink.

The unsintered nHA was added to RSF solutions to produce a composite ink which had dried weight concentrations of 100 %, 75 %, 50 % and 25 % nHA. Films produced from the inks were investigated to determine if the inclusion of the nHA within the RSF solution affected the transition of silk I to silk II during the printing of methanol, as well as altering the degradation profile of the films.

The inclusion of nHA within the film was shown to have prevented a complete transition of silk I to silk II. Instead the inclusion created a precursor to the β-sheet morphology in the form of β-turns. This resulted in films which had a predominantly silk I structure, representative of an RSF film without methanol treatment (RSF film 100 %). Upon performing degradation studies on the films, it became apparent that

the nHA/RSF films were less water soluble than RSF film 100 %, as the films did not completely degrade or dissolve in either the protease XIV or PBS solutions. The lower degradation rate could be related to a higher β-turn content, which has been shown to affect water solubility of RSF films [179].

Degradation of the nHA/RSF films in a protease solution showed that for films with RSF content (nHA/RSF films 75 %, 50 % and 25 %), there was no significant difference between their final degradation percentage mass loss after 8 days. The pure nHA film (nHA/RSF film 100 %) experienced the largest mass loss, however as the nHA would not be susceptible to proteolytic degradation, mass loss was most likely caused by nHA being removed during washes, performed before the films were weighed. nHA/RSF films 75 %, 50 % and 25 % were also shown to respond similarly when degraded in PBS, all finishing with similar mass losses. Again, the pure nHA film (nHA/RSF film 100 %) experienced substantial mass losses over the 8-day period, which was most likely caused by the washing of the sample. As the nHA/RSF films degraded similarly in both the protease and PBS solutions, the inclusion of nHA in varying concentrations is shown to not affect the short term degradation of the nHA/RSF films.

FTIR-ATR spectra and FSD data of the nHA/RSF films measured at different degradation time point, show that the films differed in structure. Differences in structure between the films could be related to the proposed RSF film structure, produced via the reactive inkjet printing processing. The proposed structure, discussed in Chapter 5: Inkjet Printing of Regenerated Silk Fibroin Films, is that the RSF films are formed out of layers of insoluble silk II encapsulating layers of water soluble silk I. The inclusion of nHA particles caused holes within the silk II layers. When the films were first submerged, the silk I structure was dissolved to different extents, dependant on the abundance of holes in the silk II layers.

This chapter has demonstrated the possibility of producing composite RSF films via reactive inkjet printing, which have varying concentrations of nHA particles. Including nHA particles within the RSF ink was shown to disrupt the transition of silk I to silk II,

instead producing an intermediate β-turn structure. The subsequent degradation study has shown that the short-term degradation rate of the nHA/RSF films is not dependant on nHA content.

Chapter 7: Cell Culture

7.1   Introduction

In the development of materials and their properties for use in tissue engineering, it is important to understand the cellular responses to the materials as this contributes to the overall success of the implant. This chapter will investigate the metabolic activity, proliferation and alkaline phosphatase (ALP) activity of MG-63 human osteosarcoma cells when seeded onto RSF and nHA/RSF films.

Cellular responses to the RSF and nHA/RSF films are compared to controls of glass, tissue culture plastic (TCP) and poly(L-lactide) (PLLA). Glass and TCP were chosen as control substrates as they are commonly used in tissue culture, whilst PLLA was chosen due to its use as a copolymer in current dental barrier membranes such as: Guidor® Matrix Barrier, Vicryl Periodontal Mesh®, Atrisorb® and Epi-Guide® Bioresorbable Barrier Matrix [27].

Cell studies were performed over a three-week period except for the metabolic activity study where the results are shown for a period of two weeks. After three weeks of incubation the fluorescence readings for metabolic activity became too high to read on the spectrometer. All of the cellular experiments were performed twice, with three repeats of each film. For the spectrometer analysis, three aliquots were taken from each sample. Therefore, the values for each film shown in the following graphs are comprised of eighteen individual spectrometer readings. Aliquots used for the PicoGreen and ALP assays were frozen at the designated time points and analysed together after cell cultivation had ended.

7.2   Results and Discussion

7.2.1   Metabolic Activity

Metabolic activity of the cells is important to assess as it gives an indication of cell viability. Lower metabolic rates can be a sign of reduced cell viability due to interactions with the films. This section will analyse the metabolic activity of the MG-

63 osteoblast-like cells via changes in fluorescence of PrestoBlue assays over a two-week period. The PrestoBlue dye, which is non-fluorescent, is able to permeate the cells where it is then broken down via metabolic activity into a fluorescent compound. Therefore, the more metabolically active the cells are, the more fluorescent the assay will become. This section will analyse the results of the RSF films and the nHA/RSF films separately which will be followed by a joint discussion of the results.

7.2.1.1 Metabolic activity of RSF films

Figure 7.1 shows the fluorescence values of the PrestoBlue assays performed on RSF films with different crystallinities. Between days 1 and 3, there was no significant increase in the fluorescence of the RSF samples nor the PLLA control. Over the same period the fluorescence of the glass and TCP samples both increased with a significance of $p<0.01$ and $p<0.001$ respectively. Between the remaining time points all samples increased with a significance of $p<0.0001$.
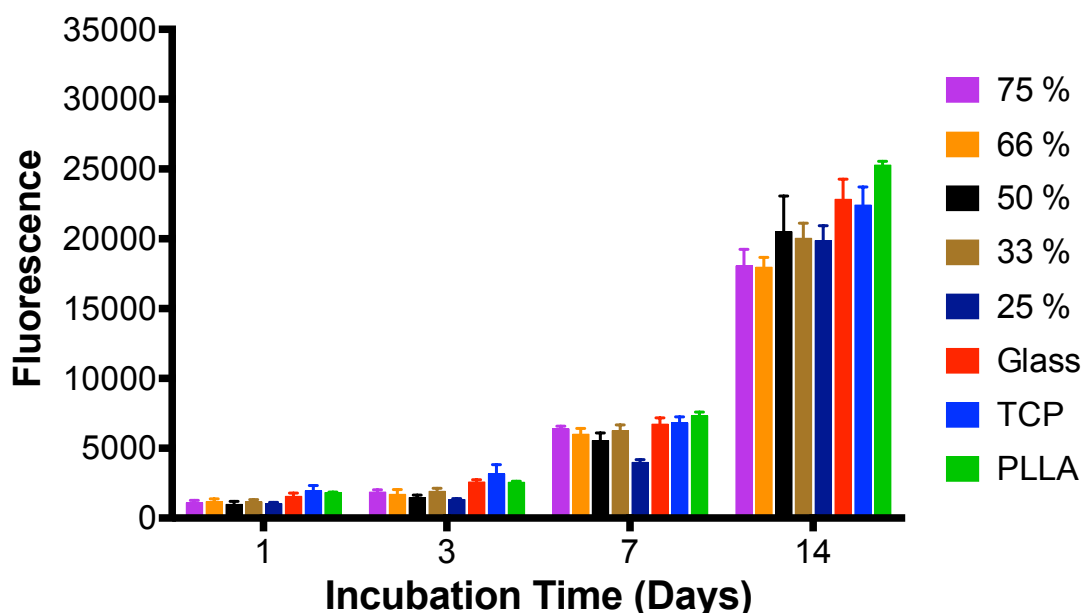
Figure 7.1: PrestoBlue analysis of RSF films with different crystallinities over a two week period. Crystallinities are produced by printing different volumes of RSF ink to methanol, whereby RSF film 75 % is the least crystalline and RSF film 25 % is the most crystalline.

After 1 day in cell culture, there was no significant difference between any of the RSF samples and the controls. By day 3 there remained no significant difference between the RSF samples, however, the fluorescence of the controls had increased slightly more than that of the RSF films causing some significant differences to develop between some of the controls and the RSF films. Glass had a larger fluorescence than that of RSF films 50 % ($P<0.05$) and 25 % ($p<0.01$), TCP was significantly larger than all of the RSF films with a significance of $p<0.05$ or greater, and the PLLA control was significantly larger than RSF film 25 % ($p<0.05$).

By day 7, differences had begun to appear in the fluorescence values of the RSF films. There was no significant difference between RSF films 75 %, 66 %, 50 % and 33 %, however, RSF film 25 % was significantly lower than the other films by a significance of $p<0.001$ and greater. The control samples continued to have fluorescence values higher than that of the RSF films. Glass had a significantly higher fluorescence than that of RSF films 50 % ($p<0.05$) and 25 % ($p<0.0001$), TCP was significantly larger than RSF films 50 % ($p<0.01$) and 25 % ($p<0.0001$), and PLLA was significantly larger than 66 % ($p<0.05$), 50 % ($p<0.001$) and 25 % ($p<0.0001$).

By day 14, RSF films 50 %, 33 % and 25 % had no significant difference between each other. There was no significant difference between RSF films 75 % and 66 %, which were both significantly lower than the other RSF films by a significance of $p<0.0001$. All of the control samples had a significantly higher fluorescence than that of the RSF films. PLLA had the largest fluorescence and was significantly higher than all of the other controls and the RSF films by a significance of $p<0.0001$. Controls glass and TCP were also significantly larger than all of the RSF films by a significance of $p<0.0001$.

7.2.1.2   Metabolic activity of nHA/RSF films

Figure 7.2 shows the fluorescence values of PrestoBlue assays performed on nHA/RSF films over 14 days in cell culture. All nHA/RSF films and control samples increased by a significance of $p<0.0001$ between each time point except for between days 1 and 3. Between days 1 and 3 there was no significant increase in fluorescence for any of the nHA/RSF films nor for the PLLA control. Controls glass and TCP

fluorescence values increased between days 1 and 3 by a significance of p<0.01 and p<0.001 respectively.
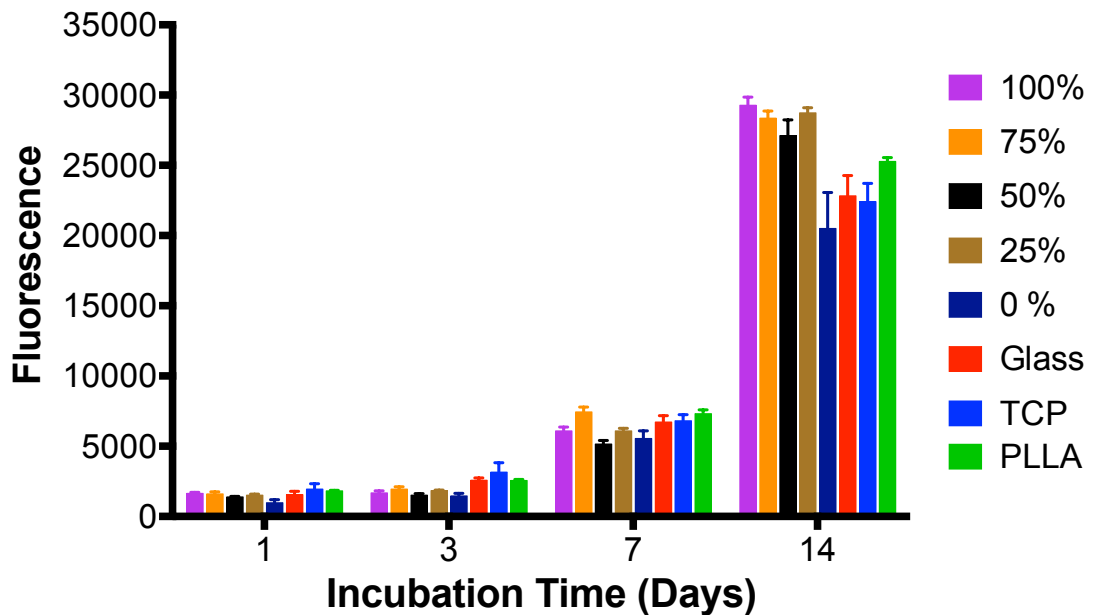
Figure 7.2: PrestoBlue analysis of nHA/RSF films with different nHA content over a two week period. Percentage values given represent the concentration of nHA within each film, whereby 100 % represents a pure nHA film and 0 % represents a pure RSF film.

After 1 day in cell culture there was no significant difference between any of the nHA/RSF films and control samples. By day 3 the nHA/RSF films had remained similar to each other, as had the control samples which had slightly higher fluorescence values. Glass was significantly higher than nHA/RSF films 50 % and 0 % (p<0.05). TCP was significantly higher than all of the nHA/RSF films by a significance of p<0.01 or greater. PLLA was similar to all of the nHA/RSF films.

After 7 days in culture, nHA/RSF film 75 % had the highest fluorescence out of all of the nHA/RSF films and control samples and was significantly higher than nHA/RSF films; 100 % (p<0.001), 50 % (p<0.0001), 25 % (p<0.01) and 0 % (p<0.0001). The other nHA/RSF films had no significant difference between each other. The control samples had similar values to each other that were slightly higher than the average fluorescence values of the nHA/RSF films. All of the controls were significantly higher

than that of nHA/RSF film 50 % (p<0.0001) and 0 % (p<0.01 or greater). The PLLA control was significantly higher than nHA/RSF films 100 % and 25 % (p<0.05).

By the final day of cell culture all of the nHA/RSF films which included nHA (all except nHA/RSF film 0 %) had a significantly higher fluorescence than that of the controls (p<0.0001). The nHA/RSF film with the highest fluorescence was nHA/RSF film 100 % which was followed by nHA/RSF film 25 % and then 75 %, with no significant difference between each other. nHA/RSF film 50 % had the lowest fluorescence of all the films that included nHA and its fluorescence was significantly smaller than nHA/RSF film 75 % (p<0.01). The nHA/RSF film which was pure RSF (nHA/RSF film 0 %) had significantly the lowest fluorescence out of all of the samples (p<0.0001). The control sample PLLA had a significantly higher fluorescence than the other control samples; glass and TCP (p<0.0001). Glass and TCP and had similar fluorescence values.

7.2.1.3 Metabolic Activity Discussion

Over the course of 14 days in cell culture all of the RSF and nHA/RSF films were shown to produce metabolically active cells which continued to increase in metabolic activity. The more crystalline RSF films (RSF films 50 %, 33 % and 25 %) were shown to have the highest levels of cell metabolic activity compared to the less crystalline RSF films (RSF films 75 % and 66 %) by the final day. This would be expected as cell types usually prefer a substrate which has similar characteristics to the tissue they originate from. Therefore, osteoblastic cells would prefer a substrate which has a hard surface [180] such as the more crystalline RSF films.

Although RSF film 25 % ended up with one of the highest metabolic rates of the RSF films, up until day 7 it had been showing significantly lower metabolic rates compared to the other films. These lower rates could be an indication that RSF film 25 % was the least favourable substrate for the cells to interact with. The low metabolic rates could be an indication of the cells producing greater amounts of extra cellular matrix in order to interact with the substrate.

After the first day in cell culture the nHA/RSF films had a similar metabolic activity as the control samples, however by day 3, both glass and TCP controls were showing higher metabolic rates. By day 7, nHA/RSF film 75 % was showing increased metabolic activity compared to the control samples as well as the other nHA/RSF films. This was followed on day 14 by increased metabolic activity above that of the controls for all of the nHA/RSF films which had nHA inclusions. nHA/RSF film 0 % (pure RSF), was the only nHA/RSF film which had a lower metabolic activity compared to the controls. The high levels of metabolic activity show that the inclusion of nHA within the films has a positive effect on the MG-63 osteoblastic cells. The results also show that a larger quantity of nHA (around 75 % concentration) may be more beneficial for instigating higher levels of metabolic activity at an earlier stage compared to other concentrations.

This section showed that the RSF and nHA/RSF films did not have an adverse effect upon the metabolic activity of the MG-63 cells. The MG-63 cells were more metabolically active upon substrates which were harder and more representative of their natural extra cellular matrix, e.g. the more crystalline RSF films, whilst the inclusion of nHA was also shown to be beneficial for metabolic activity. As the cells have continued to show increasing levels of metabolic activity, it is possible to say that the cells remained viable on all RSF and nHA/RSF films.

7.2.2   dsDNA Quantification

Double stranded DNA (dsDNA) quantification assays were performed to give an indication of cell number. dsDNA is only present in the nucleus of cells, and as cell numbers increase, so does the amount of dsDNA proportional to the number of cells. In this section, results of the RSF films are first analysed, followed by an analysis of the nHA/RSF films, and finishes with a discussion of the results.

7.2.2.1   *dsDNA Quantification of Cells Seeded onto RSF Films*

Figure 7.3 depicts the amount of dsDNA on each of the RSF films over the course of three weeks. After 7 days in cell culture, cell numbers remained relatively similar on

each substrate. RSF film 33 % had a slightly higher volume of dsDNA compared to the other RSF films, and was significantly higher than RSF films 50 % and 25 % by a significance of $p < 0.05$. The glass control had a similar volume of dsDNA to that of the RSF film 33 %, and was significantly higher than RSF films 75 %, 50 %, 25 % as well at the control TCP by a significance of $p < 0.05$. The remaining RSF films and control samples were all similar to each other.
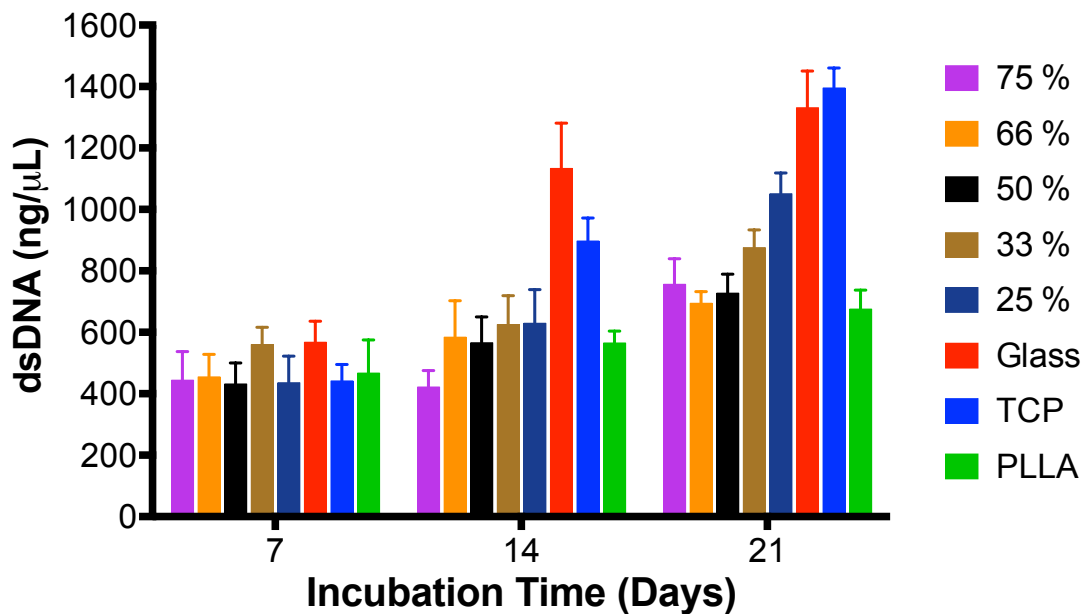
Figure 7.3: dsDNA quantification of MG-63 cells seeded onto RSF films with different crystallinities compared to controls of glass, TCP and PLLA over a 3-week period. Crystallinities are produced by printing different ratios of RSF ink to methanol, whereby RSF film 75 % is the least crystalline and RSF film 25 % is the most crystalline.

By day 14, larger differences started to occur between the RSF films and the controls. Of the RSF films, RSF films 75 % and 33 % had a similar level of dsDNA as they did on day 7, suggesting that little cell proliferation had occurred over the course of a week. The other RSF films had all increased by a similar amount to each other. RSF films 66 %, 50 %, 33 % and 25 % were all similar to each other and had significantly more dsDNA than RSF film 75 % by a significance of $p < 0.01$ or greater. The glass control had experienced substantial cell proliferation between days 7 and 14 and had significantly more dsDNA than any of the RSF films or controls ($p < 0.0001$). TCP had also experienced a large increase of dsDNA by day 14, and it too was significantly higher than the RSF films as well as the PLLA control ($p < 0.0001$). The PLLA control

was similar to that of the other RSF films except RSF film 75 % which had significantly fewer dsDNA than that of the PLLA ($p<0.01$).

Between days 14 and 21, all RSF films and controls experienced a significant increase of dsDNA. RSF films 75 %, 33 % and 25 % as well as control samples glass and TCP, increased with a significance of $p<0.0001$, RSF film 50 % by $p<0.001$, and RSF film 66 % and control PLLA with a significance of $p<0.05$.

By day 21, the RSF film which had had the fastest cell proliferation was RSF film 25 %. This was followed by RSF film 33 % which was significantly lower than RSF film 25 % by a significance of $p<0.001$. The RSF film with the next highest amount of dsDNA was RSF film 75 % which has a similar amount of dsDNA as RSF film 33 %. The RSF film which had had the lowest levels of proliferation over 21 days were RSF films 66 % and 50 % which had similar amounts of dsDNA. The controls glass and TCP had the largest amount of dsDNA compared to any of the RSF films by a significance of $p<0.0001$. The control PLLA had similar amounts of dsDNA to RSF films 75 %, 66 % and 50 %, but was significantly lower than RSF films 33 % and 25 % ($p<0.0001$).

7.2.2.2   DNA Quantification of Cells Seeded onto nHA/RSF Films

Figure 7.4 is the dsDNA data of nHA/RSF films over a three week period. After 7 days of cell culture, the nHA/RSF films all had a similar amount of dsDNA, apart from nHA/RSF film 0 % (which had no nHA content), which had slightly more dsDNA than nHA/RSF film 50 % by a significance of $p<0.05$. The glass control had experienced larger amounts of cell proliferation compared with the nHA/RSF films and other controls. The glass control was significantly higher than nHA/RSF films 100 %, 75 %, 50 % and 25 % by a significance of $p<0.0001$, and by nHA/RSF film 0 % by a significance of $p<0.01$. The PLLA control was significantly larger than nHA/RSF films 75 % ($p<0.05$), 50 % ($p<0.01$) and 25 % ($p<0.01$), whilst the TCP control was larger than nHA/RSF films 50 % ($p<0.05$) and 25 % ($p<0.05$).
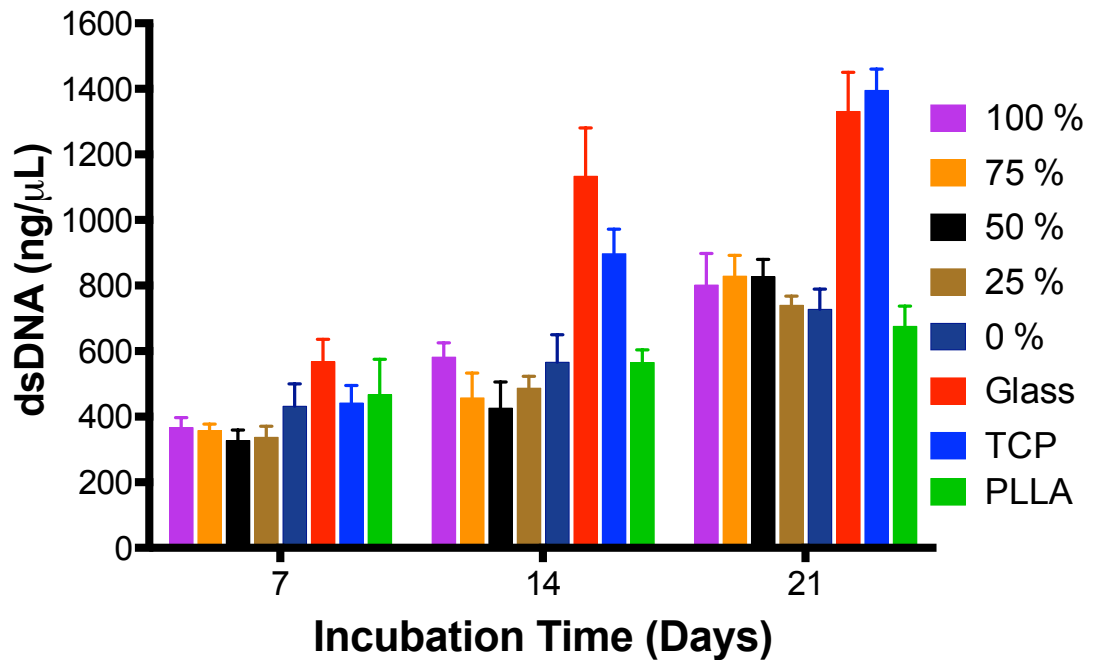
Figure 7.4:DNA quantification of MG-63 cells seeded onto nHA/RSF films with different concentrations of nHA compared to controls of glass, TCP and PLLA. Percentage values given represent the concentration of nHA within each film, whereby 100 % represents a pure nHA film and 0 % represents a pure RSF film.

By day 14, differences between the rates of cell proliferation were becoming more apparent on the nHA/RSF films. nHA/RSF film 100 %, which was pure nHA had the largest amount of dsDNA compared to the other nHA/RSF films, and was significantly higher than nHA/RSF films 75 % ($p < 0.01$) and 50 % ($p < 0.001$). The nHA/RSF film with the second highest amount of dsDNA was nHA/RSF film 0 % which was significantly larger than nHA/RSF film 75 % ($p < 0.05$) and 50 % ($p < 0.01$). The remaining nHA/RSF films were similar to each other. Both controls glass and TCP had significantly more dsDNA than all of the nHA/RSF films with a significance of $p < 0.0001$. The PLLA control was significantly larger than nHA/RSF film 75 % ($p < 0.05$) and 50 % ($p < 0 < 0.01$).

After 21 days in cell culture, nHA/RSF films with the highest nHA content (nHA/RSF films 100 %, 75 % and 50 %) appeared to have had more cell proliferation than films with the lowest nHA content (nHA/RSF films 25 % and 0 %), although there were no significant differences between any of the nHA/RSF films. The control samples glass and TCP remained significantly higher than the nHA/RSF films with a significance of $p < 0.0001$. The control PLLA had the lowest levels of dsDNA compared to the nHA/RSF

films, with nHA/RSF films 100 % (p<0.01), 75 % (p<0.001) and 50 % (p<0.001) having significantly larger amounts of dsDNA.

7.2.2.3   dsDNA Quantification Discussion

dsDNA quantities were used to monitor cell numbers. Cell numbers on RSF films was seen to be quite low in comparison to the controls of glass and TCP. Up until day 14, the rate of cell proliferation on the RSF films progressed with relative uniformity between each RSF film, except for RSF film 75 % which had significantly lower dsDNA than the other RSF films. By the final day, there was a general trend of the higher crystallinity RSF films having larger cell numbers in comparison to the less crystalline RSF films. Previous studies have shown that osteoblast cells have faster proliferation rates on less crystalline and amorphous polymer substrates [181], [182], which is in contradiction to these results. However, as discussed in Chapter 5, RSF films micro-topography became rougher with increased methanol volumes, and therefore, for the more crystalline films. Surface roughness has previously been investigated for its effect in osteoblastic cellular responses. Generally micro-scale roughness is seen to hinder cell proliferation by preventing the cells from spreading. However a study by Passeri *et al.* which used titanium surfaces with similar roughness values to that of the RSF films (ranging between 0.183 μm to 2.571 μm (Sa)) found that osteoblast cell proliferation improved with increased roughness of the surfaces [183]. Therefore, surface roughness of the RSF films might explain the higher cell numbers on the crystalline RSF films after 21 days in culture.

RSF film 75 % had experienced a large increase in dsDNA between days 14 and 21. On day 14 RSF film 75 % had the lowest dsDNA levels out of all of the samples, however by day 21 it had the third highest amount of the RSF films. It has previously been shown that a lack of porosity in films, relating to a smaller surface area, can limit proliferation of cells and instead stimulate the cells into osteogenesis [184]. In this instance the least crystalline film (RSF film 75 %) had a smooth surface and hence the smaller surface area than the more crystalline RSF films which could explain the initially lower proliferation rates. To see if RSF film 75 % had low proliferation rates

due to osteogenesis of the cells, requires investigating ALP activity, and is discussed below.

The inclusion of nHA within the RSF films was initially shown to cause slower proliferation rates compared to the pure RSF films (nHA/RSF film 0 %) and that of the controls. By day 14, cell numbers were highest on films which were either pure nHA (nHA/RSF film 100 %) or pure RSF (nHA/RSF film 0 %). nHA/RSF films 100 % and 0 % had similar dsDNA levels to the PLLA control, although significantly lower than that of the glass and TCP controls. On the final day there was no significant difference in dsDNA content between the nHA/RSF films. nHA/RSF films 100 %, 75 % and 50 % finished with significantly more dsDNA than that of the PLLA control, however still much lower than for the glass and TCP controls. These results indicate that the inclusion of nHA in the RSF films might cause a slightly slower proliferation rate to begin with, however after a longer duration of time, cell numbers even out between the films.

It has previously been shown by Yang *et al.* that osteoblastic cells grow fastest on films with high nHA content and on substrates with a high stiffness, but after a period of 24 days in cell culture, films with a low nHA content yielded higher cell numbers [53]. For the current study, the pure nHA film had the fastest cell growth whilst there was little difference between the other nHA/RSF films. However, dsDNA content had become more even by day 21, so a longer study might show larger cell numbers on RSF films with a lower nHA content. A similarity to the work by Yang *et al.* was the fastest growth occurring on the stiffest substrates [53]. The controls of glass and TCP were both much stiffer than any of the RSF films or nHA/RSF films, as well as the PLLA control. It was also seen that by day 21, on the RSF films there was a general trend for films with a higher crystallinity, hence stiffer properties, having higher dsDNA content compared to the less crystalline RSF films.

Overall, MG-63 cells were seen to proliferate the fastest on the more crystalline and rigid surfaces. The faster proliferation could be due to the rougher surfaces of the more crystalline RSF films. The combination of RSF and nHA initially limited cell

proliferation, however by day 21, there was no difference in dsDNA content between any of the nHA/RSF films

7.2.3 Alkaline Phosphatase Activity

Alkaline phosphatase (ALP) is present in all tissues, however is more concentrated in specific tissues such as bone. ALP is recognised as an early marker of osteoblastic cell activity and the beginning of calcification; during the early stages of calcification ALP expression is increased [185]. Measuring ALP activity simply indicates the amount of ALP expressed by the cells. ALP activity has been standardised to dsDNA content to give a clear representation of ALP expression of the MG-63 cells. This section begins with the analysis of the ALP activity of MG-63 cells seeded on RSF films, followed by the analysis of the cells seeded onto nHA/RSF films, and finishes with a discussion of the results.

7.2.3.1 *Alkaline Phosphatase Activity of MG-63 Seeded on RSF Films*

Over three weeks of cell cultivation ALP activity generally decreased, as seen in Figure 7.5. The most notable decrease is observed on RSF film 75 % which significantly dropped in ALP activity between each time point ($p < 0.0001$). Most of the RSF films and all of the controls saw either a continuous reduction in ALP activity over the three-week period, or, had one period where there was no significant difference between time points as well as one period where there was a significant drop in ALP activity. Only one RSF film saw an increase of ALP activity between time points; RSF film 66 % had an initial drop of ALP activity between days 7 and 14 ($p < 0.0001$) which was followed by an increase of ALP activity between days 14 and 21 ($p < 0.0001$). RSF film 33 % was the only film to experience no significant difference in ALP activity between any of the time points.

Figure 7.5: Alkaline phosphatase activity of MG-63 cells cultivated on RSF films with different crystallinities over a three week period.

After one week, ALP activity was the highest in RSF film 75 % and was significantly higher than all of the other films ($p < 0.0001$). The RSF film with the next highest average ALP activity was RSF film 50 % which was significantly higher than RSF films 33 % ($p < 0.0001$) and 25 % ($p < 0.01$), as well as the controls glass ($p < 0.0001$) and TCP ($p < 0.0001$). RSF films 66 % had a similar but slightly lower ALP activity to that of RSF film 50 %, and had a significantly higher ALP activity that RSF film 33 % ($p < 0.01$) and controls glass ($p < 0.01$) and TCP ($p < 0.01$). RSF films 33 % and 25 % had no significant difference between each other nor any of the controls.

By the second week, RSF film 75 % still had the highest ALP activity, which was significantly higher than all of the other RSF films ($p < 0.0001$). The remaining RSF films were similar to each other except for RSF film 66 % which had the lowest average ALP activity of all the RSF films and was significantly lower than that of RSF film 33 % ($p < 0.01$). The TCP and PLLA controls had no significant differences to any of the RSF films other than RSF film 75 %. The glass control was significantly smaller than RSF films 50 % ($p < 0.01$) and 33 % ($p < 0.0001$).

By the final day of cell cultivation, RSF film 75 % no longer had the highest average ALP activity, which was instead experienced by RSF film 66 %. All of the RSF films had no significant difference between each other apart from RSF film 25 % which was significantly lower than RSF films 75 % ($p<0.01$), 66 % ($p<0.0001$) and 50 % ($p<0.001$). ALP activity of the glass and TCP controls was similar, and was significantly lower than RSF films 75 %, 66 % and 50 % by a significance of $p<0.0001$, and RSF film 33 % by a significance of $p<0.05$. The PLLA control was significantly lower than RSF film 66 % ($p<0.05$), but there was no significant difference between any of the other RSF films.

7.2.3.2   Alkaline Phosphatase Activity of MG-63 Seeded on nHA/RSF Films

Figure 7.6 shows the ALP activity of the MG-63 cells seeded onto nHA/RSF films over a three-week time period. Over the three weeks, MG-63 cells showed an average decline in ALP activity. The only nHA/RSF film to have a significant increase of ALP activity was nHA/RSF film 75 % between days 7 and 14 ($p<0.0001$). The remaining nHA/RSF films either reduced or had no significant changes in ALP activity between time points.
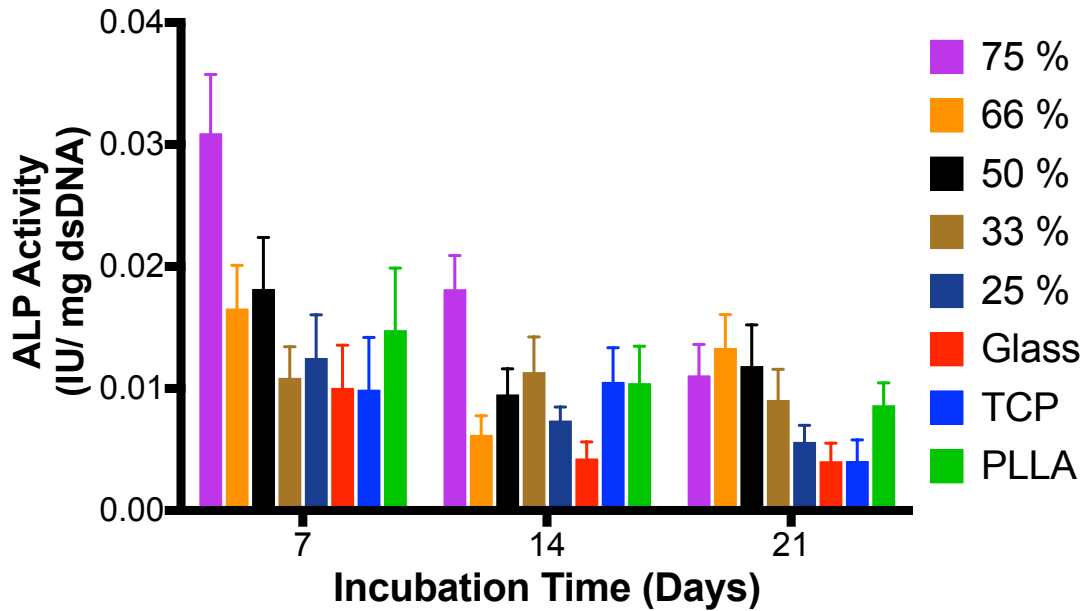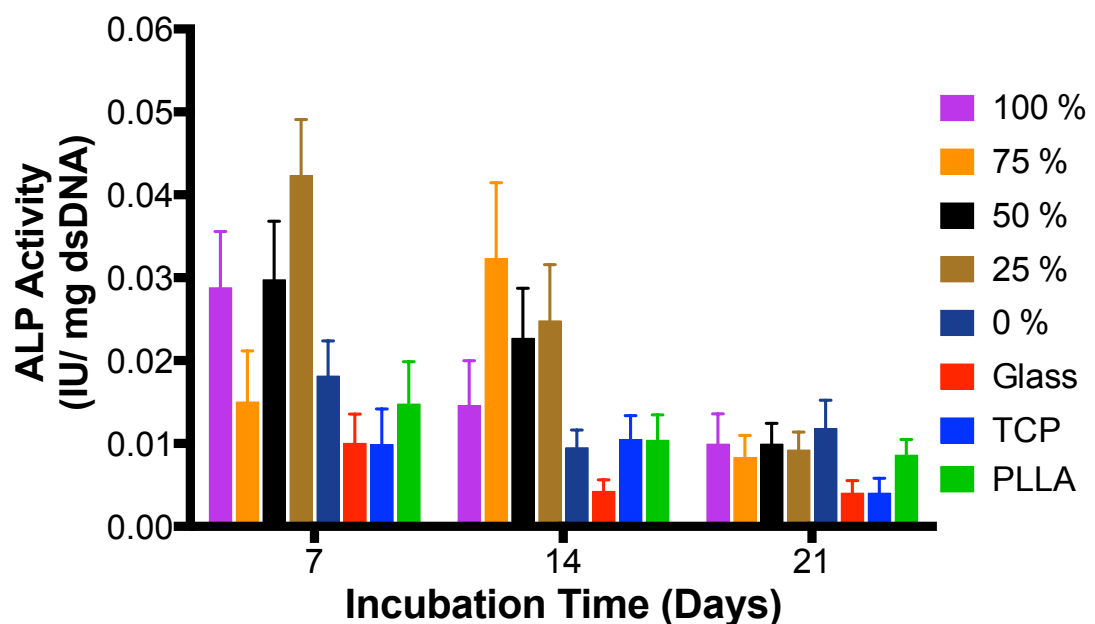

Figure 7.6: Alkaline phosphatase activity of MG-63 cells cultivated on nHA/RSF films with different nHA content over a three-week period.

After 7 days, ALP activity was the largest on nHA/RSF film 25 %, and was significantly higher than the other nHA/RSF films as well as the controls ($p<0.0001$). The nHA/RSF films with the next highest level of ALP activity were nHA/RSF films 100 % and 50 % which had similar averages. ALP activity on the nHA/RSF films 100 % and 50 % was significantly higher than the remaining nHA/RSF films and controls ($p<0.0001$). nHA/RSF film 75 % had no significant difference to the pure RSF film (nHA/RSF film 0 %) and the controls.

By day 14, nHA/RSF film 75 % had become the film with the highest ALP activity, and was significantly higher than nHA/RSF films 100 % ($p<0.0001$), 50 % ($p<0.001$), 25 % ($p<0.05$) and 0 % ($p<0.0001$), and all of the controls ($p<0.0001$). nHA/RSF films 50 % and 25 % had the next highest ALP activity; there was no significant difference between them. nHA/RSF film 50 % was significantly higher than nHA/RSF film 100 % ($p<0.01$) and 0 % ($p<0.0001$), as well as all of the controls ($p<0.0001$). nHA/RSF film 25 % was significantly higher than nHA/RSF film 100 % ($p<0.001$) and 0 % ($p<0.0001$) and all of the controls ($p<0.0001$). The pure RSF film had no significant difference to any of the controls.

After three weeks of cell cultivation, there was no significant difference in ALP activity between any of the nHA/RSF films or controls, except for nHA/RSF film 0 % which had the highest average ALP activity which was significantly higher than the glass and TCP controls ($p<0.05$).

7.2.3.3 Alkaline Phosphatase Activity Discussion

Almost all of the RSF and nHA/RSF samples experienced a drop in ALP activity over the course of the experiment. ALP activity reducing over time is a sign of the cells beginning the later stages of calcification which is characterised by a reduction in ALP expression [185]. RSF film 33 % was the only film to show no significant changes in ALP activity over the course of 21 days. A lack of change in ALP activity, which remained at a level of activity similar to those experienced by the other RSF films on day 21, could be because ALP activity had peaked earlier than the other results, and therefore before the first ALP activity measurement was made. On day 7, where most

of the samples showed peak ALP activity, it was the least crystalline samples, especially RSF film 75 %, which had the highest ALP activity.

Previously it was mentioned that RSF film 75 % had a low proliferation rate in comparison to the other films, possibly due to osteogensis caused by a flatter topography of the film [184]. A high ALP activity up until day 14 supports the possibility that the slower proliferation rates experienced on RSF film 75 % were caused by to osteogenic behaviour of cells. ALP activity was significantly higher in comparison to the other films, indicating a possible reason as to why RSF film 75 % had significantly lower dsDNA levels than the other films by day 14.

Of the nHA/RSF films, on day 7 when most of the films peaked in ALP activity, nHA/RSF film 25 % had the highest ALP activity. This could indicate that a combination of RSF and a low concentration of nHA is all that is required in order to promote a maximum osteogenic response from the cells. Bhumiratana *et al.* have previously reported that as little as 3.1 % HA inclusion within an RSF sponge was enough to get hMSCs to form a trabecular –like mineral structure [186].

The development of osteoblastic cells can be spilt into three distinct phases characterised by: phase 1) a large amount of cell proliferation, phase 2) reduced proliferation and matrix maturation with an increase in ALP expression; phase 3) matrix mineralisation and the down regulation of ALP expression [171]. From the results, it is possible that nHA/RSF film 75 % was slowest of the nHA/RSF films to reach the matrix maturation stage, having higher metabolic rates and lower ALP activity compared to the other nHA/RSF films on day 7. nHA/RSF film 75 % reaches its peak ALP activity on day 14 whilst the other films were showing reduced ALP activity. Overall, the nHA/RSF films had a higher ALP activity than that of the RSF films, which shows that the inclusion of nHA greatly improves osteogenesis of the RSF.

7.3   Summary

This chapter has investigated cellular responses to the RSF and nHA/RSF films. All of the films were shown to interact well with the MG-63 cells. Metabolic activity was highest on the hardest substrates when comparing the pure RSF films on the final day. The inclusion of nHA was seen to have a positive effect on the metabolic activity of the cells, consistently producing cells with higher metabolic rates than those on the pure RSF film at every time point.

Cell proliferation monitored through dsDNA assays showed that after 21 days of cell cultivation, the MG-63 cell numbers increased with RSF crystallinity. It is suggested that the higher proliferation rate of the MG-63 cells on the crystalline films was linked to surface roughness. Whilst some studies have shown that increased crystallinity can have a negative effect on cell proliferation rates [181], [182], surfaces with a similar range of roughness's to those of the RSF films have been shown to increase cell proliferation rates with an increase in surface roughness [183]. The inclusion of nHA was initially shown to reduce cell proliferation rates, however after 21 days there was no difference between amounts of dsDNA on the nHA/RSF films.

ALP activity was seen to peak for most samples by day 7. This indicated that the cells were quick to initiate osteogenesis. The inclusion of nHA was shown to improve ALP activity, however it was the lowest nHA content (nHA/RSF film 25 %) which had the highest ALP activity, indicating that a low concentration of nHA may be all that is required to promote osteogenesis of the barrier membranes.

Overall, higher crystallinities of the RSF films was seen to be beneficial to cell metabolic rates as well as long term cell proliferation, however, it was the least crystalline films which showed greater osteogenic effects with a higher ALP activity on day 7. The inclusion of nHA increased metabolic and ALP activity of the cells whilst producing similar levels of cell proliferation rates to that of a pure RSF film.

Chapter 8: Overall Discussion

8.1 Introduction

This thesis had the aim of determining the suitability of using reactive inkjet printing and regenerated silk fibroin (RSF) for producing dental barrier membranes. This section will discuss the objectives set out in Chapter 2 and whether they have been achieved. This chapter will finish with a summary and suggested future work.

8.2 Discussion of Objectives

At the beginning of this thesis the aims and objectives of the research were outlined. Each objective will now be discussed to determine if it has been achieved.

1) *To determine if RSF can be reactively inkjet printed, e.g. if RSF can be transformed from a silk I to silk II structure in-situ using an inkjet printer.*

To determine if RSF can be reactively inkjet printed, it was necessary to first evaluate the RSF solution for its printability. Inkjet printing usually requires inks to be formulated with a dilute concentration in order to be printable. Ink concentration can affect properties of the ink such as viscosity, surface tension and density, all of which have an effect on droplet formation. It was therefore necessary to analyse the printability of RSF solutions over a range of concentrations. Chapter 4 investigated the printable properties of RSF solutions with concentrations ranging from $10 - 120$ mg.mL^{-1}.

Viscosity and surface tension measurements were made for each concentration and used to calculate the Z number. The Z number is a dimensionless number, first used by J. E. Fromm and is used to predict printability of inks [122]. Concentration of the ink was shown to affect the infinite viscosity values (the viscosity at a high rate of shear), however concentration had less of an effect on the surface tension. Changes in surface tension were most significant between RSF ink concentrations of $50 - 70$ mg.mL^{-1}, where the surface tension dropped by around 10 %. Differences in surface tension were possibly related to a change in RSF structure at the liquid-air interface [145].

RSF solutions with concentrations between 80 – 120 mg.mL^{-1} had Z numbers within the predicted printable range for a nozzle aperture size of 80 μm (which was used in the study). All inks were set up in the inkjet printer and jetted to confirm their suitability. Although all inks had a stable droplet formation, inks with a concentration of 110 and 120 mg.mL^{-1} were likely to crust over. An RSF solution of 100 mg.mL^{-1} was therefore chosen as the most suitable for printing the barrier membranes.

Chapter 5 established that RSF could be reactively inkjet printed. RSF films were prepared by printing consecutive layers of RSF solution and methanol. These were compared to a control of RSF films printed without methanol, and, as another comparison, to ensure that β-sheet formation wasn't being induced by shear forces produced during printing, RSF films were cast onto glass coverslips.

Fourier transform infrared spectroscopy with attenuated total reflectance (FTIR-ATR) was used to compare the presence of silk I and silk II within the RSF films. This was followed by Fourier self-deconvolution (FSD) performed on the amide I regions of the FTIR-ATR spectra. FSD was used to calculate the presence of protein secondary structures within each RSF film.

FTIR-ATR spectra for cast RSF films and RSF films printed without methanol had similarly shaped spectra, indicating that there were comparable amounts of silk I and silk II. FSD data showed that there was no significant difference in the amount of β-sheet or α-helical secondary structures between either film. As the RSF films were shown to have similar structures it was concluded that under the current printing conditions, β-sheet formation was not caused by shear forces during printing.

Comparing the FTIR-ATR spectra of the two printed RSF films showed that printing methanol between layers of RSF caused a shift of intensities from a characteristic position for silk I to a characteristic silk II position within the amide I and II regions. This was supported by the FSD data which showed a substantial increase in β-sheet content for the methanol treated films. **As β-sheet formation was not induced by shear forces during printing and was controlled solely by the printing of methanol**

between layers of RSF solution, it has therefore been demonstrated that RSF can be reactively inkjet printed.

2) *To determine if the transition of silk I to silk II can be controlled so that RSF films can be produced with different characteristics based upon their β-sheet content.*

Chapter 5 also explored the relationship between the quantities of printed RSF to methanol. To determine if the transition of silk I to silk II could be controlled via reactive inkjet printing, different ratios of RSF to methanol were printed. Significant differences in concentrations in β-sheet content were produced between RSF films 50 % (100 mg RSF to 1 mL methanol), 33 % (100 mg RSF to 2 mL methanol) and 25 % (100 mg RSF to 3 mL methanol). β-sheet content was shown to increase from ~44 % for RSF film 75 % (300 mg of RSF to 1 mL methanol) to around 58 % for RSF film 25 %. RSF film 25 % had a similar crystallinity to that of the native silk cocoon and of cast RSF films submerged in methanol for 4 days, suggesting that the maximum crystallinity produced by a methanol treatment had been achieved.

By printing a range of ratios of RSF to methanol it was shown that a gradual transition of silk I to silk II could be produced, thereby establishing that reactive inkjet printing could be used to control structural characteristics of RSF films. This is important in demonstrating that reactive inkjet printing may offer greater control over barrier membrane characteristics than that of other current methods of production.

3) *Assess the degradation properties of reactively inkjet printed RSF films and determine if the degradation rate can be controlled.*

As a demonstration of the ability of reactive inkjet printing to control the characteristics of RSF films, degradation tests were performed in Chapter 5. The amount of β-sheet content has previously been shown to influence the degradation rates of RSF films [125]. Degradation tests were performed in either a protease XIV solution or in PBS. Degradation profiles for the RSF films degraded with protease XIV showed that the degradation rate was dependant on β-sheet content, hence the ratio of printed RSF to methanol. The first 24-hour period degraded with protease

XIV saw largest mass loss of the RSF films. The amount of mass lost was proportional to RSF β-sheet content. Over the following 7 days, degradation rates reduced.

RSF films degraded in PBS were expected to experience similar mass losses as the films degraded with protease XIV, over the initial 24-hour period, due to the dissolution of water soluble silk I. However, this was not the case. The RSF films that had been exposed to methanol experienced no substantial mass loss over the first 24 hours when degraded in PBS. It was hypothesised that the difference in degradation rates were due to the manner in which the RSF films were produced. Films were produced layer-by-layer with methanol printed between each layer of RSF solution. By printing the layers of methanol between the layers of RSF solution, layers of water insoluble silk II were produced which encapsulated layers of water soluble silk I beneath. When the films were submerged in PBS, the layers of silk II prevented the dissolution of the silk I. However, when the films were degraded with protease XIV, the protease degraded the layers of silk II enabling the silk I to be degraded/ dissolved.

Overall, proteolytic degradation, which would be experienced by RSF barrier membranes when positioned within the mouth, was shown to be dependent upon β-sheet content, and therefore the ratio of printed RSF to methanol. Being able to control the degradation rate of barrier membranes is important for the regeneration of bony defect sites. The barrier membrane needs to remain in position supporting regeneration by providing site seclusion and maintaining space until bony ingrowth and full regeneration have been achieved. The period of time a site will require to heal can depend upon the size and position of the defect as well as other factors such as smoking habits of the patient and patients age [187], [188]. As the defect requirements can differ between patients, selecting a barrier membrane which has been tailored to suit patient specific requirements could be ideal.

4) *Evaluate the cellular interaction of the RSF films with that of MG-63 osteosarcoma cells*

As barrier membranes aim to promote bony regeneration of a defect site, it is important to evaluate the cellular response of bone cells to the RSF membranes. Chapter 6 analysed MG-63 osteosarcoma cells when seeded on to RSF films. MG-63 cells were shown to remain metabolically active over a 2-week period. Cell proliferation rates were shown to respond differently depending upon the ratio of printed RSF to methanol. Faster cell growth was shown to occur on the more crystalline films. A suggested reason for this was the surface roughness of the films, as previous studies had linked material crystallinity with slower cell proliferation rates [181], [182]. Increasing the volume of methanol printed onto the films produced rougher surfaces, which, in a previous study, has been shown to increase osteoblast cell proliferation rates [183]. Alkaline phosphatase (ALP) activity was used to monitor osteogenic effects of the cells. ALP activity was shown to decrease with increasing crystallinity. **All of the films were shown to support viable cell growth and proliferation as well as instigate osteogenesis of the MG-63 cell.**

5) To assess if the RSF inks can be printed with an nano-hydroxyapatite bioactive component and what influence this has on the transition of silk I to silk II *in-situ*.

Chapter 6 investigated the inclusion of nano-hydroxyapatite within the RSF films. By using an inkjet printer with the capability of printing multiple inks, it is possible to manufacture membranes with a graduated structure that changes in nHA concentration. There are two possible ways of controlling nHA concentration within the films by using inkjet printing; either by printing composite inks with different concentrations of nHA, or, by printing a pure nHA suspension and controlling film nHA content by droplet densities of the nHA suspension between layers of RSF. As the MicroFab printer is limited to printing through a singular nozzle (in comparison to commercial printers where nozzle numbers can begin in the hundreds), it would be very time consuming to produce the nHA/RSF films by printing layers of RSF with a layer of methanol followed by a layer of nHA between the sequential RSF layers. To facilitate faster printing times, composite inks of nHA/RSF were produced.

As the inks would be composed of nHA as well as RSF it was important to analyse the effect of the inclusion of nHA on the transition of silk I to silk II. nHA/RSF composite inks were prepared which had a dried nHA weight percentage ranging between 0 – 100 %. Films were produced by printing methanol at a 1:1 vol% ratio related to their RSF content, i.e. 100 mg RSF to 1 mL methanol. The RSF structure was then analysed using FTIR-ATR and FSD. It was initially shown that although the nHA/RSF films had been printed with methanol, the RSF structure had a similar silk I structure to that of untreated RSF. FSD data showed that there was a similar amount of α-helix and random coil content between the nHA/RSF films and that of an untreated RSF film. However, FSD data also showed that there was a higher amount of β-turns present within the nHA/RSF films, than the RSF films treated with and without methanol. Previous studies have suggested that the β-turn structure is a precursor to the formation of β-sheets [88], [178]. This would indicate that the presence of nHA within the RSF ink, had, during methanol exposure, prevented the complete transition of silk I to silk II.

Although nHA/RSF films were shown to have a high proportion of silk I content, degradation tests performed in solutions of protease XIV or PBS showed that the films were more stable than the untreated RSF films, despite their high content of water soluble silk I. It has previously been shown that films with a silk I structure and a high amount of β-turns are non-water soluble [179]. This would confirm that the presence on nHA prevented the full transition of silk I to silk II, and an intermediate silk I structure with higher amounts of β-turns was produced.

Overall the inclusion of nHA within the RSF ink was shown to have an effect on the transition of silk I to silk II. Therefore, printing a composite ink of nHA and RSF may not be suitable for the development of RSF barrier membranes produced via reactive inkjet printing. Instead the inclusion of nHA should be controlled by printing an additional ink composed of an nHA suspension.

6) *To evaluate the effect of nHA inclusion within RSF films on MG-63 osteosarcoma cells*

Within Chapter 7, the inclusion of nHA was investigated to see if it improved osteogenic interaction of the RSF films. The inclusion of nHA within the RSF films was shown to have a positive influence on MG-63 cell metabolic activity. nHA/RSF films had significantly higher metabolic activity than that of a comparable pure RSF film after 14 days of cell culture. Cell proliferation rates were initially slower than that of cells growing on a pure RSF film. However, after 21 days there was no significant difference in the amount of dsDNA between nHA/RSF films and RSF films. ALP activity was shown to be improved by the inclusion of nHA. Although all films showed higher ALP activity than that of the pure RSF films, it was the RSF films with a dried weight of 25 % nHA which had the highest ALP activity, demonstrating that it might not be necessary to produce a barrier membrane with a high concentration of nHA to promote the best osteointegration. **Overall the inclusion of nHA within the membrane was shown to have a positive effect on cellular interactions with the MG-63 cells.**

8.3   Summary

It has been shown in this thesis that reactively inkjet printed RSF is a viable alternative for use as a dental barrier membrane. Silk has already been demonstrated to be an ideal biomaterial with characteristic traits which address the issues of current barrier membrane materials. The use of silk in its RSF form, has enabled a greater flexibility in its applications and made it possible to be processed via inkjet printing.

Inkjet printing is a precise and accurate method of manufacture, offering a high level of control in producing structures with an excellent reproducibility between samples. It offers the opportunity to control membrane structure, such as β-sheet content and concentration of bioactive inclusions. These properties can then be varied over the membrane to interact with different tissues.

Control over RSF structure and membrane composition can be performed in a singular procedural step, not possible with the alternate methods of RSF membrane

production. Reactive inkjet printing was also shown to offer a faster transition of silk I to silk II when using methanol. Previous methanol treatments have required the submersion of the RSF films in methanol over a 4-day period to induce maximum β-sheet content, however this transition could be induced during printing. These properties make inkjet printing a desirable method for barrier membrane manufacture and a promising alternative to the current methods of production.

In this study the use of reactive inkjet printing has enabled control over the transition of silk I to silk II and thereby controlling the degradation rate of RSF films. The produced RSF films were shown to be biocompatible with MG-63 osteosarcoma cells. To promote a greater osteogenic response, composite inks of nHA and RSF were produced. The inclusion of nHA was shown to improve MG-63 cellular interactions, however during the manufacturing process the presence of nHA prevented the full transition of silk I to silk II.

Further work in the development of reactively inkjet printed RSF barrier membranes should consider the effect of controlling β-sheet content on RSF film mechanical properties. A limitation of using the MicroFab DOD piezoelectric inkjet printer is that printing was limited to a singular nozzle a at a time. This meant that substantial printing times were required in order to print large amounts of material. Therefore, it was not practical to produce RSF films which were sufficiently large enough to perform mechanical testing on. Further work should consider using a printer which can print out of multiple nozzles at once, and hence produce thicker RSF membranes with a faster rate of printing.

The mechanical properties of the RSF barrier membranes is an important aspect for producing barrier membranes. When the barrier membranes are positioned *in-situ* they must be able to withstand the forces induced during mastication and prevent the collapse of defect space [5], [12], [20]-[22]. Current commercial barrier membranes have a tensile strength around 10 MPa (Appendix), however this figure represents mostly collagen based membranes due to insufficient studies regarding the mechanical properties of the non-resorbable and synthetic-resorbable

commercial membranes. Collagen membranes are also considered to have a poor structural integrity [46] in comparison to the non-resorbable and synthetic-resorbable membranes, therefore it may be necessary for RSF barrier membranes to have better mechanical properties than those reported for the collagen membranes. A way in which the mechanical properties of RSF barrier membranes could be controlled is via RSF crystallinity. As has been demonstrated in Chapter 5, reactive inkjet printing is able to control RSF crystallinity and may therefore the ability to tailor the mechanical properties of the RSF films to suit patient specific needs; regarding the size and placement of the defect.

The inclusion of nHA was shown to be beneficial for osteogenic affects. Conversely, printing of a composite ink was shown to hinder the transition of silk I to silk II. The ability of reactive inkjet printing to print bioactive inclusions within the barrier membranes at different concentrations offers huge potential for producing an ideal barrier membrane. However, due to the composite ink hindering the transition of silk I to silk II, it is recommended that future work (investigating reactive inkjet printing of RSF and nHA) should print the nHA as a separate ink to that of the RSF.

The cell work included in this thesis has concentrated on RSF film interaction with hard tissue MG63 cells. Further work would need to be conducted to investigate the influence of RSF crystallinity and topography on soft tissue cells. The requirements for soft tissue integration will be different to that of the hard tissue, and therefore, different surface properties may need to be produced for interfacing with the gingiva.

Appendix

Table 19: Summary table of commercial barrier membranes used in periodontal regeneration surgeries

Product	Material	Tensile Strength	Degradation	Comments	References
Non-Resorbable					
Gore-Tex® Regenerative Membrane	ePTFE	n/a	n/a	Coronal border with open microstructure and occlusive middle region. Discontinued for periodontal use	[6]
Cytoplast™ GBR-200,	dPTFE	n/a	n/a	Original Cytoplast™ membrane, impervious to bacteria and designed to withstand exposure	[6], [26], [189]
Cytoplast™ TXT-200,	dPTFE	n/a	n/a	Designed to withstand exposure, and can be non-surgically removed after at least 21 days	[6], [26], [190]
Cytoplast™ Ti-250,	dPTFE/ Titanium	n/a	n/a	Titanium used to increase mechanical support	[27], [191]
Resorbable Synthetic Polymer					
Guidor Membrane®, Sunstar Americas Inc.	Poly-D, L-lactide and Poly-L-lactide, blended with Acetyl tri-n-butyl Citrate	n/a	3 – 6 months	Becomes malleable at room temperature to enable easier handling	[192]
Resolut® LT, Gore	PLGA	11.7 MPa	16 – 24 weeks	Two layers; a PGLA dense occlusive layer and fibrous polyglycolide layer for tissue integration. Used for periodontal and bone repair	[27], [193], [194]

Epi-Guide®, Cursan	Polylactic acid	n/a	6 – 12 months	Three layers creating a gradient of density and porosity to allow fibrous ingrowth, as well as cell occlusion. Is hydrophilic to absorb blood.	[28], [195]
Vicryl® Periodontal Mesh, Ethicon	Polyglactin 910	n/a	8 weeks	Used for Periodontal regeneration and hernia fixation	[6]
Atrisorb®, Tolmar Inc.	Poly(DL-lactide) dissolved in N-methyl-2-pyrrolidone	n/a	9 – 12 months	Applied as a liquid *in-situ* to reduce surgical times	[27], [196]
Resorbable Natural Polymer					
Cytoplast™ RTM Collagen Membrane	Bovine Tendon, Collagen Type I	n/a	26 – 38 weeks	Longest lasting degradation rate of commercially available membranes	[29]
BioMend®, Zimmer Dental	Bovine Tendon, Collagen Type I	8 – 9 MPa	8 weeks	Semi-occlusive with nano-sized pores.	[30]
BioMend Extend®, Zimmer Dental	Bovine Tendon, Collagen Type I	9 – 9.5 MPa	18 weeks	Cross linked to increase reduce degradation rate.	[30]
Bio-Gide®, Geistlich Pharma	Porcine Skin, Collagen Type I	11.4 MPa	24 weeks	Two layers; dense region for cell occlusion and porous for bony ingrowth	[31], [197]
Parasorb Resedont®, Resorba Medical GmbH	Equine	n/a	n/a	Very thin membrane designed for delicate procedures. Used for GBR, jaw defects and sinus lifts	[32], [198]
Alloderm®, BioHorizons	Allograft, Collagen Type I	9 MPa	16 weeks	Supports rapid revascularization and white cell migration, with excellent tissue integration	[1], [33], [199]

References

[1]   M. C. Bottino, V. Thomas, G. Schmidt, Y. K. Vohra, T.-M. G. Chu, M. J. Kowolik, and G. M. Janowski, "Recent advances in the development of GTR/GBR membranes for periodontal regeneration--a materials perspective.," *Dent Mater*, vol. 28, no. 7, pp. 703–721, Jul. 2012.

[2]   P. I. Eke, B. A. Dye, L. Wei, G. O. Thornton-Evans, and R. J. Genco, "Prevalence of Periodontitis in Adults in the United States: 2009 and 2010," *Journal of Dental Research*, vol. 91, no. 10, pp. 914–920, Aug. 2012.

[3]   B. Mullally, C. Irwin, H. Ziada, E. Allen, and P. J. Byrne, "Periodontics: 3. Non-Surgical Periodontal Therapy in General Dental Practice," *Dental Update*, vol. 34, no. 6, pp. 326–328, Jul. 2007.

[4]   G. Allen, "Producing guidance for the management of patients with chronic periodontal disease in general dental practice," *British Dental Journal*, vol. 218, no. 8, pp. 461–466, Apr. 2015.

[5]   T. S. BS and J. A. MS, "The Development of Guided Regeneration: Making the Impossible Possible and the Unpredictable Predictable," *The Journal of Evidence-Based Dental Practice*, vol. 12, no. 3, pp. 101–117, Sep. 2012.

[6]   Y. D. Rakhmatia, Y. Ayukawa, A. Furuhashi, and K. Koyano, "Current barrier membranes: titanium mesh and other membranes for guided bone regeneration in dental applications.," *J Prosthodont Res*, vol. 57, no. 1, pp. 3–14, Jan. 2013.

[7]   T. Karring and P. Cortellini, "Regenerative therapy: furcation defects," *Periodontol. 2000*, vol. 19, no. 1, pp. 115–137, Feb. 1999.

[8]   G. Polimeni, A. V. Xiropaidis, and U. M. E. Wikesjo, "Biology and principles of periodontal wound healing/regeneration.," *Periodontol. 2000*, vol. 41, no. 1, pp. 30–47, 2006.

[9]   A. K. Garg, *Bone Biology, Harvesting, and Grafting for Dental Implants: Rationale and Clinical Applications*, vol. 14, no. 3. Blackwell Science Ltd, 2005.

[10]   R. B. de Santana, C. M. L. de Mattos, C. E. Francischone, and T. Van Dyke, "Superficial topography and porosity of an absorbable barrier membrane impacts soft tissue response in guided bone regeneration.," *Journal of Periodontology*, vol. 81, no. 6, pp. 926–933, Jun. 2010.

[11]   H.-T. Hu, S.-Y. Lee, C.-C. Chen, Y.-C. Yang, and J.-C. Yang, "Processing and properties of hydrophilic electrospun polylactic acid/beta-tricalcium phosphate membrane for dental applications," *Polym Eng Sci*, vol. 53, no. 4, pp. 833–842, Sep. 2012.

[12]   G. Polimeni, K.-T. Koo, M. Qahash, A. V. Xiropaidis, J. M. Albandar, and U. M. E. Wikesjo, "Prognostic factors for alveolar regeneration: effect of tissue occlusion on alveolar bone regeneration with guided tissue regeneration.," *J Clin Periodontol*, vol. 31, no. 9, pp. 730–735, Sep. 2004.

[13]   Naznin Sultana, "Study of in vitro degradation of biodegradable polymer based thin films and tissue engineering scaffolds," *Afr. J. Biotechnol.*, vol. 10, no. 81, pp. 1–7, Dec. 2011.

[14] D. Lundgren, A. K. Lundgren, L. Sennerby, and S. Nyman, "Augmentation of intramembraneous bone beyond the skeletal envelope using an occlusive titanium barrier. An experimental study in the rabbit.," *Clin Oral Implants Res*, vol. 6, no. 2, pp. 67–72, Jun. 1995.

[15] L. Kostopoulos and T. Karring, "Augmentation of the rat mandible using guided tissue regeneration.," *Clin Oral Implants Res*, vol. 5, no. 2, pp. 75–82, Jun. 1994.

[16] A. Lundgren, D. Lundgren, and A. Taylor, "Influence of barrier occlusiveness on guided bone augmentation. An experimental study in the rat.," *Clin Oral Implants Res*, vol. 9, no. 4, pp. 251–260, Aug. 1998.

[17] J. Schmid, C. H. F. Hammerle, A. J. Olah, and N. P. Lang, "Membrane permeability is unnecessary for guided generation of new bone. An experimental study in the rabbit.," *Clin Oral Implants Res*, vol. 5, no. 3, pp. 125–130, Sep. 1994.

[18] U. M. E. Wikesjo, W. H. Lim, R. C. Thomson, and W. R. Hardwick, "Periodontal repair in dogs: gingival tissue occlusion, a critical requirement for GTR?," *J Clin Periodontol*, vol. 30, no. 7, pp. 655–664, Jul. 2003.

[19] G. R. Owen, J. K. Jackson, B. Chehroudi, D. M. Brunette, and H. M. Burt, "An in vitro study of plasticized poly(lactic-co-glycolic acid) films as possible guided tissue regeneration membranes: Material properties and drug release kinetics," *J. Biomed. Mater. Res.*, vol. 95, no. 3, pp. 857–869, Sep. 2010.

[20] G. Polimeni, K.-T. Koo, M. Qahash, A. V. Xiropaidis, J. M. Albandar, and U. M. E. Wikesjo, "Prognostic factors for alveolar regeneration: effect of a space-providing biomaterial on guided tissue regeneration.," *J Clin Periodontol*, vol. 31, no. 9, pp. 725–729, Sep. 2004.

[21] G. Polimeni, K.-T. Koo, M. Qahash, A. V. Xiropaidis, J. M. Albandar, and U. M. E. Wikesjo, "Prognostic factors for alveolar regeneration: bone formation at teeth and titanium implants.," *J Clin Periodontol*, vol. 31, no. 11, pp. 927–932, Nov. 2004.

[22] G. Polimeni, J. M. Albandar, and U. M. E. Wikesjo, "Prognostic factors for alveolar regeneration: effect of space provision.," *J Clin Periodontol*, vol. 32, no. 9, pp. 951–954, Sep. 2005.

[23] U. M. E. Wikesj and R. Nilveus, "Periodontal Repair in Dogs: Effect of Wound Stabilization on Healing*," *Journal of Periodontology*, vol. 61, no. 12, pp. 719–724, Dec. 1990.

[24] C. H. F. Hämmerle and R. E. Jung, "Bone augmentation by means of barrier membranes.," *Periodontol. 2000*, vol. 33, pp. 36–53, 2003.

[25] T. V. Scantlebury, "1982-1992: a decade of technology development for guided tissue regeneration.," *Journal of Periodontology*, vol. 64, no. 11, pp. 1129–1137, Nov. 1993.

[26] "Cytoplast™ Barrier Membranes, Osteogenics Biomedical," *osteogenics.com*. [Online]. Available: https://www.osteogenics.com/v/product-family/cytoplast-barrier-membranes/v8/. [Accessed: 14-Oct-2013].

[27] P. Gentile, V. Chiono, C. Tonda-Turo, A. M. Ferreira, and G. Ciardelli,

"Polymeric membranes for guided bone regeneration.," *Biotechnol J*, vol. 6, no. 10, pp. 1187–1197, Oct. 2011.

[28]   "EpiGuide." [Online]. Available: http://curasaninc.com/products/epiguide/. [Accessed: 18-Jan-2016].

[29]   "Cytoplast RTM Collagen," *osteogenics.com*. [Online]. Available: https://www.osteogenics.com/media/uploads/productGroupDocs/2bpds 46cf0.pdf. [Accessed: 14-Oct-2013].

[30]   S. T. Li, H. C. Chen, N. S. Lee, R. Ringshia, and D. Yuen, "A Comparative Study Of Zimmer BioMend® And BioMend® Extend™ Membranes Made At Two Different Manufacturing Facilities," *zimmerdental.fr*, 2013. [Online]. Available: http://www.zimmerdental.fr/access-dam/51f0cdb2dbf9ca4635000006/1/inline/ZD1218_Biomend%20White% 20Paper_r4.pdf. [Accessed: 14-Feb-2014].

[31]   "Bio-Guide," *geistlich-na.com*, 25-Mar-2014. [Online]. Available: http://www.geistlich-na.com/en-us/professionals/membranes/bio-gide/user-benefits/. [Accessed: 14-Oct-2013].

[32]   "Resorba Dental," *resorba.com*. [Online]. Available: http://www.resorba.com/images/PDF/en/resorba_prospekt_dental_en_a nsicht_112010.pdf. [Accessed: 14-Oct-2013].

[33]   "Biologics," *biohorizons.com*. [Online]. Available: https://vsr.biohorizons.com/GetDocument?DocumentID=48056. [Accessed: 14-Oct-2013].

[34]   V. Lekovic, P. M. Camargo, P. R. Klokkevold, M. Weinlaender, E. B. Kenney, B. Dimitrijevic, and M. Nedic, "Preservation of Alveolar Bone in Extraction Sockets Using Bioabsorbable Membranes," *Journal of Periodontology*, vol. 69, no. 9, pp. 1044–1049, Sep. 1998.

[35]   D. Engler-Hamm, W. S. Cheung, A. Yen, P. C. Stark, and T. Griffin, "Ridge Preservation Using a Composite Bone Graft and a Bioabsorbable Membrane With and Without Primary Wound Closure: A Comparative Clinical Trial," *Journal of Periodontology*, vol. 82, no. 3, pp. 377–387, Mar. 2011.

[36]   A. Sculean, D. Nikolidakis, and F. Schwarz, "Regeneration of periodontal tissues: combinations of barrier membranes and grafting materials - biological foundation and preclinical evidence: a systematic review.," *J Clin Periodontol*, vol. 35, no. 8, pp. 106–116, Sep. 2008.

[37]   R. G. Caffesse, L. F. Mota, C. R. Quiñones, and E. C. Morrison, "Clinical comparison of resorbable and non-resorbable barriers for guided periodontal tissue regeneration.," *J Clin Periodontol*, vol. 24, no. 10, pp. 747–752, Oct. 1997.

[38]   J. Lindhe, R. Pontoriero, T. Berglundh, and M. Araujo, "The effect of flap management and bioresorbable occlusive devices in GTR treatment of degree III furcation defects. An experimental study in dogs," *Journal of clin*, vol. 22, no. 4, pp. 276–283, Apr. 1995.

[39]   K. Ito, K. Nanba, and S. Murai, "Effects of Bioabsorbable and Non-Resorbable Barrier Membranes on Bone Augmentation in Rabbit Calvaria," *Journal of Periodontology*, vol. 69, no. 11, pp. 1229–1237, Nov. 1998.

[40]   A. Kasaj, C. Reichert, H. Gotz, B. Rohrig, R. Smeets, and B. Willershausen, "In vitro evaluation of various bioabsorbable and nonresorbable barrier membranes for guided tissue regeneration.," *Head Face Med*, vol. 4, p. 22, 2008.

[41]   J. Neunzehn, B. Lüttenberg, and H.-P. Wiesmann, "Investigation of biomaterials by human epithelial gingiva cells: an in vitro study.," *Head Face Med*, vol. 8, no. 1, p. 35, 2012.

[42]   S. Liao, W. Wang, M. Uo, S. Ohkawa, T. Akasaka, K. Tamura, F. Cui, and F. Watari, "A three-layered nano-carbonated hydroxyapatite/collagen/PLGA composite membrane for guided tissue regeneration.," *Biomaterials*, vol. 26, no. 36, pp. 7564–7571, Dec. 2005.

[43]   S. Liao, F. Watari, Y. Zhu, M. Uo, T. Akasaka, W. Wang, G. Xu, and F. Cui, "The degradation of the three layered nano-carbonated hydroxyapatite/collagen/PLGA composite membrane in vitro.," *Dental Materials*, vol. 23, no. 9, pp. 1120–1128, Sep. 2007.

[44]   Y.-T. Chen, H.-L. Wang, D. E. Lopatin, R. O'Neal, and R. L. MacNeil, "Bacterial Adherence to Guided Tissue Regeneration Barrier Membranes Exposed to the Oral Environment," *Journal of Periodontology*, vol. 68, no. 2, pp. 172–179, Feb. 1997.

[45]   S.-H. Teng, E.-J. Lee, P. Wang, D.-S. Shin, and H.-E. Kim, "Three-layered membranes of collagen/hydroxyapatite and chitosan for guided bone regeneration.," *J. Biomed. Mater. Res. Part B Appl. Biomater.*, vol. 87, no. 1, pp. 132–138, Oct. 2008.

[46]   H. Tal, A. Kozlovsky, Z. Artzi, C. E. Nemcovsky, and O. Moses, "Cross-linked and non-cross-linked collagen barrier membranes disintegrate following surgical exposure to the oral environment: a histological study in the cat," *Clin Oral Implants Res*, vol. 19, no. 8, pp. 760–766, Aug. 2008.

[47]   M. Nevins, M. L. Nevins, P. Schupbach, S.-W. Kim, Z. Lin, and D. M. Kim, "A Prospective, Randomized Controlled Preclinical Trial to Evaluate Different Formulations of Biphasic Calcium Phosphate in Combination With a Hydroxyapatite Collagen Membrane to Reconstruct Deficient Alveolar Ridges," *Journal of Oral Implantology*, vol. 39, no. 2, pp. 133–139, Apr. 2013.

[48]   M. Lotfi, M. Nejib, and M. Naceur, "Cell Adhesion to Biomaterials: Concept of Biocompatibility," in *Advances in Biomaterials Sciences and Biomedical Applications*, no. 8, R. Pignatello, Ed. InTech, 2013.

[49]   "Inion GTR Membrane System," *curasanic.com*. [Online]. Available: http://curasaninc.com/products/inion-gtr/. [Accessed: 26-Jan-2016].

[50]   R. A. Zwahlen, L. K. Cheung, L.-W. Zheng, R. L. K. Chow, T. Li, B. Schuknecht, K. W. Grätz, and F. E. Weber, "Comparison of two resorbable membrane systems in bone regeneration after removal of wisdom teeth: a randomized-controlled clinical pilot study," *Clin Oral Implants Res*, vol. 20, no. 10, pp. 1084–1091, Oct. 2009.

[51]   C. Erisken, D. M. Kalyon, and H. Wang, "Functionally graded electrospun polycaprolactone and beta-tricalcium phosphate nanocomposites for tissue engineering applications.," *Biomaterials*, vol. 29, no. 30, pp. 4065–4073, Oct. 2008.

[52]   J. K. Park, J. Yeom, E. J. Oh, M. Reddy, J. Y. Kim, D.-W. Cho, H. P. Lim, N. S. Kim, S. W. Park, H.-I. Shin, D. J. Yang, K. B. Park, and S. K. Hahn, "Guided bone regeneration by poly(lactic-co-glycolic acid) grafted hyaluronic acid bi-layer films for periodontal barrier applications.," *Acta Biomater*, vol. 5, no. 9, pp. 3394–3403, Nov. 2009.

[53]   F. Yang, S. K. Both, X. Yang, X. F. Walboomers, and J. A. Jansen, "Development of an electrospun nano-apatite/PCL composite membrane for GTR/GBR application.," *Acta Biomater*, vol. 5, no. 9, pp. 3295–3304, Nov. 2009.

[54]   F. Mei, J. Zhong, X. Yang, X. Ouyang, S. Zhang, X. Hu, Q. Ma, J. Lu, S. Ryu, and X. Deng, "Improved biological characteristics of poly(L-lactic acid) electrospun membrane by incorporation of multiwalled carbon nanotubes/hydroxyapatite nanoparticles.," *Biomacromolecules*, vol. 8, no. 12, pp. 3729–3735, Dec. 2007.

[55]   M. Kellomäki, H. Niiranen, K. Puumanen, N. Ashammakhi, T. Waris, and P. Törmälä, "Bioabsorbable scaffolds for guided bone regeneration and generation," *Biomaterials*, vol. 21, no. 24, pp. 2495–2505, Dec. 2000.

[56]   M. C. Bottino, V. Thomas, and G. M. Janowski, "A novel spatially designed and functionally graded electrospun membrane for periodontal regeneration.," *Acta Biomater*, vol. 7, no. 1, pp. 216–224, Jan. 2011.

[57]   J. Zhang, C. Huang, Q. Xu, A. Mo, J. Li, and Y. Zuo, "Biological properties of a biomimetic membrane for guided tissue regeneration: a study in rat calvarial defects.," *Clin Oral Implants Res*, vol. 21, no. 4, pp. 392–397, Apr. 2010.

[58]   M. Yang, Y. Shuai, G. Zhou, N. Mandal, and L. Zhu, "Nucleation of hydroxyapatite on Antheraea pernyi (A. pernyi) silk fibroin film.," *Biomed Mater Eng*, vol. 24, no. 1, pp. 731–740, 2014.

[59]   K. Novotna, M. Zajdlova, T. Suchy, D. Hadraba, F. Lopot, M. Zaloudkova, T. E. L. Douglas, M. Munzarova, M. Juklickova, D. Stranska, D. Kubies, D. Schaubroeck, S. Wille, L. Balcaen, M. Jarosova, H. Kozak, A. Kromka, Z. Svindrych, V. Lisa, K. Balik, and L. Bacakova, "Polylactide nanofibers with hydroxyapatite as growth substrates for osteoblast-like cells.," *J Biomed Mater Res A*, vol. 102, no. 11, pp. 3918–3930, Nov. 2014.

[60]   T. L. Arinzeh, T. Tran, J. Mcalary, and G. Daculsi, "A comparative study of biphasic calcium phosphate ceramics for human mesenchymal stem-cell-induced bone formation.," *Biomaterials*, vol. 26, no. 17, pp. 3631–3638, Jun. 2005.

[61]   M. Schumacher, F. Uhl, R. Detsch, U. Deisinger, and G. Ziegler, "Static and dynamic cultivation of bone marrow stromal cells on biphasic calcium phosphate scaffolds derived from an indirect rapid prototyping technique.," *J Mater Sci Mater Med*, vol. 21, no. 11, pp. 3039–3048, Nov. 2010.

[62]   I. Wepener, W. Richter, D. van Papendorp, and A. M. Joubert, "In vitro osteoclast-like and osteoblast cells' response to electrospun calcium phosphate biphasic candidate scaffolds for bone tissue engineering," *J Mater Sci Mater Med*, vol. 23, no. 12, pp. 3029–3040, Sep. 2012.

[63]   A. Friedmann, M. Dard, B.-M. Kleber, J.-P. Bernimoulin, and D. D.

Bosshardt, "Ridge augmentation and maxillary sinus grafting with a biphasic calcium phosphate: histologic and histomorphometric observations," *Clin Oral Implants Res*, vol. 20, no. 7, pp. 708–714, Jul. 2009.

[64]   M. Pietruska, J. Pietruski, K. Nagy, M. Brecx, N. B. Arweiler, and A. Sculean, "Four-year results following treatment of intrabony periodontal defects with an enamel matrix derivative alone or combined with a biphasic calcium phosphate," *Clin Oral Invest*, vol. 16, no. 4, pp. 1191–1197, Sep. 2011.

[65]   F. G. Omenetto and D. L. Kaplan, "New opportunities for an ancient material.," *Science*, vol. 329, no. 5991, pp. 528–531, Jul. 2010.

[66]   C. K. S. Pillai and C. P. Sharma, "Review paper: absorbable polymeric surgical sutures: chemistry, production, properties, biodegradability, and performance.," *J Biomater Appl*, vol. 25, no. 4, pp. 291–366, Nov. 2010.

[67]   B. Kundu, R. Rajkhowa, S. C. Kundu, and X. Wang, "Silk fibroin biomaterials for tissue regenerations.," *Adv. Drug Deliv. Rev.*, vol. 65, no. 4, pp. 457–470, Apr. 2013.

[68]   C. Vepari and D. L. Kaplan, "Silk as a Biomaterial.," *Progress in Polymer Science*, vol. 32, no. 8, pp. 991–1007, 2007.

[69]   H. J. Jin, J. Park, V. Karageorgiou, U. J. Kim, R. Valluzzi, P. Cebe, and D. L. Kaplan, "Water-Stable Silk Films with Reduced β-Sheet Content," *Adv. Funct. Mater.*, vol. 15, no. 8, pp. 1241–1247, Aug. 2005.

[70]   Y. Cao and B. Wang, "Biodegradation of silk biomaterials.," *Int J Mol Sci*, vol. 10, no. 4, pp. 1514–1524, Apr. 2009.

[71]   Q. Lu, B. Zhang, M. Li, B. Zuo, D. L. Kaplan, Y. Huang, and H. Zhu, "Degradation mechanism and control of silk fibroin.," *Biomacromolecules*, vol. 12, no. 4, pp. 1080–1086, Apr. 2011.

[72]   L. Meinel, S. Hofmann, V. Karageorgiou, L. Zichner, R. Langer, D. L. Kaplan, and G. Vunjak-Novakovic, "Engineering cartilage-like tissue using human mesenchymal stem cells and silk protein scaffolds.," *Biotechnol. Bioeng.*, vol. 88, no. 3, pp. 379–391, Nov. 2004.

[73]   Y. Wang, H.-J. Kim, G. Vunjak-Novakovic, and D. L. Kaplan, "Stem cell-based tissue engineering with silk biomaterials.," *Biomaterials*, vol. 27, no. 36, pp. 6064–6082, Dec. 2006.

[74]   L. Meinel, S. Hofmann, V. Karageorgiou, C. Kirker-Head, J. McCool, G. Gronowicz, L. Zichner, R. Langer, G. Vunjak-Novakovic, and D. L. Kaplan, "The inflammatory responses to silk films in vitro and in vivo," *Biomaterials*, vol. 26, no. 2, pp. 147–155, Jan. 2005.

[75]   B. B. Mandal and D. L. Kaplan, "Biologic Biomaterials: Silk," in *Biomaterials*, J. Wong, J. Bronzino, and D. Peterson, Eds. CRC Press, 2012, pp. 7.1–7.20.

[76]   B. D. Lawrence, M. Cronin-Golomb, I. Georgakoudi, D. L. Kaplan, and F. G. Omenetto, "Bioactive silk protein biomaterial systems for optical devices.," *Biomacromolecules*, vol. 9, no. 4, pp. 1214–1220, Apr. 2008.

[77]   B. Cirillo, M. Morra, and G. Catapano, "Adhesion and function of rat liver cells adherent to silk fibroin/collagen blend films.," *The International Journal of Artificial Organs*, vol. 27, no. 1, pp. 60–68, Jan. 2004.

[78]   Y. G. Chung, D. Tu, D. Franck, E. S. Gil, K. Algarrahi, R. M. Adam, D. L. Kaplan, C. R. Estrada Jr, and J. R. Mauney, "Acellular Bi-Layer Silk Fibroin Scaffolds Support Tissue Regeneration in a Rabbit Model of Onlay Urethroplasty," *PLoS ONE*, vol. 9, no. 3, p. e91592, 2014.

[79]   T.-L. Liu, J.-C. Miao, W.-H. Sheng, Y.-F. Xie, Q. Huang, Y.-B. Shan, and J.-C. Yang, "Cytocompatibility of regenerated silk fibroin film: a medical biomaterial applicable to wound healing.," *J Zhejiang Univ Sci B*, vol. 11, no. 1, pp. 10–16, Jan. 2010.

[80]   R. Ghassemifar, S. Redmond, Zainuddin, and T. V. Chirila, "Advancing towards a tissue-engineered tympanic membrane: silk fibroin as a substratum for growing human eardrum keratinocytes.," *J Biomater Appl*, vol. 24, no. 7, pp. 591–606, Mar. 2010.

[81]   C. Z. Zhou, F. Confalonieri, M. Jacquet, R. Perasso, Z. G. Li, and J. Janin, "Silk fibroin: Structural implications of a remarkable amino acid sequence," *Proteins*, vol. 44, no. 2, pp. 119–122, 2001.

[82]   S. Inoue, K. Tanaka, F. Arisaka, S. Kimura, K. Ohtomo, and S. Mizuno, "Silk fibroin of Bombyx mori is secreted, assembling a high molecular mass elementary unit consisting of H-chain, L-chain, and P25, with a 6:6:1 molar ratio.," *J. Biol. Chem.*, vol. 275, no. 51, pp. 40517–40528, Dec. 2000.

[83]   B. Panilaitis, G. H. Altman, J. Chen, and H. J. Jin, "Macrophage responses to silk," *Biomaterials*, vol. 24, pp. 3079–3085, 2003.

[84]   P. Aramwit, S. Kanokpanont, W. De-Eknamkul, and T. Srichana, "Monitoring of inflammatory mediators induced by silk sericin," *J. Biosci. Bioeng.*, vol. 107, no. 5, pp. 556–561, May 2009.

[85]   C. Z. Zhou, F. Confalonieri, N. Medina, Y. Zivanovic, C. Esnault, T. Yang, M. Jacquet, J. Janin, M. Duguet, R. Perasso, and Z. G. Li, "Fine organization of Bombyx mori fibroin heavy chain gene," *Nucleic Acids Res.*, vol. 28, no. 12, pp. 2413–2419, 2000.

[86]   S.-W. Ha, H. S. Gracz, A. E. Tonelli, and S. M. Hudson, "Structural Study of Irregular Amino Acid Sequences in the Heavy Chain of BombyxmoriSilk Fibroin," *Biomacromolecules*, vol. 6, no. 5, pp. 2563–2569, Sep. 2005.

[87]   C. Fu, Z. Shao, and V. Fritz, "Animal silks: their structures, properties and artificial production.," *Chem. Commun. (Camb.)*, no. 43, pp. 6515–6529, Nov. 2009.

[88]   D. Wilson, R. Valluzzi, and D. L. Kaplan, "Conformational transitions in model silk peptides.," *Biophysical Journal*, vol. 78, no. 5, pp. 2690–2701, May 2000.

[89]   T. Asakura and J. Yao, "13C CP/MAS NMR study on structural heterogeneity in Bombyx mori silk fiber and their generation by stretching," *Protein Science*, vol. 11, no. 11, pp. 2706–2713, Apr. 2009.

[90]   J. G. Hardy, L. M. Römer, and T. R. Scheibel, "Polymeric materials based on silk proteins," *Polymer*, vol. 49, no. 20, pp. 4309–4327, Sep. 2008.

[91]   J. Magoshi, Y. Magoshi, and S. Nakamura, "Physical properties and structure of silk. VII. Crystallization of amorphous silk fibroin induced by immersion in methanol," *Journal of Polymer Science: Polymer Physics Edition*, vol. 19, no. 1, pp. 185–186, Jan. 1981.

[92]   D. Huemmerich, U. Slotta, and T. Scheibel, "Processing and modification

of films made from recombinant spider silk proteins," *Appl. Phys. A*, vol. 82, no. 2, pp. 219–222, Nov. 2005.

[93]   I. Greving, M. Cai, F. Vollrath, and H. C. Schniepp, "Shear-Induced Self-Assembly of Native Silk Proteins into Fibrils Studied by Atomic Force Microscopy," *Biomacromolecules*, vol. 13, no. 3, pp. 676–682, Mar. 2012.

[94]   X. Hu, D. L. Kaplan, and P. Cebe, "Determining Beta-Sheet Crystallinity in Fibrous Proteins by Thermal Analysis and Infrared Spectroscopy," *Macromolecules*, vol. 39, no. 18, pp. 6161–6170, Sep. 2006.

[95]   X. Chen, Z. Shao, N. S. Marinkovic, L. M. Miller, P. Zhou, and M. R. Chance, "Conformation transition kinetics of regenerated Bombyx mori silk fibroin membrane monitored by time-resolved FTIR spectroscopy.," *Biophys. Chem.*, vol. 89, no. 1, pp. 25–34, Jan. 2001.

[96]   G. H. Altman, F. Diaz, C. Jakuba, T. Calabro, R. L. Horan, J. Chen, H. Lu, J. Richmond, and D. L. Kaplan, "Silk-based biomaterials.," *Biomaterials*, vol. 24, no. 3, pp. 401–416, Feb. 2003.

[97]   M. Li, M. Ogiso, and N. Minoura, "Enzymatic degradation behavior of porous silk fibroin sheets.," *Biomaterials*, vol. 24, no. 2, pp. 357–365, Jan. 2003.

[98]   K. Numata, P. Cebe, and D. L. Kaplan, "Mechanism of enzymatic degradation of beta-sheet crystals.," *Biomaterials*, vol. 31, no. 10, pp. 2926–2933, Apr. 2010.

[99]   K.-H. Kim, L. Jeong, H.-N. Park, S.-Y. Shin, W.-H. Park, S.-C. Lee, T.-I. Kim, Y.-J. Park, Y.-J. Seol, Y.-M. Lee, Y. Ku, I.-C. Rhyu, S.-B. Han, and C.-P. Chung, "Biological efficacy of silk fibroin nanofiber membranes for guided bone regeneration.," *J. Biotechnol.*, vol. 120, no. 3, pp. 327–339, Nov. 2005.

[100]   J.-Y. Song, S.-G. Kim, J.-W. Lee, W.-S. Chae, H. Kweon, Y.-Y. Jo, K.-G. Lee, Y.-C. Lee, J.-Y. Choi, and J.-Y. Kim, "Accelerated healing with the use of a silk fibroin membrane for the guided bone regeneration technique.," *Oral Surg Oral Med Oral Pathol Oral Radiol Endod*, vol. 112, no. 6, pp. e26–33, Dec. 2011.

[101]   Y. Y. Ha, Y. W. Park, H. Y. Kweon, Y. Y. Jo, and S. G. Kim, "Comparison of the physical properties and in vivo bioactivities of silkworm-cocoon-derived silk membrane, collagen membrane, and polytetrafluoroethylene membrane for guided bone regeneration," *Macromol. Res.*, 2014.

[102]   C. Meechaisue, P. Wutticharoenmongkol, R. Waraput, T. Huangjing, N. Ketbumrung, P. Pavasant, and P. Supaphol, "Preparation of electrospun silk fibroin fiber mats as bone scaffolds: a preliminary study," *Biomed Mater*, vol. 2, no. 3, pp. 181–188, Sep. 2007.

[103]   S. Y. Yang, T. H. Hwang, L. Che, J. S. Oh, Y. Ha, and W. Ryu, "Membrane-reinforced three-dimensional electrospun silk fibroin scaffolds for bone tissue engineering," *Biomedical Materials*, vol. 10, no. 3, Jun. 2015.

[104]   R. S. Hayden, K. P. Quinn, C. A. Alonzo, I. Georgakoudi, and D. L. Kaplan, "Quantitative characterization of mineralized silk film remodeling during long-term osteoblast–osteoclast co-culture," *Biomaterials*, vol. 35, no. 12, pp. 3794–3802, Apr. 2014.

[105]   J.-H. Kim, D.-K. Kim, O. J. Lee, H. W. Ju, J. M. Lee, B. M. Moon, H. J. Park, D. W. Kim, J. H. Lee, and C. H. Park, "Osteoinductive silk fibroin/titanium

dioxide/hydroxyapatite hybrid scaffold for bone tissue engineering," *International Journal of Biological Macromolecules*, vol. 82, pp. 160–167, Jan. 2016.

[106]   J.-Y. Kim, B.-E. Yang, J.-H. Ahn, S. O. Park, and H.-W. Shim, "Comparable efficacy of silk fibroin with the collagen membranes for guided bone regeneration in rat calvarial defects.," *J Adv Prosthodont*, vol. 6, no. 6, pp. 539–546, Dec. 2014.

[107]   "Seri Surgical Scaffold," *seri.com*. [Online]. Available: http://www.seri.com/. [Accessed: 18-Aug-2017].

[108]   "A Prospective Open-Label Study to Evaluate the Safety of the Meniscal Repair Scaffold, FibroFix™ Meniscus, in the Treatment of Meniscal Defects," *clinicaltrials.gov*. [Online]. Available: https://clinicaltrials.gov/ct2/show/NCT02205645. [Accessed: 18-Aug-2017].

[109]   Y. Wang, D. D. Rudym, A. Walsh, L. Abrahamsen, H.-J. Kim, H. S. Kim, C. Kirker-Head, and D. L. Kaplan, "In vivo degradation of three-dimensional silk fibroin scaffolds.," *Biomaterials*, vol. 29, no. 24, pp. 3415–3428, Aug. 2008.

[110]   R. Suntivich, I. Drachuk, R. Calabrese, D. L. Kaplan, and V. V. Tsukruk, "Inkjet Printing of Silk Nest Arrays for Cell Hosting," *Biomacromolecules*, vol. 15, no. 4, pp. 1428–1435, Apr. 2014.

[111]   H. Tao, B. Marelli, M. Yang, B. An, M. S. Onses, J. A. Rogers, D. L. Kaplan, and F. G. Omenetto, "Inkjet Printing of Regenerated Silk Fibroin: From Printable Forms to Printable Functions," *Adv. Mater.*, vol. 27, no. 29, pp. 4273–4279, Jun. 2015.

[112]   P. J. Smith and A. Morrin, "Reactive inkjet printing," *Journal of Materials Chemistry*, pp. 10965–10970, 2012.

[113]   P. Calvert, "Inkjet printing for materials and devices," *Chemistry of Materials*, 2001.

[114]   B. J. de Gans, P. C. Duineveld, and U. S. Schubert, "Inkjet printing of polymers: state of the art and future developments," *Adv. Mater.*, 2004.

[115]   B. Derby, "Bioprinting: inkjet printing proteins and hybrid cell-containing materials and structures," *J Mater Chem*, 2008.

[116]   H. Yoo and C. Kim, "Generation of inkjet droplet of non-Newtonian fluid," *Rheol Acta*, vol. 52, no. 4, pp. 313–325, Feb. 2013.

[117]   E. Tekin, P. J. Smith, and U. S. Schubert, "Inkjet printing as a deposition and patterning tool for polymers and inorganic particles," *Soft Matter*, pp. 703–713, 2008.

[118]   H. Dong, W. W. Carr, and J. F. Morris, "An experimental study of drop-on-demand drop formation," *Phys. Fluids*, vol. 18, no. 7, p. 072102, 2006.

[119]   B.-J. de Gans, E. Kazancioglu, W. Meyer, and U. S. Schubert, "Ink-jet Printing Polymers and Polymer Libraries Using Micropipettes," *Macromol. Rapid Commun.*, vol. 25, no. 1, pp. 292–296, Jan. 2004.

[120]   P. P. Bhat, S. Appathurai, M. T. Harris, M. Pasquali, G. H. McKinley, and O. A. Basaran, "Formation of beads-on-a-string structures during break-up of viscoelastic filaments," *Nature Physics*, vol. 6, no. 8, pp. 625–631, Jun. 2010.

[121]   D. C. Vadillo, T. R. Tuladhar, A. C. Mulji, S. Jung, S. D. Hoath, and M. R. Mackley, "Evaluation of the inkjet fluid's performance using the 'Cambridge Trimaster' filament stretch and break-up device," *J. Rheol.*, vol. 54, no. 2, pp. 261–23, 2010.

[122]   J. E. Fromm, "Numerical-Calculation of the Fluid-Dynamics of Drop-on-Demand Jets," *Ibm Journal of Research and Development*, vol. 28, no. 3, pp. 322–333, 1984.

[123]   M. Singh, H. M. Haverinen, P. Dhagat, and G. E. Jabbour, "Inkjet printing-process and its applications.," *Adv. Mater. Weinheim*, vol. 22, no. 6, pp. 673–685, Feb. 2010.

[124]   B. Derby, "Inkjet printing of functional and structural materials: fluid property requirements, feature stability, and resolution," *Annu. Rev. Mater. Res.*, 2010.

[125]   Y. Hu, Q. Zhang, R. You, L. Wang, M. Li, Y. Hu, Q. Zhang, R. You, and L. Wang, "The Relationship between Secondary Structure and Biodegradation Behavior of Silk Fibroin Scaffolds," *Advances in Materials Science and Engineering*, vol. 2012, no. 6, pp. 1–5, Aug. 2012.

[126]   I. Elgali, A. Turri, W. Xia, B. Norlindh, A. Johansson, C. Dahlin, P. Thomsen, and O. Omar, "Guided bone regeneration using resorbable membrane and different bone substitutes: Early histological and molecular events," *Acta Biomater*, vol. 29, pp. 409–423, Jan. 2016.

[127]   D. N. Rockwood, R. C. Preda, T. Yucel, X. Wang, M. L. Lovett, and D. L. Kaplan, "Materials fabrication from Bombyx mori silk fibroin.," *Nat Protoc*, vol. 6, no. 10, pp. 1612–1631, Oct. 2011.

[128]   M. K. Sah and K. Pramanik, "Regenerated Silk Fibroin from B. mori Silk Cocoon for Tissue Engineering Applications," *International Journal of Environmental Science and Development*, vol. 1, pp. 404–408, 2010.

[129]   C. Mo, C. Holland, D. Porter, Z. Shao, and F. Vollrath, "Concentration State Dependence of the Rheological and Structural Properties of Reconstituted Silk," *Biomacromolecules*, vol. 10, no. 10, pp. 2724–2728, Oct. 2009.

[130]   J. Lopes, M. Dias, and V. Da Silva, "Production method for calcium phosphate nano-particles with high purity and their use," 17-Jan-2008.

[131]   J. Schindelin, C. T. Rueden, M. C. Hiner, and K. W. Eliceiri, "The ImageJ ecosystem: An open platform for biomedical image analysis," *Molecular Reproduction and Development*, vol. 82, no. 7, pp. 518–529, Jul. 2015.

[132]   A. Daerr and A. Mogne, "Pendent_Drop: An ImageJ Plugin to Measure the Surface Tension from an Image of a Pendent Drop," *Journal of Open Research Software*, vol. 4, no. 7, p. 676, Jan. 2016.

[133]   J. Schindelin, I. Arganda-Carreras, E. Frise, V. Kaynig, M. Longair, T. Pietzsch, S. Preibisch, C. Rueden, S. Saalfeld, B. Schmid, J.-Y. Tinevez, D. J. White, V. Hartenstein, K. Eliceiri, P. Tomancak, and A. Cardona, "Fiji: an open-source platform for biological-image analysis," *Nature Methods*, vol. 9, no. 7, pp. 676–682, Jul. 2012.

[134]   X. Hu, K. Shmelev, L. Sun, E. S. Gil, S.-H. Park, P. Cebe, and D. L. Kaplan, "Regulation of Silk Material Structure by Temperature-Controlled Water Vapor Annealing," *Biomacromolecules*, vol. 12, no. 5, pp. 1686–1696, May 2011.

[135]   A. F. Stalder, G. Kulik, D. Sage, L. Barbieri, and P. Hoffmann, "A snake-based approach to accurate determination of both contact points and contact angles," *Colloids and Surfaces A: Physicochemical and Engineering Aspects*, vol. 286, no. 1, pp. 92–103, Sep. 2006.

[136]   "Protease Type XIV from Streptomyces greiseus," *sigmaaldrich.com*. [Online]. Available: http://www.sigmaaldrich.com/life-science/metabolomics/enzyme-explorer/analytical-enzymes/protease-type-xiv.html. [Accessed: 22-Aug-2017].

[137]   E. M. Pritchard, X. Hu, V. Finley, C. K. Kuo, and D. L. Kaplan, "Effect of silk protein processing on drug delivery from silk films.," *Macromol Biosci*, vol. 13, no. 3, pp. 311–320, Mar. 2013.

[138]   R. L. Horan, K. Antle, A. L. Collette, Y. Wang, J. Huang, J. E. Moreau, V. Volloch, D. L. Kaplan, and G. H. Altman, "In vitro degradation of silk fibroin.," *Biomaterials*, vol. 26, no. 17, pp. 3385–3393, Jun. 2005.

[139]   M. A. de Moraes, R. F. Weska, and M. M. Beppu, "Effects of sterilization methods on the physical, chemical, and biological properties of silk fibroin membranes.," *J. Biomed. Mater. Res. Part B Appl. Biomater.*, vol. 102, no. 4, pp. 869–876, May 2014.

[140]   "Quant-iTTM PicoGreen ® dsDNA Reagent and Kits," *tools.thermofisher.com*, 11-Jun-2008. [Online]. Available: https://tools.thermofisher.com/content/sfs/manuals/mp07581.pdf. [Accessed: 11-Nov-2014].

[141]   "Alkaline Phosphatase, Diethanolamine Detection Kit," *sigmaaldrich.com*, 2013. [Online]. Available: https://www.sigmaaldrich.com/content/dam/sigma-aldrich/docs/Sigma/Bulletin/1/ap0100bul.pdf. [Accessed: 11-Nov-2014].

[142]   B. Derby and N. Reis, "Inkjet Printing of Highly Loaded Particulate Suspensions," *MRS Bulletin*, vol. 28, no. 11, pp. 815–818, Nov. 2003.

[143]   E. Y. Arashiro and N. R. Demarquette, "Use of the pendant drop method to measure interfacial tension between molten polymers," *Materials Research*, vol. 2, no. 1, pp. 23–32, 1999.

[144]   T. Petrova and R. B. Dooley, *Revised Release on Surface Tension of Ordinary Water Substance*. The International Association for the Properties of Water and Steam, 2014.

[145]   Y. Yang, C. Dicko, C. D. Bain, Z. Gong, R. M. J. Jacobs, Z. Shao, A. E. Terry, and F. Vollrath, "Behavior of silk protein at the air–water interface," *Soft Matter*, vol. 8, no. 37, pp. 9705–9712, Aug. 2012.

[146]   N. Reis, C. Ainsley, and B. Derby, "Ink-jet delivery of particle suspensions by piezoelectric droplet ejectors," *Journal of Applied Physics*, vol. 97, no. 9, p. 094903, 2005.

[147]   L. S. Wray, X. Hu, J. Gallego, I. Georgakoudi, F. G. Omenetto, D. Schmidt, and D. L. Kaplan, "Effect of processing on silk-based biomaterials: Reproducibility and biocompatibility," *J. Biomed. Mater. Res.*, vol. 99, no. 1, pp. 89–101, Jun. 2011.

[148]   S. Tanvir and L. Qiao, "Surface tension of Nanofluid-type fuels containing suspended nanomaterials," *Nanoscale Res Lett*, vol. 7, no. 1, p. 226, Apr. 2012.

[149]   M. H. U. Bhuiyan, R. Saidur, M. A. Amalina, R. M. Mostafizur, and A. Islam, "Effect of Nanoparticles Concentration and Their Sizes on Surface Tension of Nanofluids," *Procedia Engineering*, vol. 105, pp. 431–437, 2015.

[150]   F. Ravera, E. Santini, G. Loglio, M. Ferrari, and L. Liggieri, "Effect of Nanoparticles on the Interfacial Properties of Liquid/Liquid and Liquid/Air Surface Layers," vol. 110, no. 39, pp. 19543–19551, Oct. 2006.

[151]   N. Sultana and T. H. Khan, "Water Absorption and Diffusion Characteristics of Nanohydroxyapatite (nHA) and Poly(hydroxybutyrate-co-hydroxyvalerate-) Based Composite Tissue Engineering Scaffolds and Nonporous Thin Films," *Journal of Nanomaterials*, vol. 2013, no. 21, pp. 1–8, May 2013.

[152]   M. I. Hassan, N. Sultana, and S. Hamdan, "Bioactivity Assessment of Poly(ε-caprolactone)/Hydroxyapatite Electrospun Fibers for Bone Tissue Engineering Application," *Journal of Nanomaterials*, vol. 2014, no. 8, pp. 1–6, Jul. 2014.

[153]   J. Guzowski, M. Tasinkevych, and S. Dietrich, "Free energy of colloidal particles at the surface of sessile drops," *Eur. Phys. J. E*, vol. 33, no. 3, pp. 219–242, Nov. 2010.

[154]   Y. S. Won, D. K. Chung, and A. F. Mills, "Density, viscosity, surface tension, and carbon dioxide solubility and diffusivity of methanol, ethanol, aqueous propanol, and aqueous ethylene glycol at 25 …," *Journal of Chemical Engineering Data*, vol. 26, no. 2, pp. 141–144, 1981.

[155]   X. Zhang and P. Wyeth, "Using FTIR spectroscopy to detect sericin on historic silk," *Sci. China Chem.*, vol. 53, no. 3, pp. 626–631, Mar. 2010.

[156]   H. Teramoto and M. Miyazawa, "Analysis of structural properties and formation of sericin fiber by infrared spectroscopy," *Journal of Insect Biotechnology and …*, 2003.

[157]   A. Barth and C. Zscherp, "What vibrations tell about proteins," *Quarterly Reviews of Biophysics*, vol. 35, no. 4, pp. 369–430, Nov. 2002.

[158]   B. Aksakal, "Temperature effect on the recovery process in stretched Bombyx mori silk fibers," *Spectrochimica Acta Part A: Molecular and Biomolecular Spectroscopy*, vol. 152, pp. 629–636, Jan. 2016.

[159]   B. L. Mojet, S. D. Ebbesen, and L. Lefferts, "Light at the interface: the potential of attenuated total reflection infrared spectroscopy for understanding heterogeneous catalysis in water," *Chem Soc Rev*, vol. 39, no. 12, pp. 4643–4655, 2010.

[160]   G. Keresztury, M. Incze, F. Soti, and L. Imre, "CO2 inclusion bands in ir spectra of KBr pellets," *Spectrochimica Acta Part A: …*, vol. 36, no. 11, pp. 1007–1008, 1980.

[161]   M. Boulet-Audet, F. Vollrath, and C. Holland, "Identification and classification of silks using infrared spectroscopy," *Journal of Experimental Biology*, vol. 218, no. 19, pp. 3138–3149, Oct. 2015.

[162]   A. Barth, "Infrared spectroscopy of proteins.," *Biochim. Biophys. Acta*, vol. 1767, no. 9, pp. 1073–1101, Sep. 2007.

[163]   X. Luo, J. Wu, A. Intisar, J. Geng, L. Wu, K. Zheng, and Y. Du, "Study on Light Aging of Silk Fabric by Fourier Transform Infrared Spectroscopy and Principal Component Analysis," *Analytical Letters*, vol. 45, no. 10, pp.

1286–1296, Apr. 2012.

[164]   R. Hienerwadel, A. Boussac, J. Breton, B. A. Diner, and C. Berthomieu, "Fourier Transform Infrared Difference Spectroscopy of Photosystem II Tyrosine D Using Site-Directed Mutagenesis and Specific Isotope Labeling ," *Biochemistry*, vol. 36, no. 48, pp. 14712–14723, Dec. 1997.

[165]   T. Asakura, K. Suita, T. Kameda, S. Afonin, and A. S. Ulrich, "Structural role of tyrosine in Bombyx mori silk fibroin, studied by solid-state NMR and molecular mechanics on a model peptide prepared as silk I and II," *Magnetic Resonance in Chemistry*, vol. 42, no. 2, pp. 258–266, Feb. 2004.

[166]   Tetsuo Asakura, Rena Sugino, Juming Yao, A. Hidehiko Takashima, and R. Kishore, "Comparative Structure Analysis of Tyrosine and Valine Residues in Unprocessed Silk Fibroin (Silk I) and in the Processed Silk Fiber (Silk II) from Bombyx mori Using Solid-State 13C,15N, and 2H NMR†," *Biochemistry*, vol. 41, no. 13, pp. 4415–4424, Mar. 2002.

[167]   X. Hu, D. L. Kaplan, and P. Cebe, "Dynamic protein-water relationships during beta-sheet formation," *Macromolecules*, vol. 41, no. 11, pp. 3939–3948, 2008.

[168]   X. Hu, Q. Lu, D. L. Kaplan, and P. Cebe, "Microphase Separation Controlled β-Sheet Crystallization Kinetics in Fibrous Proteins," *Macromolecules*, vol. 42, no. 6, pp. 2079–2087, Mar. 2009.

[169]   D. Gupta, A. Agrawal, and A. Rangi, "Extraction and characterization of silk sericin," *Indian Journal of Fibre & Textile Research (IJFTR)*, vol. 39, no. 4, pp. 364–372, 2014.

[170]   S. Marković, L. Veselinović, M. J. Lukić, L. Karanović, I. Bračko, N. Ignjatović, and D. Uskoković, "Synthetical bone-like and biological hydroxyapatites: a comparative study of crystal structure and morphology," *Biomed Mater*, vol. 6, no. 4, p. 045005, Aug. 2011.

[171]   J. J. Li, E. S. Gil, R. S. Hayden, C. Li, S.-I. Roohani-Esfahani, D. L. Kaplan, and H. Zreiqat, "Multiple Silk Coatings on Biphasic Calcium Phosphate Scaffolds: Effect on Physical and Mechanical Properties and In Vitro Osteogenic Response of Human Mesenchymal Stem Cells," *Biomacromolecules*, vol. 14, no. 7, pp. 2179–2188, Jul. 2013.

[172]   K. Venkateswarlu, A. Chandra Bose, and N. Rameshbabu, "X-ray peak broadening studies of nanocrystalline hydroxyapatite by Williamson–Hall analysis," *Physica B: Condensed Matter*, vol. 405, no. 20, pp. 4256–4261, Oct. 2010.

[173]   L. Berzina-Cimdina and N. Borodajenko, "Research of Calcium Phosphates Using Fourier Transform Infrared Spectroscopy," in *Infrared Spectroscopy - Materials Science, Engineering and Technology*, no. 6, T. Theophile, Ed. InTech, 2012.

[174]   P. Gentile, C. Wilcock, C. Miller, R. Moorehead, and P. V. Hatton, "Process Optimisation to Control the Physico-Chemical Characteristics of Biomimetic Nanoscale Hydroxyapatites Prepared Using Wet Chemical Precipitation," *Materials*, vol. 8, no. 5, pp. 2297–2310, Apr. 2015.

[175]   A. Paz, D. Guadarrama, M. López, J. E González, N. Brizuela, and J. Aragón, "A comparative study of hydroxyapatite nanoparticles synthesized by different routes," *Química Nova*, vol. 35, no. 9, pp. 1724–1727, 2012.

[176] I. Rehman and W. Bonfield, "Characterization of hydroxyapatite and carbonated apatite by photo acoustic FTIR spectroscopy," *J Mater Sci Mater Med*, vol. 8, no. 1, pp. 1–4, Jan. 1997.

[177] J. R. Woodard, A. J. Hilldore, S. K. Lan, C. J. Park, A. W. Morgan, J. A. C. Eurell, S. G. Clark, M. B. Wheeler, R. D. Jamison, and A. J. Wagoner Johnson, "The mechanical properties and osteoconductivity of hydroxyapatite bone scaffolds with multi-scale porosity," *Biomaterials*, vol. 28, no. 1, pp. 45–54, Jan. 2007.

[178] T. Yamane, K. Umemura, Y. Nakazawa, and T. Asakura, "Molecular Dynamics Simulation of Conformational Change of Poly(Ala-Gly) from Silk I to Silk II in Relation to Fiber Formation Mechanism of BombyxmoriSilk Fibroin," *Macromolecules*, vol. 36, no. 18, pp. 6766–6772, Sep. 2003.

[179] Q. Lu, X. Hu, X. Wang, J. A. Kluge, S. Lu, P. Cebe, and D. L. Kaplan, "Water-insoluble silk films with silk I structure.," *Acta Biomater*, vol. 6, no. 4, pp. 1380–1387, Apr. 2010.

[180] S.-W. Tsai, H.-M. Liou, C.-J. Lin, K.-L. Kuo, Y.-S. Hung, R.-C. Weng, and F.-Y. Hsu, "MG63 Osteoblast-Like Cells Exhibit Different Behavior when Grown on Electrospun Collagen Matrix versus Electrospun Gelatin Matrix," *PLoS ONE*, vol. 7, no. 2, p. e31200, Feb. 2012.

[181] N. R. Washburn, K. M. Yamada, C. G. Simon Jr., S. B. Kennedy, and E. J. Amis, "High-throughput investigation of osteoblast response to polymer crystallinity: influence of nanometer-scale roughness on proliferation," *Biomaterials*, vol. 25, no. 7, pp. 1215–1224, Mar. 2004.

[182] H. Cui and P. J. Sinko, "The role of crystallinity on differential attachment/proliferation of osteoblasts and fibroblasts on poly (caprolactone-co-glycolide) polymeric surfaces," *Front. Mater. Sci.*, vol. 6, no. 1, pp. 47–59, Dec. 2011.

[183] G. Passeri, A. Cacchioli, F. Ravanetti, C. Galli, E. Elezi, and G. M. Macaluso, "Adhesion pattern and growth of primary human osteoblastic cells on five commercially available titanium surfaces," *Clin Oral Implants Res*, vol. 21, no. 7, pp. 756–765, Jul. 2010.

[184] V. Karageorgiou and D. L. Kaplan, "Porosity of 3D biomaterial scaffolds and osteogenesis," *Biomaterials*, vol. 26, no. 27, pp. 5474–5491, Sep. 2005.

[185] E. E. Golub and K. Boesze-Battaglia, "The role of alkaline phosphatase in mineralization," *Current Opinion in Orthopaedics*, 2007.

[186] S. Bhumiratana, W. L. Grayson, A. Castaneda, D. N. Rockwood, E. S. Gil, D. L. Kaplan, and G. Vunjak-Novakovic, "Nucleation and growth of mineralized bone matrix on silk-hydroxyapatite composite scaffolds," *Biomaterials*, vol. 32, no. 11, pp. 2812–2820, Apr. 2011.

[187] Y. Wu, G. Dong, W. Xiao, E. Xiao, F. Miao, A. Syverson, N. Missaghian, R. Vafa, A. A. Cabrera-Ortega, J. C Rossa, and D. T. Graves, "Effect of Aging on Periodontal Inflammation, Microbial Colonization, and Disease Susceptibility," *Journal of Dental Research*, p. 0022034515625962, Jan. 2016.

[188] K. F. Al-Shammari, A. K. Al-Khabbaz, J. M. Al-Ansari, R. Neiva, and H.-L. Wang, "Risk Indicators for Tooth Loss Due to Periodontal Disease,"

Journal of Periodontology, vol. 76, no. 11, pp. 1910–1918, Nov. 2005.

[189]   "Cytoplast™ Barrier Membranes GBR-200 & GBR-200 Singles, Osteogenics Biomedical," *osteogenics.com*. [Online]. Available: https://www.osteogenics.com/v/product-group/GBR-200-GBR-200-Singles/v9/. [Accessed: 24-Aug-2017].

[190]   "Cytoplast TXT-200," *osteogenics.com*. [Online]. Available: https://www.osteogenics.com/media/uploads/productGroupDocs/1246o6c79ukq.pdf. [Accessed: 24-Aug-2017].

[191]   "Cytoplast™ Barrier Membranes Ti-250 Titanium-Reinforced, Osteogenics Biomedical," *osteogenics.com*. [Online]. Available: https://www.osteogenics.com/v/product-group/Ti-250-Titanium-Reinforced/vb/. [Accessed: 25-Aug-2017].

[192]   "GUIDOR® Bioresorbable Matrix Barrier." [Online]. Available: http://us.guidor.com/guidorr-bioresorbable-matrix-barrier.html. [Accessed: 24-Aug-2017].

[193]   "Resolut Adapt LT Technical Considerations," *www.flexident.ch*. [Online]. Available: http://www.flexident.ch/upload/flexident/files/Resolut_Adapt_LT_Techn-Considerations.pdf. [Accessed: 24-Aug-2017].

[194]   E. Milella, P. A. Ramires, E. Brescia, G. La Sala, L. Di Paola, and V. Bruno, "Physicochemical, mechanical, and biological properties of commercial membranes for GTR.," *J. Biomed. Mater. Res.*, vol. 58, no. 4, pp. 427–435, 2001.

[195]   F. Hermann, "Clinical Observations on the New Epi-Guide Barrier Matrix in Periodontological and Implantological Indications ," *Implants*, vol. 3, pp. 24–29, 2007.

[196]   L. T. Hou, J. J. Yan, A. Y. M. Tsai, C. S. Lao, S. J. Lin, and C. M. Liu, "Polymer-assisted regeneration therapy with Atrisorb® barriers in human periodontal intrabony defects," *J Clin Periodontol*, vol. 31, no. 1, pp. 68–74, Jan. 2004.

[197]   A. Bozkurt, C. Apel, B. Sellhaus, S. van Neerven, B. Wessing, R. D. Hilgers, and N. Pallua, "Differences in degradation behavior of two non-cross-linked collagen barrier membranes: an in vitro and in vivo study," *Clin Oral Implants Res*, vol. 25, no. 12, pp. 1403–1411, Dec. 2014.

[198]   "PARASORB RESODONT®," *resorba.com*. [Online]. Available: http://www.resorba.com/index.php/en/dental-surgery/collagens-for-implantology/resodont.html. [Accessed: 25-Aug-2017].

[199]   A. P. Sclafani, S. A. McCormick, and R. Cocker, "Biophysical and microscopic analysis of homologous dermal and fascial materials for facial aesthetic and reconstructive uses," *Arch Facial Plast Surg.*, vol. 4, pp. 164–171, 2002.